HIGHLY EMISSIVE MOLECULAR PROBES FOR

TARGETED CELLULAR IMAGING USING

SUPER RESOLUTION OPTICAL MICROSCOPY

Department of Chemistry
University of Sheffield

A Thesis submitted for the Degree of Doctor of Philosophy

April 2018

By

SREEJESH SREEDHARAN

To my loved ones

ABSTRACT

In this work a range of organic, metal complex and nanoparticle architectures have been investigated and optimized as probes and drug delivery agents. With the aid of a range of super-resolution techniques the role of these new molecular systems in detecting and imaging structures, organelles and biological processes within cells were delineated. These studies have identified new probes to image mitochondria and nuclear DNA at <50 nm resolutions, investigated the potential of organic probes to image reactive oxygen and nitrogen species in live cells, assessed the potential of new nanocapsules as putative drug delivery agents, and identified a new paradigm for the construction of probes based on organelle targeted two-photon upconversion nanoparticles.

Research output arising from this Ph.D

❖ Lei Song, Yuan Guo, Deborah Roebuck, Chun Chen, Min Yang, Zhongqiang Yang, **Sreejesh Sreedharan**, Caroline Glover, **Jim A Thomas**, Dongsheng Liu, Shengrong Guo*, Rongjun Chen*, Dejian Zhou* Terminal PEGylated DNA–Gold Nanoparticle Conjugates Offering high resistance to Nuclease degradation and efficient intracellular delivery of DNA binding Agents. *ACS Applied Materials & Interfaces,* **2015**, *7*, 18707–18716

❖ **Sreejesh Sreedharan**, Martin R Gill, Esther Garcia, Hiwa K Saeed, Darren Robinson, Aisling Byrne, Ashley J Cadby, Tia E Keyes, Carl G Smythe, Patrina Pellett*, Jorge Bernardino de la Serna*, **Jim A Thomas*** Multi model Super-resolution microscopy using a Transition metal complex probe provides unprecedented capabilities for imaging both nuclear chromatin and mitochondria. *Journal of the American Chemical Society,* **2017,** *139,* 15907-15913

❖ Firoj Ali, **Sreejesh Sreedharan**, Anila H A, Hiwa K Saeed, Carl G Smythe, **Jim A Thomas***, Amitava Das* A Super-resolution probe to monitor HNO levels in the Endoplasmic Reticulum of RAW cells**.** *Analytical Chemistry,* **2017**, *89*, 12087-12093

❖ Sumit Kumar Pramanik[#]*, **Sreejesh Sreedharan**[#], Harwinder Singh, Nicola H Green, Carl G Smythe, **Jim A Thomas***, Amitava Das* Imaging cellular trafficking processes in real time using lysosome targeted up-conversion nanoparticles. *Chemical Communications,* **2017**, *53*, 12672-12675

❖ Firoj Ali[#], Sunil Aute[#], **Sreejesh Sreedharan**[#], Anila H A, Hiwa K Saeed, Carl G Smythe*, **Jim A Thomas***, Amitava Das* A Luminescent probe for Super-resolution imaging of Endogenous HOCl in multiple Cellular Compartments in Macrophages. *Chemical Communications,* **2018,** *54,* 1849-1852

❖ **Sreejesh Sreedharan**[#], Alessandro Sinopoli[#], Paul. J. Jarman, Darren Robinson, Christopher Clemmet, Paul A. Scattergood, Craig R. Rice, Carl. G. W. Smythe, **James A Thomas***, Paul I.P. Elliott* Mitochondria-localizing DNA binding biscyclometalated phenyltriazole iridium(III) dipyridophenazene complexes: syntheses and cellular imaging properties. *Dalton Transactions,* **2018,** *47,* 4931-4940

❖ Anila H A, **Sreejesh Sreedharan**, Firoj Ali, Carl G Smythe, **Jim A Thomas***, Amitava Das* Polysulfide-Triggered Fluorescent Indicator Suitable for Super-Resolution Microscopy and Application in Imaging. *Chemical Communications,* **2018** (**DOI:** 10.1039/C8CC01332B)

Although not discussed herein, the candidate also contributed to the following paper:

❖ Hiwa K Saeed, Paul J Jarman, Stuart Archer, **Sreejesh Sreedharan**, Ibrahim Q Saeed, Luke K Mckenzie, Julia A Weinstein, Niklaas J Buurma, Carl G Smythe, **Jim A Thomas*** Homo and heteroleptic phototoxic dinuclear metallo-intercalators based on Ru[II](dppn) intercalating moieties: synthesis, optical and biological studies. *Angewandte Chemie International Edition,* **2017**, *56*, 12628-12633

ACKNOWLEDGEMENTS

DECLARATION

The work within this thesis is original. It has not been submitted, in whole or in part, for any other degree. The results shown within this thesis are original and they exclusively belong to the author. Some of these results have already been published in peer-reviewed journals and they are included in this thesis.

Sreejesh Sreedharan
April 2018

CONTENTS

1.0 INTRODUCTION

2.0 SUPER-RESOLUTION MICROSCOPY STUDIES ON LUMINESCENT METAL COMPLEXES

3.0 DETECTION OF INTRACELLULAR REACTIVE OXYGEN/NITROGEN SPECIES AND SPECIFIC IMAGING OF MITOCHONDRIA USING SUPER-RESOLUTION MICROSCOPY PROBES

4.0 IN CELL OPTICAL MICROSCOPY STUDIES ON NANOMATERIALS

5.0 EXPERIMENTS AND ANALYSIS

CONCLUSION AND FUTURE WORK

REFERENCES

APPENDIX

LIST OF FIGURES

ABBREVIATIONS USED IN TEXT

A	Adenine
AS	Angeli's salt
Bipy	Bipyridine
Bp	Base pair
C	Cytosine
CD	Circular Dichroism
CT-DNA	Calf Thymus DNA
dCLSM	Deconvoluted Confocal laser scanning microscopy
Dppz	Dipyrido [3,2-a:2',3'-c] phenazine
DTT	Dithiothreitol
DNA	Deoxyribonucleic acid
ER	Endoplasmic Reticulum
FIB	Focussed ion beam
G	Guanine
Golgi	Golgi complex (or) Golgi apparatus
HOMO	Highest occupied molecular orbital
ICT	Intramolecular-charge-transfer
ISC	Inter system crossing
LC	Ligand centered
LD	Linear Dichroism
LPS	Lippopolysaccharides
LPNC	Luminescent polymer nanocapsules
LTDR	Lyso Tracker Deep Red
LUMO	Lowest unoccupied molecular orbital
Lyso	Lysosomes
Mito	Mitchondria
MLC	Metal ligand complexes
MLCT	Metal-to-ligand-charge-transfer
MTDR	Mito Tracker Deep Red
NA	Numerical aperture
NMR	Nuclear magnetic resonance

NP	Nanoparticle
OTF	Optical transfer function
PALM	Photoactivated localisation microscopy
Phen	Phenanthroline
PSF	Point spread function
RNA	Ribonucleic acid
RNS	Reactive nitrogen species
RNC	Red nanocapsules
ROS	Reactive oxygen species
ROXS	Reducing and Oxidising system
Ru	Ruthenium
SIM	Structured illumination microscopy
STED	Stimulated emission by depletion
STORM	Stochastic optical reconstruction microscopy
T	Thymine
TFA	Trifluoroacetic acid
TFO	Triplex forming oligonucleotide
TIRF	Total internal reflection
Tpphz	Tetrapyrido[3,2-a:2',3'-c:3'',2''-h:2''',3'''-j]phenazine
UV	Ultra violet
YNC	Yellow nanocapsules

1.0 INTRODUCTION

1.1 THE STRUCTURE OF DNA

Deoxyribose nucleic acid (DNA) is a biopolymer chain that contains three components; a deoxyribose sugar, a base and a phosphate. The polynucleotide chain is formed by phosphodiester linkages between the 3'-hydroxyl group of one nucleotide and the 5'-hydroxyl group of the next.
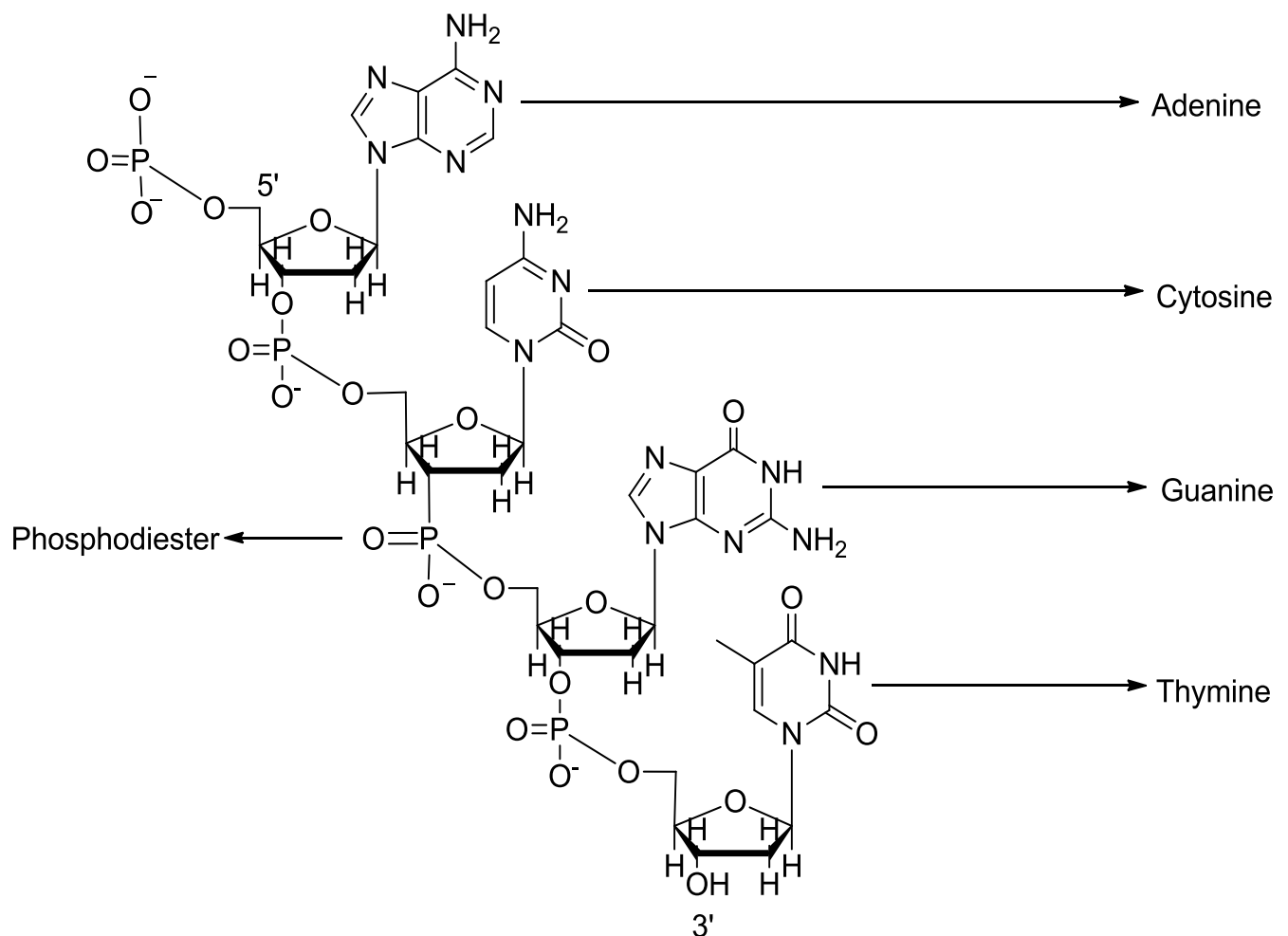
Figure 1.1: The linkage of nucleotides via phosphodiester bonds

Two complementary polynucleotide DNA strands wrap around each other in a right-handed anti-parallel helical orientation; one strand runs from 3'→ 5' and the other strand runs from 5'→ 3' and it forms a coil or a double helix[1,2].
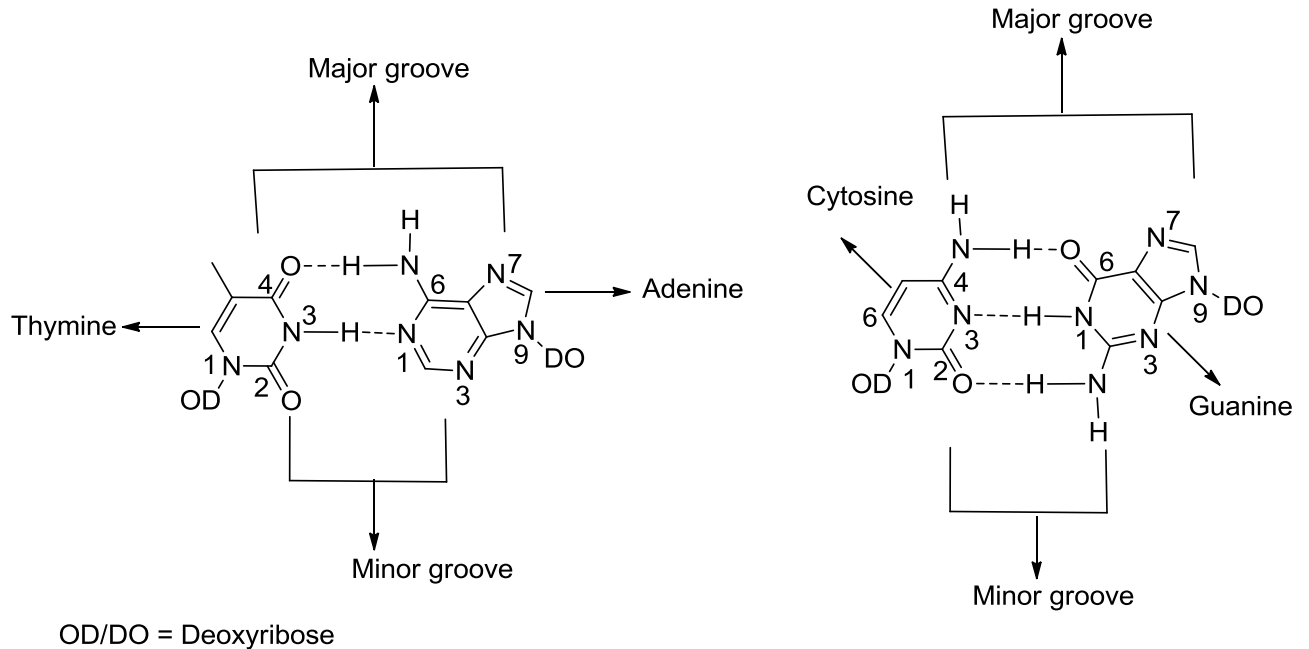
Figure 1.2: Watson-Crick base pairs in DNA. The orientation of bases A, T, G and C relative to their major and minor grooves of DNA is also shown.

The formation of the double helix relies on the pairing of the nucleic acid bases in a specific way. Guanine in one strand pairs up with cytosine (G·C base pair) on the complementary strand through three hydrogen bonds and adenine pairs with thymine (A·T base pair) by two hydrogen bonds. Thus, a bicyclic purine base always pairs with a smaller monocyclic pyrimidine base, this gives rise to a constant diameter of ~10 Å and a rise of 3.4 Å between adjacent base pairs of the double helix[3,4]. The most common form of DNA, known as B-DNA, is the right-handed double helix conformation of DNA observed *in vivo*. The B form of DNA has a diameter of 2 nm and base pair (bp) separation of 0.34 nm with the structure repeating every 10 base pair.

2
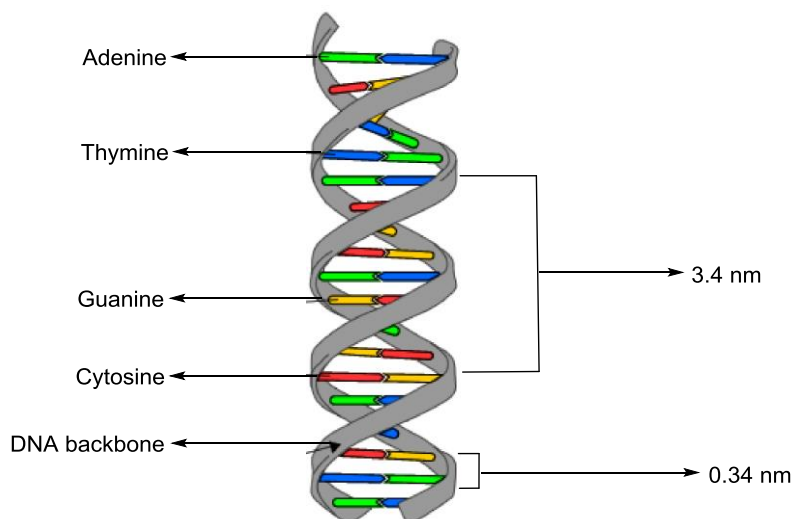
Figure 1.3: A DNA double helix

1.2 TYPE OF DNA INTERACTIONS

1.2.1 The nature of the grooves

As the two individual DNA strands wrap around each other in this right-handed fashion, they create two helical grooves along the length of the double stranded DNA. These are referred to as major and minor grooves. For B-form DNA, the major groove is ~12 Å wide and the minor groove is ~6 Å wide. These grooves are defined structurally by the orientation of the base pairs[5].

For a molecule to be able to bind to a particular groove, it has to match the dimensions of that groove and interact with the groove walls. Thus shape, polarity and hydrophobicity of a drug have a distinct impact in groove binding and hence recognition of specific sites either in the major or minor groove. Typically, both major and minor groove binders consist of several aromatic rings connected by bonds with torsional freedom, which undergo minor rotation to fit into the grooves and form Van der Waals contacts without distorting the DNA structure[6].

3

1.2.2 Irreversible interactions

One of the most studied metal complex used in medicine is cis-diamminedichloroplatinum, Cisplatin(I), as it is known to exhibit anti-tumour activity. It was first used for this purpose in the late 1970s and remains one of the most widely used chemotherapeutics today. Cisplatin binds irreversible to DNA and this drug's main therapeutic targets are testicular, ovarian, bladder and head tumours. Under the physiological conditions that occur inside the cell, chloride concentration is low and hydrolysis of the complex takes place[8]. The chloride ligand is a better leaving group than the ammonia ligand, hence the ammonia ligands remain while the chloride ions are displaced by water. The sequence of events is first hydrolysis of one chloride ligand following by reaction with one guanine ligand then hydrolysis of the second chloride ligand followed by attachment of the second guanine. The water ligands are replaced by N-donors from nucleobases of the DNA strand. The preferred point of attachment has been found to be at the N7 atoms of the imidazole rings of guanine due to their strong basic properties and they are the most accessible and reactive nucleophilic sites for platinum binding[9].

Lippard and co-workers[8] reported the x-ray crystal structure of double stranded dodecamer–platinum (II) unit in 1995. This confirmed the point of platination as an intrastrand cross-link and also revealed that it causes bending of the helix. Cisplatin is successfully used in chemotherapy, but is effective only against a narrow range of tumours. Cisplatin derivatives lack activity against cancer which are resistant to the parent drug, because they form a similar type of adducts to DNA.

1.2.3 Reversible interactions

1.2.3.1 Electrostatic binding

DNA is a highly charged polymer which must condense a significant number of cations from solution to exist in stable conformations. Whilst electrostatic interactions involve binding of cations to the negatively charged phosphates located in the DNA backbone they are generally non-specific and reversible, however this interaction can still result in an increase in the stability of the DNA conformation. Polyamines bind to DNA through such interactions as they are usually fully protonated at physiological conditions; thus the negatively charged phosphate backbone of the DNA serves as the complementary site for interactions. Spermidine and spermine are typical molecules that employ this type of interaction[10].
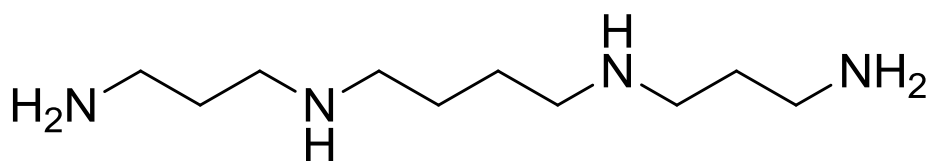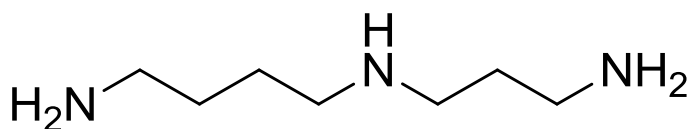
Figure 1.4: Structure of spermine and spermidine

1.2.3.2 Groove binding

The major groove is 22 Å wide whilst the minor grove is 12 Å wide. Natural and synthetic molecules can bind to either of these features. For example, single strands of DNA can bind in the major groove. Felsenfield *et al*[7] reported that poly-U can wind smoothly within the major groove of polyU·polyA double helix forming Hoogsteen base triplets (U-A·U). It was not until 1987 that Moser *et al* found that a short oligonucleotide could specifically bind into the major groove of double stranded DNA, thus forming a section of triple stranded DNA. This has the potential to inhibit replication and transcription of a particular gene. In order to eradicate or completely suppress DNA replication and transcription of a particular sequence, molecules can be designed to bind and induce irreversible damage to DNA[11].

Minor DNA groove binders are another type of DNA binders. The most well known minor groove binders are the polyamide anti-tumour antibiotics, netropsin, distamycin and lexitropsin. They are all AT-specific binders. For example, netropsin binds to the minor groove of the sequence 5'-AATT-3', whereas distamycin binds to the 5'-AAATT-3' sequence. These groove binder structures are very similar in that they both contain *N*-methylpyrrole carboxamides in chains of similar length[12]. Their structures are important because they are curved in such a way that they resemble the curve of the DNA minor groove, clearly enabling shape complementarity.

Hoechst 33258 like the other groove binders, binds with an affinity of ~ 5 x 10^8 M^{-1} to minor groove sites that have at least four A-T pairs. It is similar in structure to netropsin and distamycin A, but shows some significant differences. In contrast to distamycin and netropsin, H33258 has a stronger affinity for AATT than for TATA and displays higher binding to AATT than to AAAA. The binding of H33258 to DNA involves hydrogen-bonds from the benzimidazole-NH groups to O2 of thymine and N3 of adenine[13].
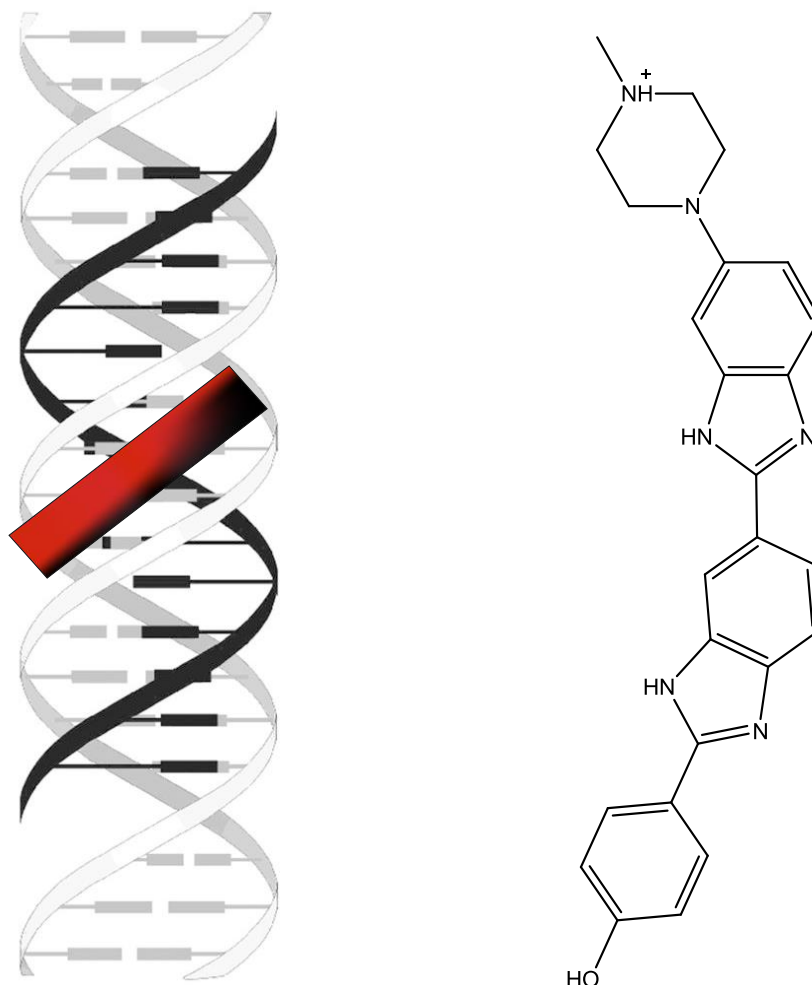
Figure 1.5: Left: Structure of the complex between the DNA and Hoechst **Right:** Chemical structure of Hoechst

Generally speaking, large molecules such as proteins are likely to bind in the major groove and smaller molecules prefer the minor groove.

1.2.3.3 Intercalation

Intercalation refers to the reversible insertion of a guest molecule into a lamellar host structure. In the context of DNA binding, the small molecule (or intercalator) reversibly inserts between two base pairs (the base pairs are an analogue of a lamellar structure). The guest intercalator is usually a molecule with a planar aromatic ring system which intercalates between two adjacent DNA base pairs through electrostatic, dipole-dipole and dispersive interactions as well as π stacking. The intercalation unit may be the whole molecule or only a part of a larger architecture. Depending on their electronic nature, intercalators may be divided into two categories: organic intercalators and metal coordination complexes (also called metallo-intercalators)[14]. Organic intercalators are important DNA binding agents. Small organic intercalators may carry a positive charge as organic cations (e.g. ethidium, daunorubicin, doxorubicin) so that there is an attraction with negatively charged double stranded DNA, while others may not require such a charge[15].
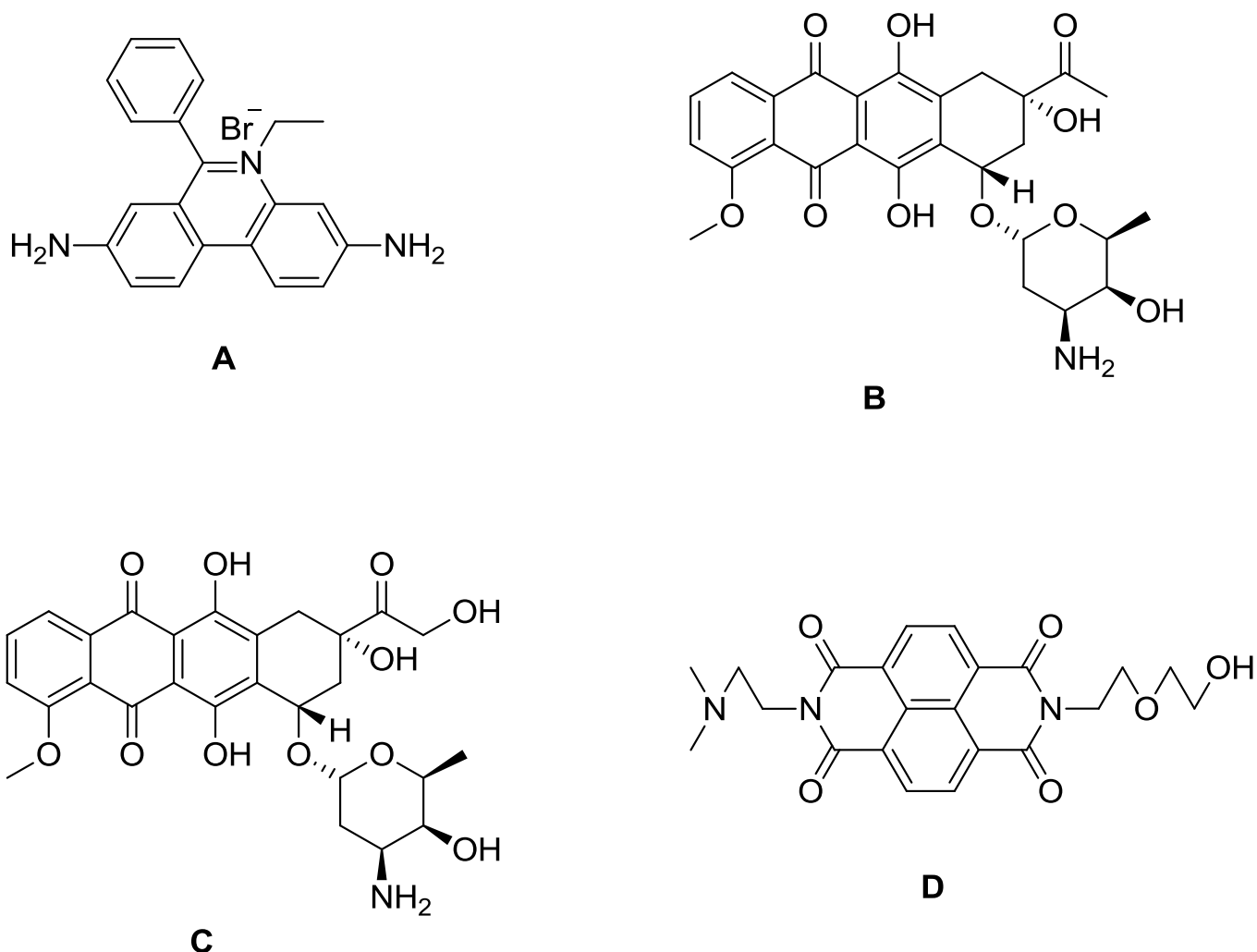
Figure 1.6: Ethidium (**A**), daunorubicin (**B**), Doxorubicin (**C**) and NDI intercalator (**D**)

Intercalators can induce distortion in the DNA double helix conformation. Firstly, in order for the intercalation process to be complete, the space of the intercalation point is enlarged. This leads to an angle change of the DNA strand. Secondly, the DNA strand becomes 3.4 Å longer than before, for each intercalated unit. This is concomitant with DNA double strand unwinding, as well as with a change in the conformation of the sugars which connect with phosphates. Thirdly, once the intercalation process is complete, the neighbouring binding sites are not able to accept a second intercalator. This is due to the fact that the local DNA structure has been changed by the first intercalation process, so the conformation of its neighbouring binding sites also change accordingly. In a phenomenon called the neighbour

exclusion principle[15] they become compressed so that another intercalator cannot now fit between them.

1.3 METAL COMPLEXES AS DNA BINDING AGENTS

1.3.1 Brief description:

Four decades ago most of the synthetic and natural DNA binding molecules were organic in nature, but as researchers delineated on a molecular level how genetic information is expressed, a more complete understanding of how to target DNA sites with specificity was developed. This in turn has led to possible new chemotherapeutic agents and probes such as transition metal complexes[16]. Complexes of d^6 transition metals are very suitable as DNA binding agents due to their inertness and stability under physiological conditions. Coupling this with their well-defined and tunable molecular architecture, and their high solubility in aqueous media, there is huge potential for developing these molecules as site-specific DNA binding agents. The primary mode of binding for these transition metal complexes is intercalation and they have become known as metallo-intercalators. All this group of complexes contain an extended aromatic ligand, which protrudes away from the metal centre and is ideally set up for intercalation. It has also been shown that the nature of the ancillary ligands has a marked effect on the binding affinity and selectivity of these DNA binding molecules. By systematically changing the nature of these ancillary ligands it is possible to tune the DNA binding properties and the photo-reactive properties of the molecules. More over by taking advantage of the rich photophysical handles that these complexes possess it is easy to monitor and quantify their binding to DNA. Due to the rich photochemical and redox properties of these complexes it is also possible to perform chemistry on the DNA bases themselves[17].
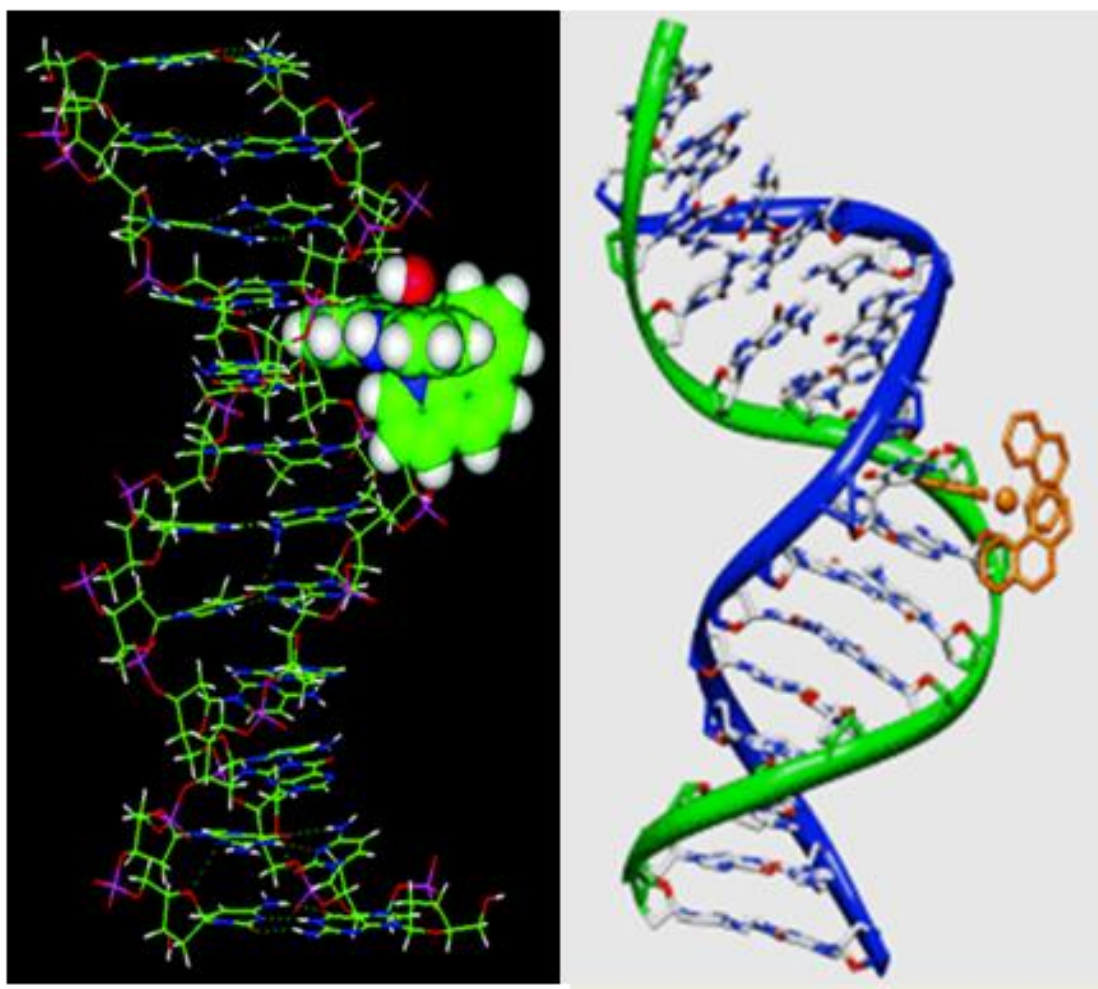
Figure 1.7: Left: Structure of complex intercalated to the minor groove of DNA.

        Right: DNA bend upon interaction with complex (Adapted from Lawrence, D.; Vaidyanathan, V.G.; Unni Nair, B. Synthesis, Characterization and DNA binding studies of two mixed ligand Complexes of Ruthenium(II). *J. Inorg. Biochem.* **2006**, *100*, 1244 – 1251)

1.3.2 Photophysical properties of Ruthenium based metallo intercalators

The spectral properties of Ruthenium based complexes arise from their unique electron states. The d-orbitals of the metal ion are split in three energetically lower and two higher orbitals in the presence of the ligands. The extent of the energy difference between the orbitals is dependent on the crystal field strength Δ. The six electrons of the Ruthenium(II) fill the three d‑orbitals with lower energies. Transition between the orbitals is formally forbidden. Although *d-d* transition can occur, the probability of the radiative transition is very low and the emission is quenched.

d-d excited states are usually unstable due to the fact that electrons in the e-orbitals are antibonding regarding the metal – ligand bonds. In complexes, a transition involving a charge transfer between the metal, in this case ruthenium, and the ligand can occur and is known as a metal-to-ligand charge transfer transition (MLCT). This causes the intense absorption of the ruthenium MLCs near 450 nm[24].
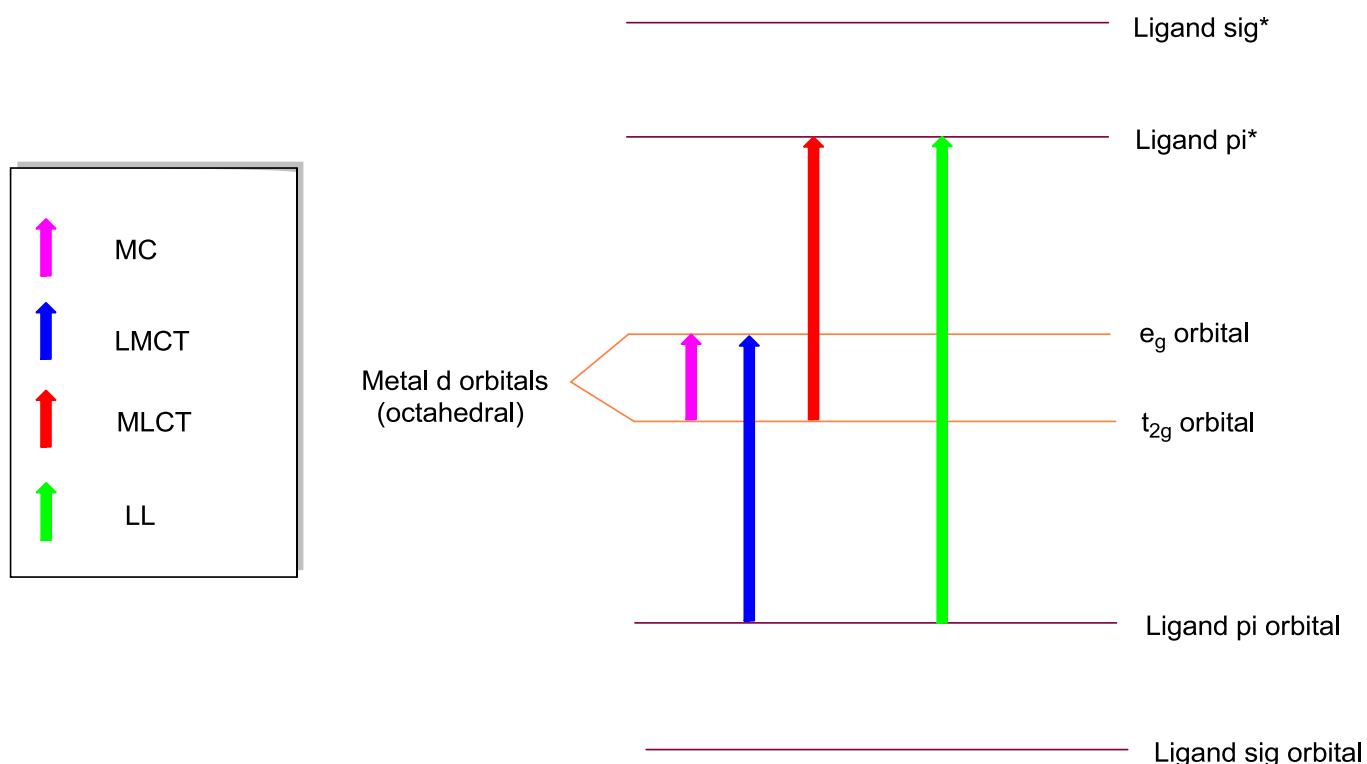
Figure 1.8: Types of charge transfer

Emission from these states is phosphorescence, but is shorter lived. Due to spin-orbit coupling of the heavy metal atom, the normally forbidden transition to the ground state is more allowed, and so Ruthenium have a shorter luminescence lifetime. After photoexcitation, the electrons undergo intersystem crossing from the singlet to the triplet MLCT state. This event proceeds rapidly and with high efficiency. Hence, the excited state decays by radiative and non-radiative pathways. The probability of non-radiative decay is higher than that of the radiative decay, so that the decay times are determined by the non-radiative decay rates. For a MLCT to be luminescent it is necessary that the MLCT state is located at a lower energy level than the *d-d* state. In the case of this criterion is fulfilled and the *d-d* levels are not

accessible for radiationless decay. Therefore Ruthenium metal complexes are highly luminescent[25].

1.3.3 Previous study on Ruthenium complexes

After Lippard and co-workers[8] first established that a square planar metal complex containing an aromatic heterocyclic ligand could bind to DNA through intercalation. Barton and co-workers[15] soon extended the complexes to three dimensions, when they started using octahedral metal centres. The early studies focused on the tris(phenanthroline) complexes of zinc, cobalt and ruthenium through NMR and photophysical studies. They suggested that the cationic tris(phenanthroline) complexes bound to DNA through all three of the noncovalent modes discussed earlier. One important observation to come from these early studies was that there was a small but significant preference for the right-handed Δ isomer when bound to right-handed B-form DNA. However the binding modes and exact orientation of these tris-(phenanthroline) ruthenium(II) complexes was open to much debate.

In the early papers to emerge from Barton's lab the mode of interaction of $[(phen)_3Ru]^{2+}$ with B-form DNA was deemed to involve electrostatic and hydrophobic contacts with the DNA in the major groove, with partial intercalation of one of the phenanthroline ligands into the DNA base stack. Equilibrium dialysis experiments showed that the intrinsic binding constant was small and highly dependent upon salt concentration, which indicates a large electrostatic component to the binding free energy. Luminescence quenching experiments revealed a bi-exponential decay indicating two emitting species were present, one of which is quenched more readily than the other. Barton proposed that the species which was more readily quenched was groove bound, and was therefore more accessible to the quenching agent, whereas the other species was intercalated deep within the major groove of DNA and was much less accessible to the quenching agent.

The chiral discrimination of the binding event was rationalised by assuming the propeller twist of Δ-$[(phen)_3Ru]^{2+}$ was symmetry matched to the right handed helix found in B-form DNA, allowing it to bind more preferentially compared to Λ-$[(phen)_3Ru]^{2+}$. Barton also reported sequence selectivity based upon steady-state polarisation of excited states, which showed that the preference for the Δ-$[(phen)_3Ru]^{2+}$ increases upon increasing GC content of the DNA. This has been rationalised by the fact that the major groove becomes narrower with increasing GC content and therefore closer in width to the diameter of $[(phen)_3Ru]^{2+}$ thus amplifying the important steric contacts between the complex and the sides of the groove needed for chiral discrimination.

However it is now established that tris- phenanthroline ruthenium (II) complexes do not intercalate into the base stack of DNA at all[14,18]. In 1992 Norden and co-workers published the results of an NMR study they had undertaken, seemingly contradicting all of the structural elucidations proposed by Barton. They described NOE data which showed that both Δ and Λ-[(phen)$_3$Ru]$^{2+}$ bind to the AT region of the self-complementary oligonucleotide [d(CGCGATCGCG)]$_2$ in the minor groove. The cross peaks observed between protons on the metal complex and the oligonucleotide showed they are at distances of less that 5 Å apart. The H2 of adenine located at the bottom of the minor groove was shown to interact with protons on one of the phenanthroline rings and sugar protons H1'and H4', which both face the minor groove, interact with the phenanthroline protons. Both enantiomers exhibit similar cross peaks, however more were observed with the Λ enantiomer but higher concentrations of drug were needed to see them. The oligonucleotide cross peaks are not affected in any way upon binding of the complex indicating no change in conformation on interaction, suggesting no intercalation takes place. The binding kinetics are rapid and the complex is in fast exchange resulting in sharp signals, which again is an indication of no intercalation taking place. In summary both Λ and Δ [(phen)$_3$Ru]$^{2+}$ bind to the AT region of [d(CGCGATCGCG)]$_2$ through electrostatic and groove binding interaction within the minor groove[11]. The issue of intercalation was disproved once-and-for-all, when Chaires *et al*[9] published viscosity data showing only a very small increase in viscosity upon binding of tris-phenanthroline ruthenium (II) to DNA indicating a non-intercalative mode of interaction.

Finally a detailed spectroscopic and modelling account by Rodger *et al* showed that the equilibrium binding constant was dependent upon the degree of saturation of the DNA by the drug complex. They also reported two modes of interaction. Λ-[(phen)$_3$Ru]$^{2+}$ was shown by CD and LD studies to orientate in the major groove through partial insertion of one of the phen moieties into the major groove. The phen moiety orientates itself within the major groove in plane with the base pairs although phen does not protrude far enough away from the metal centre to facilitate full intercalation. The Δ-[(phen)$_3$Ru]$^{2+}$ species binds exclusively in the minor groove by slotting a phen moiety vertically into the groove nearly perpendicular to the plane of the base pairs. This mode results in considerable widening of the minor groove to maximise interactions between the backbone and the other two phen ligands on the complex. Again strong preferences were seen for AT regions of DNA over GC regions. Although tris-phenanthroline ruthenium (II) complexes were shown to bind to DNA and show a degree of symmetry recognition, the binding affinities for DNA were unimpressive, and were highly dependent upon sequence, salt and temperature. In order for these metallo-

intercalators to become useful in chemotherapeutics all of these problems needed to be addressed[27].

The Molecular light switch effect

Barton *et al*, realised that to enhance binding affinities, the surface area of the putative intercalating species needed to be extended. This led to the synthesis of $[Ru(bpy)_2dppz]^{2+}$, which not only demonstrated enhanced DNA binding ($K_b = 10^6$ M^{-1} as reported by Haq *et al*.), but also a photophysical result known as the light switch effect[26,53].
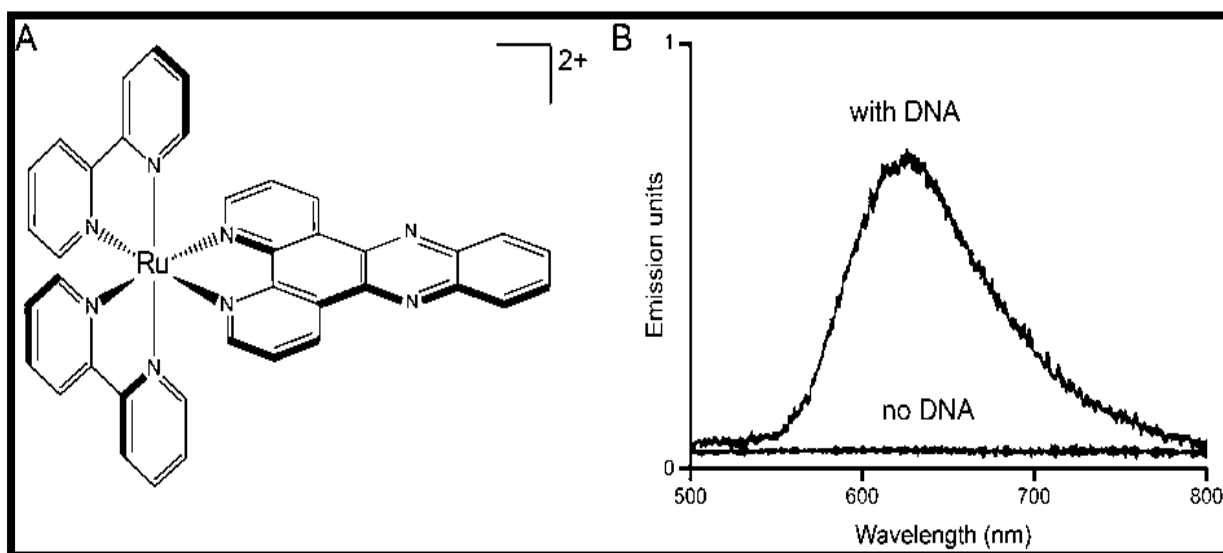
Figure: 1.9: $[Ru(bpy)_2dppz]^{2+}$ - Photophysical property: **(A)** Structure of $[Ru(bpy)_2dppz]^{2+}$ **(B)** Optical titration showing MLCT emission due to $[Ru(bpy)_2dppz]^{2+}$ binding to DNA

Solvatochromic luminescence is the ability of a chemical substance to change emission colour due to a change in solvent polarity. A molecular light switch deviates from this in the sense that upon moving from one environment into another the transition from no luminescence to intense luminescence is seen. The complex is essentially switched 'off' in one environment (with little to no luminescence), and then 'on' in the other, thus making the comparison of switching on a light. This feature is useful because it can be used to detect changes in micro-environment. In the case of $[Ru(bpy)_2dppz]^{2+}$ the complex emission is 'off' in aqueous solvent but 'on' when interacting with DNA[26,53].
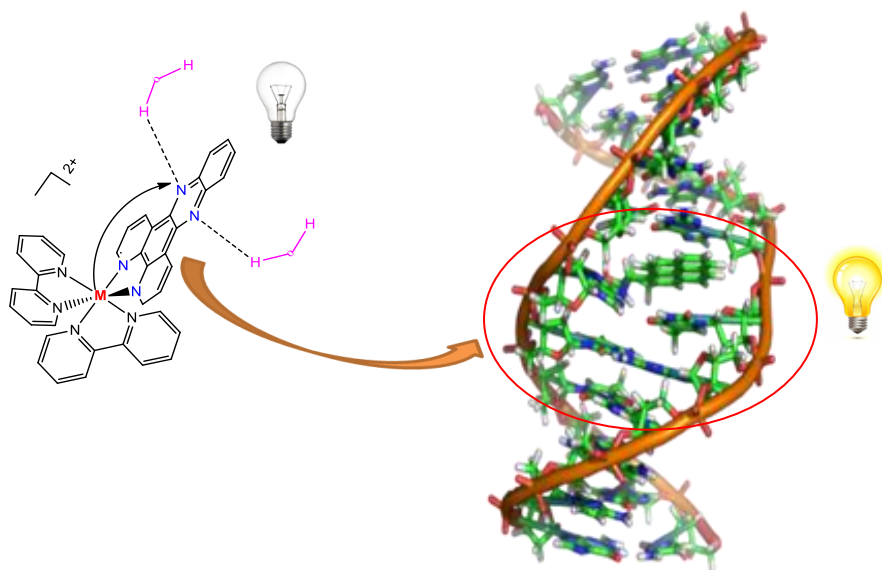
Figure: 1.10: Molecular Light-switch effect

The observed luminescence is as a result of the Ru-dppz moiety. Light induced charge transfer of an electron from an orbital predominantly metal in character to an orbital predominantly ligand in character (MLCT) causes electron excitation onto the dppz ligand. The charge-separated excited state is localised on the bpy or phen part of the dppz ligand. This ^{1}MLCT excited state then decays rapidly via intersystem crossing (ISC) to a ^{3}MLCT excited state primarily localised on the phenazine nitrogen atoms[28,29].

There are two possible deactivation pathways for the excited state; emissive and non-emissive. This complex shows luminescence in organic solution, but not in aqueous solvent. This is because in aqueous solution, water molecules deactivate the excited state through hydrogen bonding with the endocyclic nitrogen atoms of the intercalating ligand. Thus a non-emissive deactivation pathway of the excited state occurs. In the presence of organic solvent, these interactions cannot occur, thus the excited state deactivates emissively. In the context of DNA, this transition can be seen as the free metal complex in solution inserts between base pairs, becoming protected from the aqueous solvent, resulting in an intense rise in luminescence. The extent to which the molecular light switch effect is seen depends on the degree of protection[31].

1.4 SUPER-RESOLUTION OPTICAL MICROSCOPY

Light microscopy methods either require samples to be coloured, or it is necessary to utilise differences in phase as light passes through specimens in order to make out their features. Phase contrast methods involve converting the phase shifts in light passing through the sample to variations in brightness in the image, whilst stains increase the contrast of a sample in areas where they are attached. An extension of traditional colour staining methods is to use fluorescent dyes, as these have a very large contrast with a dark background when excited using UV (or in some cases visible) light. As with any optical technique, however, the resolution achievable using fluorescence microscopy is limited by the diffraction of light. The Rayleigh criterion gives a minimum distance for which two light sources can be optically resolved[56,57].

Equation: 1.7 $\quad \Delta l = \lambda / NA$

Where λ is the wavelength of illuminating light and *NA* is the numerical aperture of the optical system. The distance Δl represents the separation of the centroids of each marker's point spread function (PSF); the fluorophores are optically resolvable if Δl is greater than the radius of the marker's airy disk. In the case of biological samples labelled with fluorescent markers, two closely neighbouring fluorophores active at the same time will not be resolvable using visible light.

Various optical microscopy methods using fluorescent markers have been devised to obtain spatial resolutions below the diffraction limit of light. These have been termed super-resolution microscopy, or sometimes nanoscopy. Several of the most popular techniques fall into two categories, targeted and stochastic super-resolution. Targeted readout techniques reduce the size of the effective fluorescence point spread function (PSF), whilst in stochastic techniques random subsets of fluorophores much further apart than Δl according to the Rayleigh criterion are imaged sequentially[59,60].

1.4.1 STED

Stimulated Emission Depletion (STED) microscopy works by depleting a zone around the edge of the focal region of emitting fluorophore. In Stimulated emission by depletion (STED), the sample is scanned with a combined excitation/depletion beam[74,75]. STED is the first super resolution microscopy technique to employ far-field super resolution imaging and is based on imaging an ensemble of photostable molecules. Excited fluorophores exposed to the STED beam are instantly transferred back to their ground states by means of stimulated emission[40].
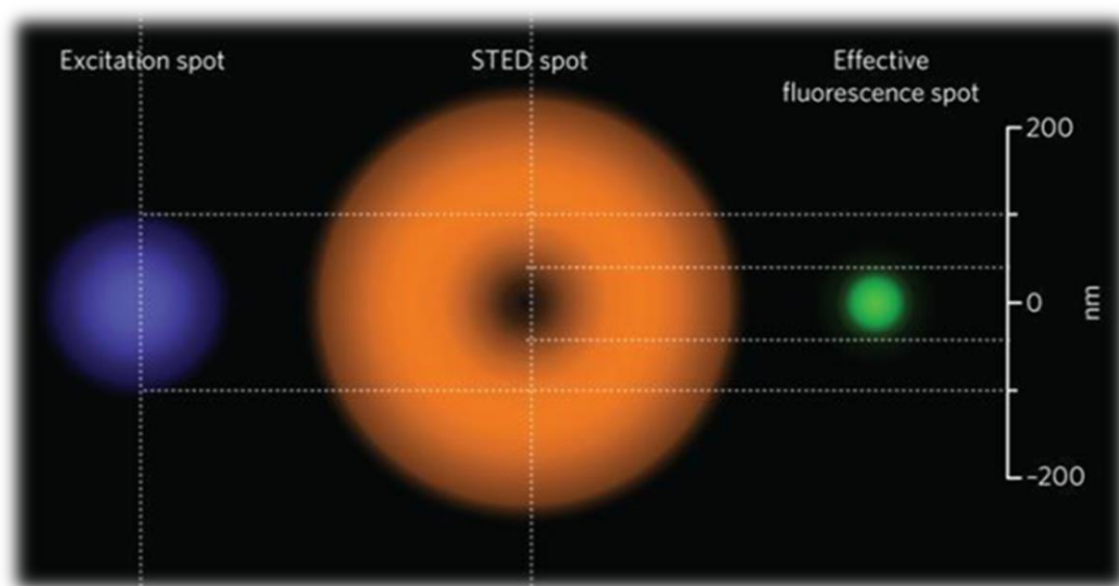
Figure: 1.11 STED microscopy resolution (Adapted from Abbott, A. The glorious resolution. *Nature*, **2009**, *45*, 4 − 5)

This is achieved by switching the fluorophore in the depletion zone to a dark state by stimulating its emission with a high intensity laser that matches the emission wavelength (usually the red edge of the emission) of the fluorophore. This effectively reduces the spot size of the incident laser to below the diffraction limit[76,77]. STED uses a method of controlled de-excitation of previously excited fluorophores. Fluorophores slightly off the centre of the PSF will be illumination by the stimulated emission depletion beam, which has a doughnut shape with a zero intensity at the very centre. The success of obtaining a good STED image depends on the duration of the STED pulse and a good quality of the zero intensity of the centred STED beam. The fluorescence from the central regions must be spectrally separated

from the red shifted beam, this nonlinearity is essential to obtain high quality STED images[46]. STED is dependent to a greater extent on the stability of the probe, probes with large broad Stokes shift, high quantum yield like the Atto dyes can be employed as a STED probe. Multicolour STED is commonly hampered by strict requirements for the probe such as non overlapping excitation, emission and depletion bands[47]. For STED, sub-50 nm resolution has been reported. The key strengths of STED are; the resolution improvement is molecular, thus, data does not typically need additional post-processing, STED has achieved the lowest resolution (sub-50 nm) of all of the super-resolution methods[78,79]. STED resolution depends on the extent of saturation of emission depletion therefore maximization of STED emission depletion is essential to improve STED resolution and this could be achieved by either increasing the intensity of the STED pulse or decrease the intensity required to send a fluorophore to the dark state[40]. A further advantage is that optical sectioning is intrinsic to the STED method enabling acquisition of planes of roughly 100 nm. Indeed, 3-dimensional structures several tens of microns deep inside tissue have even been achieved. Finally, relatively fast image acquisition of several images per second means that it can be used on live samples. STED has also been used widely to carry out super-resolution imaging to probe innate confirmations changes of various proteins involved in bio-signalling pathways, there by STED acts as a gateway imaging super-resolution platform to probe cellular dynamics.

1.4.2 STORM

Stochastic imaging techniques depend on the activation of a subset of fluorophores spread across the sample with the rest remaining in a dark state, allowing the bright fluorophores to be resolved spatially. STORM is a localization based microscopy technique that utilizes time resolved localization and sequential activation of photoswitchable fluorophores resulting in the generation of high quality super resolution images. The technique depends on a small number of molecules being switched on at any time after excitation, although all of the probes in the sample will eventually be recorded. Stochastic techniques produce images with spatial resolutions of ~30 nm; these images are usually obtained using an inverted Total-internal-reflection (TIRF) microscope, which minimises the likelihood of background fluorescence from the sample. Despite the vast number of different stochastic techniques recorded in the literature, it should be noted that all rely upon the ability to switch between different, optically resolvable subsets of fluorophores repeatedly, and that the only major difference is the methods by which the dyes are made to "blink" through cycling between on

and off states[56,57]. Depending on the technique employed, this blinking is accomplished in a number of ways.

Both Heilemann and Hell demonstrated the automatic switching of conventional fluorophores with a single laser excitation wavelength, significantly reducing the complexity of imaging compared to STORM. These techniques are called direct STORM (*d*-STORM), or ground state depletion followed by individual molecule return (GSDIM) by the respective groups. For obvious reasons, collectively these methods - and others derived from them - are often labelled as 'blink' microscopy[61,62]. When time is used to separate the emission from dye molecules many localised positions can be assembled into high resolution images of the sample in a method termed pointillism, in analogy to the artistic painting technique. In this way the chance of detecting particles with overlapping signals in one image is reduced to almost zero as the number of simultaneously emitting particles is limited. Such series of a few thousand images can then be processed and this is how high resolution images reaching resolutions in the range of 30 nm can be accomplished. To sum up STORM relies on some basic concepts, it requires photoswitchable or photoactivable fluorescent molecule which means the molecule should go through the process of on/off transitions which would translate to transient blinking – this could be a fluorescent molecule or a fluorescent protein[114]. Probes which do not show these characteristics cannot be applied as probes in STORM imaging. The main currently employed STORM probes include certain reversibly photoactivated luminophores, for example; fluorescent proteins like GFP, and small molecules like rhodamines, dronpa, rsCherry, diaryl ethenes, and other cyanine analogues. Certain non-genetically engineered macromolecule probes like inorganic quantum dots can also be employed as STORM probes[40]. Achieving superior localization accuracy is an essential criteria for generating a perfect SIM image.

1.4.3 SIM

A third commonly employed super-resolution method, SIM, provides lower resolutions but is more applicable to a wider range of optical probes.

SIM – Importance and Application

Structured illumination microscopy illuminates a sample with a series of sinusoidal striped patterns of high spatial frequency. This pattern is typically generated by laser light passing through a movable optical grating and projected via the objective onto the sample. When illuminating a fluorescent sample containing fine structures, coarser interference patterns (moiré fringes) arise in the emission distribution and these coarse fringes can be transferred to

the image plane by the microscope[46]. The excitation patterns are obtained in different orientations and processing all acquired images using computer algorithms, a high-resolution image of the underlying structure can be generated. With this approach the lateral resolution increases by a factor of two beyond the classical diffraction limit. With three-dimensional SIM (3D-SIM), an additional twofold increase in the axial resolution can be achieved by generating an excitation light modulation along the z-axis using three-beam interference and processing a z-stack of images accordingly. Thus, with 3D-SIM an approximately eightfold smaller volume can be resolved in comparison to conventional microscopy[66,67].

An attractive feature of structured illumination for cell biological applications is the fact that because standard dyes and staining protocols can be used, multiple cellular structures can be simultaneously imaged with optical sectioning in three dimensions (Schermelleh *et al*). The multicolour capability of 3D-SIM allows the imaging of several cellular components and the mapping of their relative positions in macromolecular complexes, enabling the study of their spatial relationship within the surrounding cellular contexts[72,73]. Resolution of SIM image for a great part depends on the reconstruction; with good signal-to-noise ratios unknown structures can be rendered into well-resolved images. Low contrast in SIM images can contribute to artefacts; this can only be prevented by using a suitable probe which does not photobleach easily. Imaging conditions like percentage transmittance, laser power, and scanning time all need to be optimized to acquire the perfect highly resolved SIM image without artefacts. Probe suitability is not a problem in SIM as it was in the case of STORM and STED. SIM allows the use of the same chemical dyes used in widefield microscopy. As SIM is a widefield techniques all dyes which could be used in widefield imaging could potentially be used as a SIM probe[47].

1.5 CELLULAR IMAGING USING TRANSITION METAL COMPLEXES

Photophysical properties of a molecule must be considered if it is to act as a bio-imaging probe. The useful photophysical properties of some transition metal complexes have resulted in them being heavily investigated for applications as cellular imaging agents. Transition metal residing in the 2nd and 3rd row of the periodic table, with d^6, d^8 and d^{10} electronic configurations, result in more effective ISC than 1st row complexes producing highly intense phosphorescent emission. As outlined in previous sections, heavy transition metals with a d^6 configuration such as Ru(II), Re(I), Ir(III) and Os(II), when bonded to one or more aromatic bidentate ligands show the ideal photophysical and redox properties required to be useful luminophores. Additionally, the cationic charges associated with metals of this nature increase the likelihood of them being able to interact with the negative surface of the cell and therefore enter the cells. The photophysical properties of a Transition metal (TM) complex are reliant on the ligands attached, in the case of MLCT systems, the ligand attached acting as an electron acceptor. Having both a high degree of stability and tenability, diimine ligands (specifically polypyridines) are generally employed for this role. The diimines, 1,10'-phenanthroline and 2,2'-bipyridine have attracted the greatest attention due to the suitable energy of their lowest occupied molecular orbital (π^*). If the level of the π^* orbital is too low it can result in an increase in the rate of non-radiative decay. If the level of the π^* orbital is too high the rate of the both the ^{3}MLCT and non-radiative decay decrease[36,37]. Both extremes produce poor luminophores. It is possible to have more than one diimine ligand attached to the transition metal and to also have variation in the diimine ligand structure[33,34]. Variation of the diimine ligand structure not only allow for the electronic properties of the complex to be finely tuned, but can provide a route to subcellular targeting.

As mentioned above, transition metal complexes have interesting photophysical properties. Their MLCT means they display bright emission, and exhibit high quantum yields, which means they could potentially be applied as probes for a variety of super-resolution microscopy techniques. But, at the moment, there are not many metal complexes being used in this role, this might be because of the special requirements for each of these super-resolution microscopy techniques with respect to the suitability of the probes.

Super resolution microscopy techniques have been used to probe many biological systems and processes especially at the cell level. However, the vast majority of these studies,

especially in the case of STORM, involve fluorescent proteins or small molecules like photoswitchable fluorophores like cyanine dyes (e.g. Cy5[44,48]), Dronpa, rsCherry and non-genetically coded inorganic quantum dots[40],. As mentioned in the previous sections, STORM and variants such as DNA-PAINT[107] requires a photoswitchable probe and heavily rely on a probe with an activation and de-activation cycle. STED on the other hand requires a probe with high photostability, brightness and long life times. Large Stokes shift for a STED dyes always helps to allow the dye to be employed in multicolour imaging. Currently, ATTO dyes are widely employed as STED probes[40]. Other dyes for STED include fluorescent rhodamines, fluorogenic carbopyronines[41], and other hydroxylated fluorescent dyes.[42] All of these probes have excellent photophysics as they do not bleach out leading to excellent STED images. In the first report of its kind, Keyes, *et al*[97] have also reported a non-intrinsic ruthenium metal probe which was conjugated to a target specific peptides which shows excellent photophysics and produces clear STED images. This particular example showed that the excellent photophysical, photochemical properties exhibited by the transition metal complexes could be utilized in super resolution microscopy. Structured illumination microscopy (SIM) does not require any special characteristics for the probes to be used but again the intrinsic photophysical and photochemical properties of fluorescent proteins and organic dyes with appreciable quantum yield are employed as a SIM probe. Most commercial trackers and antibodies can be applied for dual colour SIM imaging. The use of ruthenium metal complexes as super resolution microscopy probe (SIM and STED) especially complexes with DNA binding characteristics opens up new possibilities in understanding cellular structure and processing at greater detail.
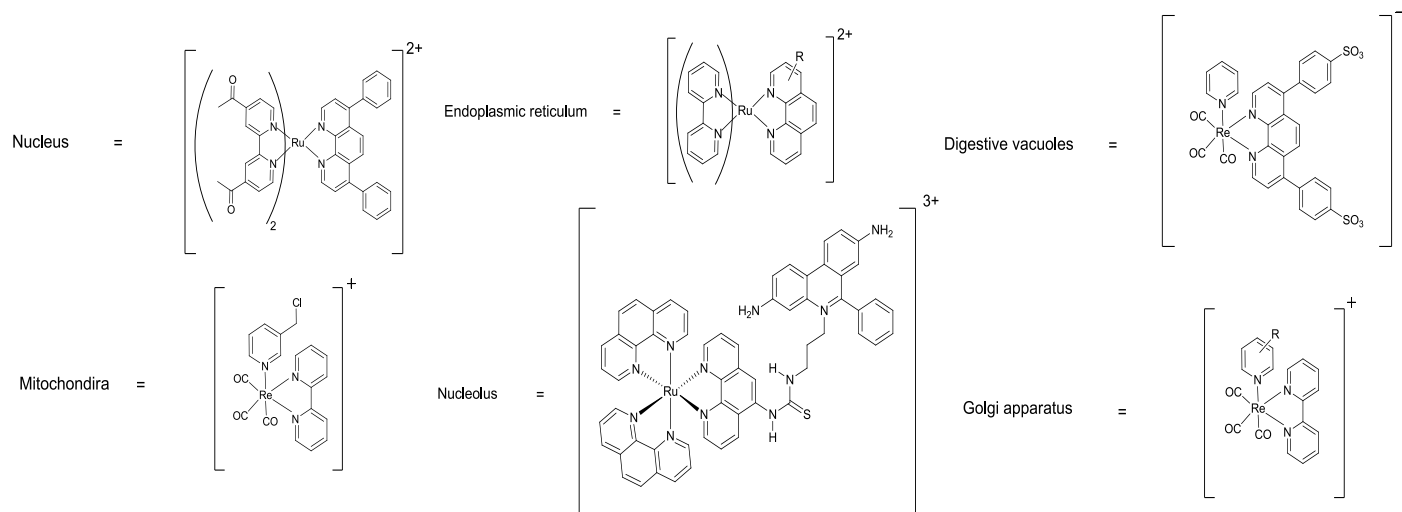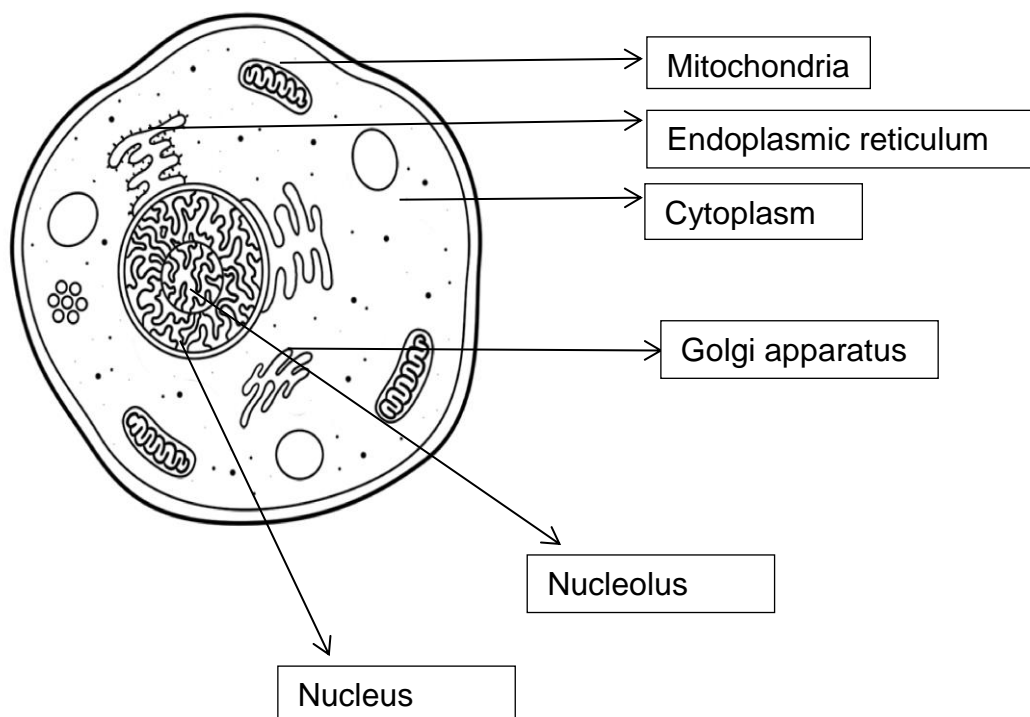
Figure: 1.12: Localisation patterns of various d^6 metals (Adapted from: Chem. Commun., 2010, 46, 186 - d^6 metals in cell imaging)

1.6 AIMS

The main objective of this work is to examine the properties of a previously reported dinuclear ruthenium(II) cell probe for super-resolution imaging.

A good STED probe should exhibit high intensity red to NIR emission, good photostability, a long lived emissive state and good overlap of emission spectrum with the STED laser whilst avoiding re-excitation through ground state absorbance or promotion of the compound through excited state absorption to a long-lived dark state/photobleach. It should also be capable of permeating the cell membrane and in particular it should target with high precision and selectivity, the site of interest[33,34]. The Ru(II) polypyridyl complex that forms the focus of this study, is a red-emitting probe that exhibits a number of important properties that makes it a useful alternative to organic probes for exploitation in STED microscopy. The most important is its large Stokes shift, long-lived emissive states and good photostability. Such complexes emit at room temperature with relatively high quantum yields, but with peak to peak separation between their absorbance and emission maxima of between 120 and 200 nm. This means that effective overlap of the depletion laser with the emission spectrum is enabled without the possibility of re-absorption by the ground state of the dye[53,54]. In addition, stimulated emission from the phosphorescent state can be observed in transient spectroscopy of the ruthenium complexes whereas only weak transient absorption is typically observed in the region of stimulated emission. Furthermore, large Stokes shifts allow their study in microscopy at high concentrations without dye performance being compromised by self-quenching, so such complexes can be accumulated at high concentration into small volumes such as organelles. The experiments discussed herein pave the way for optimising Ruthenium based probes as a new paradigm in super-resolution microscopy techniques and real time 3D-super-resolution imaging.

Apart from metal complexes discussed above, in this thesis specific probes and nanomaterials developed by other lab will be investigated. Specifically their cell uptake and in cell optical properties will be assessed. In particular, their compatibility with the least photochemically demanding super resolution technique, SIM, will also be explored.

In these studies, probes that detect products of various biological processes in cells are a particularly interesting area to explore using super-resolution techniques. For example, understanding the generation of reactive oxygen species within cells can yield interesting information with regard to disease progression and can also unravel complicated biological

processes happening in cells. Exploring such entities using super resolution microscopy might provide interesting information related to their intracellular localisation and dissect the function of their analyte species.

2.0 SUPER-RESOLUTION MICROSCOPY STUDIES ON LUMINESCENT METAL COMPLEXES

2.1 DNA BINDING METAL COMPLEXES AS SUPER-RESOLUTION MICROSCOPY PROBES

DNA binding molecules can provide valuable insight into understanding processes connected to the origin of many diseases, especially cancer. In particular, the development of straightforward cell-permeable, non-toxic, microscopy probes would enable essential information about biological processes involving DNA to be acquired. Although many cell-permeable organic probes have been reported for microscopy, inorganic probes which specifically bind to DNA are still relatively rare[85,86].

The most studied Ru(II) systems are based around tris-diimine complexes. Despite the favourable photophysical properties of complexes of this type, when compared to the number of Ru-based complexes investigated for applications as O_2 sensors or DNA intercalators, there are still relatively few examples of Ru-based complexes reported as suitable cellular imaging agents[88,89]. A report by Musatkina *et al*[52]. demonstrated how the uptake of Ru(II)-polypyridyl type complexes is dependent on the nature of the diimines. Whilst bipy analogue ligands show poor cellular uptake, extended hydrocarbon system of batho-phenanthroline show nuclear staining. Puckett *et al*[19], demonstrated the inclusion of targeting peptides can further improve the uptake efficiency of a Ru(II) tris-diimine complex. So, although $[Ru(bipy)_2(dppz)]^{2+}$ showed poor cellular uptake, when conjugated with octarginine, staining of the endosomes was observed and when conjugated with fluorescein, nuclear staining was observed. The difference in localisation of the two complexes was attributed to the differences in their lipophilicity. The difference in their lipophilicity was later confirmed with the synthesis of two $[Ru(phen)(dppz)(bipy)]^{2+}$ type complexes attached to octarginine. The first of the two complexes was linked to octarginine only and displayed cytoplasmic staining; the second complex was inclusive of octarginine, but also incorporated a fluorescein conjugate and staining of the cytosol, nuclei and nucleoli of the HeLa cells was observed.

The Thomas group carried out cellular imaging using the $[\{Ru(phen)_2\}_2tpphz]^{4+}$ complex and achieved target specific nuclear imaging[53,54]. They were able to image both duplex and quadruplex DNA specifically using this complex. By effecting subtle changes in the structure

of the previously mentioned bimetallic ruthenium complex, the Thomas group also succeeded in imaging the intracellular environment again, this time targeting the endoplasmic reticulum[104]. In this chapter, one of the metal complexes developed by the Thomas group for confocal microscopy is investigated as a probe for several different super resolution techniques.

2.2 STORM AND SIM EXPERIMENTAL SET UPS AND INITIAL SUPER RESOLUTION MICROSCOPY STUDIES IN CELL FREE CONDITIONS

Having discussed the concept of super resolution microscopy in the previous chapter, experimental details and an assessment of the suitability of metal complexes for these techniques are first discussed in this chapter. This is followed by initial cell free studies, which were used to select which techniques would be pursued in fixed and live cell studies.

2.2.1 STORM IMAGING EXPERIMENTAL SET UP
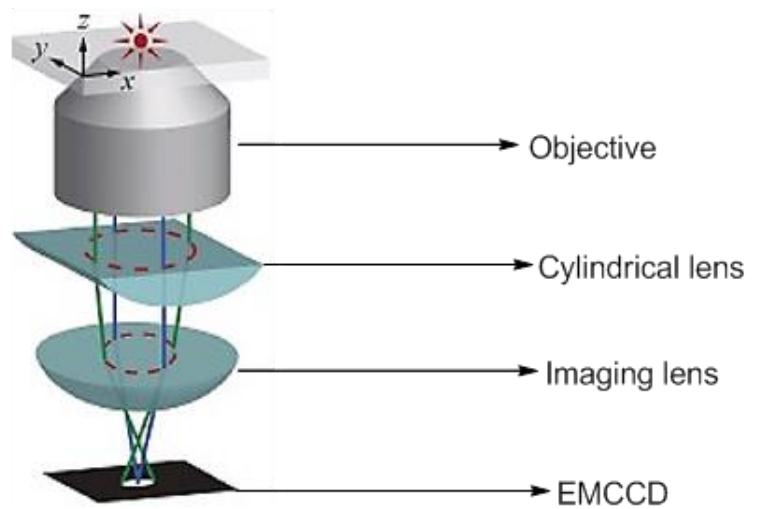
(A)   (B)

Figure: 2.1 (A) N-STORM (SR Apo TIRF 100x), **(B)** STORM optical train (**Source**: LMF, University of Sheffield)

The initial STORM experiments were performed by using the N-STORM with 3D capability, motorised stage controller with piezo insert, petri dish holder and slide holder for stage, temperature controlled incubator, EM-CCD camera, separate PC for image reconstruction work, Laser lines: 405 nm, 488 nm, 561 nm, 647 nm, Lenses: SR Apo TIRF 100x, Filterset: Quad cube for blue/green/red and far red.

2.2.2 SIM IMAGING EXPERIMENTAL SET UP
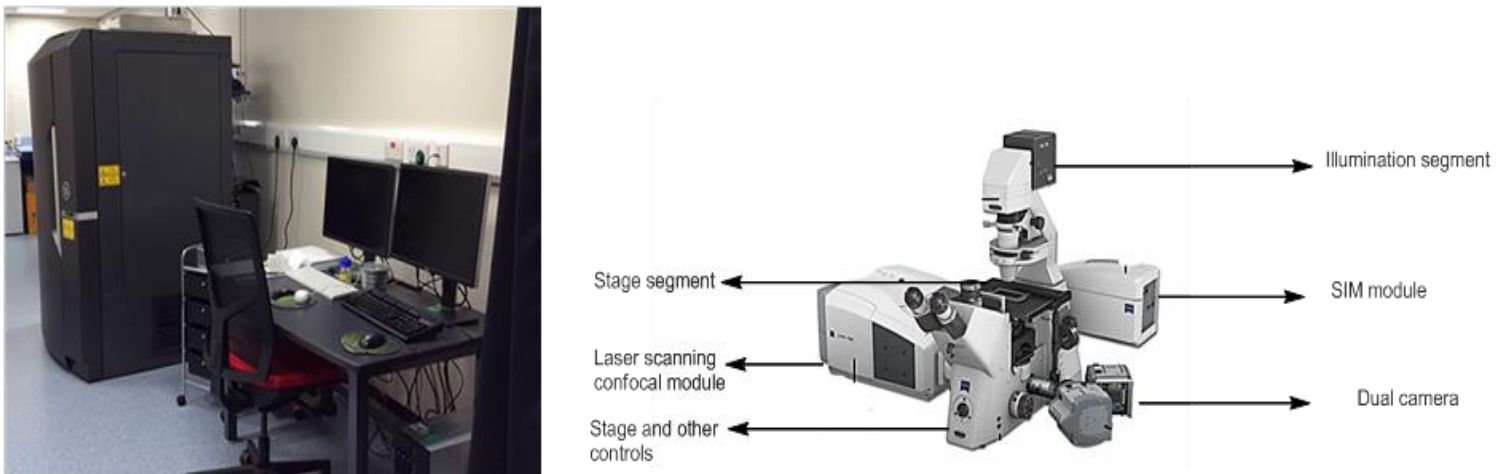
Figure: 2.2 Delta vision/GE OMX Optical microscope for Structured illumination (**Source**: LMF, University of Sheffield)

Although SIM has lower spatial resolution than the previously mentioned technique, it overcomes some of its drawbacks as, it works with most types of luminophore and requires lower excitation power on the order of only 1–10 W/cm^2, making SIM particularly well suited for investigating living biological samples without exposure to deleterious light intensities[66].

2.2.3 SR-SIM

The optical configuration and point-spread function improvement for super resolution structured illumination microscopy (SR-SIM) is shown in the image. The microscope configuration consists of a laser source directed into the microscope optical train using a multimode fiber coupler. The laser light, which is scrambled before entering the microscope, is directed through a polarizer and a diffraction grating, and is then projected onto the specimen. Only the -1, 0, and +1 diffraction orders are focused onto the objective rear aperture, and these are collimated by the objective in the specimen focal plane where they interfere and generate a three-dimensional (lateral and axial) sinusoidal illumination pattern. Fluorescence emission generated by illumination of the specimen is captured by a CCD camera system. The lateral resolution of SR-SIM approaches 100 nm or better, whereas the axial resolution is improved to approximately 300 nm[67].
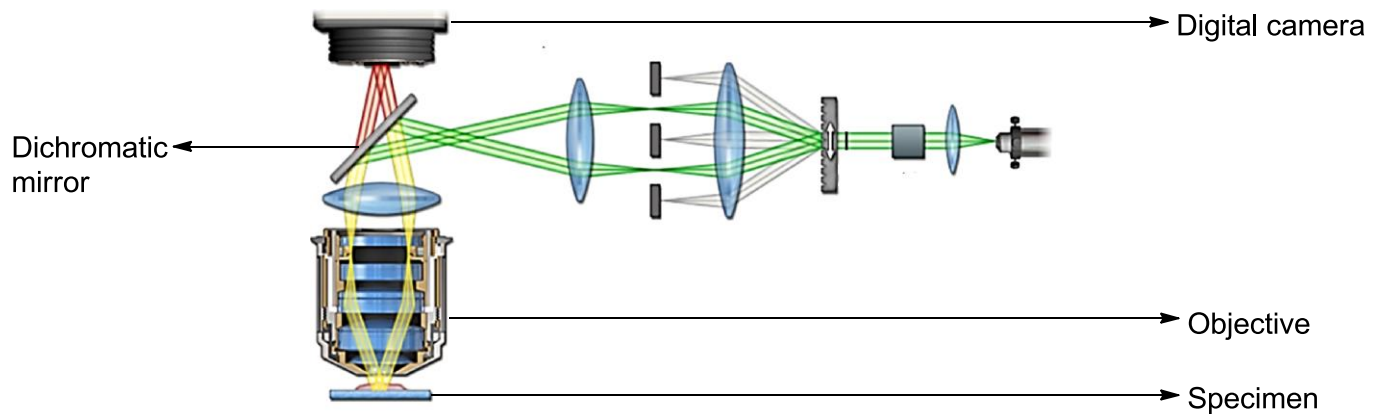
Figure: 2.3 SIM optical train

In SIM, a non-uniform illumination pattern is formed by the interference of three linearly polarised laser beams. Their polarisation is perpendicular to the plane of incidence, or s-polarised, to generate maximum contrast in the illumination pattern. For optimal resolution enhancement, the fourier components of the interference intensity pattern need to be located close to the boundary of the Optical transfer function (OTF) support. Through frequency mixing of the illumination pattern and the underlying sample information, normally unobservable regions of frequency space (i.e., the regions outside the OTF support) are made observable, thus extending resolution beyond the classic diffraction limit[66].

2.3 STORM AND SIM – Sample set up for cell free studies

The initial SIM experiments were performed by using the Delta vision/GE-OMX optical microscope for structured illumination (3D SIM), ultimate focus hardware autofocus module, x,y,z nano-motion sample stage with fast piezo z axis system, six colour wide field illumination module and ring TIRF, temperature and carbon dioxide controlled, software: Delta vision OMX softworx 6.0, Laser lines: 405 nm, 445 nm, 514 nm, 568 nm, 642 nm, Lenses: 60X 1.42 oil planapochromat; 60X Apo TIRF 1.49 oil, Filterset: 436/31 (DAPI), 528/48 (Alexa fluor 488), 609/37 (Alexa fluor 568, mCherry), 683/40 (Alexa fluor 647, Cy5).

STORM buffer preparation (only for STORM):

STORM buffer was prepared by using TN buffer (50 mM Tris (pH 8.0) and 10 mM NaCl, an oxygen scavenging system (0.5 mg ml^{-1} glucose oxidase (Sigma-Aldrich), 40 µg mL^{-1} catalase (Roche or Sigma-Aldrich) and 10% (w/v) glucose) and 10 mM MEA (Fluka)). MEA was stored as a solid at 4 °C and prepared fresh as a 1 M stock solution in water with pH adjusted to ~8 with 1 M aqueous KOH. This stock solution was kept at 4 °C and used within 1–2 weeks of preparation.

Metal complex stock solution (for both STORM and SIM)

The ruthenium complex was converted into its water soluble chloride derivative for carrying out the experiments. This was done by dissolving the 0.15 mM [{Ru(phen)}$_2$tpphz](PF$_6$)$_4$ in acetone. To this complex solution 10 eq tetrabutylammonium chloride (also dissolved in acetone) ≈ 1.53 mM is added and the formation of [{Ru(phen)}$_2$tpphz](Cl)$_4$ is achieved by allowing it to precipitate under cold conditions.

The stock solution of the chloride salt was diluted according to experimental requirements. A 1 mM complex solution was prepared by using the STORM buffer as mentioned above or TRIS buffer for SIM.

DNA stock solution (for both STORM and SIM)

Calf Thymus DNA (CT-DNA) was purchased from Sigma-chemicals as its lyophilised solid sodium salt and used without further purification. An average length of 200-300 base pairs was achieved using a modified preparation by Chaires *et al,* in which stock solutions of CT-DNA were prepared by dissolving 100 mg of the solid material in 20 mL of tris buffer (5 mM Tris, 25 mM NaCl) and then subjected to discontinuous sonication. This was conducted at ice bath temperatures for a total of 30 minutes to ensure homogeneity, ensuring that five minute periods of sonication were followed by 5 minutes of cooling.

DNA samples were quantified in terms of quality and concentration by conventional absorbance measurements. Nucleic acids have an absorbance maximum at 260 nm and contaminants such as proteins and single stranded DNA/RNA absorb maximally at 280 nm. The purity of a sample is assessed by calculating the ratio of contaminants to DNA, with $A_{260}/A_{280} > 1.9$ indicating a protein free sample. The concentration of the resulting solutions was also determined per base pair (bp) by UV spectroscopy using $\varepsilon_{260} = 13200$ $M^{-1}cm^{-1}$ for CT-DNA.

Structure of $[\{Ru(phen)\}_2 tpphz]^{4+}$, the molecular probe used in experiments:
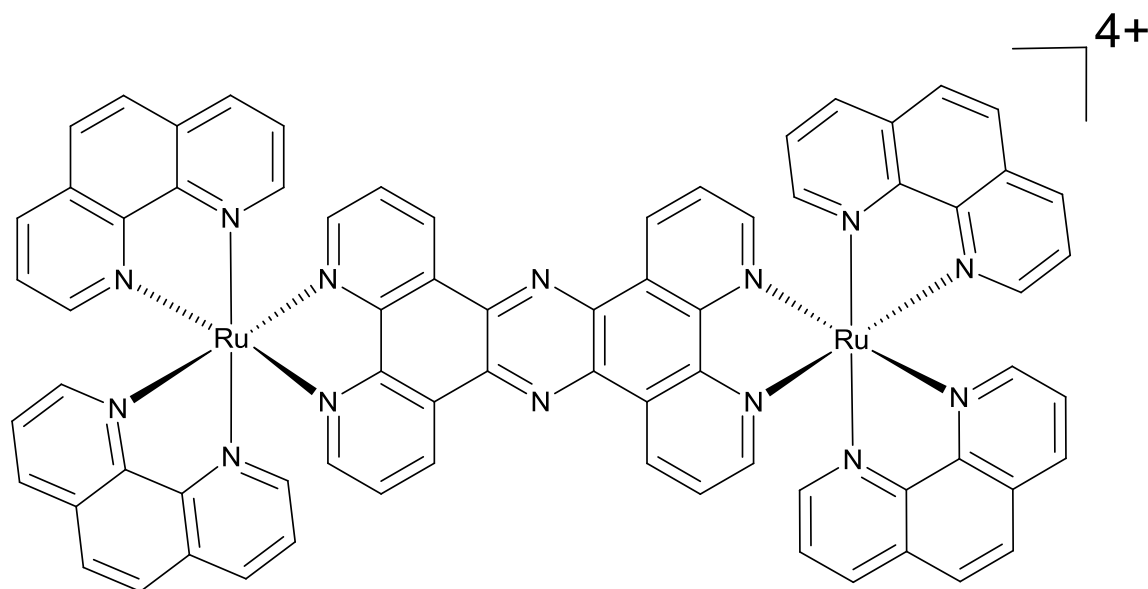
DNA staining procedure (STORM and SIM)

DNA staining was carried out by incubating 15 µL of 1 mM DNA with 15 µL of 20 µM of probe for 24 hours. The complex stock solution was prepared by using the relevant buffer and diluted to 20 µM. The staining was carried out solely though standing and no sonification was carried out. The staining was confirmed by carrying out photophysics studies on the sample. The sample was stored under cold conditions during staining. The samples were prepared fresh for each experiment.

SIM and STORM experiment – Cell free DNA imaging sample preparation

Microscopy slides, 25.4 X 76.2 mm and coverslips, 22 X 22 (thickness, 0.17 mm) were used for STORM experiments. The microscopy slides and coverslips were washed with 1% HCl and then with 70% ethanol for 30 min at room temperature on a shaker. The coverslip was washed with DI water. The coverslip was incubated with poly-l-lysine, about 15 µL of complex stained DNA is added on the poly-l-lysine coated coverslip and dried using nitrogen gas. One drop of mounting reagent (Prolong gold mounting media, life technologies) was added in such a way that no air bubble formation occurs. The coverslips was slowly tilted over the microscopy slide in such a way so that, again, no air bubble was formed and then it was tightly sealed with an adhesive. The samples are then exposed to laser of wavelength 405 nm and measurement was done by using the Quad cube filter set (STORM) or the DAPI filter set (SIM).
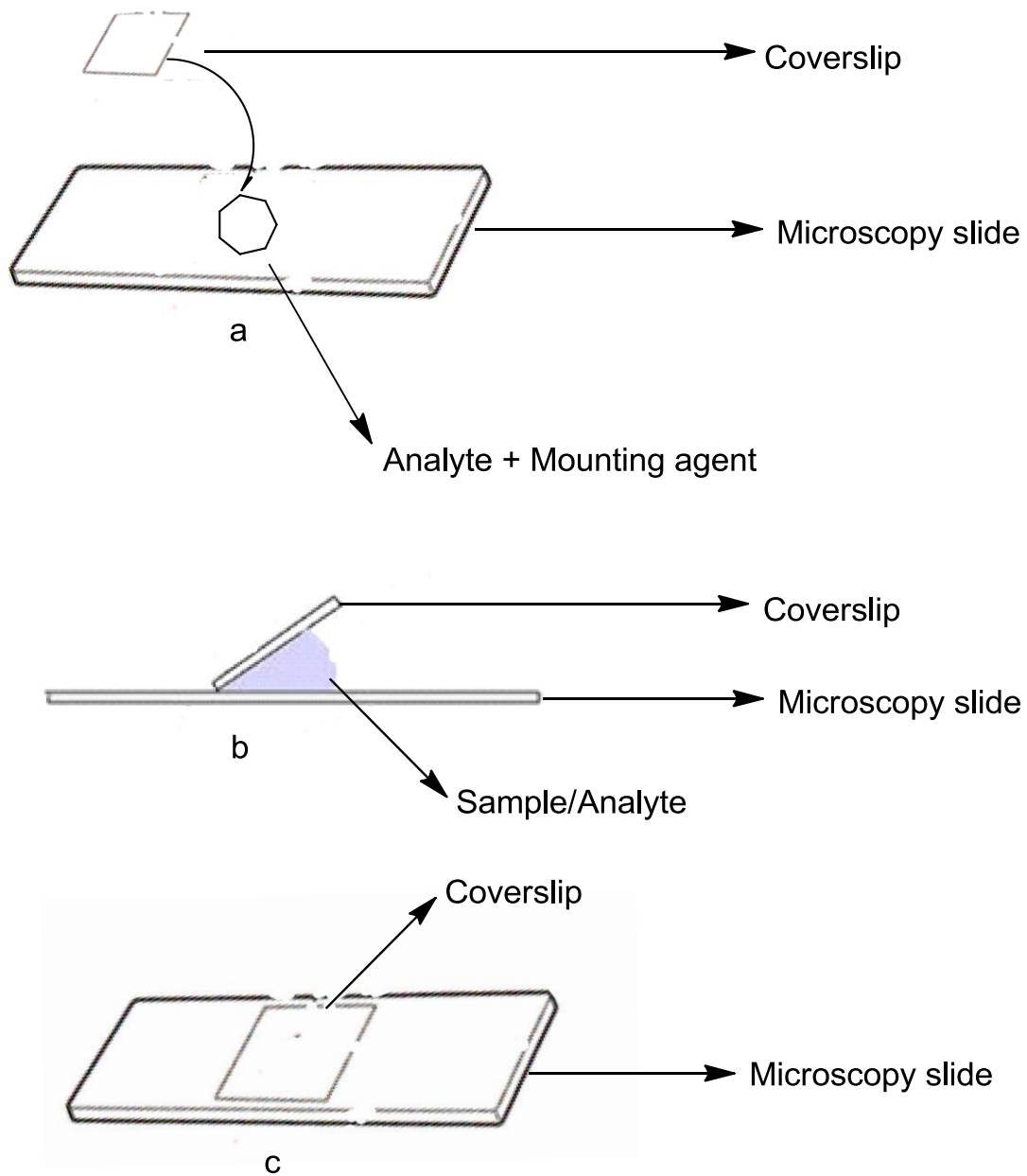
Figure: 2.4 Step by step illustration of sample preparation for Microscopy analysis

2.4 STORM Experiment

Two neutral experiments were carried out with DI water and STORM buffer and the impurities present were bleached away with bright laser source, this was done to remove the background from the actual experiment. To achieve a blinking effect the sample (complex) should be photo-bleachable but moderately stable to achieve a switching effect which is essential in STORM. The initial images obtained did show some evidence of a blinking effect over the time scale of the experiment, presumably due to individual complexes deactivating. However these images were not well resolved, presumably because the lifetime of the excited complex is too long lived to achieve true blinking. However, the complex could potentially be used as a STORM probe in certain circumstances: further experiments need to be planned to investigate whether modulating the concentration of the complex affects the blinking effect, or the use of a redox quencher could produce true blinking effects. If this could be accomplished, studies could then be extended to cellular imaging.
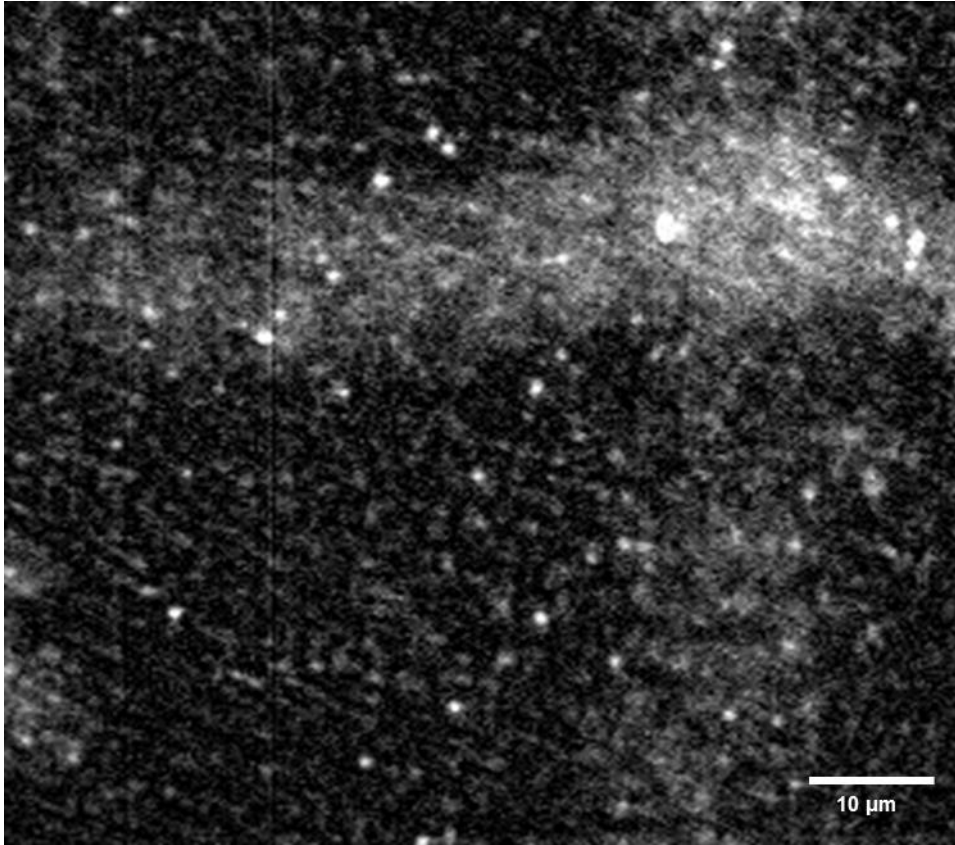
Figure: 2.5 Initial STORM image of 1 mM CT-DNA stained with 20 µM RRP

2.5 SIM Experiment

The initial SIM experiments with the probe were carried out by using 20 µM complex incubated for 2 days. Even in these non-optimised conditions, it is clear that good quality images of DNA fibres could be imaged using the metal complex probe in SIM experiments.
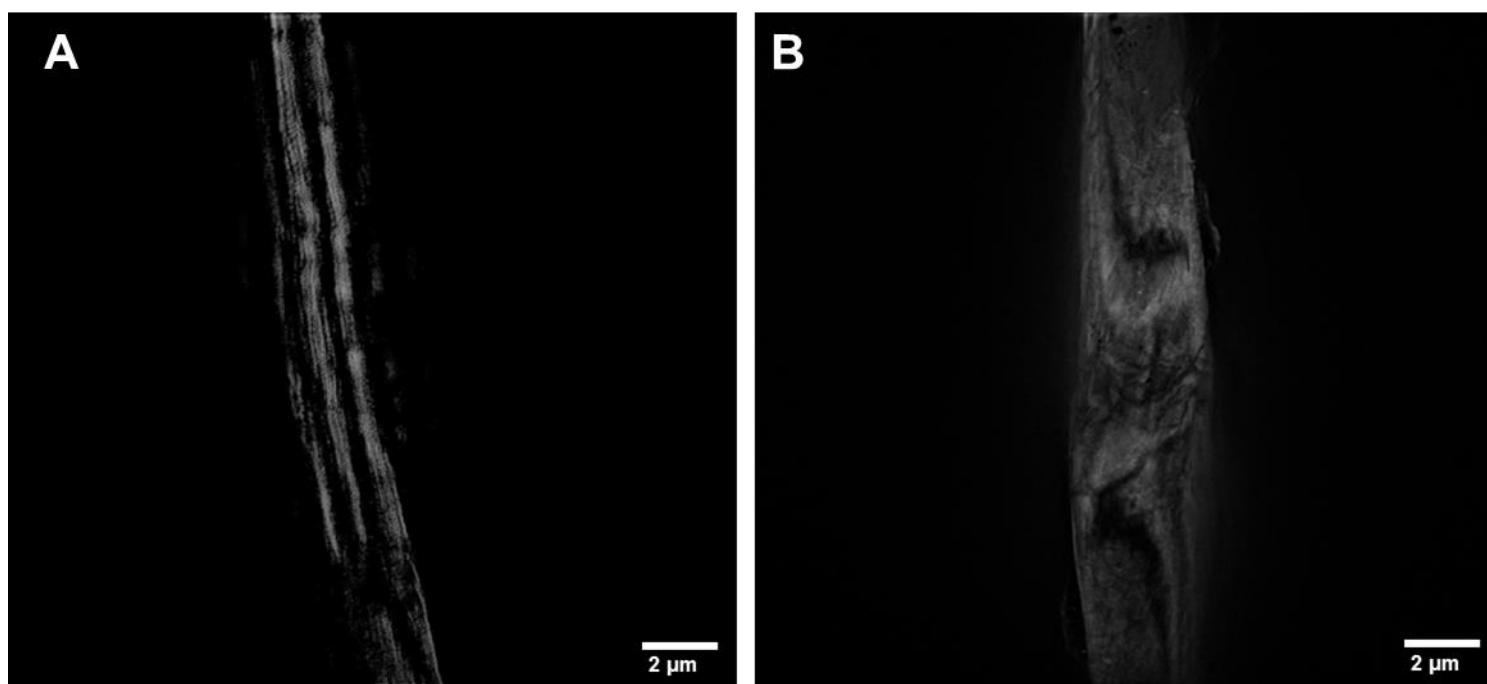
Figure: 2.6 (A) Initial SIM image of 1 mM CT-DNA stained with 20 µM RRP (Area 1)
(B) SIM image of 1 mM CT-DNA stained with RRP (Area 2)

The initial cell-free investigations with fixed CT-DNA using STORM and SIM confirmed that the dinuclear RuRu probe cannot be used in STORM on its own because the probe is long-lived and possess high quantum yield, but SIM experiments suggested that the probe is suitable as a DNA imaging super-resolution probe. Since using SIM within cells would effect lateral resolution of 120 nm which is nearly double the resolution achieved through confocal laser scanning microscopy (CLSM), optimising the probe as a cellular SIM probe could potentially enable the retrieval of valuable information about chromatin architecture through complex-DNA interactions. Additionally the exceptional quantum yield and life time exhibited by the probe inspired us to seek out facilities to explore the use of the probe STED-based cellular imaging.

2.6 CELLULAR UPTAKE OF RUTHENIUM METAL COMPLEXES (RRP, [{Ru(phen)}$_2$tpphz]$^{4+}$): WIDEFIELD MICROSCOPY

2.6.1 Cellular uptake study in MCF7 cells at diverse RRP concentration

The live cellular uptake characteristics of RRP have been determined already but these experiments were carried out at a high fixed concentration monitored by confocal microscopy[54]. Cell permeable DNA imaging agents play essential roles in the visualization of numerous healthy cellular processes, for example cell division involving nuclear chromatin, as well as those involved in disease progression directly related to the DNA. Therefore a detailed study of the probe was carried out to determine the minimum concentration of RRP required so that nuclear uptake could be observed, and to determine the exact concentration required to optimize super-resolution microscopy imaging. RRP shows minimum cytotoxicity, high level of brighness, high photostability[53,54] and these characteristics enable it to be characterized at even low concentrations on cellular uptake, this prompted a concentration dependent uptake experiment of RRP to study its innate cellular localization. These experiments were initially carried out using the conventional widefield mode of the OMX-SIM, imaging MCF7 cells (breast cancer cell line) and performed at a wide range of concentration from 250 nM to 300 μM with post processing carried out offline using FIJI software. Surprisingly, apart from the previously reported nuclear uptake, at low concentration (from 250 nM to 10 μM) signals were observed coming from the cytosol region. This phenomenon was then explored in more detail. As can be seen from Figure 2.7 (A), in-cell emission was observed even at the low concentration of 250 nM. As the concentration moved up from 250 nM, bright spots were observed in the cytosol regions indicating specific localization of RRP in regions within the cytosol. Figure 2.7 (B) indicates an increase in brightness with respect to increase in concentration. As concentration of RRP increases its localization in the nucleus becomes more pronounced; this could be seen at RRP concentration greater than 20 μM.
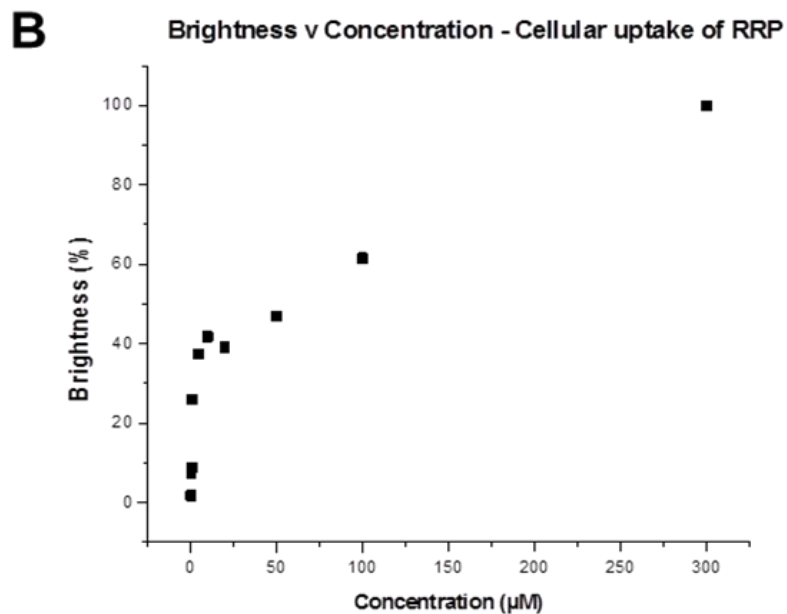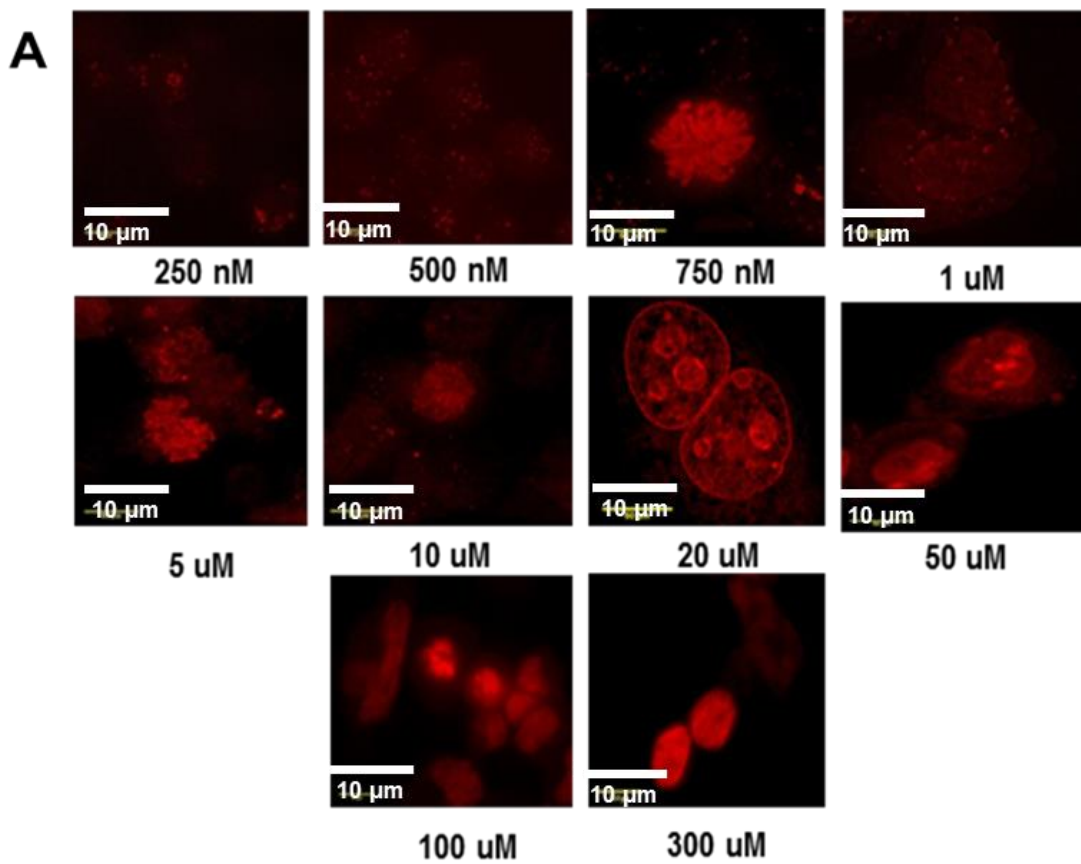
Figure 2.7 (A) Widefield images of RRP cellular uptake at diverse concentrations in MCF7 cells. **(B)** Plot showing increase of *in cellulo* luminescence at diverse concentration of RRP

2.6.2 Concentration dependent nuclear and uptake studies in MCF7 cells

The striking results produced in the initial concentration dependent uptake experiments prompted us to carry out another set of uptake experiment particularly focussing over the 4 µM to 25 µM concentration range in which non-nuclear staining appeared to be most pronounced. As seen from Figure 2.8, at concentration below 10 µM localization of RRP in the cytosol regions is observed in MCF7 cells. Widefield images and deconvolved widefield images were obtained as shown in Figure 2.8 and this proves this point. Pearson's correlation coefficients were generated from these widefield images and this supports the observed results.

To identify localisation within the cytosol, colocalisation experiments were carried out. Since lipophilic cations are often taken up by mitochondria, co-staining with commercial Mito Tracker probes was first investigated. In these experiments Mito Tracker Red was excited at 568 nm and its emission was collected at the Alexa fluor 568 channel between 570 to 620 nm. We did investigate other Mito Tracker probes for widefield imaging, but the SIM experiment only worked well with Mito Tracker Red; in all likelihood this is because its higher photostability best tolerated SIM imaging conditions. Niehorster *et al*[113] have already shown that multiple probes can be used for simultaneous super-resolution imaging in conjugation with FLIM imaging, opening up avenues for imaging multiple targets involved in different bio-signalling pathways to track disease progressions. The localization pattern exhibited by RRP at different concentration provides evidence of concentration dependent uptake in multiple cellular organelles. This characteristic could mean that RRP could be used as a flexible fluorescent probe to track diverse cellular mechanisms involving multiple organelles.

We also found that true dual colour SIM images using RRP in combination with Mito Tracker Red could only be generated at RRP concentrations above 25 µM, as at higher concentrations RRP preferentially localizes in the nucleus. At lower concentrations this was not the case.

Figure 2.8 (A) Left to Right: Widefield images showing cellular localization of RRP (4 μM), Mito Tracker Red (MTR) (1 μM) (Individual channel), Colocalized image of RRP (4 μM) and MTR (1 μM), Pearson's plot for the same. **(B) Left to Right:** Widefield images showing cellular localization of RRP (6 μM), Mito Tracker Red (MTR) (1 μM) (Individual channel), Colocalized image of RRP (6 μM) and MTR (1 μM), Pearson's plot for the same. **(C) Left to Right:** Widefield images showing cellular localization of RRP (12 μM), Mito Tracker Red (MTR) (1 μM) (Individual channel), Colocalized image of RRP (12 μM) and MTR (1 μM), Pearson's plot for the same. **(D) Left to Right:** Widefield images showing cellular localization of RRP (18 μM), Mito Tracker Red (MTR) (1 μM) (Individual channel), Colocalized image of RRP (18 μM) and MTR (1 μM), Pearson's plot for the same. The experiments were carried on MCF7 cell line. **Scale bar:** 50 μM

43

Pearson's correlation coefficients, as shown by the colocalization maps in Figure 2.8 and the coefficients in Table 2.1, prove that the localization of RRP in the mitochondria is more observed at low concentration of RRP. As RRP is a charged molecule the uptake and binding of RRP could depend to a large extent on this. The localization of RRP into the mitochondria could be due to the mitochodrial potential, which helps in the uptake of a charged species like RRP. The colocalization experiments were performed using a variety of standard trackers which stains mitochondria some of them tested include Mito Tracker Red, Mito Tracker Green and Mito Tracker Deep Red. This was done in order to confirm the observations. As the imaging experiments were carried out using widefield microscopy, and RRP has a broad emission profile extending from $600 - 750$ nm, there is always a possibility of crosstalk between channels. Therefore experiments with all available standard Mito Trackers were carried out to remove any doubts with regard to the authenticity of the findings. Colocalization of RRP with Mito Tracker Red is observable at concentration below 10 µM and is especially clear below 8 µM. As it was difficult to process signals obtained from the cytosol regions below 1 µM, we choose slightly higher concentration of about 4 µM to carry out full colocalization experiments using wide field deconvolution microscopy.

As the following figures illustrate, the live cell experiments using Mito Tracker Green and Deep Red confirmed that RRP localizes within mitochondria at these concentrations (Figure 2.9 and 2.10). Mito Tracker Green was employed in order to confirm the results obtained from the colocalization experiments using Mito Tracker Red. Widefield microscopy images obtained as shown in Figure 2.9 indicates that RRP is localizing in mitochondria at concentrations of RRP as low as 4 µM. In this experiment Mito Tracker Green emission was collected in the FITC channel ($500 - 550$ nm) which is far from RRP emission channel.
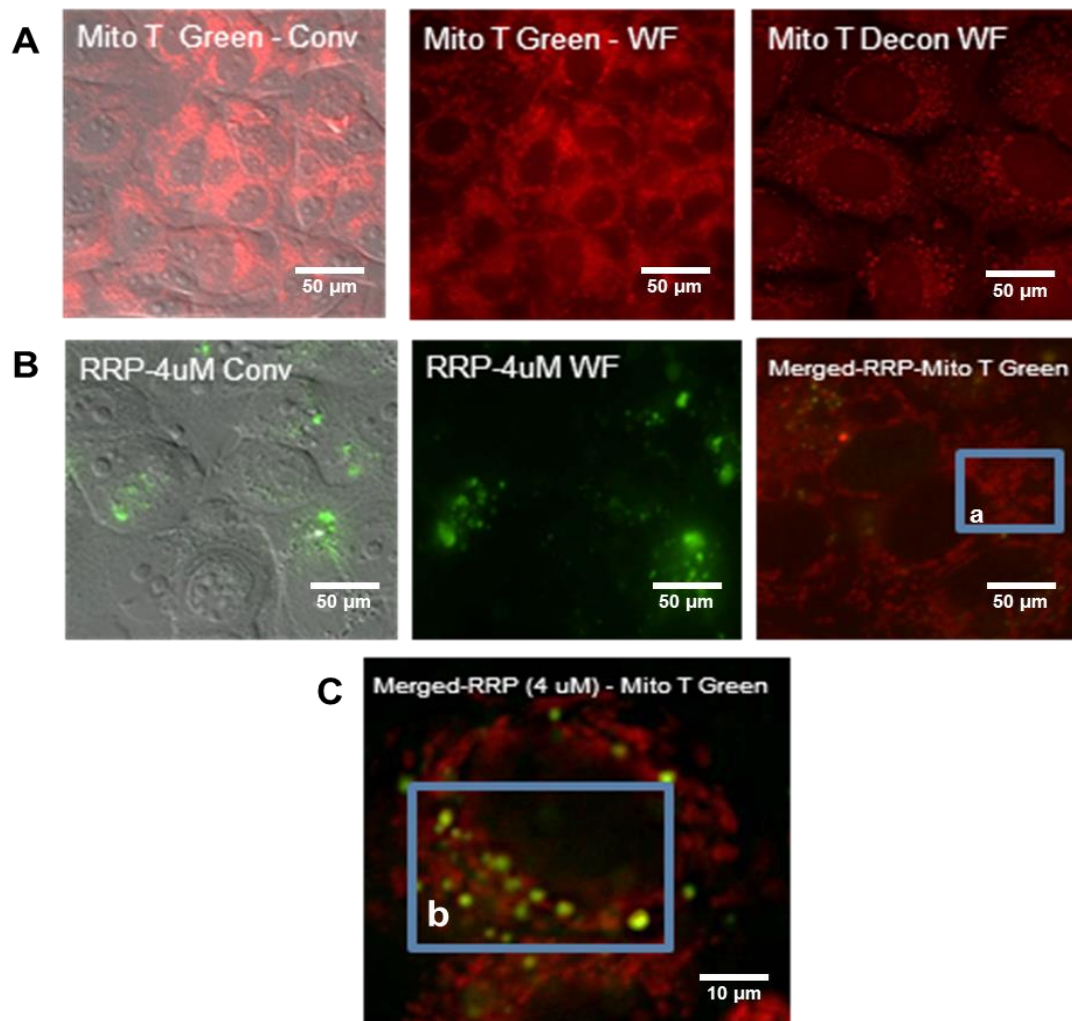
Figure 2.9 (A) Left to Right: Widefield images showing the cellular localization of Mito Tracker Green (MTG) (phase contrast and fluorescence merged), widefield fluorescence image of MTG, widefield deconvoluted image of MTG. **(B) Left to Right:** Widefield image showing cellular localization of RRP, 4 µM (Phase contrast and Fluorescence merged), Widefield fluorescence image of RRP, 4 µM, widefield deconvoluted merged image of RRP 4 µM and MTG. **(C)** Widefield deconvoluted merged image of RRP 4 µM and MTG. **Boxed regions (a and b)** shows colocalized regions. All experiments were carried out on MCF7 cells

Additional colocalization experiments were carried out using Mito Tracker Deep Red which has an emission profile in the far red region. This was done deliberately to avoid co-excitation of RRP. Mito Tracker Deep Red excitation is at 644 nm which is far from the excitation exhibited by RRP. The experimental results as shown in Figure 2.10 again confirmed the localization of RRP on the mitochondria. Intensity profiles generated for these images showed the Mito Tracker Deep Red (Red line) overlapping the RRP (blue line) confirming colocalization.
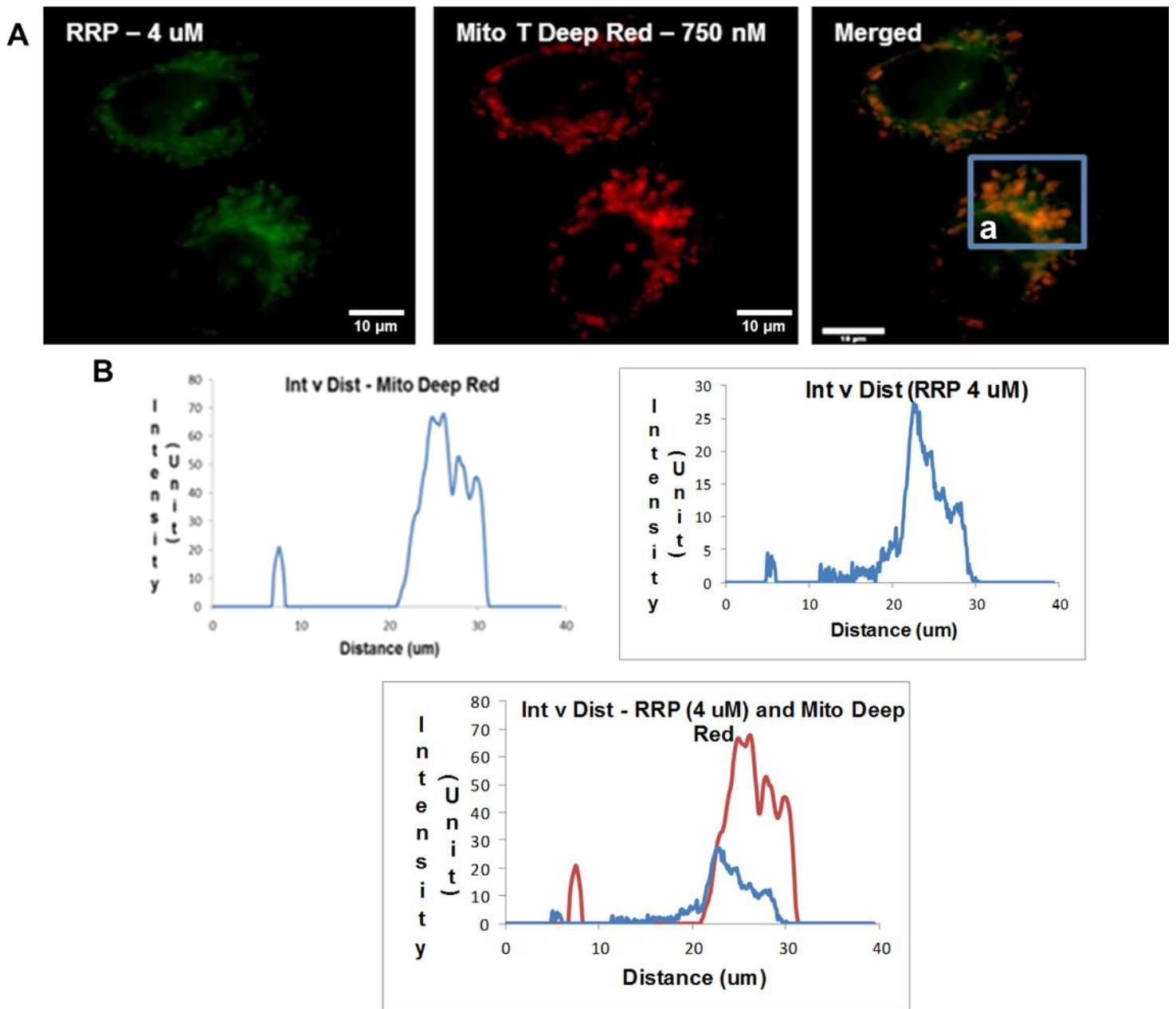
Figure 2.10 (A) Left to Right: Widefield images showing cellular localization of RRP (4 µM), Mito Tracker Deep Red (MTDR) (750 nM) (Individual channel), Colocalized image RRP (4 µM) and MTDR (750 nM). **(B) Left to Right:** Intensity v Distance plot for MTDR, RRP (4 µM), **Bottom:** Intensity v Distance plot for RRP (4 µM) and MTDR (750 nM) merged. **Boxed region: (a)** shows RRP and MTDR colocalization. All experiments were carried out on MCF7 cells. **Scale bar:** 10 µM

As mentioned in the earlier sections, Concentration dependent mitochondrial localization was confirmed by an analysis of the co-staining data using Pearson and Mander's coefficients, which showed that high overlap coefficient with Mito Tracker Red were only obtained at lower concentrations of RRP uptake - Table 2.1. Pearson's coefficient values and Mander's coefficient values were generated using Volocity, an off-line software package which employs the widefield image data input to construct a correlation map. The Pearson's coefficient values are taken into consideration because they are more dependable compared to the Mander's coefficient values. The pitfalls of Mander's coefficient when compared to Pearson's coefficient include, the hybrid measurement approach as it combines correlation with a heavy weighted form of co-occurrence, it also favours high-intensity combinations. On the other hand the Pearson's coefficient measures only the exact correlations; it does not overlook combinations with high and low intensity pixels and it also does not ignore blank pixels, which plays an important part in the Pearson's correlation coefficient calculations. This is the reason why the Pearson's coefficient is regarded as the most well-established coefficient to support colocalization characteristics exhibited when two or more dyes are used during a particular imaging experiment. Mander's coefficient was introduced only as a supporting tool to compliment the findings of Pearson's coefficient[188].

Concentration of RRP (µM)	Pearson's Coefficient	Mander's Coefficient (M1)	Mander's Coefficient (M2)
4 µM	0.771	0.977	0.894
6 µM	0.654	0.982	0.969
12 µM	- 0.096	0.992	0.843
18 µM	-0.259	0.657	0.992

Table 2.1 Colocalization measurments: Pearson's coeffcients

It was found that even at these low concentrations, Airyscan experiments could be used to be obtain high resolution microscopy images showing RRP localizing within mitochondria. Airyscan images shown in Figure 2.11 gives a clearer picture of mitochondrial and nuclear localization exhibited by RRP at lower (8 µM) and higher (18 µM) concentrations of RRP. These images obtained from Airyscan are at higher spatial resolution and they confirm the fact that the change in preferential uptake of RRP on altering its concentration can be observed very clearly in MCF7, breast cancer cells. Airyscan microscopy is a high resolution microscopy technique invented by Zeiss. Airyscan provides images with better spatial resolution compared to conventional confocal microscopy. In addition an excellent lateral resolution of 140 nm is achieved by Airyscan which is on par with certain super-resolution microscopy techniques like SIM. The superior resolution in Airyscan is achieved by rejecting out of focus light through a sophisticated technique which images a point-like source in an extended airy disc pattern. The Airyscan technique substantially eliminates the possibility of artefacts and autofluorescence and as a result it improves the signal to noise ratio to obtain a high resolved image. Thus, greater resolution on RRP localization in the mitochondria and nuclei was acchieved by employing RRP as an Airyscan cellular imaging probe. A

comparison between confocal and Airyscan HR shows the improvement in resolution. The lateral resolution is nearly doubled in Airy scan HR compared to the confocal – Fig 2.11.
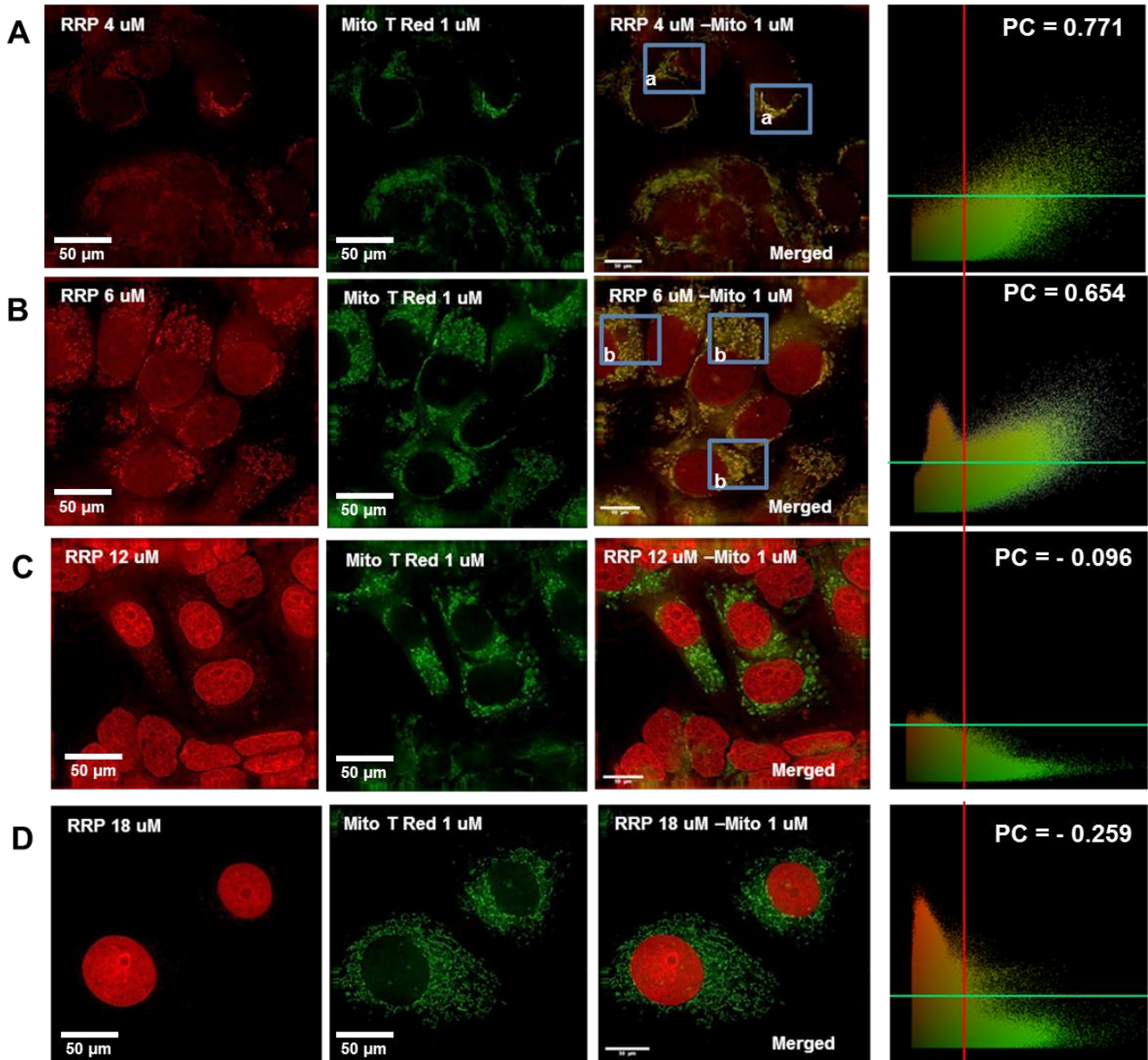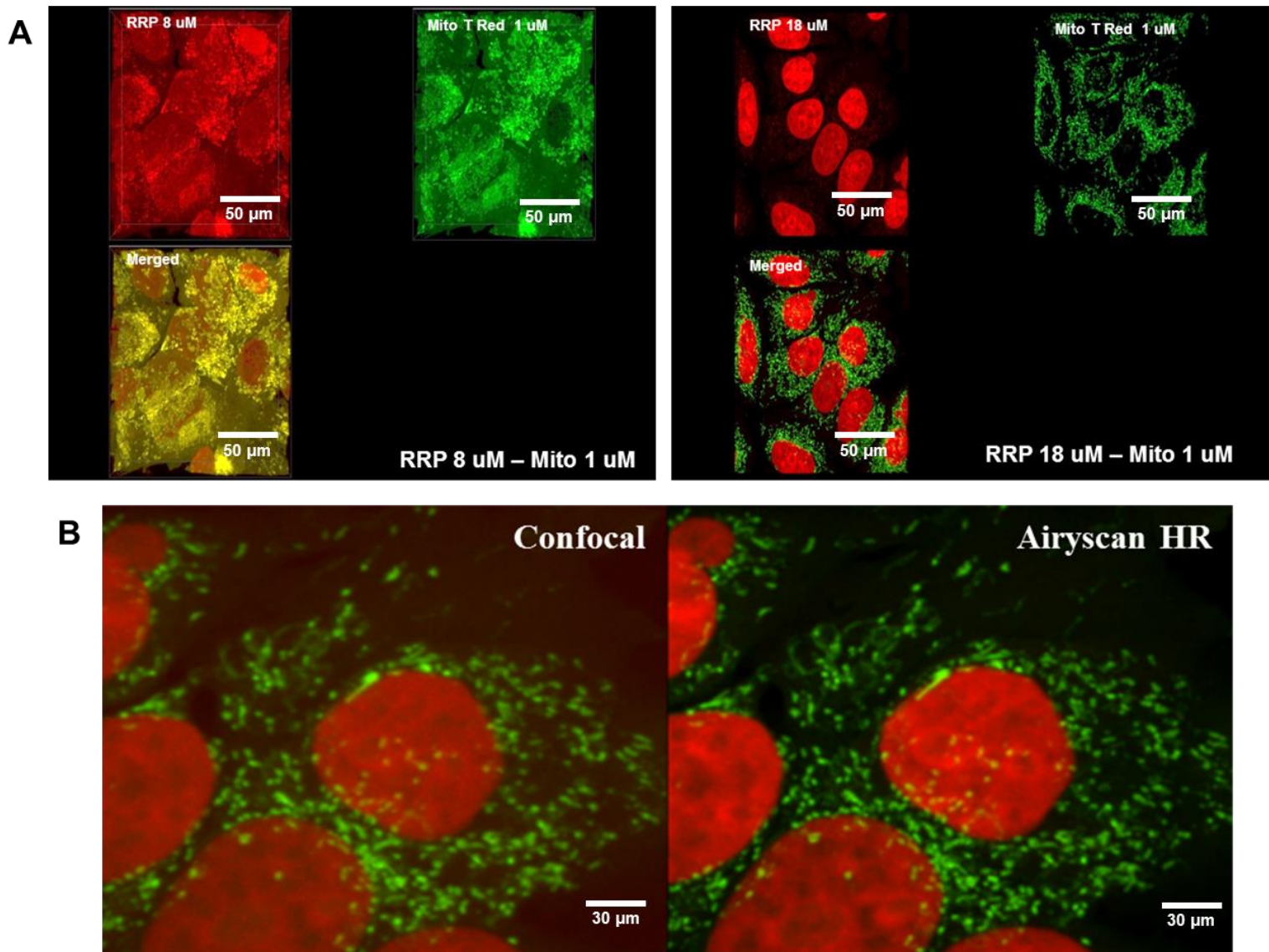

Figure 2.11 (A) Left to Right: Airyscan High resolution images showing cellular localization of RRP (8 μM), Mito Tracker Red (MTR) (1 μM) (Individual channel), Colocalized image RRP (8 μM) and MTR (1 μM). Airyscan High resolution images showing cellular localization of RRP (18 μM), Mito Tracker Red (MTR) (1 μM) (Individual channel), Colocalized image RRP (18 μM) and MTR (1 μM). **(B)** Comparitive image Confocal and Airyscan High resolution colocalized image of RRP and MTR. All experiments were performed on MCF7 cells

2.6.3 Time dependent uptake study in MCF7 cells using RRP probe

Time lapse uptake experiments were used to determine the finer details of RRP uptake with regard to preferential localization in more than one intracellular organelle. Having explored the concentration effects on take up, time lapse uptake experiments were performed to determine the rate of uptake of RRP in mitochondria and nuclei. In order to determine whether a substantial amount of mitochondrial localization was happening over specific time periods, colocalization experiment featuring a fixed concentration of RRP and a series of Mito trackers namely, Mito Tracker Red, Green and Deep Red were performed. The only variant in this colocalization time lapse experiment was time. The results, shown in Figure 2.12, revealed that the rate of uptake of RRP into both mitochondria and nuclei happens very quickly, with staining observed within 2 minutes for concentration as low as 10 µM.
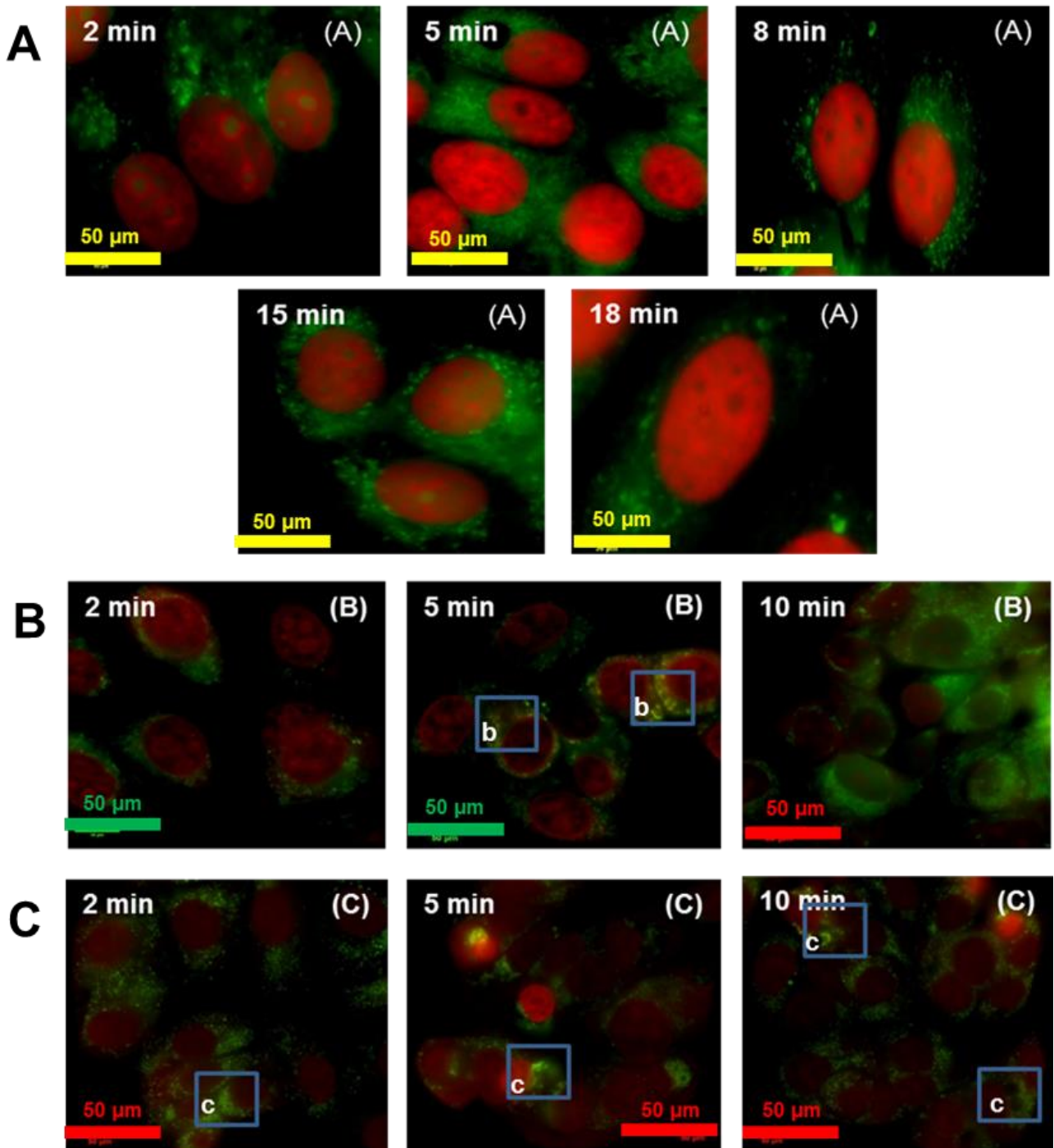
Figure 2.12 (A) (Left to Right): Time lapse Widefield images of cellular internalization of RRP (10 µM), Mito Tracker Red (1 µM) merged at diverse time intervals from 2 min. to 18 min. **(B) (Left to Right):** Time lapse Widefield images of RRP (10 µM) and Mito Tracker Deep Red (750 nM) merged at diverse time intervals from 2 min. to 10 min. **(C) (Left to Right):** Time lapse Widefield images of RRP (10 µM) and Mito Tracker Green (1 µM) merged at diverse time intervals from 2 min. to 10 min. **Boxed regions (b and c)** show colocalized regions. MCF7 cells were employed

52

2.7 CONCENTRATION EFFECTS ON THE CELL CYCLE OF A2780 CELLS

The previous sections provides substantial evidence to indicate that RRP is a unique probe because of its ability to localize in two different intracellular organelle at varying concentrations. At higher concentration RRP is preferentially localized in the nucleus and it stains the chromosomes. Imaging of sub-chromosomal structure using super resolution microscopy with RRP could provide a great deal of information. Many cellular processes involving diseased organism depend a great deal on the cell cycle. Determination of cell proliferation and its distinction from incomplete cell cycle progression forms a critical element in understanding the details of diseased pathways[106]. The M-phase of the cell cycle involves substantial alterations with regard to mid-body arrangement and mitotic spindles. As cells travel through the different stages this phase, the chromosomal arrangement and configuration varies greatly. As RRP probe preferentially binds to nuclear chromatin at high concentration, a deeper study on the effect of varied concentrations on cell division was carried out. This study was carried out on ovarian cancer A2780 cells as they show superior and distinctive nuclear uptake of RRP even at concentration as low as 1 μM.

Although quantification experiments for specific organelles have not been performed, qualitative imaging experiments indicated that nuclear uptake of RRP was greater for A2780 cells compared to MCF7 cells, allowing us to obtain nuclear images over a higher range of concentrations. These observations led to experiments in which the effect of changing RRP concentration on cellular processes within A2780 cells were studied. In these experiments cells were exposed to concentrations of 1 μM, 5 μM and 50 μM and then observed for a time interval of 100 minutes.
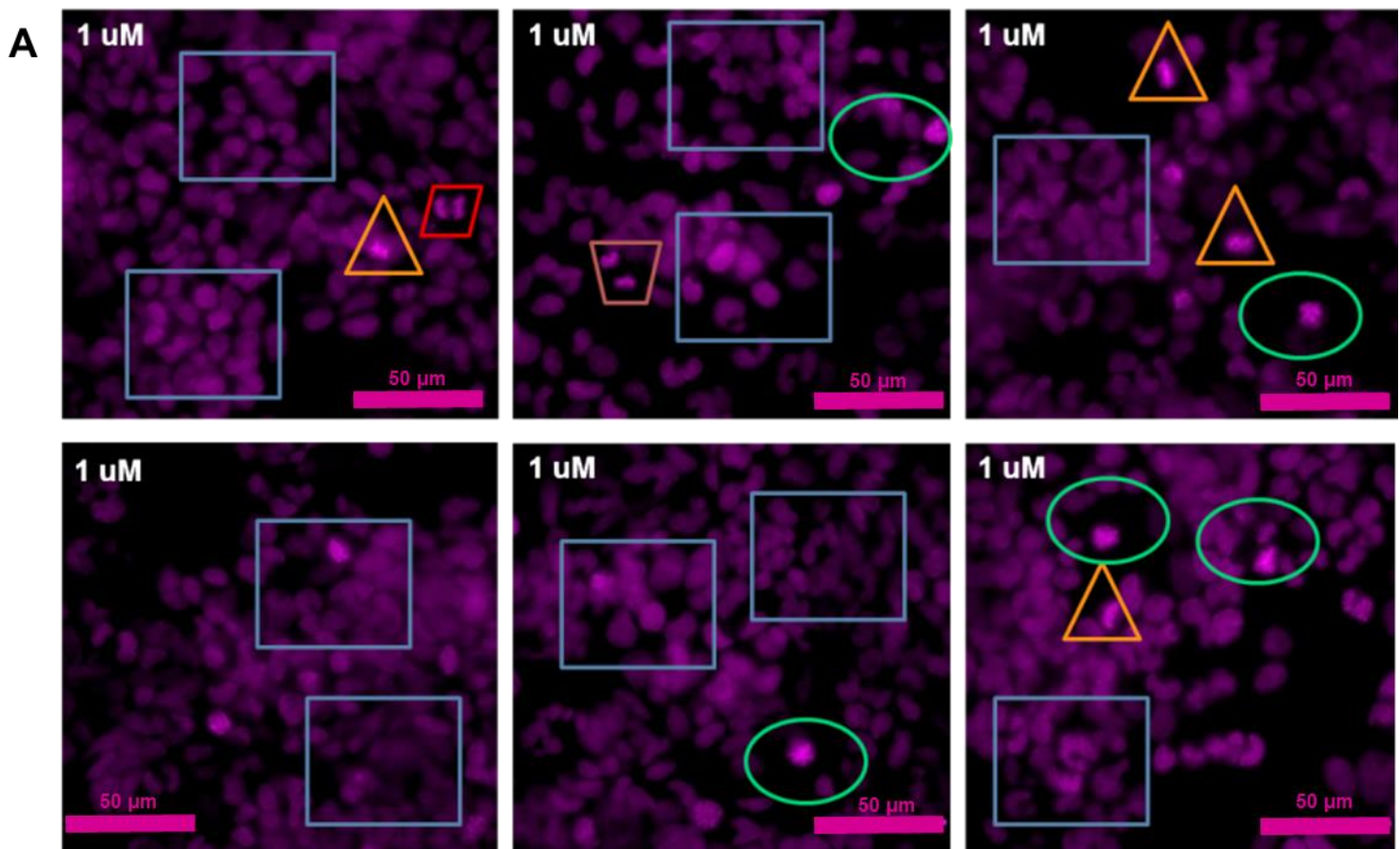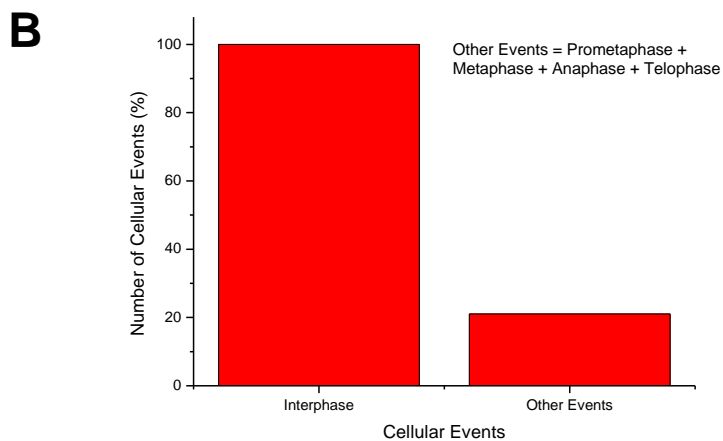
Figure 2.13 (A) Widefield images showing effect of RRP (1 μM) on the different cellular processes happening in A2780 cells. The different cellular events happening are Interphase ☐ Prometaphase ◯ Metaphase △ Anaphase ▱ Telophase ⬡ as shown. **(B)** Bar chart showing the percentage of interphase against other events happening during RRP (1 μM) uptake

From the widefield images acquired over this period, it was clear that the number of cellular division events observed was higher at lower RRP concentrations, for example: the number of prometaphase, metaphase, anaphase and telophase events was found to be far lower at 50 µM RRP. These results indicate that although the probe is not classically cytotoxic, RRP uptake is affecting cellular processes. It is evident that progress through the cell cycle has been affected by RRP. The concentration dependent experiment with respect to preferential uptake in the nucleus with regard to A2780 cells reveals that 5 µM looks the appropriate concentration of RRP required for imaging.
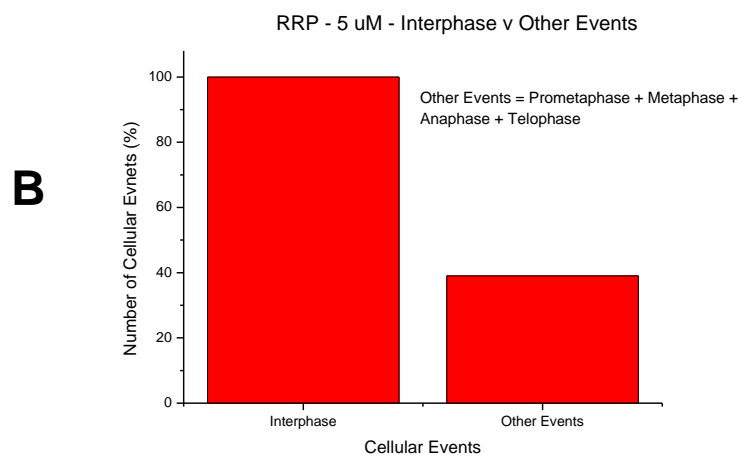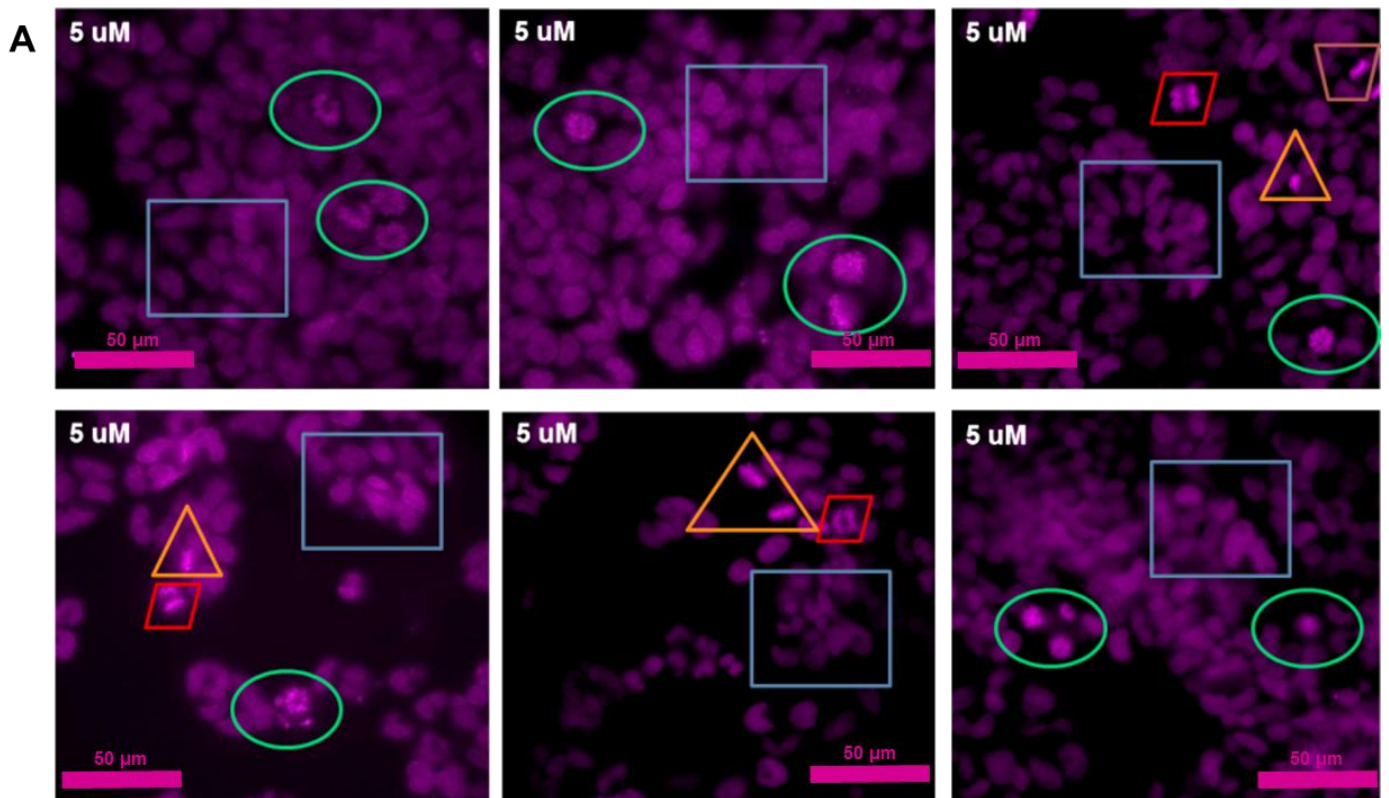
Figure 2.14 (A) Widefield images showing effect of RRP (5 µM) on different cellular processes within A2780 cells. The different cellular events happening are Interphase ▢ Prometaphase ◯ Metaphase △ Anaphase ▢ Telophase ▽ as shown. **(B)** Bar chart showing the percentage of interphase against other events happening during RRP (5 µM) uptake

Ongoing studies within the Thomas group are exploring these cell cycle effects in much more detail; however, it is clear that at lower concentration, RRP functions as an effective nuclear probe in A2780, ovarian cancer cells allowing biological processes involving chromatin architecture to be followed in a detailed way without affecting cellular processes.
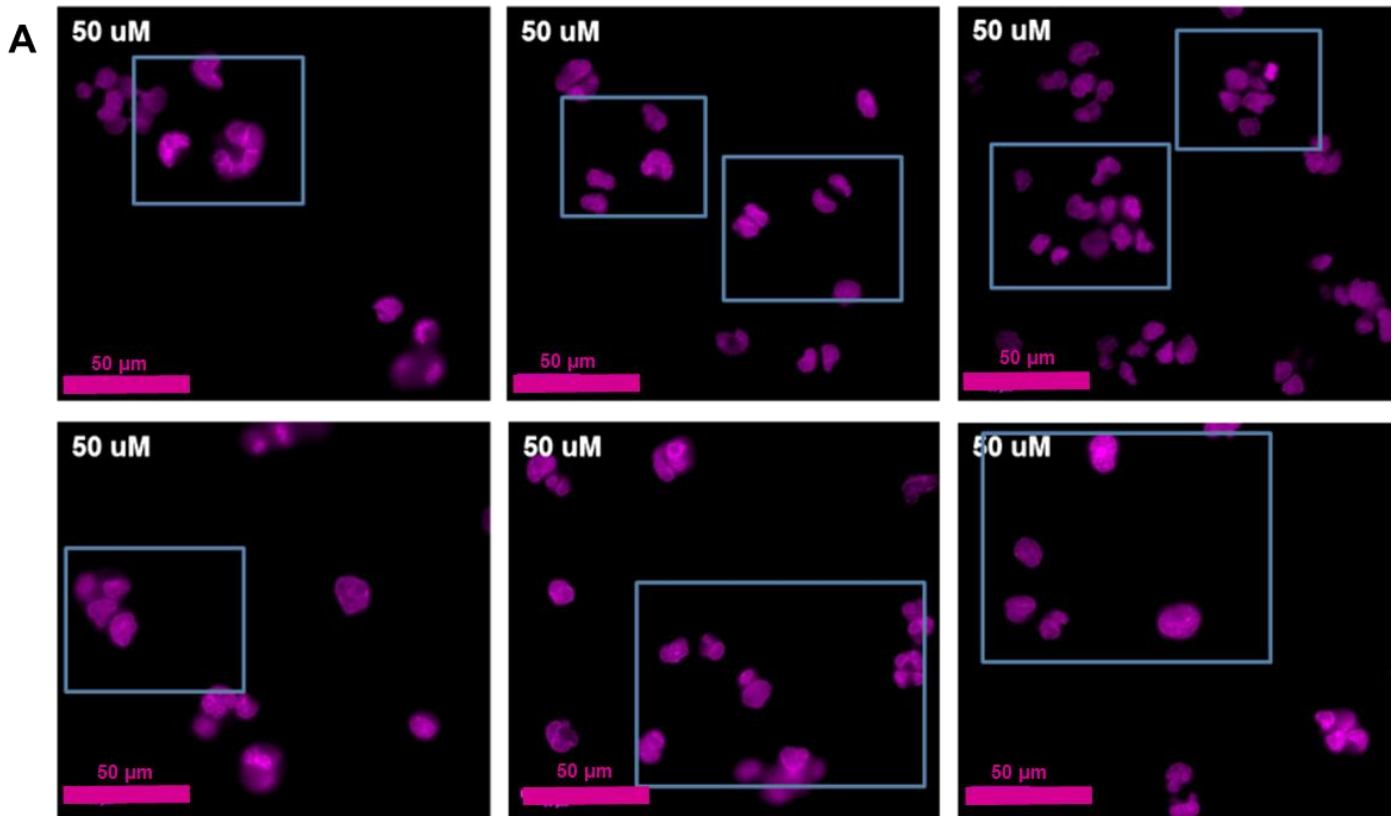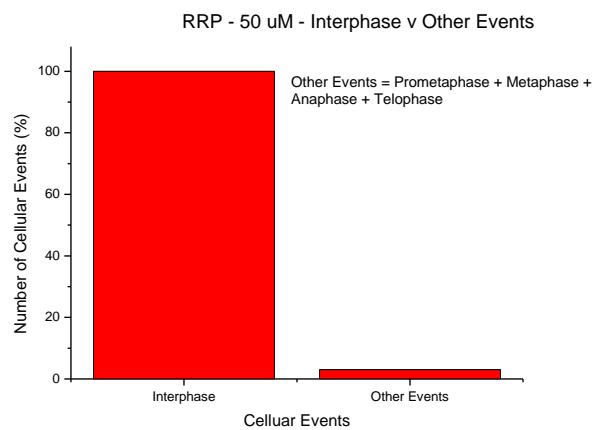
Figure 2.15 (A) Widefield images showing effect of RRP (50 µM) on the different cellular processes happening in A2780 cells. The cellular events happening is predominantly Interphase ☐ as shown. **(B)** Bar chart showing the percentage of interphase against other events happening during RRP (50 µM) uptake

2.8 PHOTOSTABILITY

The concentration dependent uptake experiments and colocalization experiments performed using widefield microscopy and Airyscan microscopy gave a great deal of information with regard to the diversity of localization of the RRP within the mitochondria and the nucleus. These novel finding can be studied at a deeper level through super-resolution microscopy. The super-resolution microscopy techniques SIM and particularly STED impose strict restrictions over the probe suitability particularly related to its photophysical attributes. As the most essential requirement for applying the RRP probe as a STED probe is its photostability, a time dependent photobleaching assessment experiment to determine the photostability of $[\{Ru(phen)\}_2tpphz]^{4+}$ (RRP) relative to standard Mito Tracker dyes was carried out. These experiments were performed on MCF7 cells stained with RRP, Mito Tracker Red and Mito Tracker Green using scans at 60 second time interval per frame (during image acquisition). The photostability experiments for RRP and other dyes were performed by using verified scans of light radiations using the conventional widefield microscopy mode of the OMX-SIM. Laser power, time interval of image acquisition, number of scans per minute were all maintained at the same setting for all the dyes. Post-processing of the imaging data set was carried out by using Fiji/Image J offline software. A robust and continuous emission with minimum photobleaching was exhibited by RRP compared to the other dyes indicating a superior photostability – an essential criteria for super resolution microscopy. The photostability of RRP against conventional dyes is clearly shown in Figure 2.16.
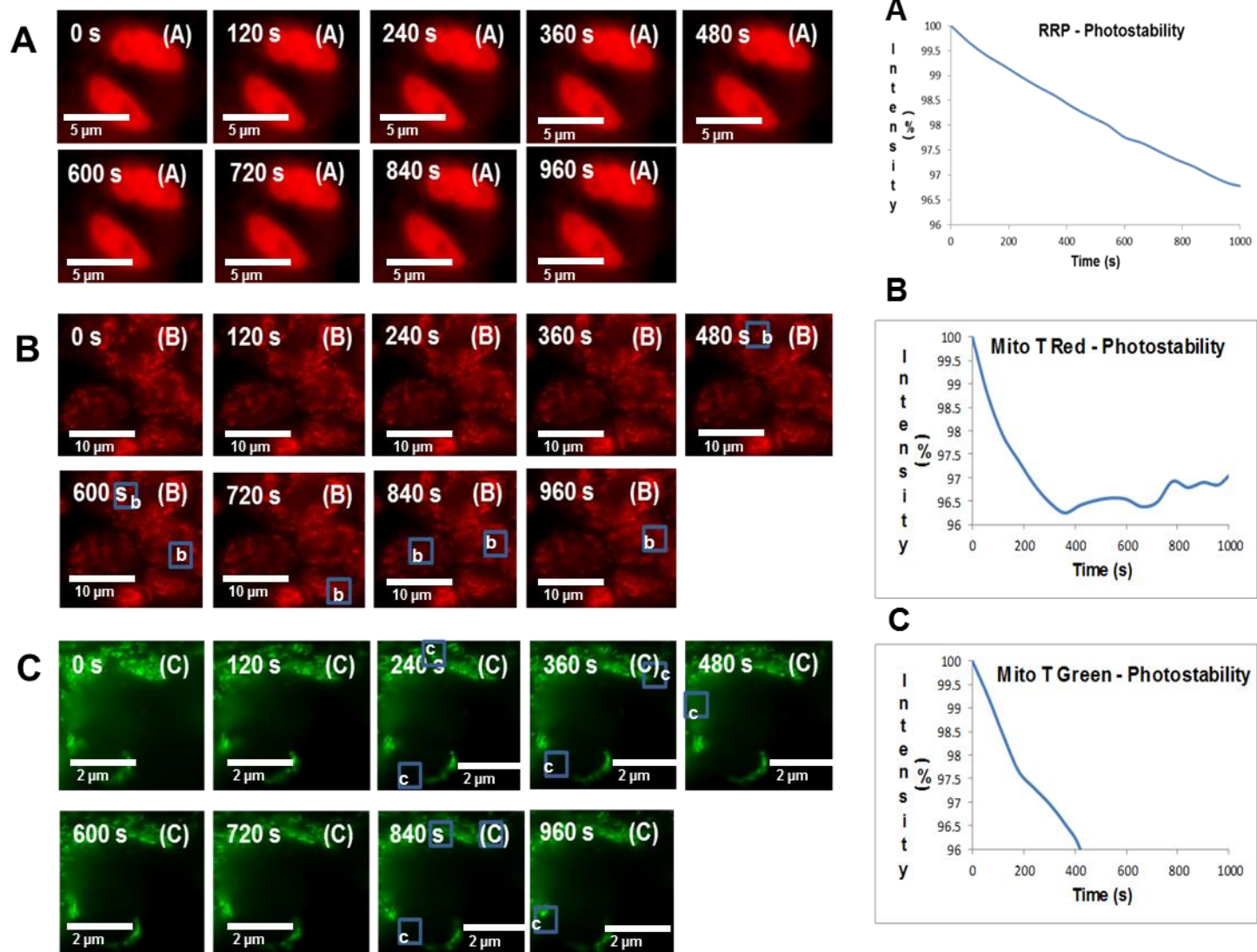
Figure 2.16 (A) Sequence of widefield images acquired over a period 1000 seconds of RRP stained MCF7 cells complimented by Intensity – Time plot demonstrating the photostability of the complex. **(B)** Sequence of Widefield images demonstrating the same for Mito Tracker Red stained MCF7 cells complimented by Intensity – Time plot **(C)** Demonstrating the same for Mito Tracker Green stained MCF7 cells. Boxed regions (**b, c**) indicate bleached out regions during the course of continuous imaging (scan)

2.9 SIM IMAGING OF NUCLEAR CHROMATIN AND DUAL COLOUR IMAGING USING [{Ru(phen)}$_2$tpphz]$^{4+}$ (RRP)

Advanced light microscopy is essential in carrying out nanostructure analysis of chromatin structure. DNA staining dyes essentially provide information into the details of chromatin and the changes it undergoes during cell proliferation. In super-resolution studies, such as STORM, YOYO is a dye commonly used to stain DNA because of its blinking nature; it is used as a DNA stain in cell free as well as in cellular condition.[108]. YOYO interacts with the double helical DNA through intercalation and can be conjugated with other molecules to target other organelles in cells. Like YOYO, RRP interacts with DNA by binding reversibily, but unlike YOYO it is a groove-binder of DNA. Optimization of RRP as a super-resolution microscopy probe could provide a great deal of information regarding the organization and behaviour of nuclear chromatin in detail, in addition the added advantage of concentration based targetting of multiple intracellular organelle could help to maximize its biological applicability from the super resolution microscopy point of view. Therefore, initial studies were carried out on using RRP as a Structured illumination microscopy (SIM) probe.

Cells were incubated for 10 minutes with 50 µM RRP. RRP was excited at 405 or 488 nm and emission at > 650 nm was collected. The broad Stoke's shift and extraordinary stability and brightness of RRP are some of the essential characteristics required for an ideal SIM probe[176,178]. Using these conditions the structure of chromatin nuclear architecture was clearly visualized by the OMX-SIM as shown in Figure 2.17. The 3D SIM projection was processed by IMARIS software.
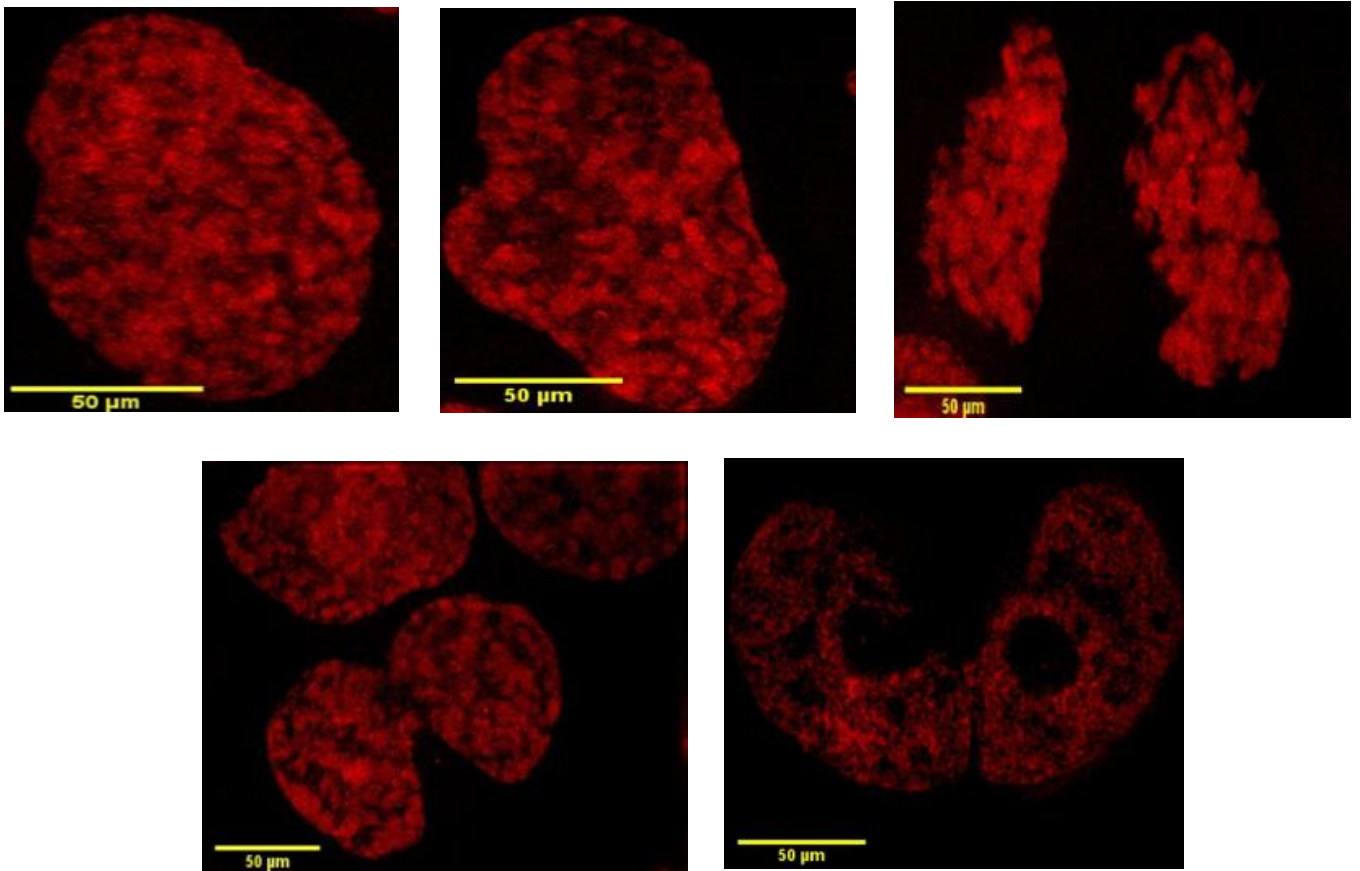
Figure 2.17 Top (Left to Right): SIM Images of RRP (50 µM) stained nucleus of A2780 showing different areas. **Bottom:** Two more different areas. These SIM Images show that RRP at high concentration could used as an effective Super resolution probe to generate single colour SIM Images showing greater nuclear chromatin detail. The imaging was carried out on A2780 cells

Comparison Single colour SIM v WF:

The comparison between SIM and widefield images (Figure 2.18) of RRP stained A2780 cells indicates the superior resolution achieved obtained by using RRP as a SIM probe. These single colour experiments were carried out using A2780 cells because of the superior RRP nuclear uptake observed for this cell line.
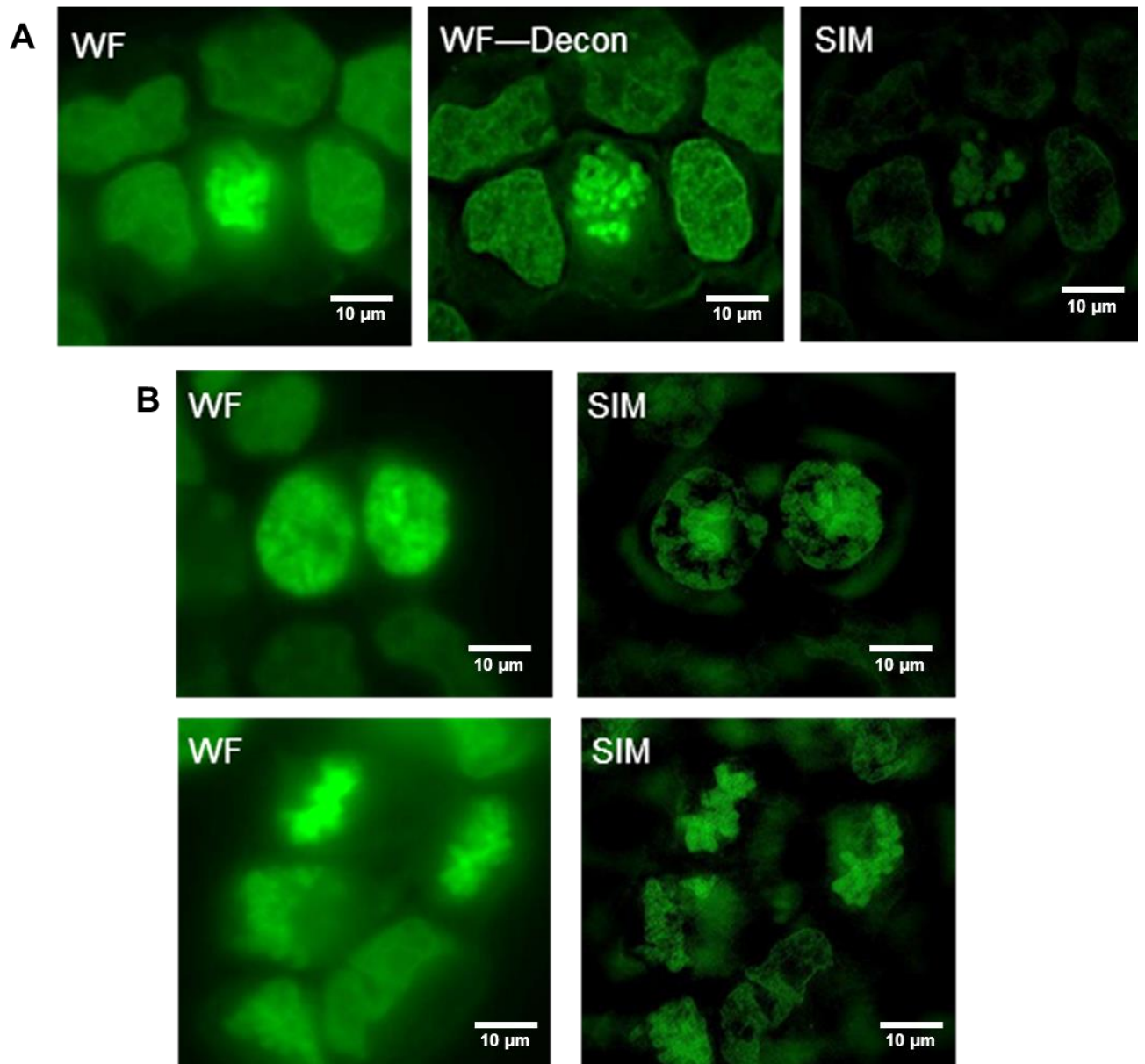
Figure 2.18 (A) Left to Right: Widefield image of RRP (50 μM) stained nucleus, Widefield deconvoluted image of the same area, SIM image of the same area. **(B) Top:** Comparitive Widefield and SIM image of RRP (50 μM) stained nucleus of the same area. **Bottom:** Comparitive Widefield and SIM image of RRP (50 μM) stained chromosomes. The experiments were carried out on A2780 cells

2.10 DUAL COLOUR SIM IMAGING USING [{Ru(Phen)}$_2$Tpphz]$^{4+}$ (RRP)

Multicolour imaging forms a very important aspect of applying super resolution microscopy toward imaging multiple biological targets within cells. Two-colour or Three-colour super resolution imaging relies on applying multiple probes simultaneously to study simultaneous biological mechanisms in several cellular organelle. Lacoste *et al*[117], have shown that dual colour super-resolution microscopy can be used to image multiple cellular targets simultaneously by labelling them with specific biomarkers such as fluorescent antibodies. Although RRP is a concentration dependent multiple organelle targeting super resolution microscopy probe, at high concentrations (> 20 μM) it could be employed for two colour super resolution imaging with another probe. Choosing dyes with totally different spectral characteristics targeting different regions in cells is an important criterion in multicolour super resolution imaging. Therefore, SIM was carried out over a sample containing RRP and Mito Tracker Red. In the conditions developed for nuclear staining which involves RRP localizing purely on to the nucleus at high concentrations, the SIM experiment resulted in minimum colocalization between RRP and Mito Tracker Red and therefore we were able to acquire high quality dual colour SIM images as shown in Figure 2.19. Again, 3D-SIM projections for the Dual colour SIM images were generated by using IMARIS software to understand the greater details obtained from SIM.
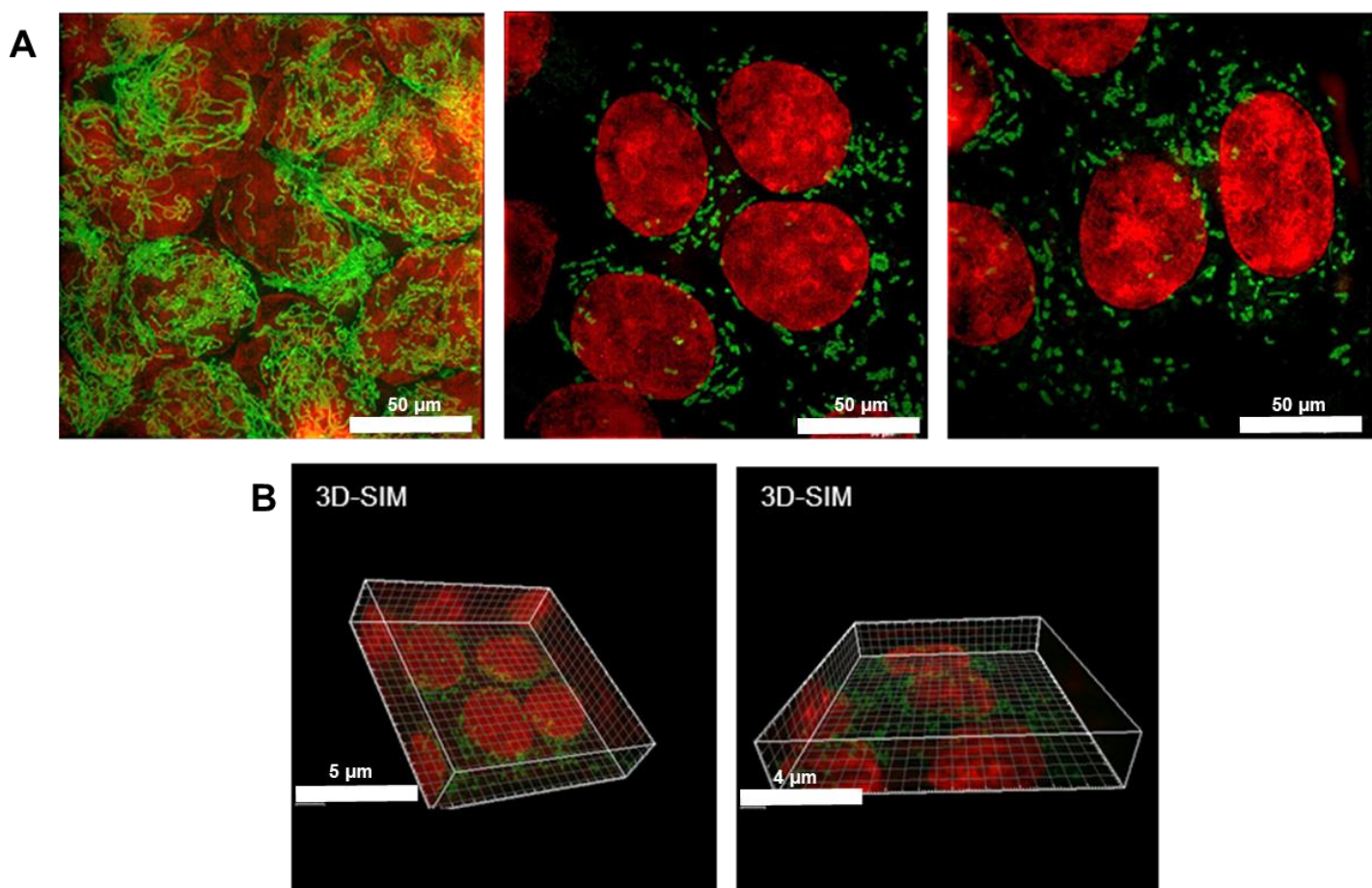
Figure 2.19 (A) Left to Right: Dual colour SIM Images of RRP (25 µM) stained nucleus, the mitochondria is stained by Mito Tracker Red (MTR, 1 µM). **(B)** 3D-SIM projections of the above Dual colour SIM Image generated by using offline software FIJI. The experiments were carried out on MCF7 cells

Comparison SIM and Wide field (Dual colour):

As shown in Figure. 2.20, a comparison between SIM and high-resolution widefield dual colour images illustrates the improvement in resolution obtained by this technique which is further portrayed in the intensity plots constructed for both nucleus and mitochondria. The intensity profiles for both RRP and Mito Tracker Red was generated separately for both widefield and SIM images and this analysis shows the superior resolution achieved in SIM when compared to the widefield. The intensity profiles were generated by using offline FIJI software. The dual colour imaging experiments were carried out on MCF7, ovarian cancer cells.
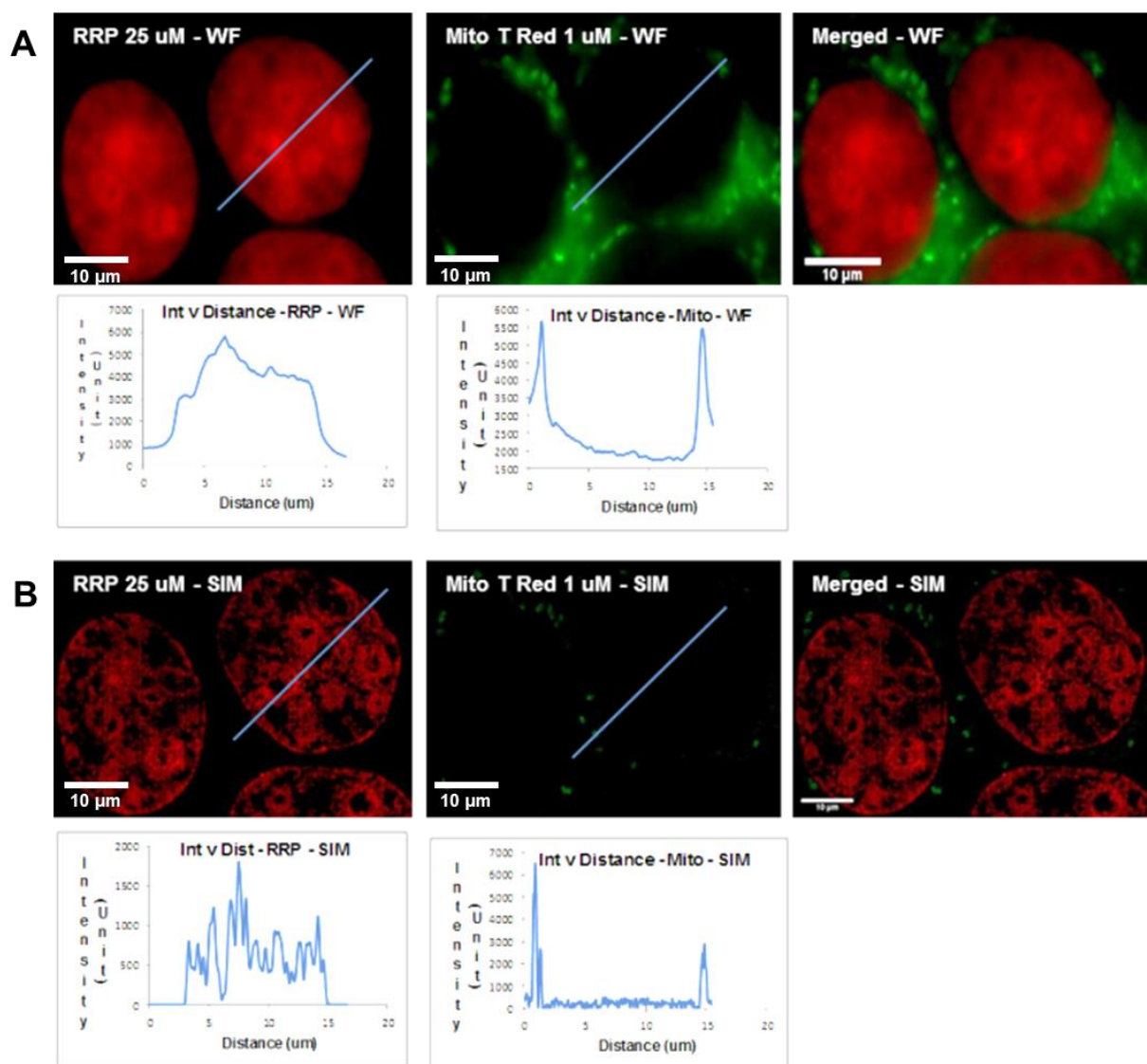
Figure 2.20 (A) Top (Left to Right): Widefield images of RRP (25 μM) staining the nucleus, Mitochondria stained with Mito Tracker Red (1 μM) (Individual channel), Dual colour wide field image, RRP (25 μM) and MTR (1 μM) merged. **Bottom:** Corresponding Intensity profiles for widefield images of RRP (25 μM) and MTR (1 μM) individual channels respectively. **(B) Top (Left to Right):** Comparative SIM images of the same area for RRP (25 μM) stained nucleus, Mitochondria stained with Mito Tracker Red (MTR), 1 μM (Individual channel), Dual colour SIM image, RRP (25 μM) and MTR (1 μM) merged. **Bottom:** Corresponding Intensity profiles for SIM images of RRP (25 μM) and MTR (1 μM) individual channels respectively. The experiment was carried out on MCF7 cells

2.11 STED IMAGING USING [{Ru(phen)}$_2$tpphz]$^{4+}$ (RRP)

Following the success of optimising RRP as a single and dual colour SIM probe its suitability for a second super-resolution techniques was assessed. The main objective for this research was to further improve resolution, as SIM only improves lateral resolution to 120 nm. An attractive option was STED as, despite its advantages in terms of resolutions, comparatively few STED probes have been reported[97]. This is because the requirements for STED microscopy probes are far more demanding than for SIM; high photostability, long life-times and high brightness being essential criteria. Moreover, very few molecules with large Stokes' shift have been reported as STED probes, yet this is advantageous. Since each STED probe requires three separate wavelengths (excitation, depletion, and emission) a wide "spectral window" will be useful for multicolour STED. As STED requires a probe with high photostability, strong brightness, RRP could be be a great candidate for carrying out STED imaging because of its intrinsic photophysical properties. Keyes, *et al*[97] have already reported a ruthenium metal complex conjugated with target specific peptides and carried out target specific STED imaging of more than one cellular organelle. With its instant cellular uptake, and attractive photophysics RRP could be optimised as a STED probe and this might provide crucial information on chromatin dynamics, finer details of sub-cellular chromatin, 3D super resolved chromatin architecture and so on.

Initial STED experiments - carried out in DCU, Dublin in the lab of Prof. Tia Keyes - using a standard 660 nm depletion line on 470 nm excitation were unsuccessful. The probe appeared to show irreversible photobleaching, resulting in considerable loss of emission and the images obtained showed no real improvement in resolution compared to the conventional microscopy. This response is consistent with the depletion line further exciting RRP into a "dark state"[97]. Further examination of the spectral profile of the probes and its broad spectra enabled us to identify another experiment involving a lower energy light depletion beam (775 nm). An experimental setup that could meet these conditions was found to be available in the Rutherford Appleton Laboratory in Oxfordshire. Using the conditions available at RAL the probe gave excellent results leading to significant improvement in resolutions.

2.11.1 Fixed cell STED Imaging:

STED - Localization of RRP on to the Mitochondria:

Multicolour STED imaging work done by Hell *et al*[76,77] has been reported and it involves employing highly photostable flurophores like luminescent organic dyes, proteins to specifically label selected intracellular targets. As outlined previously, localization of RRP over mitochondria only occurs at low concentrations and this could be used to specifically image mitochondria. This led to us to explore the possibility of STED imaging using these conditions.

As described in the previous sections of this chapter, RRP as a multi organelle localizing probe at varied concentration with high photostability that could essentially be employed to image specifically at different concentrations to produce high quality STED images of individual intracellular organelle on which it localizes, namely mitochondria at 6 μM and Nuclei at 60 μM. Image 2.21 clearly shows high quality STED images obtained for RRP when it stains mitochondria and illustrates the superior resolution of STED in comparison to deconvoluted CLSM. The mitochondria specific STED imaging of RRP was carried out in MCF7, ovarian cancer cells.

As Figure 2.21 show, STED imaging proved to be possible even at these low concentration. The figure presents a comparision between dCLSM (Hyvolution - a high-resolution confocal microscopy technique) and STED in RRP stained mitochondria illustrating the increased resolution.
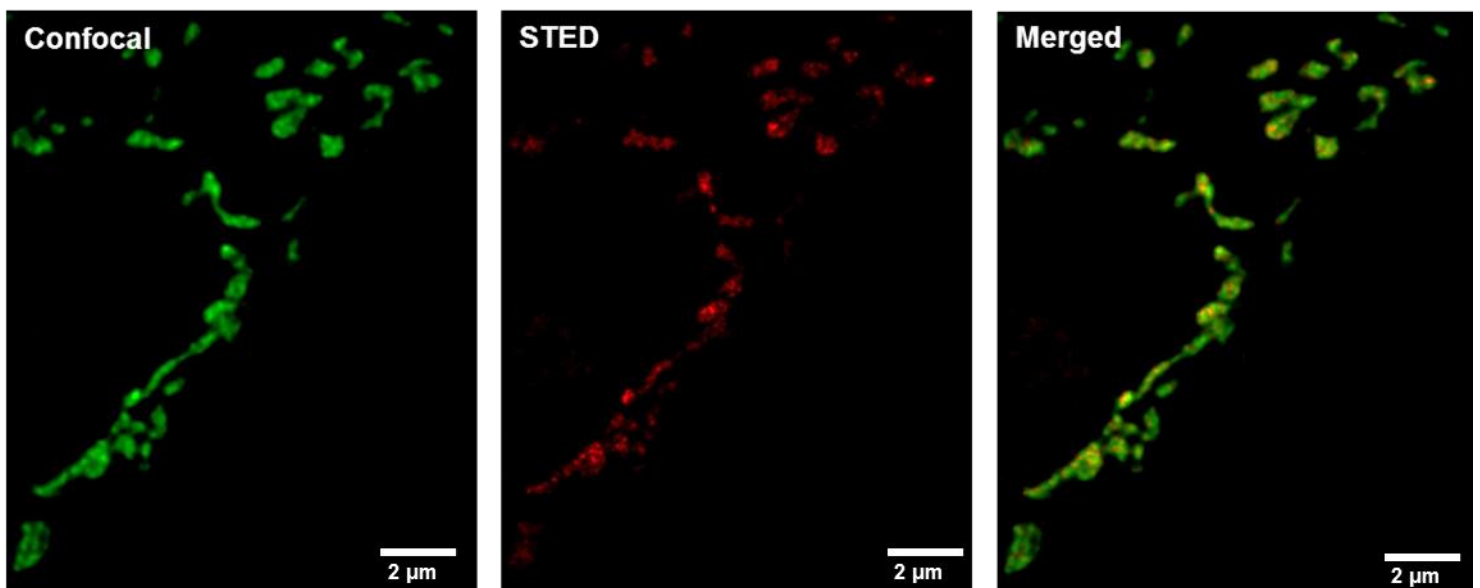
Figure 2.21 Left to Right: dCLSM (Confocal) Image, STED Image, Merged Image of RRP (6 μM) stained Mitochondria in MCF7 cells

2.11.2 STED – Nuclear imaging using [{Ru(phen)}$_2$tpphz]$^{4+}$ (RRP)

At higher concentrations the nuclear localization of RRP (60 µM) has the potential to provide chromatin images of unprecedented quality and this could help in dissecting hidden information pertaining to the complexity of the genome. Although SIM images of RRP stained nuclei could be obtained, as discussed before there are limitations in resolution in the SIM method. Through STED this has been successfully overcome, resulting in unravelling greater details with regard to chromatin architecture. Figure 2.22 and 2.23 shows RRP staining of a nucleus and chromosomes of A2780 cells illustrating its STED resolution. These figures show a comparison between deconvolved high resolution confocal Hyvolution imaging and STED super-resolution.
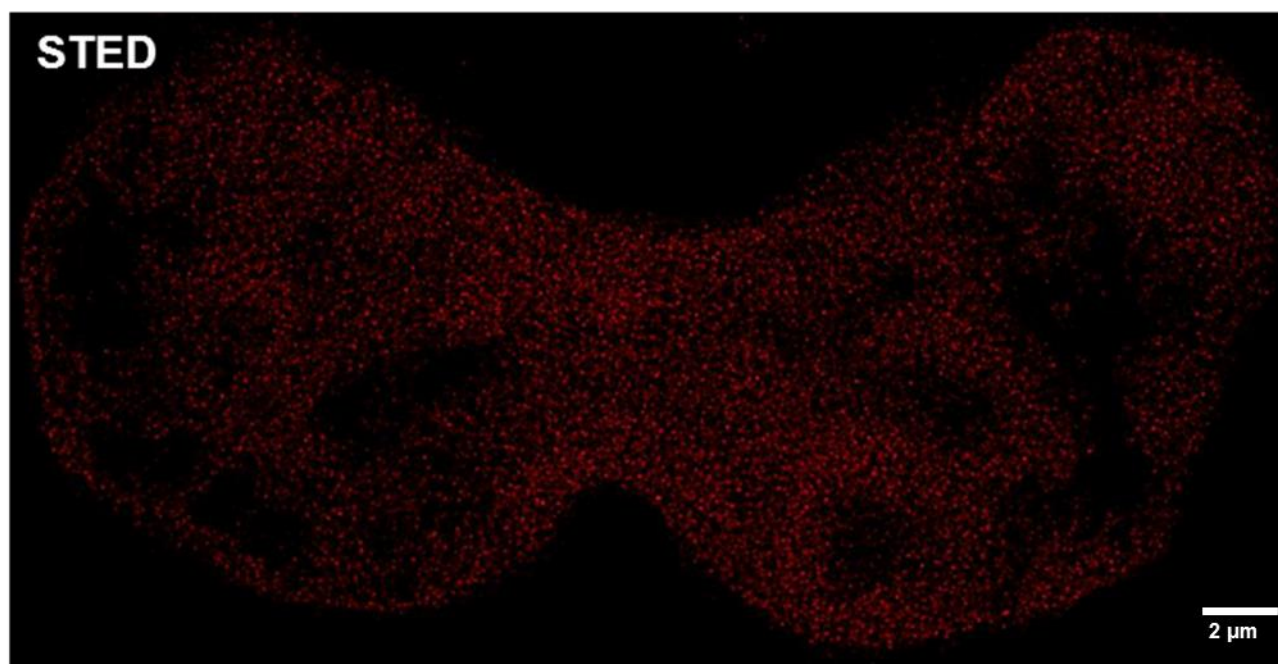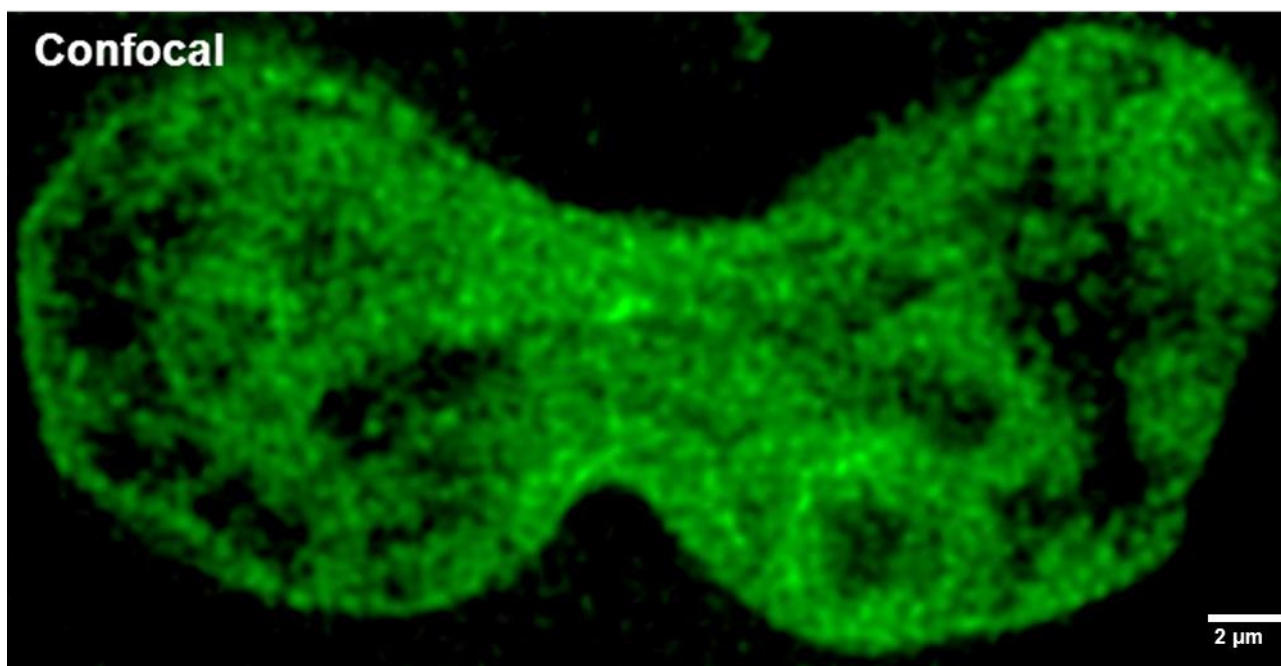
Figure 2.22 Comparitive dCLSM (Confocal) and STED Image of a nucleus of an A2780 cell stained by RRP (60 µM)
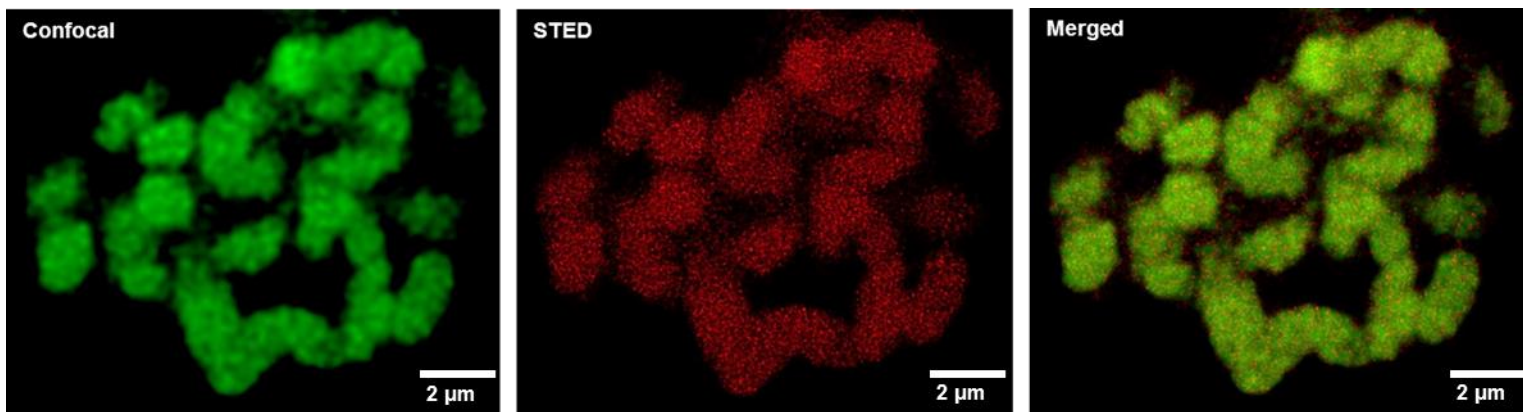
Figure 2.23 Left to Right: dCLSM (Confocal), STED and Merged images for RRP (60 µM) chromosomes of an A2780 cell

STED imaging was carried out over fixed A2780 cells at 60 µM RRP concentration. In these conditions high quality STED images of resolutions below 50 nm was obtained. STED images obtained for nuclei and chromatin shown in these figures indicates that there is extraordinary improvement in resolution compared to dCLSM. The red spots seen in the merged images in Figure 2.23 indicates the locations where significant improvements in resolution through STED has been achieved. The use of RRP as a STED probe was possible only because the probe exhibited superior photostability and withstood the whole imaging STED imaging cycle. The probe was able to provide resolution improvement for not only high concentrations of 60 µM but also for low concentration (around 6 µM, shown in figure 2.21), in the later case the concentration effect was in full swing as super-resolution was achieved to visualize mitochondria. The concentration dependent uptake results obtained using widefield fluorescence microscopy was confirmed and taken one step further, verifying that RRP is a multipurpose probe for STED microscopy.

Intensity v Distance: Comparison dCLSM and STED:

The intensity profile diagrams of merged images from dCLSM and STED for fixed A2780 cell nuclei indicates an improvement in resolution shown in Figure 2.24 where the red spots in the merged images indicates the areas with improved resolution in STED. The superior resolution is also seen in the intensity profiles which reveals resolution beyond 50 nm has been achieved.
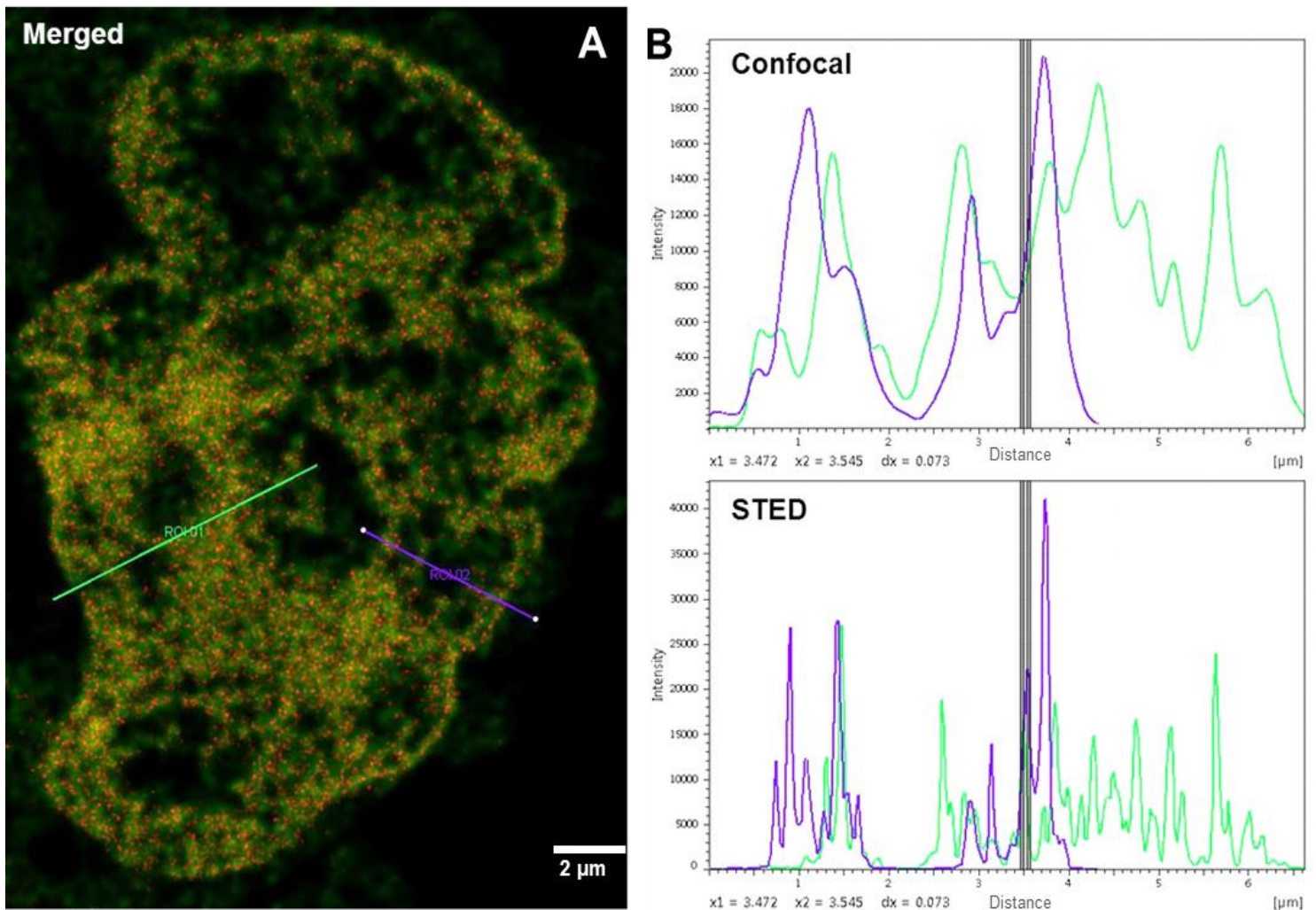
Figure 2.24 (A) dCLSM (Confocal) and STED merged image of RRP stained nucleus of A2780 cells. **(B)** Intensity profile comparison of dCLSM (Confocal) and STED of areas in the nucleus drawn by Green and Violet lines

2.12 3D-STED IMAGING

2.12.1 3D-STED: Resolution improvement

The excellent photostability exhibted by the RRP probe was used with particularly great effect in 3D-STED. This is a demanding technique, greatly depending on the stability of the probe as considerable emission can be lost due to photobleaching during STED depletion. A 3D-STED stack was obtained in RRP stained A2780 nuclei, the probe's extraordinary stability provided the opportunity image across the whole nuclear volume with extraordinary enhancement of resolution across the X,Y, and Z planes (Figure 2.25). Improvement in STED resolution could be acchieved across all dimensions simultaneously (that is, axial and lateral). The optical sectioning of the 3D-STED volume into individual planes was carried out using the inbuilt software in Leica STED, more precisely the resolution across the whole 3D STED volume is improved by the algorithms used in the Huygen's software. The superior resolution achieved heavily relies on the fitting of the polynomials connected to drift at selected imaging positions across planes[105]. The superior STED resolution across all the optical planes XY, XZ, and YZ throughout the whole 3D cross image cross-section is shown in Figure 2.25. The merged images of 3D-dCLSM and 3D-STED involving the individual planes shows this superior resolutions in a detailed way as shown in Figure 2.26.
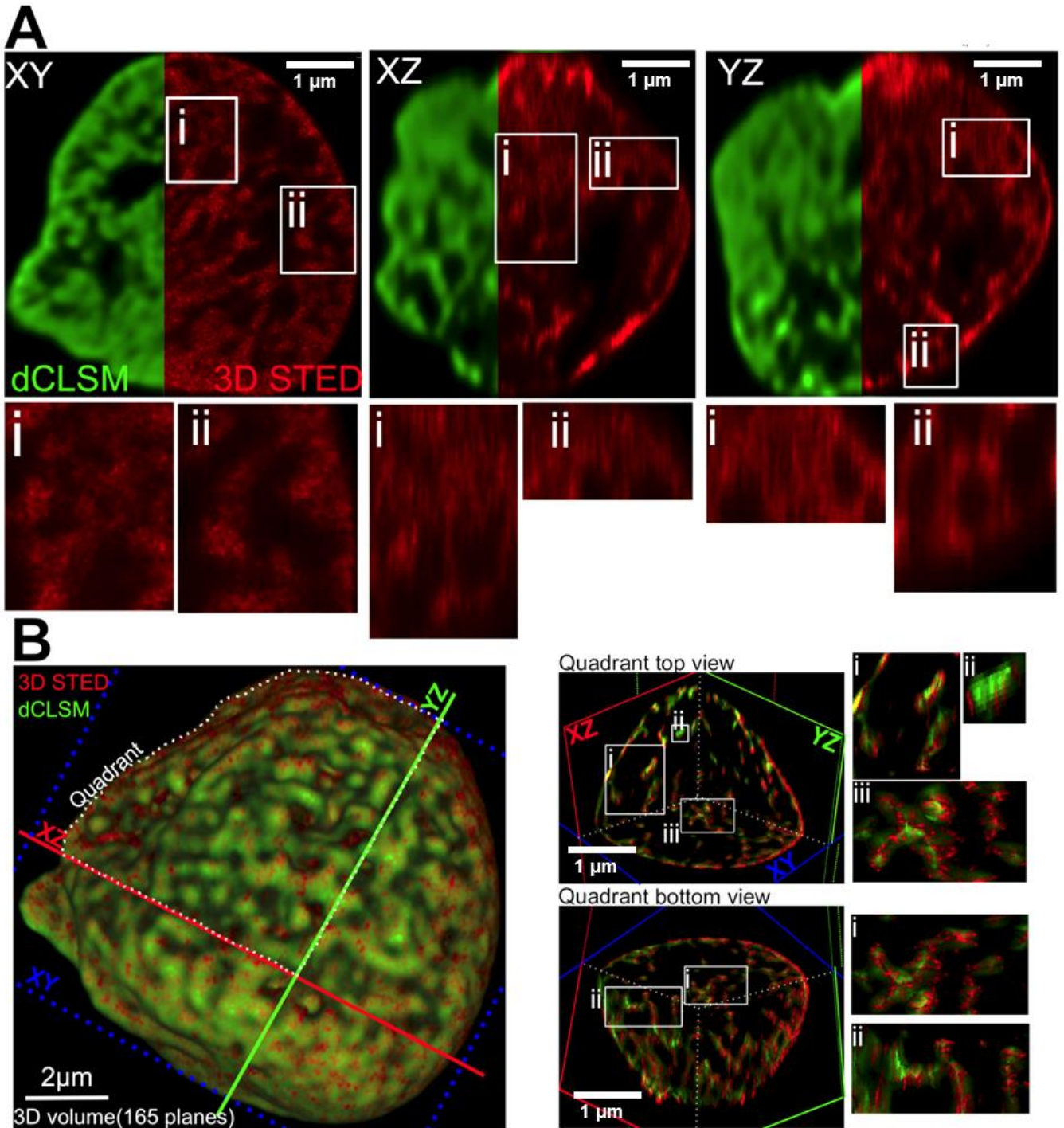
Figure 2.25 (A) Top row (Left to Right): Comparitive 3D-dCLSM and 3D-STED images of individual planes XY, YZ, YZ. **Bottom row: Boxed regions (i and ii)** showing magnifications of STED regions in individual planes **(B) (Left to Right):** 3D-STED and 3D-dCLSM merged whole volume constructed from 165 sections or planes, Combined 3D-dCLSM and 3D-STED sliced quadrants from the 3D-STED and 3D-dCLSM merged volume. **Boxed regions (i, ii and iii)** showing magnifications merged 3D-STED and 3D-dCLSM regions from sectioned quadrants. The red spots indicating improvement in 3D-STED resolution over 3D-CLSM. The experiment was carried out in A2780 cells

74

2.12.2 3D-STED Intensity profiles

As shown above, substantial resolution improvement has been achieved across the whole 3D cross section of the nucleus stained by RRP. 3D-STED slicing was carried out using the inbuilt Leica STED microscope software. The 72nd plane of a total of 165 planes which were STED super-resolved is shown in Figure 2.26. The intensity profiles for specific areas of the merged images (dCLSM and STED) are also presented in the Figure 2.26, indicating the extraordinary resolution improvement (< 40 nm) achieved across all three planes. The 3D-STED experment of RRP stained A2780 nucleus was possible only because of the extraordinary photostability exhibited by RRP, which withstood the demanding STED irradiation conditions (for duration as long as ~ 40 min.) required to accumulate the 3D-STED image.
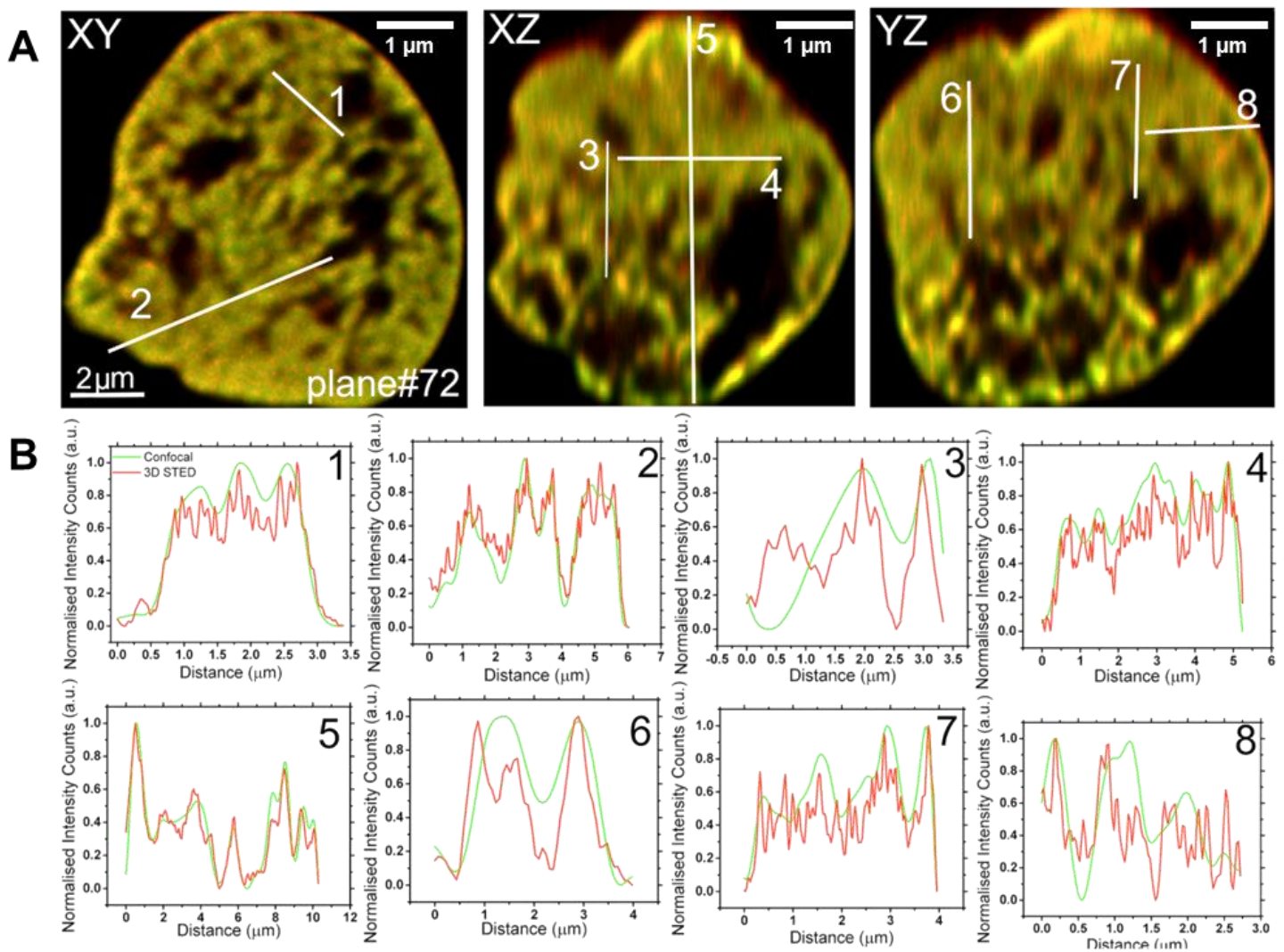
Figure 2.26 (A) Left to Right: Merged 3D-dCLSM and 3D-STED individual plane sliced from the combined 3D-dCLSM and 3D-STED Image volume XY, XZ and YZ respectively. **(B) Left to Right:** Comparative intensity profiles (3D-dCLSM (Green) and 3D-STED (Red)) generated for areas represented by white lines 1 and 2 for XY plane, 3, 4 and 5 for XZ plane, 6, 7 and 8 for YZ plane showing resolution improvement. A2780 cell line was employed

76

2.12.3 3D-dCLSM (Hyvolution) v 3D-STED: Individual plane:

The extraordinary super resolution obtained among each individual plane of the complete 3D stack acquired is shown in Figure 2.27. Again, the superior resolution is clearly evident from the comparison between 3D-dCLSM and 3D-STED for one particular plane.
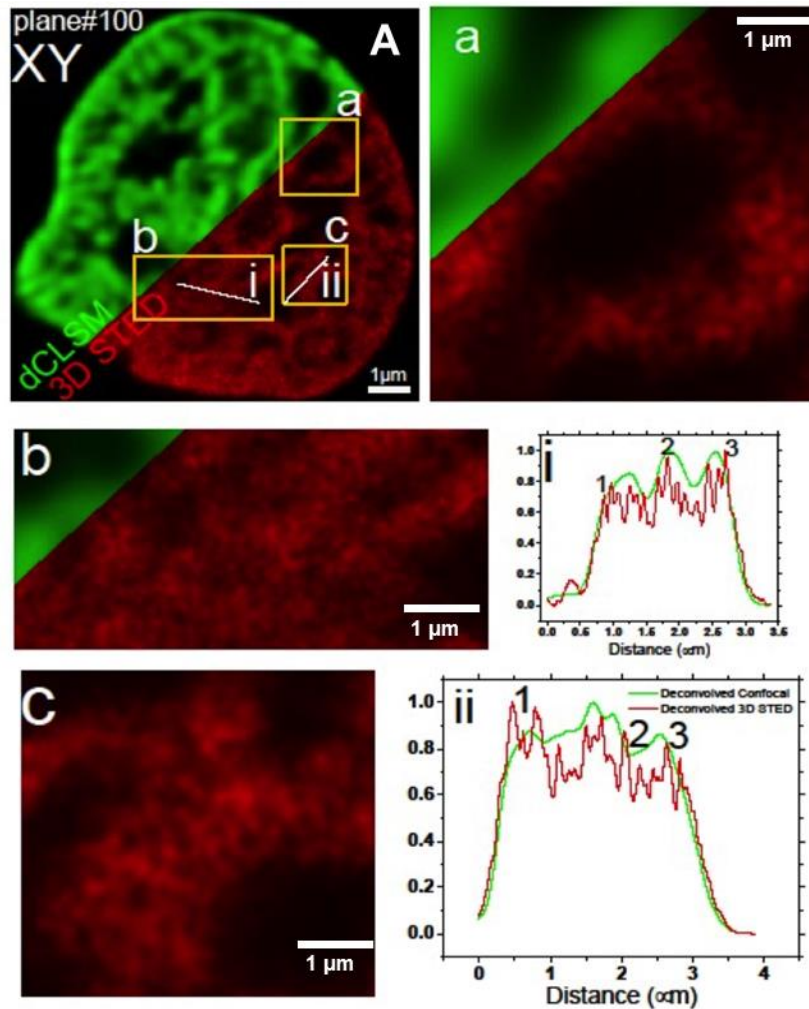
Table 1. Dimentions of the resolved structures		
(nm)	i	ii
FWHM Peak 1	67	71
FWHM Peak 2	73	81
FWHM Peak 3	44	37

Figure 2.27 (A) Comparative 3D-dCLSM and 3D-STED images of individual plane from the whole merged 3D-dCLSM and 3D-STED volume. (**a) and (b)** showing comparison between 3D-dCLSM and 3D-STED for magnified regions as indicated by boxes (**a) and (b)** in (**A**). **C** showing details of magnified 3D-STED. **i and ii** showing comparative intensity profiles for 3D-dCLSM (Green line) and 3D-STED (Red line) indicating enhancement in resolution. **Table 1** showing the dimensions of resolved structures calculated from the intensity profiles

2.12.4 Live cell STED Imaging

To compliment the fixed cell STED experiments, live cell STED imaging was also carried out. Nagerl *et al*[111,] Thompson *et al*[109] had reported STED imaging of live nerve cells and they were able to obtain greater details of neuronal circuits and understand the in-depth information of neuronal plasticity. To carry out live cell STED experiments, higher RRP concentrations around 500 µM was employed as this had been found to produce high-quality CLSM images. Gratifyingly, live STED imaging of RRP using MCF7 cell line yielded high quality STED super-resolution images, showing great detail of nuclear chromatin in live cells. Again resolutions below 50 nm were obtained. Figure 2.28 shows a comparison between dCLSM, STED and 3D-STED of live MCF7 cells. The striking live STED images exemplify the extraordinary super-resolution ability of RRP. Again, a comparison between the dCLSM and STED live cell images of the same area (nuclei) shows the extent of improvement of STED resolution over dCLSM. The resolution is amplified across the three dimensional space in 3D-STED showing greater details of chromatin which could have been potentially unexplored by conventional imaging techniques. Live cell STED imaging is more challenging than the fixed cell STED imaging - largely because of the high laser power employed by the STED depletion beam which needs to be controlled considerably to avoid cell damage. STED data processing was carried out by using Leica LAS software.
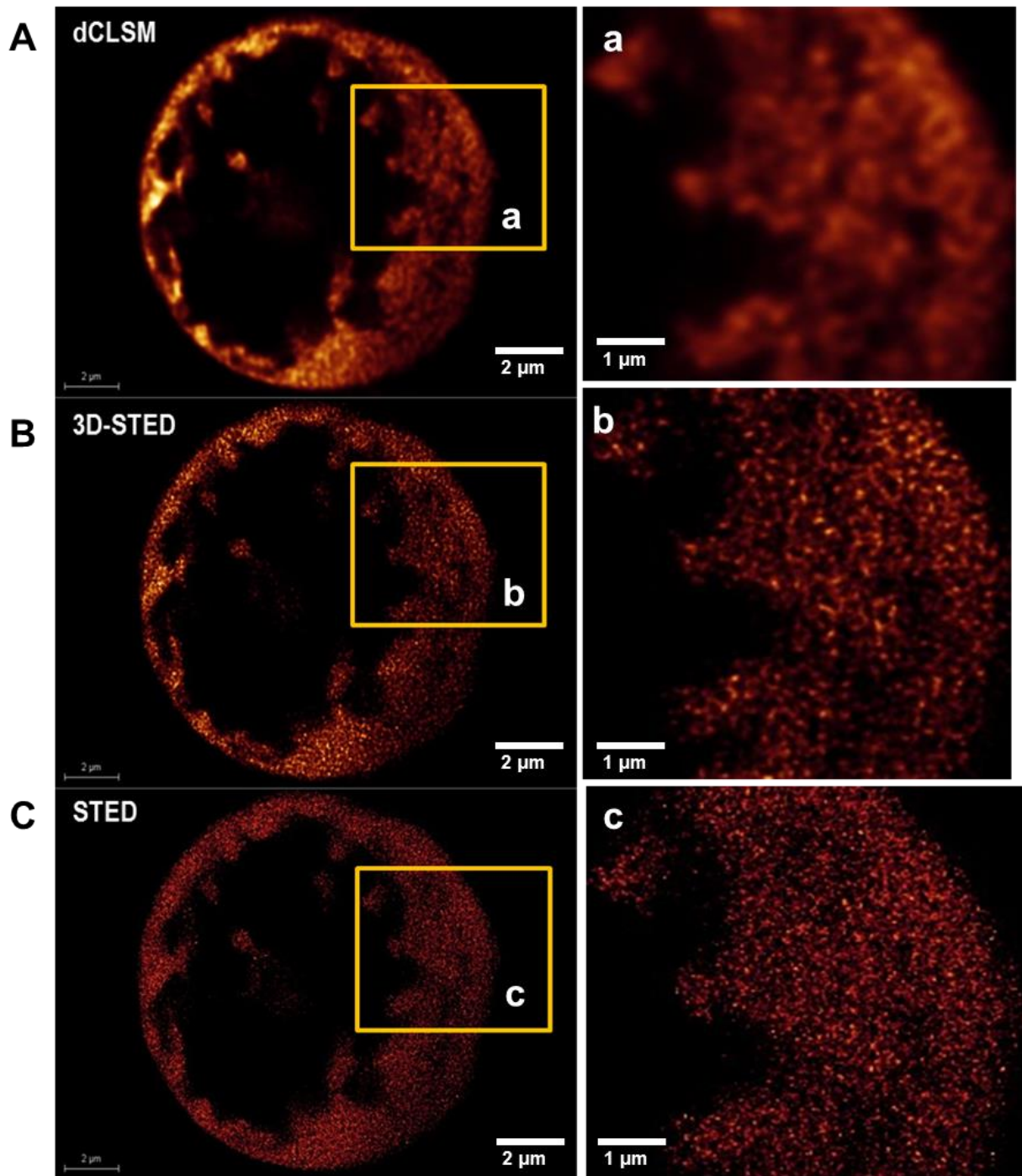
Figure 2.28 (A) dCLSM live cell image of RRP (500 µM) stained nucleus. **Boxed region (a)** showing magnification of a particular area in the nucleus. **(B)** 3D-STED live cell image of RRP (500 µM) stained nucleus. **Boxed region (b)** showing magnification of a particular area in the nucleus. **(C)** STED live cell image of RRP (500 µM) stained nucleus. **Boxed region (c)** showing magnification of a particular area in the nucleus. MCF7 cell line was employed

2.12.5 Dual colour STED

RRP suitablility to act as a dual colour super-resolution probe was already proven when it was used successfully as a dual colour structured illumination microsocpy (D-SIM) probe. The excellent photophysics again helped it to be opitmized as a dual colour STED microscopy probe. High quality dual colour STED images were obtained for MCF7 cells. The large Stokes' shift shown by RRP provided a window to accommodate another probe with different spectral characteristics compared to RRP. Following the success with SIM, Mito Tracker Red was investigated as its spectral characteristics complimented with that of RRP, the experiment was carried out with high concentration of RRP along with Mito Tracker Red as the complimentary dye. RRP and Mito Tracker Red was STED depleted at 775 nm and 660 nm respectively. By using nuclei localizing high concentration (> 18 µM) RRP could be used a dual colour probe along with Mito Tracker Red. to obtain striking dual colour STED images such as that shown in Figure 2.29.
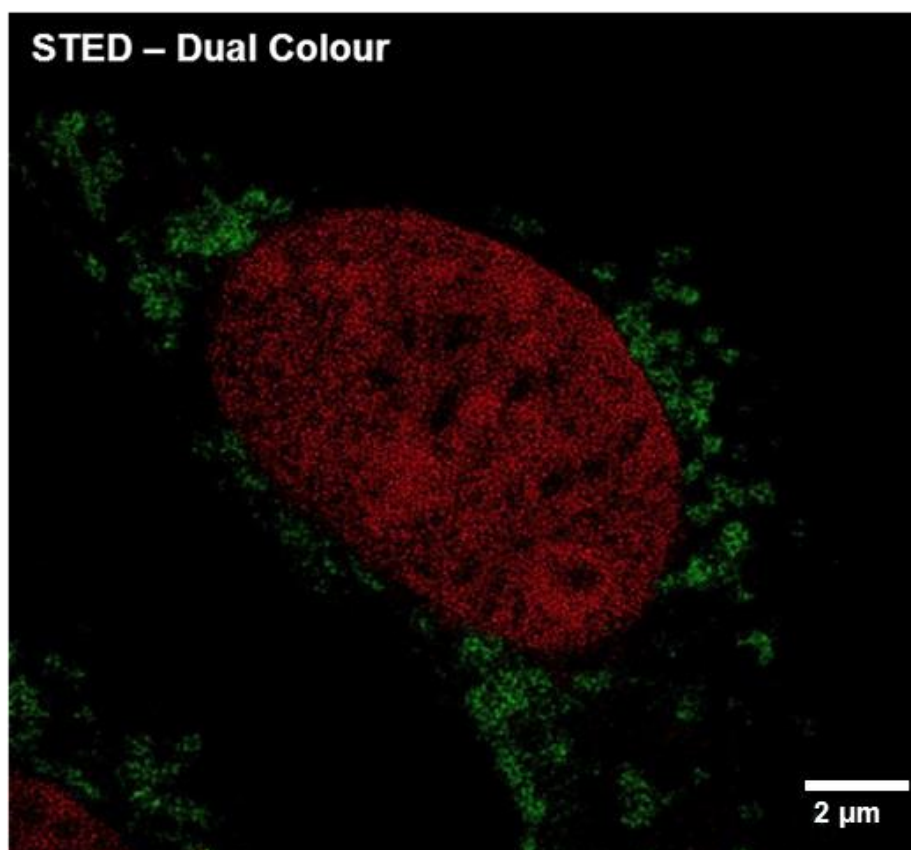
Figure 2.29 Dual colour STED image: RRP (20 µM) staining the nucleus and Mito Tracker Red (1 µM) staining Mitochondria. MCF7 cell line was employed

2.12.6 Differentiating DNA structures using RRP in STED Mode

The ends of a eukaryotic chromosome is composed of a repeating DNA sequence which is associated with proteins. This special structure is called a telomere. The telomere has the crucial role of maintaining the structure of the genome, as it prevents the fusion or degradation of chromosome ends. Furthermore, during chromosome duplication the telomere shortens and this happens regularly during the cell cycle, thus providing the mechanism by which the Hayflick Limit for cell division is defined. The telomere as such is packed with G-rich DNA than can form quadruplex structures. Unfortunately, due to spatial resolution restrictions, conventional optical microscope cannot resolve the finer details telomeres. Since super-resolution microscopy breaks the diffraction barrier of optical microscopy, we hoped that it might be possible to explore the structure of the telomeres beyond the diffraction limit. STED could be used as an ideal platform to overcome the limitation set by conventional microscopy and could let us understand the interesting features of G-quadruplexes and the telomeres as a whole.

Previous confocal experiments had shown that, apart from duplex imaging at wavelengths around 660-680 nm, RRP can be used to image specific quadruplex DNA structures through a emission signal at $620 - 640$ nm. This is caused by the different binding geometry when the complex interacts with duplex and quadruplex DNA. Therefore we set out to investigate whether these experiments could be duplicated in STED experiments. RRP with its unique combination of photophysics, cellular loclization, and sensitivity to DNA structure could be a probe for the structure of DNA within telomeres.

The relevant STED microscopy experiments were peformed using RRP to stain A2780 cells. In these experiments, emission was collected at two different wavelength windows and the results are shown in Figure 2.30. These images show that the two different wavelength outputs do not colocalize indicating that the high and low energy outputs are coming from entirely different regions. This is consistent with the previous experiments and suggests that duplex binding of the probe is shown by the low energy channel, whilst the image obtained from the high energy channel may be due to quadruplex structures.
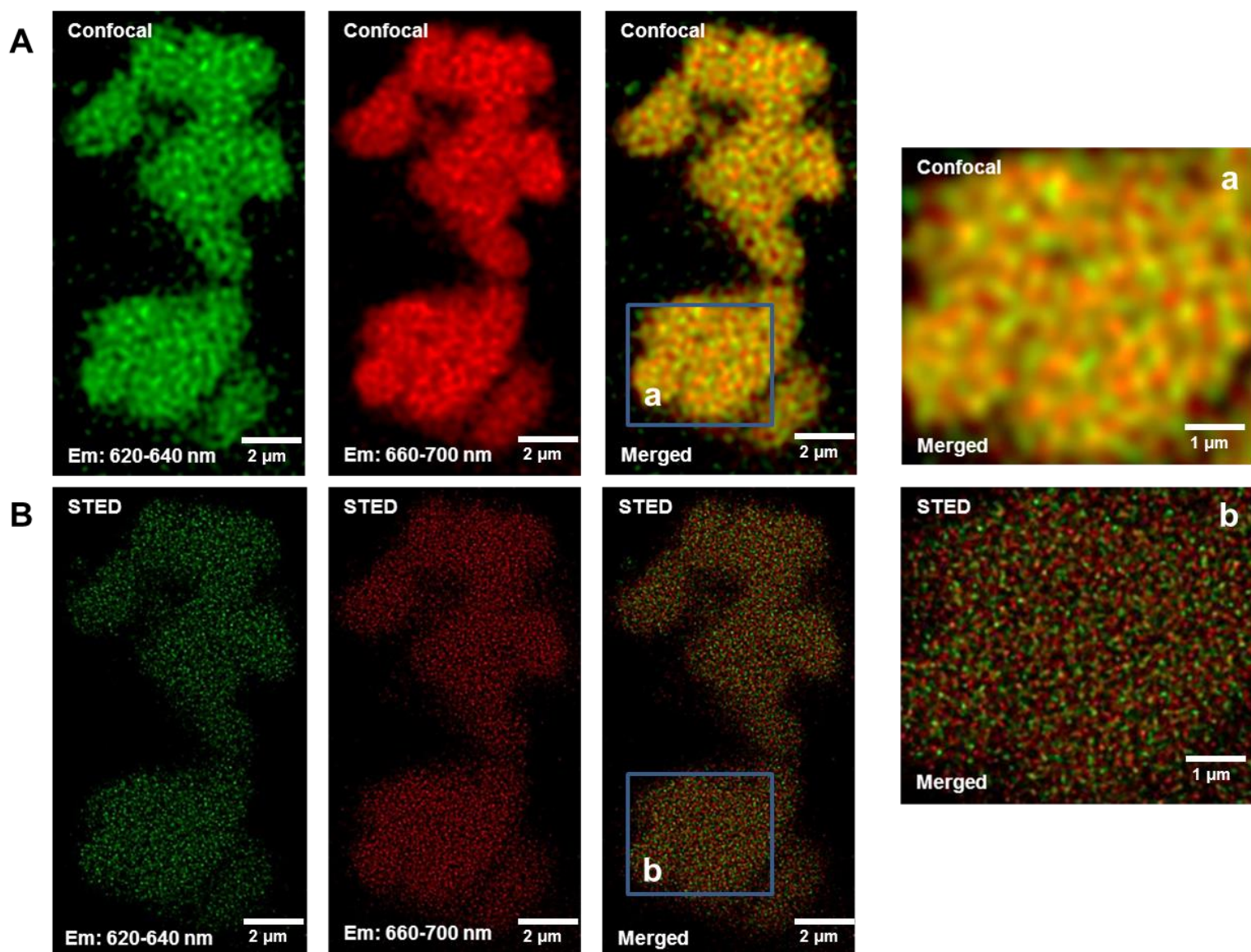
Figure 2.30 (A) Left to Right: dCLSM (Confocal) images of emission originating from two different channels for RRP stained chromosomes (Individual channel), Merged image of both the channels. **Boxed region (a)** showing magnifcation of a particular area of the merged image. **(B) Left to Right:** Corresponding STED Images of emission originating from two different channels for RRP stained chromosomes (Individual channel), Merged image of both the channels. **Boxed region (b)** showing magnifcation of a particular area of the merged image. A2780 cell line was employed

2.13 NOVEL IRIDIUM METAL COMPLEXES AS OPTICAL PROBES FOR CELLULAR IMAGING

Introduction:

As the previous section illustrates d^6 metal complexes display brightness and extraordinary stability which can be attributed to highly emissive MLCT states. In this section, studies are extended to other d^6 metal complexes and the photophysical and specific cellular imaging properties of Iridium bi-cylcometalated metal complexes as cell probes were investigated and assessed.

The two biscyclometalated complexes shown in Figure 2.31 were prepared using a two steps procedure by Dr. Alessandro Sinopoli in the lab of Dr. Paul Elliot at the University of Huddersfield. In this procedure, iridium (III) chloride and the corresponding 4-phenyl-1,2,3-triazole ligand were first reacted together and then the Dppz ligand was added the crude product of the first reaction. The final product, supplied to our lab in Sheffield as a hexafluorophosphate salt, had been purified by chromatography.

2.14 PHOTOPHYSICS OF IRIDIUM METAL COMPLEXES CC 203 [(Ir(Ph-L)$_2$Dppz]$^+$) AND CC 204 [(Ir(Et-L)$_2$Dppz]$^+$)

2.14.1 Optical titrations

Luminescence titrations:

In analogy to other M(dppz) systems, water molecules can quench the excited state of such complexes when they form hydrogen bonds with dppz of [Ir(Ph-L)$_2$dppz]$^+$ and [Ir(Et-L)$_2$dppz]$^+$, but when the dppz interacts with the hydrophobic interior of the DNA, the excited state lifetime of the complex changes considerably, producing large changes in emission intensity. These changes can be used as a spectroscopic tool for studying the binding interactions with DNA: if DNA is titrated into a solution of the metal complex of known concentration the degree change in the emission spectrum is proportional to the fraction of complex bound to the DNA[99,100,103].
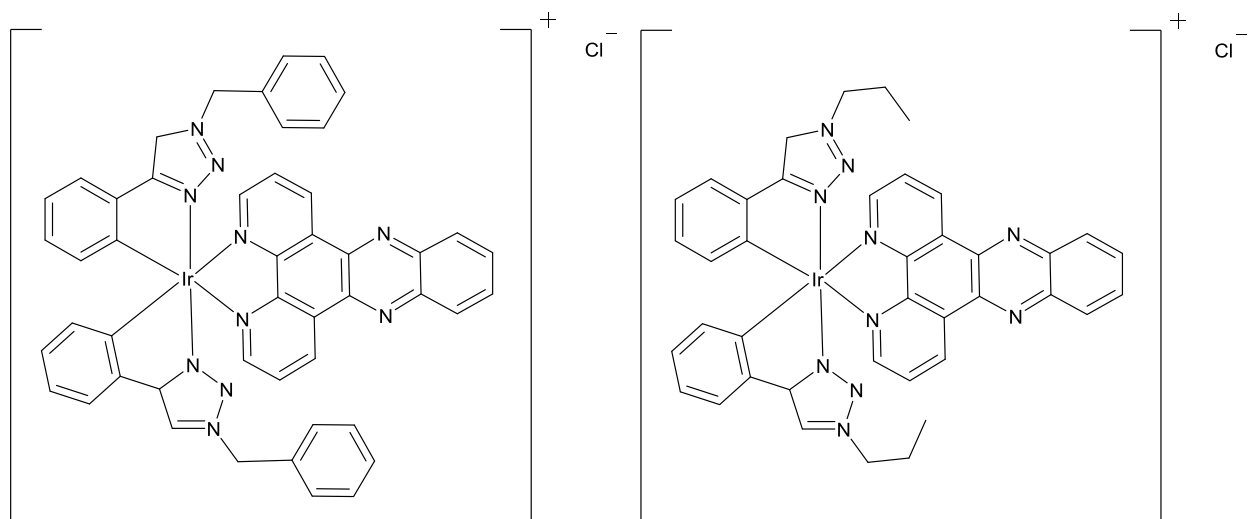
Figure 2.31 Bicyclometallated Iridium metal complexes ($[Ir(Ph-L)_2dppz]^+$ CC 203 (left) and $[Ir(Et-L)_2dppz]^+$ CC204)

The changes in fluorescence intensities on addition of CT-DNA was measured by exciting ($[Ir(Ph-L)_2dppz]^+$, CC 203, and $[Ir(Et-L)_2dppz]^+$, CC 204, at 450 nm which is the excitation wavelength for the ^{1}MLCT band of both the complexes leading to a ^{3}MLCT emission that extends from 580 nm to 700 nm with an maximum around 660 nm (Figure 2.32). Emission spectra are measured as a function of increasing CT-DNA concentration. Relative intensities are directly related to the extent of the DNA interaction with the metal complex. Hence when calculating the binding coefficients the calculated fluorescence intensities obtained from the luminescence titrations play a prominent role[121].

Absorbance titration:

When the complexes interact with CT-DNA, the spectral characteristics of the complex changes and this is because the complex is subjected to changes in microenvironment as it moves from being completely solvated in aqueous solution to being in the hydrophobic environment of the DNA helices[101,102,103]. Therefore UV visible titrations are also an effective tool for deducing binding of metal complexes with DNA. The interaction of metal complex with base pair causes hypochromic shift with small blue or red shift[120]. Addition of CT-DNA to a solution of 50 μM of the Ir metal complexes resulted in a hyprochromic shift being observed which is signified by a shift in the absorbance bands. The bands at 270, 353 and 369 nm in CC 203 and the bands at 290 and 400 nm in CC 204 display hypochromicity as CT-DNA is titrated into the complex solution.
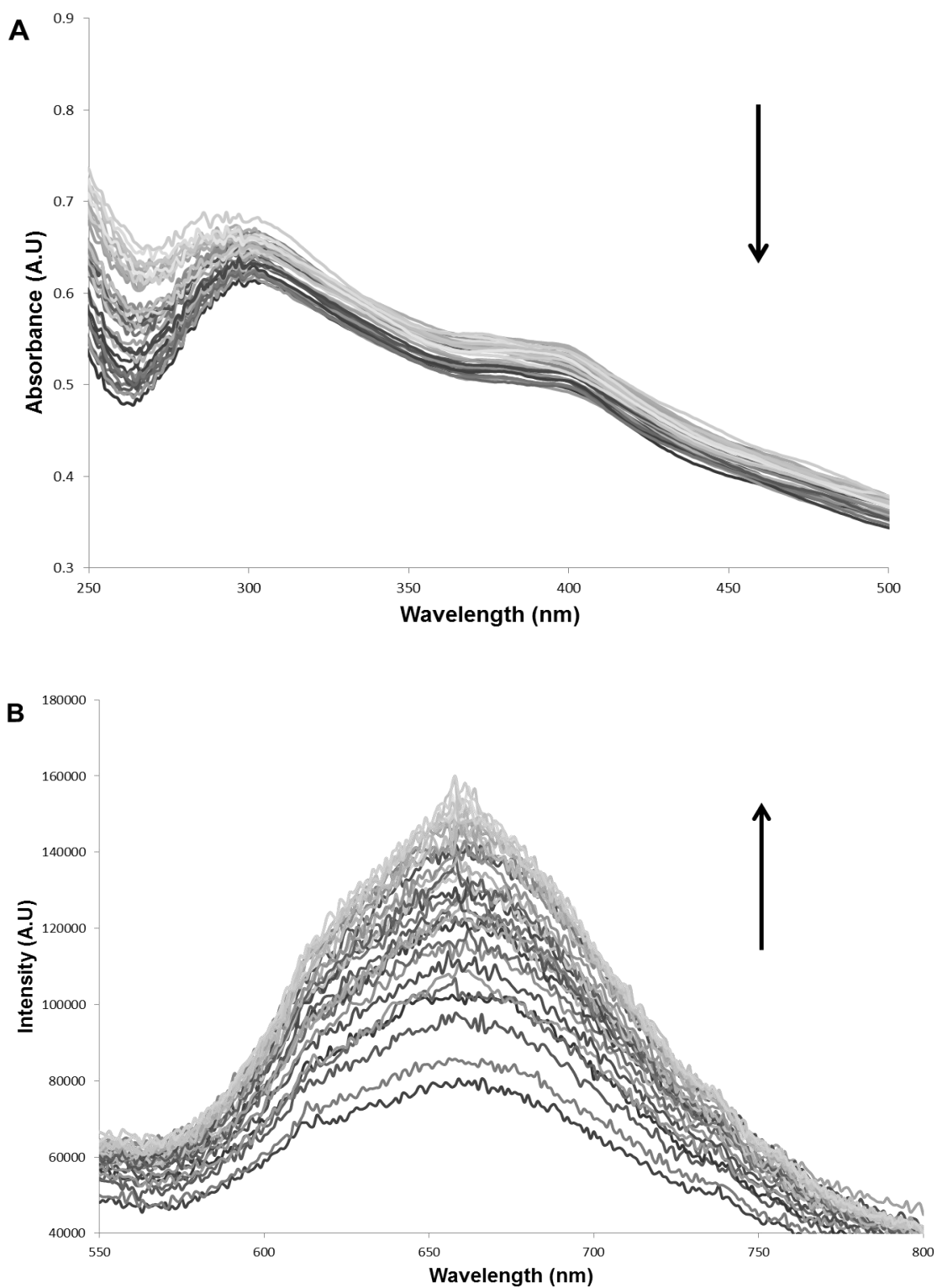
Figure 2.32 Optical titrations, **(A)** Absorbance, **(B)** Luminescence carried out by adding 16.4 mM CT-DNA into a solution of 50 μM [Ir(Et-L)$_2$dppz]$^+$ (CC 203), **Experimental conditions:** 5 mM Tris buffer, 25 mM NaCl pH 7.4 at 25 °C, λ_{ex} = 450 nm[99]

2.14.2 Binding studies: CC 203 (Ir(Ph-L)$_2$dppz) and CC 204 (Ir(Et-L)$_2$dppz):

In order to compare the binding affinity of the complexes to DNA, an equilibrium binding constants (K) was calculated and this calculation was carried out using McGhee Van hippel (MVH) model. The binding constants for the interaction of CC 203 (Ir(Ph-L)$_2$dppz) and CC 204 (Ir(Et-L)$_2$dppz) with CT-DNA were calculated by constructing a non-linear Scatchard plot using the changes in luminescence and fitting this data to the McGhee-von Hippel model for non-cooperative binding[99,100,103]. The model fitted the data well with an R^2 value of 0.94 for both complexes (see Figure 2.33 for the relevant data for CC 203). From the data obtained by this method, a comparison of equilibrium binding constants indicated that CC 204 binds to the DNA slightly more strongly compared to CC 203.

CC 203

A
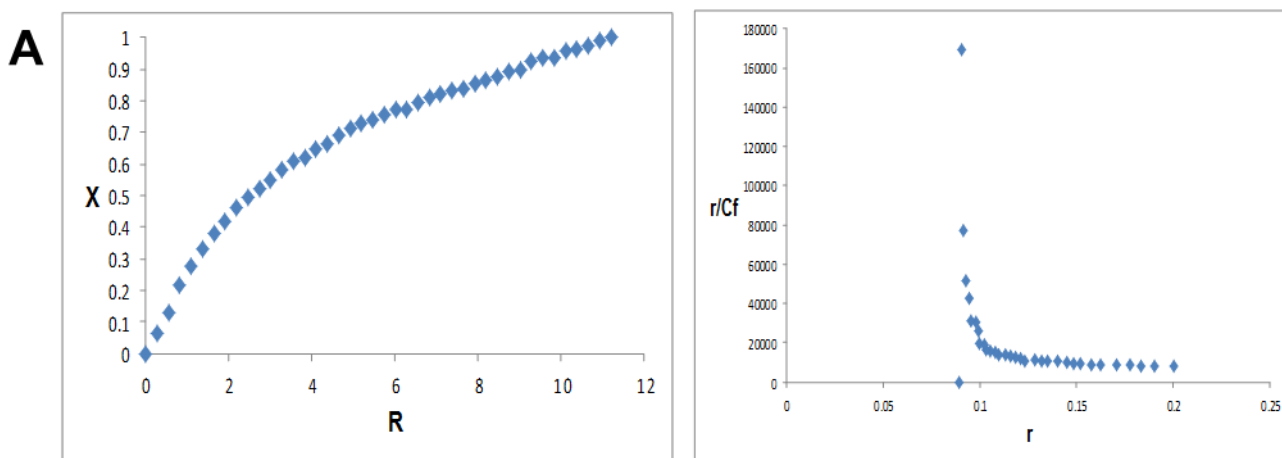
B

Compound	K (M^{-1})	n (bp)
CC 203	2.38 X 10^4	2.7
CC 204	5.37 X 10^4	9.5

Figure 2.33 (A) Left to Right: A Theoretical binding curve for CC 203 binding to CT-DNA (were, **X** = Fraction bound, **R** = Ratio of Concentration of DNA and Concentration of metal complex), Scatchard plot for the same (were, **r/C$_f$, r** = Ratio of Concentration of metal complex bound to DNA and Concentration of DNA, **C$_f$** = Concentration of free metal complex in solution). **(B)** Table showing Binding constants and the number of base pairs binding to CC 203 and CC 204 respectively

2.15 CELLULAR IMAGING STUDIES OF CC 203 – 204

2.15.1 Cell dependent uptake of CC 203 - 204

The DNA binding experiments encouraged us to investigate the potential of both CC 203 and CC 204 as cellular probes. Cellular uptakes of iridium metal complexes have been well reported[118,123]. Bicyclometallated iridium metal complexes like CC 203 and CC 204 could therefore be tested as cellular imaging agents to understand their interactions within a biological environment. When added to the ovarian cancer cell line A2780, both complexes showed instant cellular uptake at concentrations starting from 50 μM when subject to a 24 hour incubation period. The widefield images acquired shows that localization of CC 203 and CC 204 is mostly in the cytosol region of the A2780 cells (Figure 2.34). The images were acquired by excitation at 470 nm and emission was collected in the RFP channel filter set at the wavelength range of 570 nm to 620 nm. These uptake experiments were extended to the MCF7 breast cancer cell line. These cells also showed uptake of both the complexes similar to that observed in the A2780 cell line.
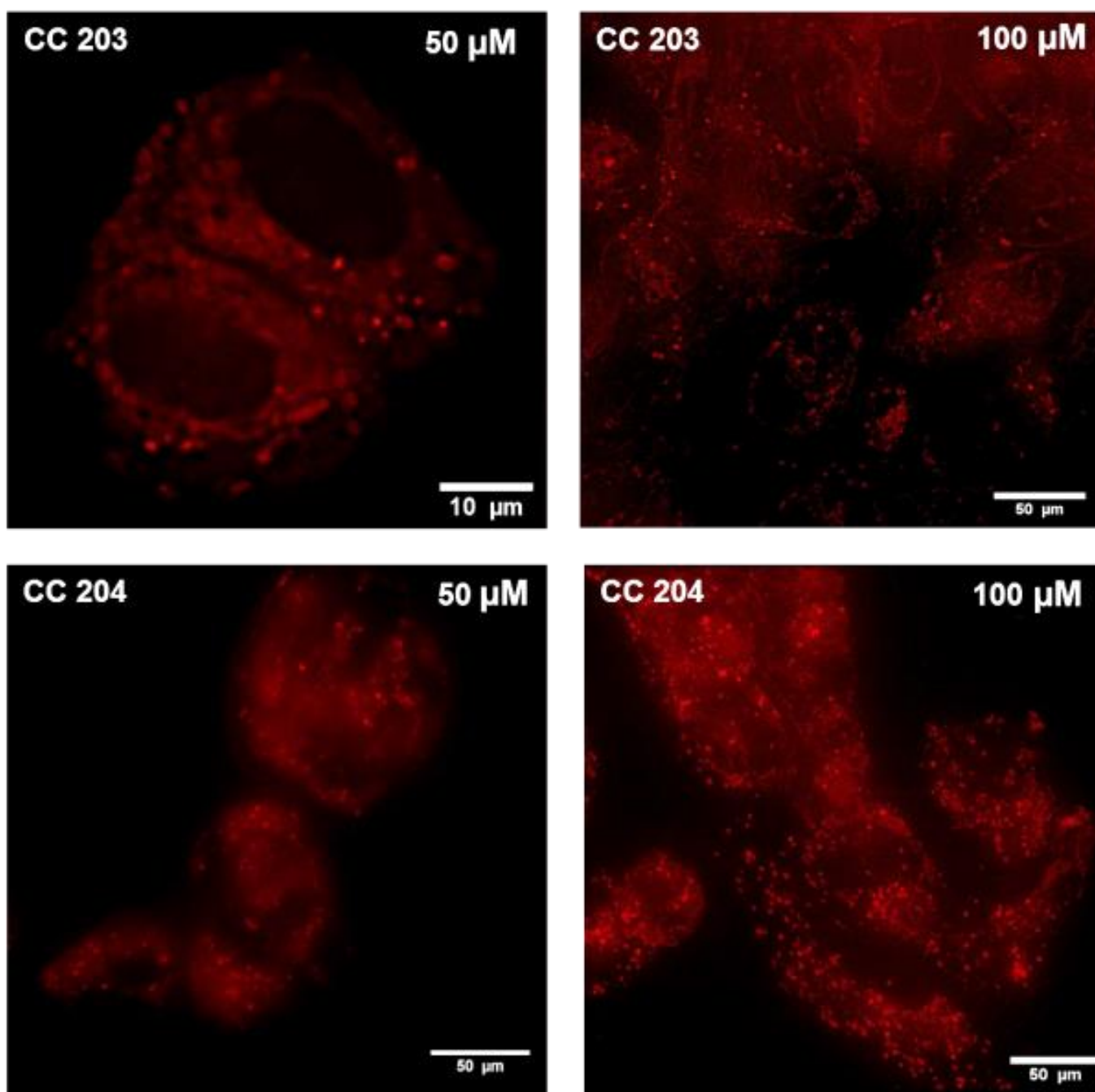
Figure 2.34 Top: Widefield images showing cellular uptake of CC 203 (50 μM and 100 μM) in A2780 cells. **Bottom:** Widefield images showing cellular uptake of CC 204 (50 μM and 100 μM) in A2780 cells

In cellulo intensity profile – CC 203 (Ir(Ph-L)₂dppz):

Intensity v Distance plots generated offline indicated that both CC 203 and 204 were not localizing in the nucleus of cells but were localizing in other intracellular organelles present in the cytosol regions of both the cell lines (Figure 2.35). The deconvolved widefield images obtained using the Dual cam Nikon wide field microscope[104] indicated structures similar to that of mitochondria and this prompted studies on intracellular organelle tracking.
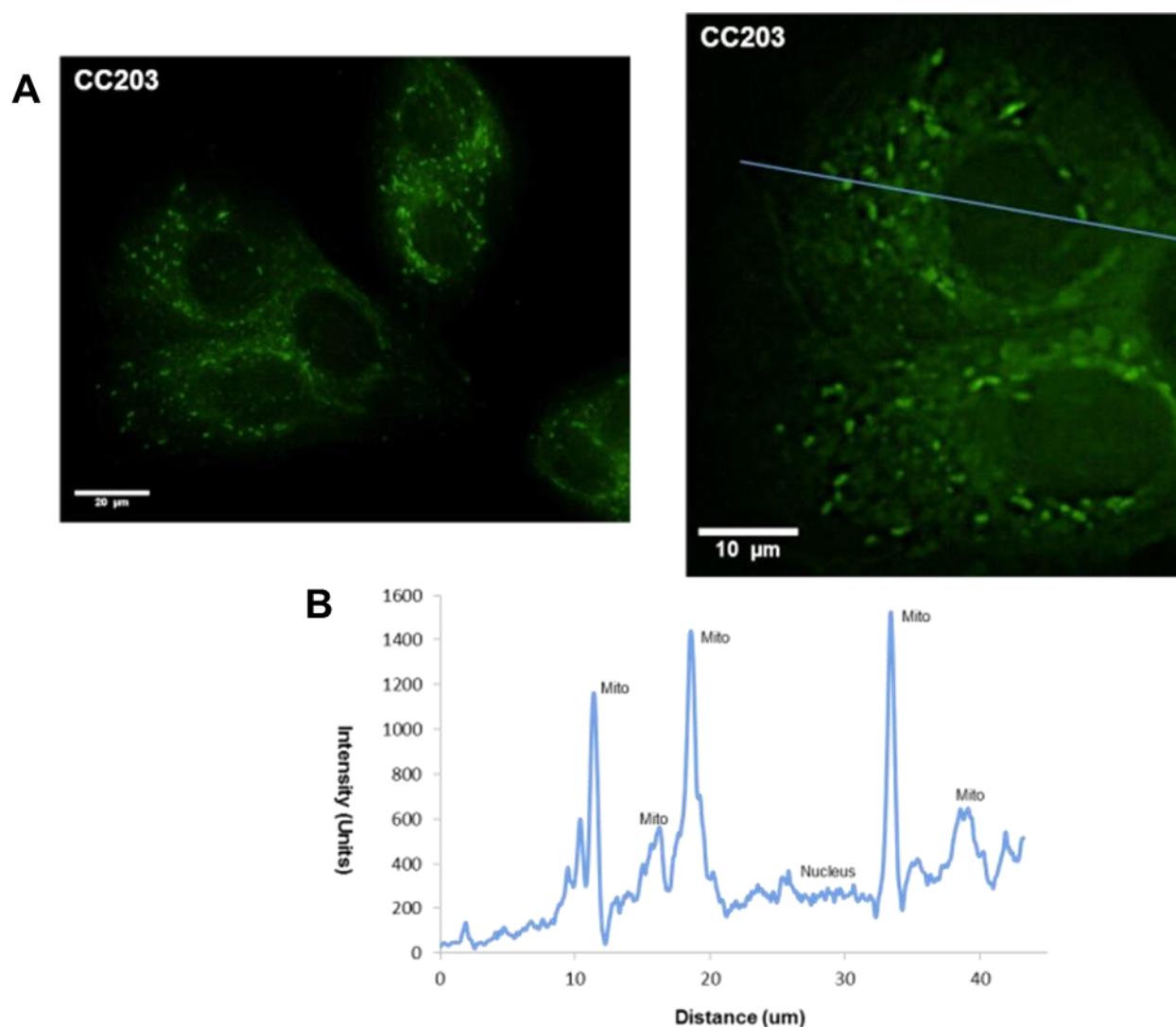
Figure 2.35 (A) Widefield images showing the Incellulo luminescence exhibited during the cellular uptake of CC 203 in A2780 cells. **(B)** Intensity v Distance plot for the area marked by the blue line.

2.15.2 Intracellular localization of CC 203 - 204:

The cellular imaging potential of CC 203 and 204 would be enhanced if these imaging agents were found to image intracellular organelle in a specific manner. Many iridium metal complexes reported so far have imaged mitochondria, for example see the reports by Jin *et al*[118] and Wang *et al*[123]. Mitochondrial accumulation of charged metal complexes occurs because of the distinctive mitochondrial membrane potential attracts lipophilic cations.

In order to explore whether the emission signals observed in the cytosol region are arising from localization of the complexes within mitochondria; initial intracellular tracking experiments were carried out for CC 203 using Mito Tracker Green (Figure 2.36) which shows emission in the GFP channel, namely 500 nm to 540 nm on excitation at 470 nm. This tracking experiment confirmed that the CC 203 is indeed localizing on to the mitochondria.
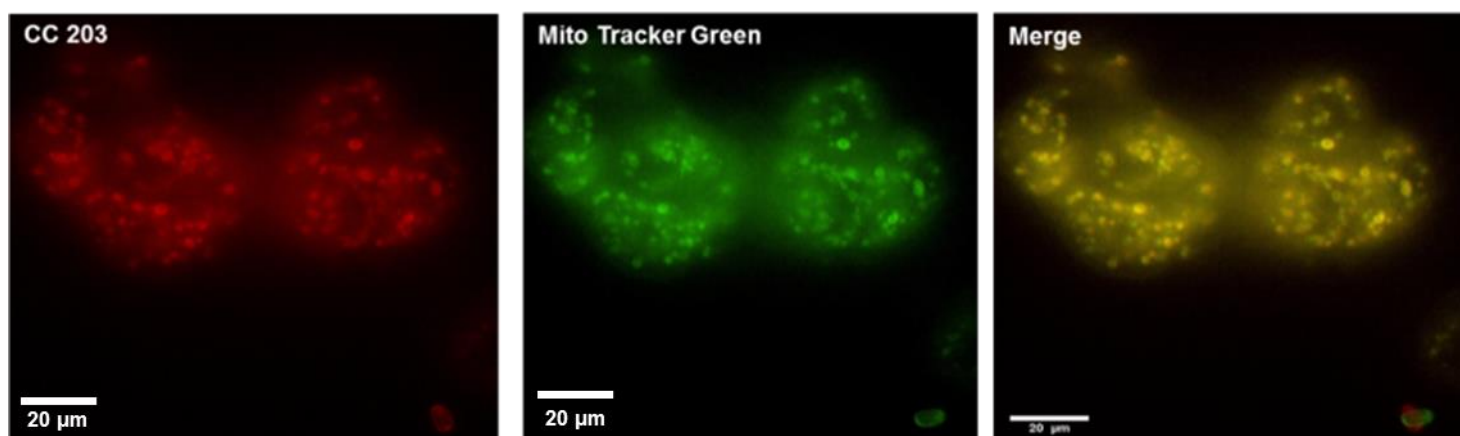
Figure 2.36 Left to Right: Widefield images showing cellular localization of CC 203, Mito Tracker Green (Individual channel), Colocalized image of CC 203 and Mito Tracker Green. A2780 cell line was employed

Mito Tracker Green localizes mainly over the membrane of the mitochondria, as the CC 203 shows DNA binding characteristics it could be envisaged that the complex binds to mitochondrial DNA in particular. Widefield fluorescence microscopy is not a pointilistic technique like confocal microscopy and as it involves fast scanning across different focal planes resulting in the generating of image volumes, the possibility of crosstalk between adjacent channels could not be ruled out.

To confirm again the localization of both the complexes over mitochondria, additional tracking experiments with Mito Tracker Deep Red was carried out (Figure 2.37). Mito Tracker Deep Red has spectral characteristics showing emission in the Far Red Cy5 channel (> 650 nm) of the widefield fluorescence microscope filter set. This probe was excited at 640 nm and collected at 660 nm to 700 nm (Cy5 region).
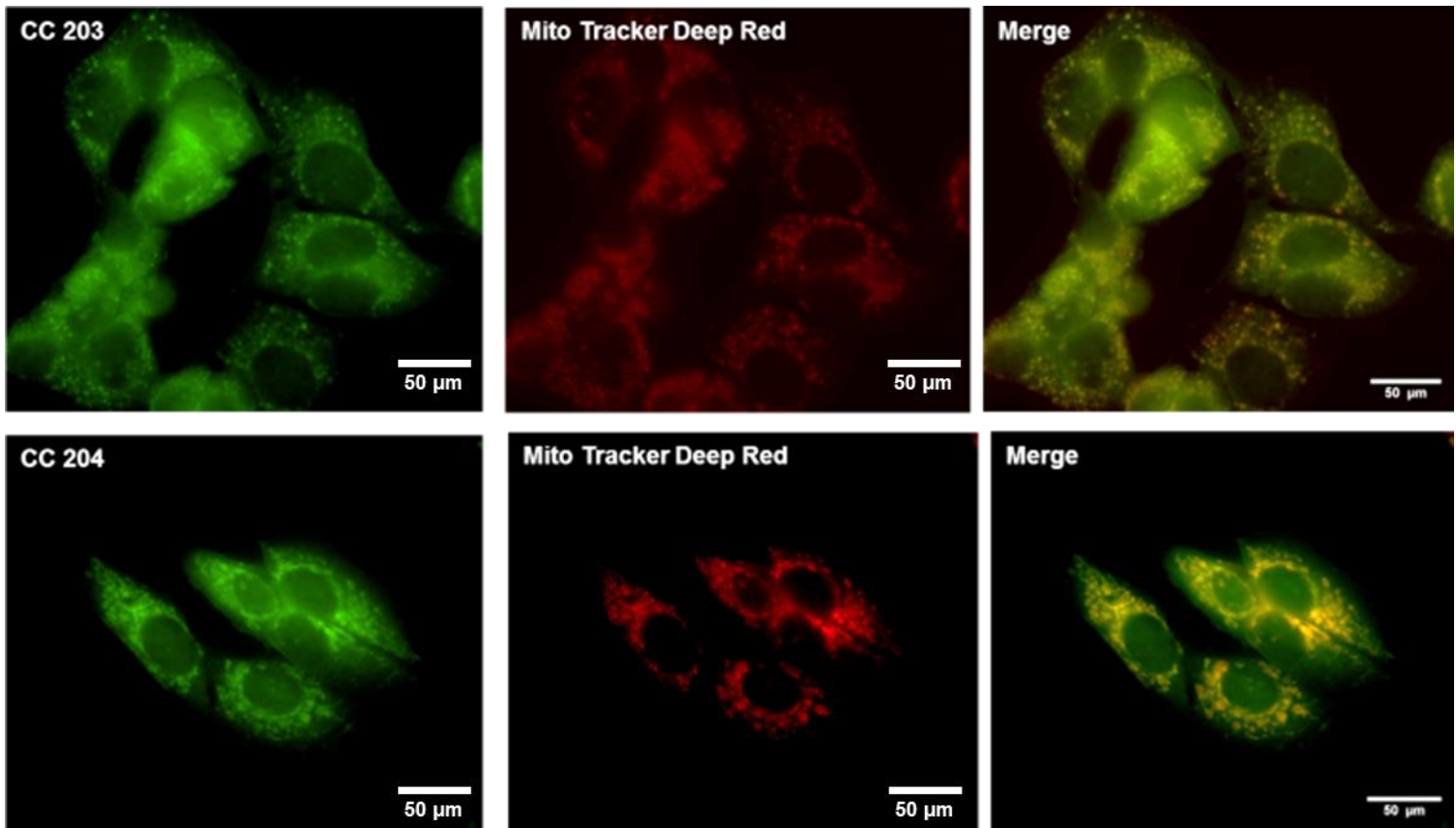
Figure 2.37 Top (Left to Right): Widefield images showing cellular localization of CC 203, Mito Tracker Deep Red (Individual channel), Colocalized image of CC 203 and Mito Tracker Deep Red. **Bottom (Left to Right):** Widefield images showing localization of CC 204, Mito Tracker Deep Red (Individual channel), Colocalized image of CC 204 and Mito Tracker Deep Red. A2780 cell line was employed

Eliminating the possibility of crosstalk between channels it was confirmed that both complexes localize in mitochondria. Indeed, intensity *vs* distance plots confirmed that there is a near perfect colocalization in mitochondria. The inset box area shown in the merged colocalization image (Figure 2.38) shows that both channels match, however it also reveals differences in brightness of both the probes.
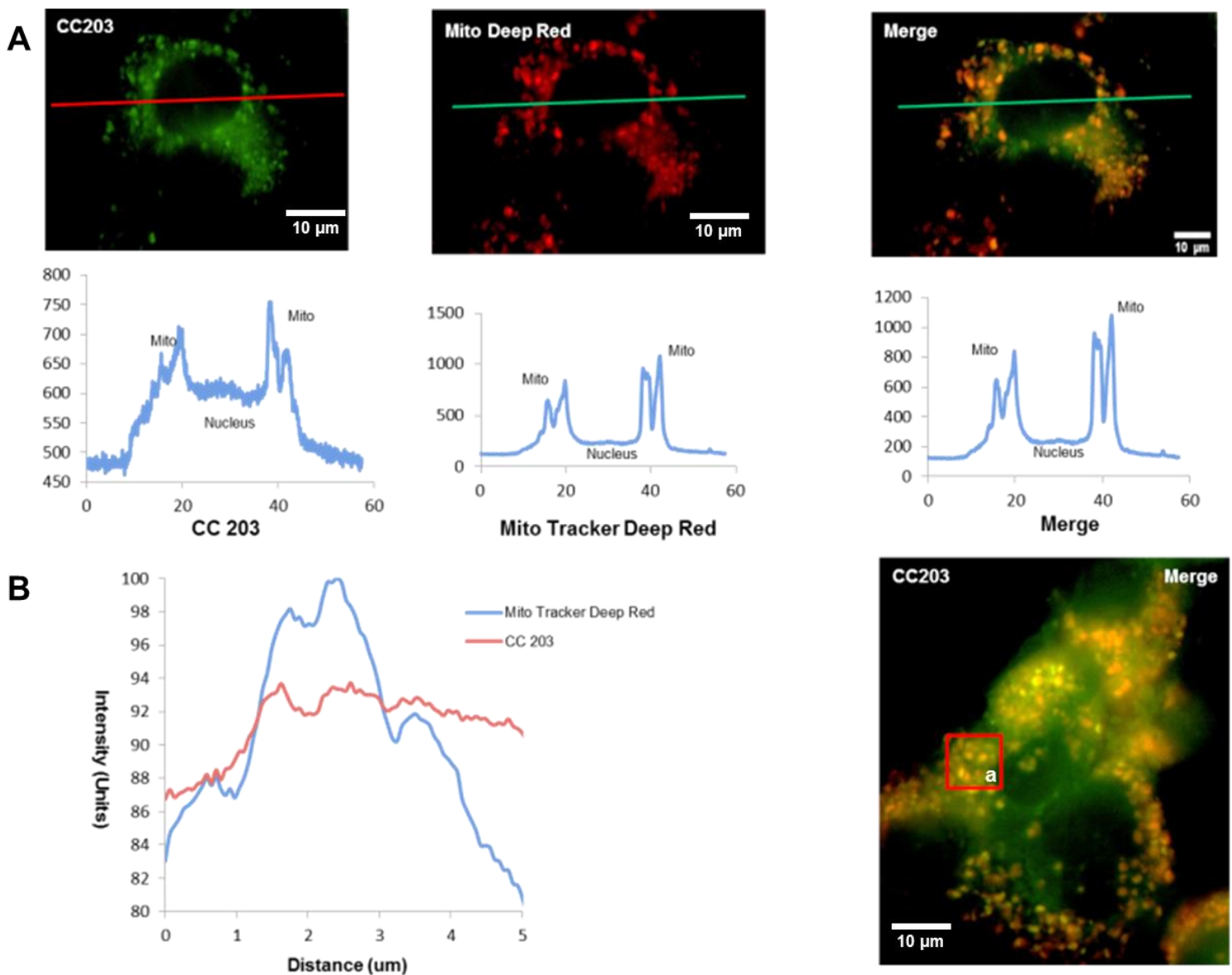
Figure 2.38 (A) Top (Left to Right): Widefield images showing cellular localization of CC 203, Mito Tracker Deep Red (Individual channel), Colocalized image of CC 203 and Mito Tracker Deep Red. **Bottom (Left to Right):** Intensity profiles corresponding to the localization of CC 203, Mito Tracker Deep Red (Individual channel) and merged channel. **(B)** More detailed Intensity profile analysis of the **boxed region (a)** of the merged image of CC 203 and Mito Tracker Deep Red. The experiments were carried out on A2780 cell line

94

As Pearson's correlation is by far the best correlation coefficient in terms of accuracy in comparison to Mander's coefficient, it has been utilized to measure the colocalization between the CC 203 or CC 204 emission channel and the Mito Tracker channel (Deep Red or Green). As mentioned in the previous chapter Pearson's coefficient takes in to account all combinations with respect to both the channels in terms of pixel by pixel and does not ignore blank pixels thereby providing an authentic data set with is more reliable compared to Mander's coefficient[188].

Pearson's coefficients were calculated for all the colocalization experiments and are shown in the Table 2.3. The results indicate a 90% colocalization with Mito trackers (Deep Red and Green) for both CC 203 and CC 204 and this further confirms the mitochondrial localization of both CC 203 and CC 204. Taken together, the data indicates that although CC 203 and CC 204 were shown to be DNA binders in cell free conditions, it appears they localize in the membrane and other areas of mitochondria, which perhaps includes mitochondrial DNA.

Compound	Pearson's Coefficient	Mander's M1	Mander's M2	Costaining Tracker
CC 203	0.943	0.839	0.929	MitoTracker Green
CC 203	0.903	0.999	0.925	MitoTracker Deep Red
CC 204	0.885	0.986	0.863	MitoTracker Deep Red

Table 2.3 Pearson's coefficients of colocalization experiments for CC 203 and CC 203 with Trackers

2.16 CYTOTOXICITY OF CC 203 and CC 204

The need to employ non-toxic, cell friendly probes is essential in carrying out cellular studies - especially cellular imaging. An ideal cellular probe should minimally affect the cellular systems even when they are employed at higher concentrations. Therefore for a new probe, an an evaluation cytotoxicity and any potential to cause cellular damage needs to be carried out[118]. CC 203 and CC 204 were tested for cytotoxicity against a standard of cisplatin in two different cell lines to confirm this. Against HeLa cells and A2780 cells, both CC 203 and CC 204 show relatively low cytotoxicity (Figure 2.39), although there were differences.

Against the HeLa cell line, no significant cytotoxicity was observed. Even in the most concentrated treatment of 200 μM there were still 74±3% of cells (CC 203) or 102±1% (CC 204) in comparison to standard (Cis-platin) was still viable. Against the A2780 cell line, there was appreciable cell death but, in comparison to cisplatin, lower cytotoxicity was still observed. The calculated IC_{50} values for the complexes were 59 μM (CC 203) and 151 μM (CC 204) respectively. These relatively low cytotoxicities indicate that CC 203 and 204 could be leads for safe cellular imaging agents.

A

B
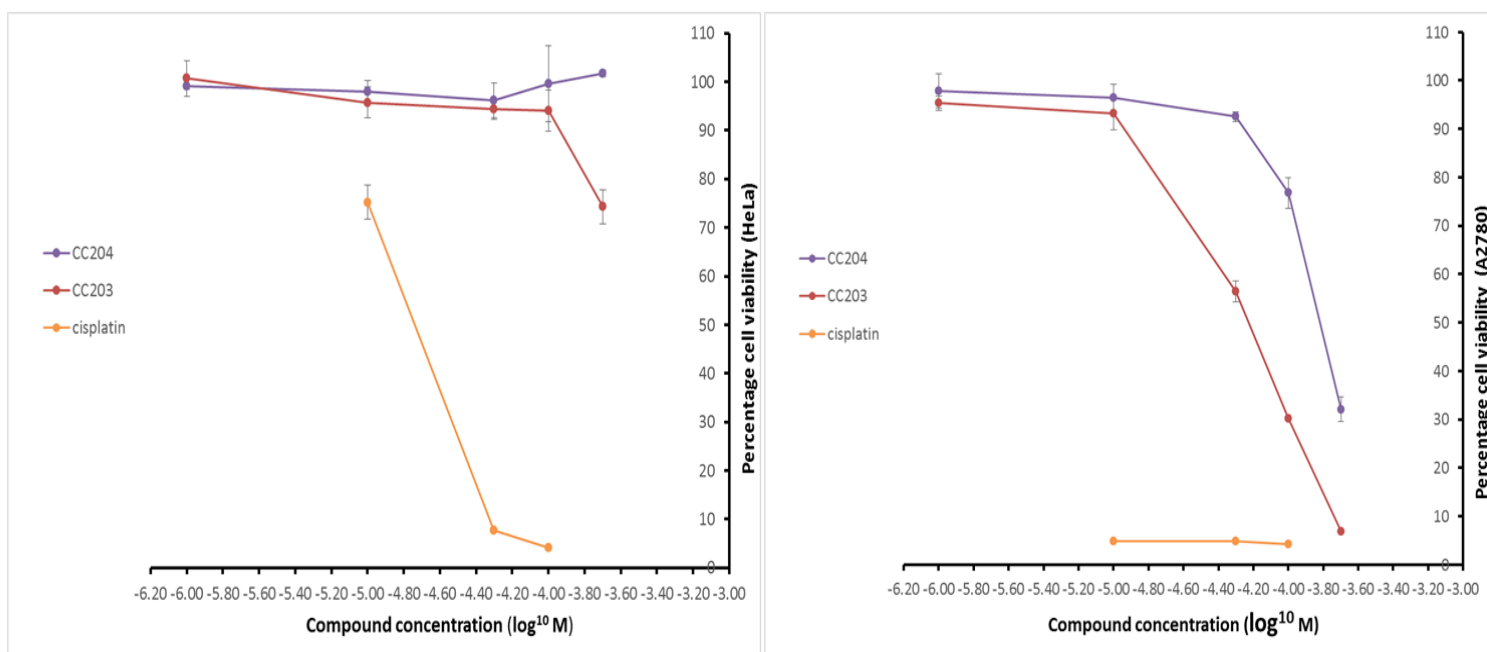
Cell Line	CC 203 (μM)	CC 204 (μM)
HeLa	>200	>200
A2780	59	151

Figure 2.39 (A) A Plot showing logarithmic scale of compound concentration with standard deviations incorporated (X-axis) Versus percentage of inhibition (or) cell viability (Y-axis) for CC 204, CC 203 in HeLa and A2780 cell line respectively. **(B)** Table showing the determined IC_{50} values for CC 204, CC 203 for HeLa and A2780 cell lines respectively

2.17 SPECIFIC CELLULAR UPTAKE OF CC 203 and CC 204

The concentration dependent uptake experiment of CC 203 and CC 204 carried out using A2780 ovarian cancer cell lines indicated the potential of both of them to be applied as effective cellular imaging agents. It also enabled to determine the dosage of CC 203 and CC 204 required to illuminate the intracellular compartments. As the dosage employed in the concentration dependent cellular uptake study does not reveal the detailed in-cell accumulation of the complexes (CC 203 and 204), there is a need to determine this. Therefore, in-cell accumulation was determined by ICP-MS as reported by Jin *et al*[118] and Wang *et al*[123]. ICP-MS experiments were carried out in order to definitively determine cellular uptake in different cell lines. CC 203 and CC 204 was tested against the two different cell lines used in the microscopy experiments. In both cell lines, CC 203 accumulates within cells at higher concentrations compared to CC 204, to be precise by a factor of 3 in A2780 and a factor of 11 in MCF-7. Complex CC 203 is more lipophilic, so this could translate to a difference in diffusion across the cell membrane (Figure 2.40). The 1 and 24 hour time points show there is steady accumulation over the 24 hour time period, and this is suggestive of passive diffusion across the membrane.

A

B
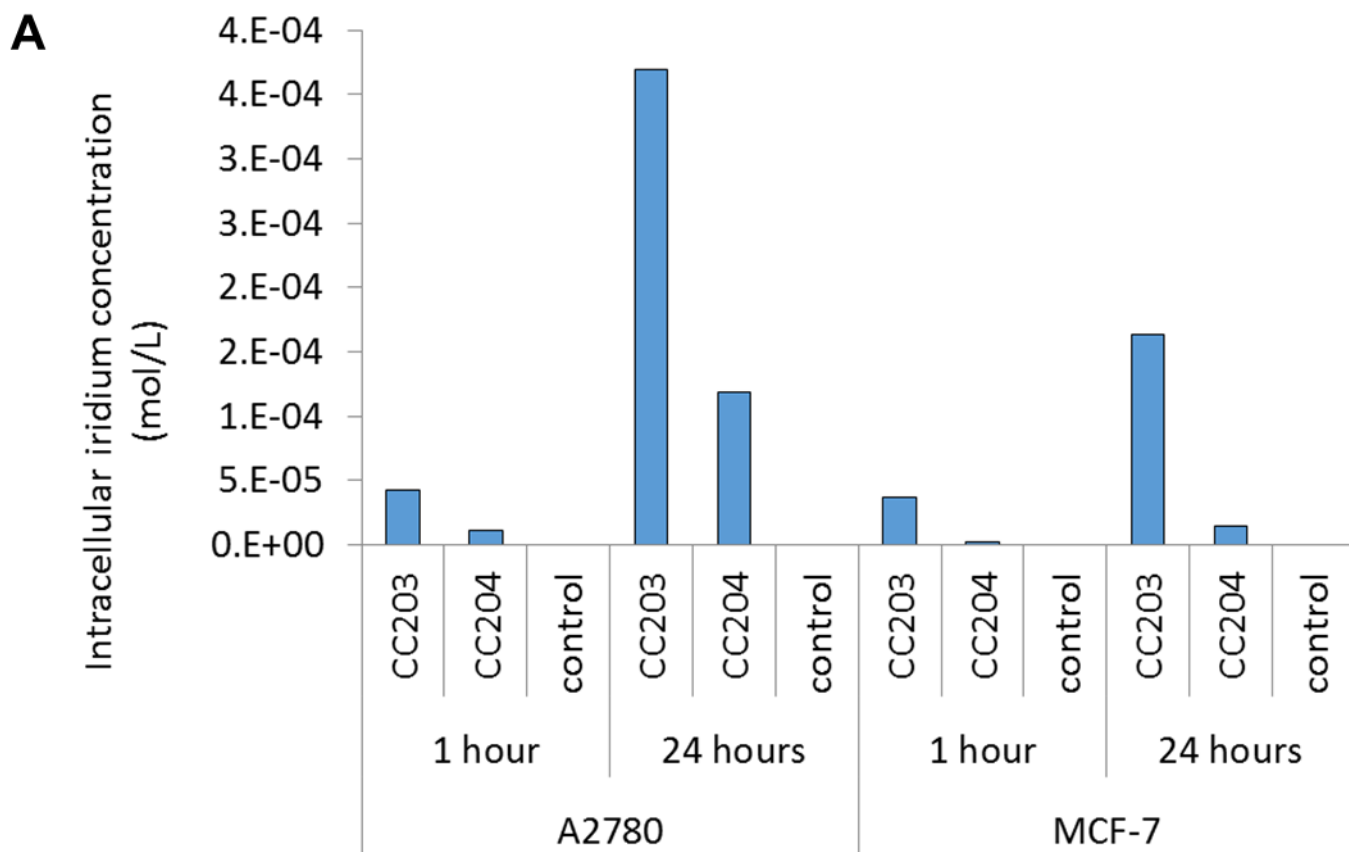
Cell Line	CC 203 (μM)	CC 204 (μM)
A2780	369	119
MCF7	163	14

Figure 2.40 (A) Bar chart showing the comparative Cellular uptake of CC 203, CC 204 against control in A2780, MCF7 cell line determined over a period of 24 hours by ICP-MS. **(B)** Table showing the exact values to confirm the extent of cellular accumulation of CC 203 and CC 204 against A2780 and MCF7 cell lines

2.18 SUMMARY

[{Ru(phen)}$_2$tpphz]$^{4+}$ (RRP) was optimised as a super resolution microscopy cellular imaging probe for both STED and SIM experiments The concentration dependent intracellular localisation characteristics exhibited by the probe was investigated thoroughly and it was found that mitochondrial and nuclear localisation occurred in a concentration dependant manner. Furthermore 3D-STED experiments proved that extraordinary resolutions across all dimensions could be achieved by the probe. The 3D super resolution capability of the probe has expanded the horizons of cellular imaging from the super resolution microscopy point of view and further studies pertaining to selective binding to G-quadruplexes should be undertaken.

In addition to RRP, bicyclometallated iridium metal complexes (CC 203 and 204) with attractive photophysical properties were investigated as optical microscopy probes. These complexes were found to specifically localize in mitochondria.

3.0 DETECTION OF INTRACELLULAR REACTIVE OXYGEN/NITROGEN SPECIES AND SPECIFIC IMAGING OF MITOCHONDRIA USING SUPER-RESOLUTION MICROSCOPY PROBES

3.1 MECHANISM OF ROS (HOCl) GENERATION IN CELLS

Reactive oxygen species (ROS) and reactive nitrogen species (RNS) such as superoxide, hydrogen peroxide, and peroxynitrite are highly reactive and cause oxidative modifications of biomacromolecules[145,146]. Exogenous ROS and RNS can be produced from pollutants, tobacco, smoke, drugs, xenobiotics, or radiation; whereas endogenously ROS are produced intracellularly through multiple mechanisms. Depending on the cell and tissue types, the major sources of these species are NADPH oxidase complexes in cell membranes, mitochondria, peroxisomes, and the endoplasmic reticulum[125,126]. Oxidative reactions in tissue can involve Fenton's reactions in which free metal ions can interact with peroxide, yielding oxidised products like hydroxyl radical and super oxide[150].

Mitochondria produce superoxide radical (O_2^-) when oxygen is prematurely and incompletely reduced. Myeloperoxidase (MPO), which is released from cytoplasmic granules of activated phagocytes by a degranulation process, reacts with H_2O_2 and chloride ions to generate hypochlorous acid/hypochlorite (HOCl/OCl$^-$). In turn, the strong oxidant HOCl can react with proteins to modified their structure[174,175,176]. Monocytes and neutrophils typically contain larger amount of MPO and the oxidative stress they can induce plays multiple role in the development of atherosclerosis particularly with regard to modifications of lipoproteins. RNS are derived from nitric oxide (NO) and superoxide (O_2) via the enzymatic activity of inducible nitric oxide synthase (NOS). The reaction of nitric oxide (NO) with superoxide (O_2^-) leads to the formation of highly reactive peroxynitrite (ONOO$^-$)[128,129].

The combination of O_2 production and myeloperoxidase release gives neutrophils a broad and unique oxidative role. Through the processes involving hydrogen peroxide and myeloperoxidase discussed above, hypochlorous acid (HOCl) is the major end product of the neutrophil respiratory burst. The powerful antimicrobial nature of HOCl and its conjugate base, hypochlorite (-OCl) is very important. It is the active ingredient in household bleach and the species responsible for the microbicidal properties of chlorinated water supplies. The

production of HOCl by neutrophils is an integral part of the ability of these cells to kill a wide range of pathogens[172,173,175]. However, the properties that make it such a useful antimicrobial agent also place the host at considerable risk, because HOCl has the potential to damage host tissue through the same processes used in the destruction of invading microorganisms. Neutrophil oxidants have been implicated in the tissue injury associated with inflammatory diseases, including respiratory distress, ischemia-reperfusion injury, acute vasculitis, arthritis, and glomerulonephritis.

Why is ROS and RNS detection important?

As outlined above, intracellular generated reactive species of oxygen or nitrogen are essential regulators of several physiological processes, ranging from intermediary metabolism to the inflammatory response[137,141]. With regard to cardiovascular disease, the effects of HOCl on tissue are enormous. Hypochlorite can cause endothelial cell apoptosis, which, in the long term, can result in thrombosis. Also hypochlorite can promote foam cell formation in Macrophages[150]. Foam cells are fat laden M2 macrophages that serve as a hallmark of early atherosclerotic lesion formation, which results in an increased risk of heart attack and stroke as a result of arterial narrowing. An understanding of the complexity of ROS signalling requires the determination of their spatiotemporal distribution with high resolution, specificity, and sensitivity. Toward this aim, significant progress in ROS imaging at the level of intact cells, tissues and whole organs, as well as living organisms, has been achieved in the last decade[134,135]. The development of novel synthetic fluorescent ROS indicators and *in vivo* imaging technologies have played an important role in these advances. Imaging ROS dynamics *in vivo* has also provided information that is proving to be beneficial in disease management and treatment[139,147,148].

3.2 SUPER RESOLUTION IMAGING USING ROS AND RNS PROBES

To study the effect of oxidative species and understand the details of mechanisms in relation to various disease processes they are involved in, there is a need for suitable probes to detect these species. Most current ROS probes are not specific and they detect more than one ROS as shown in the work by Jiao *et al*[156]. One method to detect and monitor intracellular ROS involves fluorescent probes with appropriate cellular uptake characteristics[130,133,147]. Molecular imaging is a powerful tool to visualize and characterise biological processes at the cellular and molecular level. Molecular imaging utilises fluorescent probes to probe the details of specific biological processes. In the case of ROS detecting probes, luminescent "*turn-on*" probes which shows sufficient signal enhancement on interaction with a target are particularly attractive[151].

The main characteristic expected of an emissive probe to monitor ROS, and the processes in which they participate, is that it should be cell-permeable, non-toxic, organelle specific, photostable, and bright[131,133]. While much progress has been made in the design of such entities, presently there are very few super-resolution microscopy probes that can image ROS in live cells. A turn-on probe with an ability to show a considerable amount of signal enhancement could be optimized as a super resolution microscopy probe. As super resolution microscopy always requires a probe with considerable amount of photostability and brightness to provide images with enhanced resolutions. Such a probe would provide insights into the finer details of biological mechanisms involving ROS/RNS generation. A ROS specific SR probe which could specifically detect Hypchlorite (HOCl) or Nitroxyl (HNO), which are the most common ROS generated during various disease progression, could help to understand in greater detail the role played by these different ROS *in vivo*.

In this chapter a number of ROS and RNS probes synthesized at the National Chemical Laboratories, NCL, Pune in the lab of an Indian Collaborator, Dr Amitava Das, are investigated as *in cellulo* probes and their suitability for use with the super resolution technique, SIM are assessed.

3.3 ROS PROBE-1 FOR DETECTING HOCl WITHIN MACROPHAGES

3.3.1 Synthesis and Live cell detection of HOCl inside cells:

The ROS probe-1 was synthesised in the NCL by Dr. Firoj Ali through the reaction of a BODIPY (Boron-dipyrromethene (IUPAC: 4,4-difluoro-4-bora-3a,4a-diaza-s-indacene) core, 3,4-dihydroxy benzaldehyde, glacial acetic acid, and piperidine. As shown in Figure 3.1 this probe is designed to specifically react with HOCl and produce a luminescent derivative. As discussed in the work of Gao *et al*[152], BODIPY probe are characterized by their photostability, brightness, high extinction coefficient. These are ideal requirement for the probe to be optimised as a super resolution microscopy probe.

Live cell experiments in Sheffield were initially carried out using widefield fluorescence microscopy. In these experiments HOCl was added to cells that were previously treated with the ROS probe. With gradual addition of HOCl, bright widefield images were observed as shown in Figure 3.2. Live cell experiments showed a gradual increase in emission. The reaction of ROS probe-1 with HOCl is fast and is completed within 10 to 15 minutes. After the completion of the reaction, brightness decreases indicating a saturation level has been reached in the detection of HOCl by the ROS probe-1. As excess Hypochlorite (HOCl) is always harmful to cells, after prolonged exposure to HOCl cell death is inevitable, this is seen in the final frame of the image sequence shown in Figure 3.2.

A

ROS probe 1

B

HOCl

ROS probe 1

ROS probe 1 - Luminescent
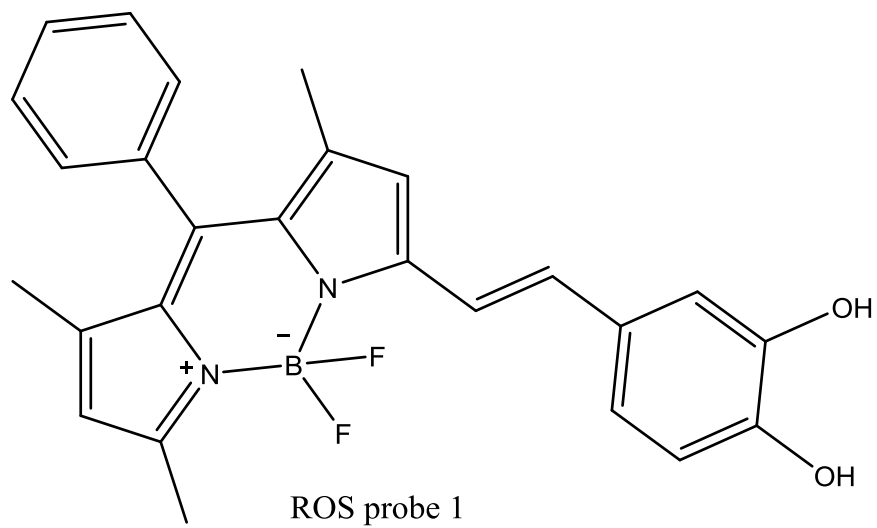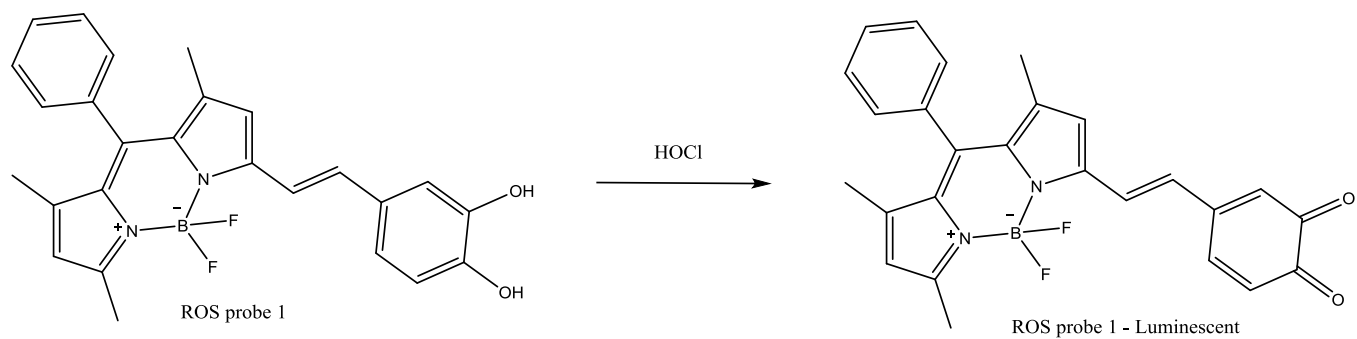
Figure 3.1 (A) Structure and **(B)** Reaction scheme depicting HOCl detection by ROS probe-1
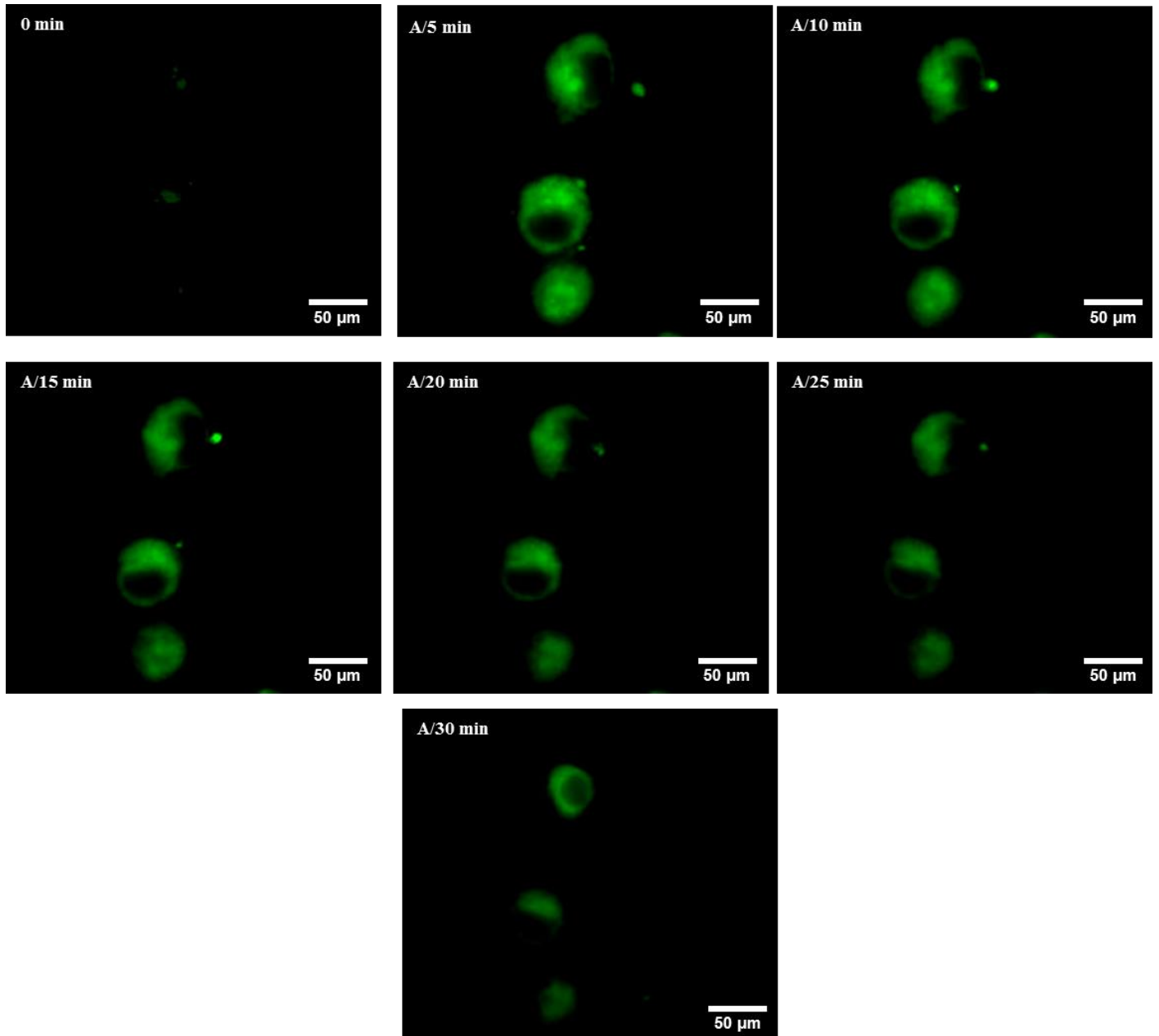
Figure 3.2 Widefield microscopy time lapse images showing ROS probe-1 detecting externally added HOCl in live RAW Macrophages

3.3.2 Detection of HOCl in macrophages by ROS probe-1 using SIM

As mentioned in the previous sections, a significant emission enhancement of ROS probe-1 in the presence of HOCl and its chemical robustness prompted us to investigate its use in SIM imaging, which requires a bright, photostable probe. Structured illumination microscopy imaging depends on various factors which includes characteristics of the probe, type of cell line under investigation. SIM is a widefield technique which involves scanning the sample across the optical plane in all dimensions to generate a Z-stack which is then refined by a reconstruction to arrive at the super-resolved image, significant loss of emission is often a consequence of the quest to improve resolution.

Since live cell experiments carried out in the previous sections gave sufficient evidence to suggest that the probe has the ability to detect hypochorite (HOCl), its use in SIM was investigated. First, fixed cell experiments were carried out to determine the localization characteristics of the probe and also to investigate the ROS detection characteristics of ROS probe-1 across cellular regions.

The experiments were performed by incubating ROS probe-1 (10 μM) for 25 min in live RAW Macrophages. Cells treated with only ROS probe-1 (10 μM) did not show any observable intracellular fluorescence. Next cells were treated by externally adding (20 μM) NaOCl for 30 minutes, then fixed with 4% Paraformaldehyde and imaged using OMX-SIM. Bright incellular fluorescence was observed on the interaction of probe ROS probe-1 with HOCl. The probe was highly photostable and did not bleach out in SIM conditions. Striking SIM images were obtained showing extra structural details of ROS probe-1 detecting HOCl. Comparative SIM and widefield images as shown in Figure 3.3 indicating the resolution enhancement achieved in SIM, confirmed by Intensity v Distance plots generated by using offline FIJI software. Over all, this comparison proves the effectiveness of ROS probe-1 in its application for this super resolution microscopy technique.
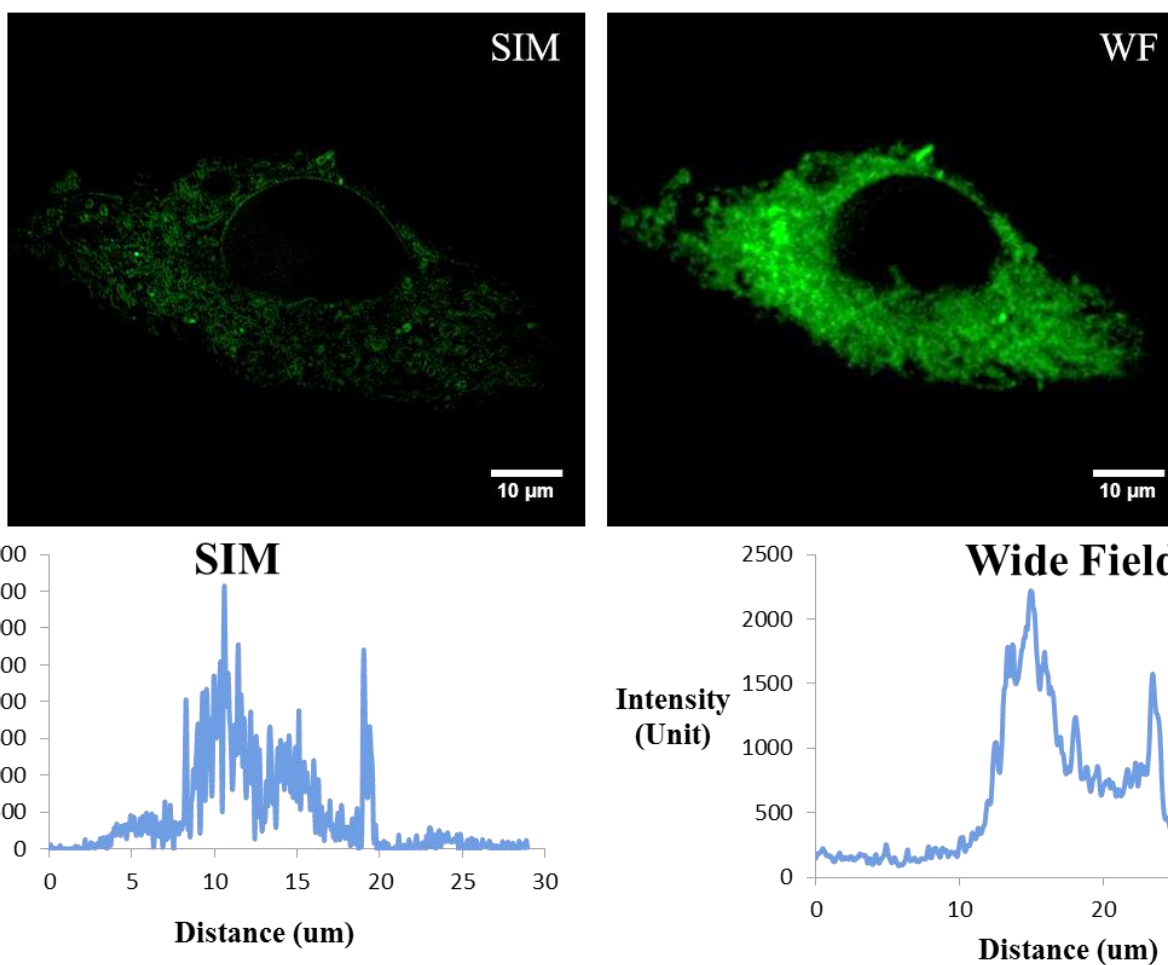
Figure 3.3 Top row: Comparative SIM and Widefield images showing the HOCl detection by ROS probe-1 same area showing improvement of resolution in SIM, **Bottom row:** Comparative Intensity profiles of SIM and Widefield of above images confirming improvement in resolution. The experiment was performed on RAW Macrophages

3.3.3 3D SIM for HOCl detection using ROS probe-1:

The initial SIM experiments carried out in fixed cells demonstrated that the ROS probe-1 could indeed be applied to detect HOCl in RAW macrophages and the generated images can definitely give finer details into the cellular distribution of HOCl. 3D projections confirm that the intracellular luminescence from the probe appears to come from the cytosol and there is no luminescence observed in the nucleus as shown in Figure 3.4. Indeed, a closer scrutiny of the 3D-SIM images generated using ROS probe-1 suggested it is detecting HOCl in specific intracellular compartments in the cytosol. Before conducting experiments to investigate this issue in detail, we first investigated the effect of changing HOCl concentration on the emission output of the ROS probe. Changing the HOCl concentration is necessary because one of the main objectives of this work is to more precisely assess the levels of ROS generated, to understand any threshold level of generation, and discover how excess generation of HOCl affects the cells.
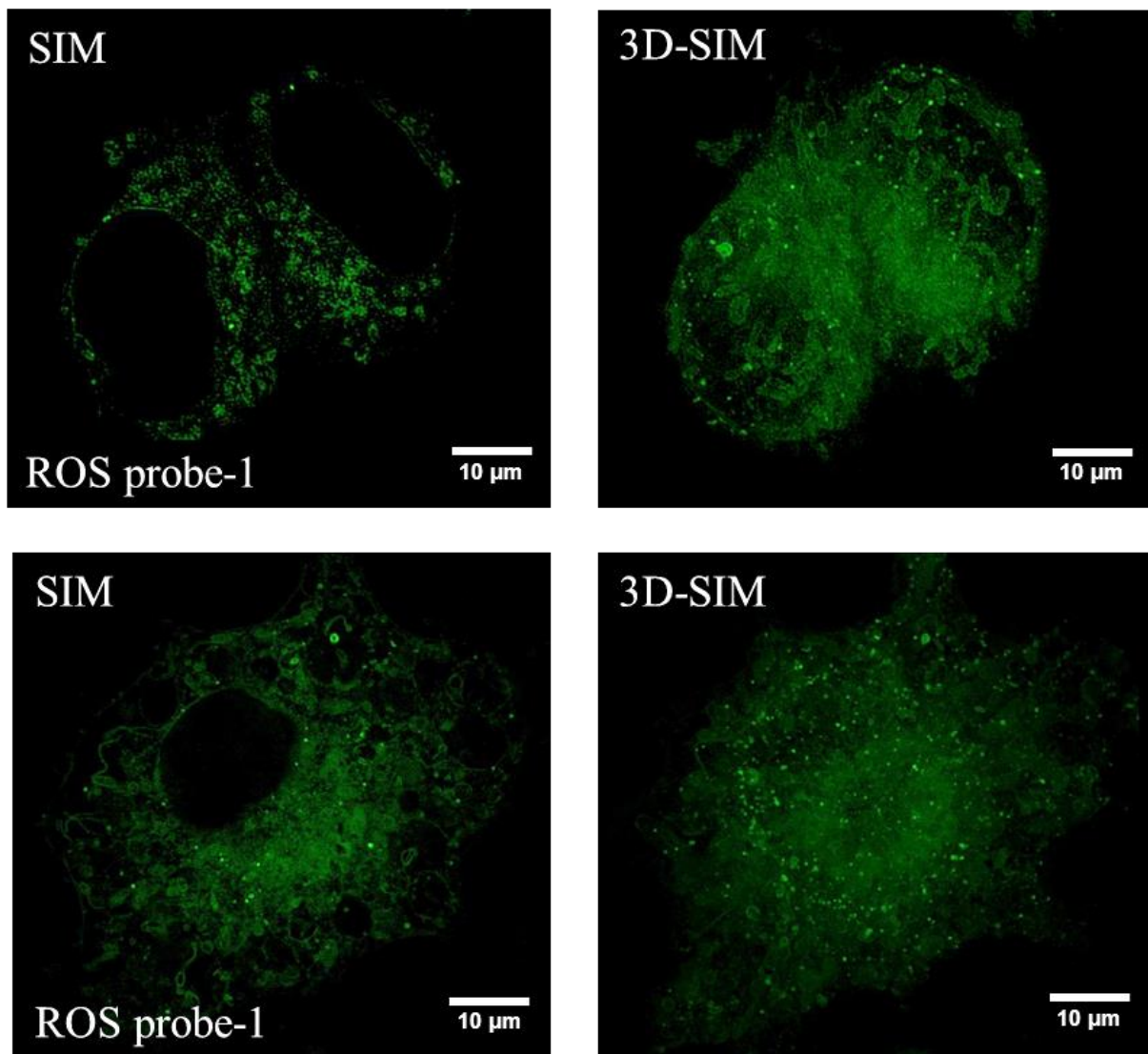
Figure 3.4 Top and Bottom row: Comparative SIM and 3D-SIM images of two different areas in RAW Macrophages showing HOCl detection by ROS probe-1 in the cytosol

3.3.4 Concentration dependent HOCl detection

After confirming the efficient cellular internalisation of the probe, experiments were then performed in which HOCl was added externally or generated endogenously by a biochemical process. As expected, live RAW macrophages treated with only ROS probe-1 (10 µM) showed minimal intracellular fluorescence. However, cells exposed to increasing concentrations of HOCl show a concomitant increase in ROS probe-1 emission. The gradual increase in emission observed as HOCl was added externally or generated internally by LPS indicated the sensitivity of the probe to HOCl in the cellular environment.

The obtained super-resolved images showed clearly resolved HOCl signal generation, which then spread into the intracellular environment. Detailed images for both externally added and endogenously generated HOCl are shown in Figure 3.5 and 3.6. These are well supported by FIJI generated 3D-surface plots which shows the signal enhancements at a wide range of HOCl concentrations as detected by ROS probe-1 in its fluorescent state.

For experiments withr externally added HOCl, RAW macrophages were pre-treated with the ROS probe (10 µM) for 30 minutes and then treated with a range of concentration of NaOCl from 0 µM to 20 µM, for 30 minutes; both these treatments were on live cells which were consequently fixed using 4% paraformaldehyde and imaged using OMX-SIM.
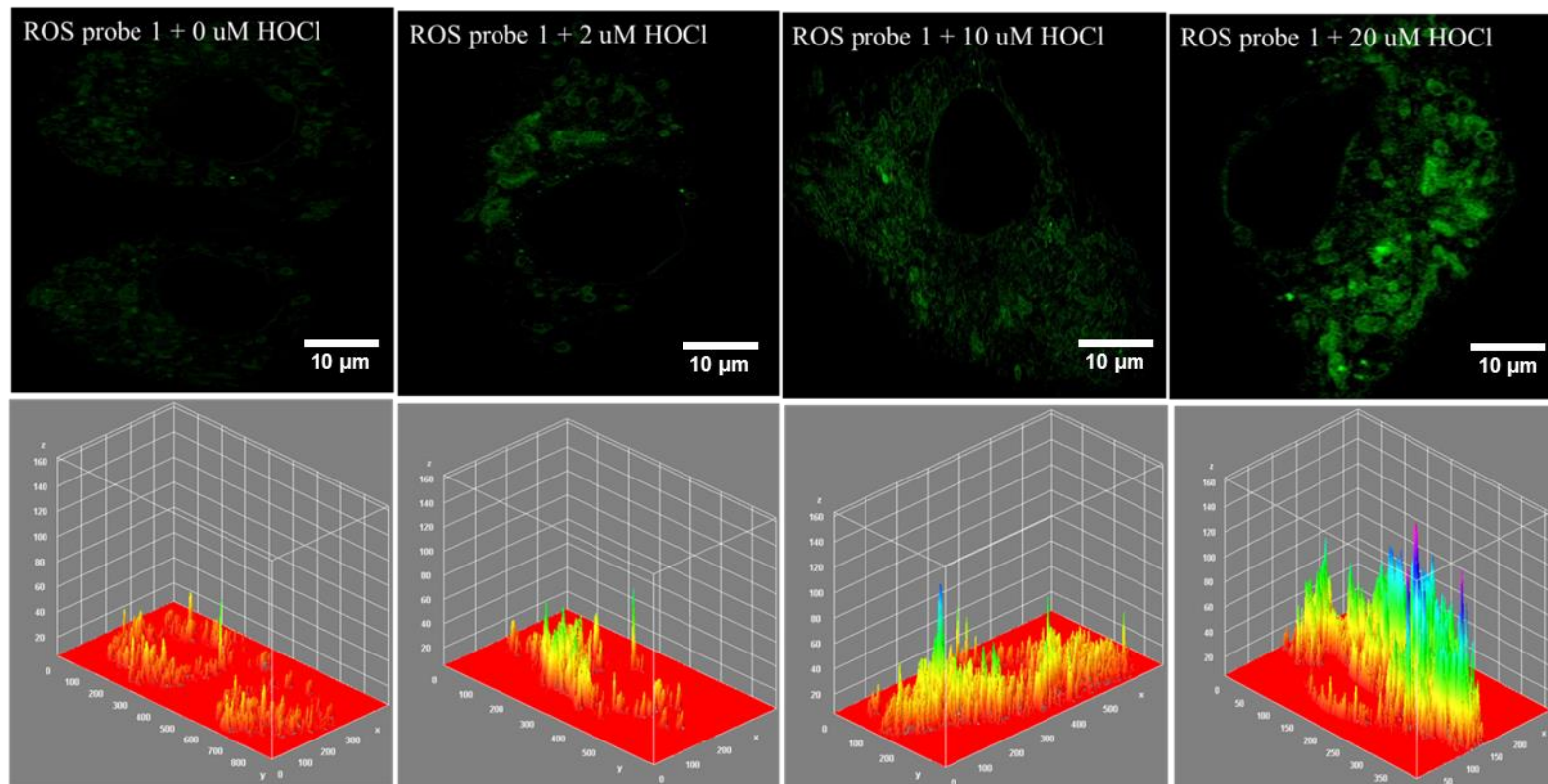
Figure 3.5 Top row: SIM Images of ROS probe-1 detecting HOCl at different concentration of externally added HOCl in RAW Macrophages, **Bottom row:** The corresponding 3D Surface plots for the same

Detection of Endogenously generated HOCl:

Since RAW Macrophages are known to generate HOCl, when they are stimulated by lipopolysaccharide (LPS), cells were incubated with LPS at concentrations ranging from 250 ng/mL to 5000 ng/mL for 24 h in a DMEM culture medium with 10% FBS and then further treated with ROS probe-1 (10 µM) for another 30 minutes. SIM images showed a bright fluorescence signal from the cells. A control experiment, where cells were treated only with ROS probe-1 (10 µM) was also carried out and this showed no intracellular fluorescence. From these LPS dose dependent studies it was observed that increasing concentrations of LPS led to enhanced intracellular fluorescence from the probe. Initially, there were intense signal observed from certain round or punctated structures, but then the SIM images showed significant signal attenuation. However, the main objective was achieved in that the varying levels of internally generated HOCl could be vividly seen in the acquired SIM images and well supported by the 3D-surface plots generated from them, Figure 3.6.
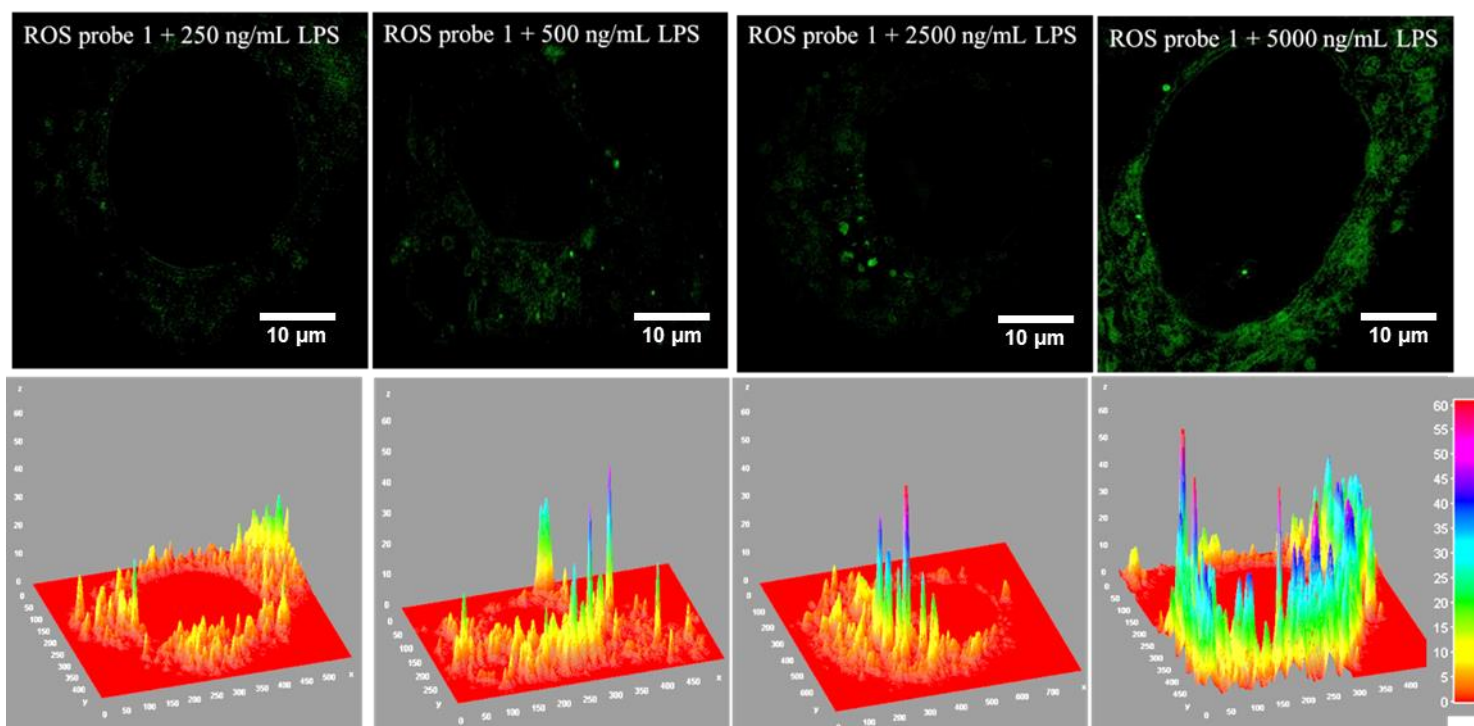
Figure 3.6 Top row: SIM Images of ROS probe-1 detecting endogenously generated HOCl at different concentration of LPS in RAW Macrophages, **Bottom row:** The corresponding 3D Surface plots for the same

3.3.5 Time dependent detection of Endogenous generation of HOCl

The initial SIM experiments, on the detection of different levels of HOCl, produced a deeper understanding of the ability of the ROS probe-1 to detect HOCl in cells from the super resolution point of view. However, this led to many questions with regard to the area of localization of the ROS probe-1 and where HOCl is generated in cells. SIM experiments indicated that one or more intracellular organelle may be involved in the generation of HOCl as examination of the images indicated the presence of punctuated and diffuse structures. As the above hypotheses needed to be confirmed, time-lapse experiments to understand the initial point of HOCl generation and the signal spread seemed to be essential as they may aid in understanding bio-signalling mechanisms.
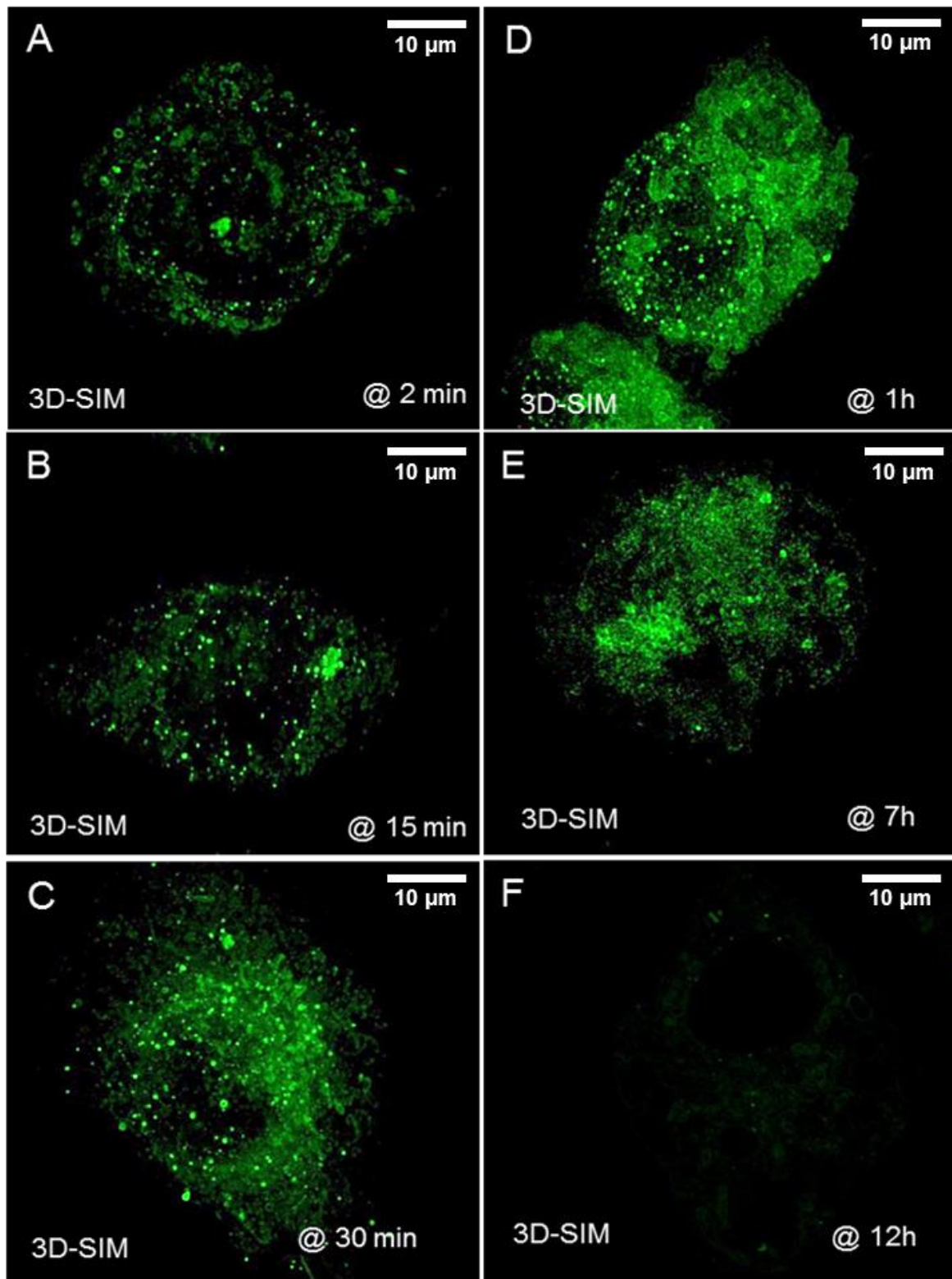
Figure 3.7 (A – F) 3D-SIM images for the endogenous detection of HOCl (stimulated by LPS) by ROS probe-1 at different time intervals of LPS showing signal attenuation and spread. The experiment was performed on RAW Macrophages

The 3D-SIM projections generated from the acquired SIM images were obtained by conducting a time-lapse experiment over RAW macrophages which involved treating the cells with ROS probe (10 µM) and further incubation of fixed concentration of LPS (2500 ng/mL) over multiple time durations, before fixing them with 4% paraformaldehyde. These time dependent LPS experiments were carried out at time intervals ranging from 2 minutes to 12 hours.   After 12 hours the signals die out indicating possible cell death due to prolonged generation of endogenous HOCl. The imaging was carried was carried out using OMX-SIM at the LMF, University of Sheffield.

3.4 INTRACELLULAR LOCALIZATION OF ROS PROBE-1

It was evident from the collected widefield and SIM images that the probe was not localized in the nucleus. Rather, it appeared to be localized in specific region of the cytoplasm. Concentration dependent, time-lapse LPS experiments led to the generation of high quality super-resolved images. These super-resolved images gave indication of not only HOCl detection and high signal attenuation, but also showed signal spread across the intracellular environment from punctated structures across the cytosol, therefore establishing the identity of these structures become the next aim of these studies.

Several HOCl detecting probe with high degrees of target specificity have been reported in the literature. For example, Zhou *et al*[160] have reported a mitochondria specific HOCl detecting probe based on Rhodamine and Wang *et al*[164] have reported a lysosome specific HOCl detecting probe based on seminaphthorhodafluor. In addition to this, Yuan *et al*[163], have reported a fluorescent probe based on acedan which detects HOCl generation in two different organelles namely mitochondria and lysosomes. As mentioned in the introduction, ROS detection is very challenging and the invention of many organelle specific fluorescent probes has helped to probe the various intracellular locations where HOCl generation seems to happen. Therefore, colocalization studies using ROS probe-1 to obtain further details of its exact sub-cellular localization were explored.

Initial colocalization studies on RAW Macrophages employed ER Tracker Green as a co-stain. SIM images from co-staining with ROS probe-1, show low colocalization, with a calculated Pearson's correlation coefficient (PCC) < 0.05 indicating that the probe is not localizing to the endoplasmic reticulum. There was minimum overlap between the ER Tracker Green channel (500 − 550 nm) and the ROS probe-1 channel (570 − 620 nm).

However, ER Tracker Green photobleaches more easily when compared to the ROS probe-1 and this process may be affecting the results, therefore widefield imaging was also employed as this may give a greater idea of true colocalization. These widefield images (Figure 3.8) and accompanying calculated Pearson's coefficient (Table 3.1) values confirmed that ROS probe-1 is not detecting HOCl in endoplasmic reticulum.
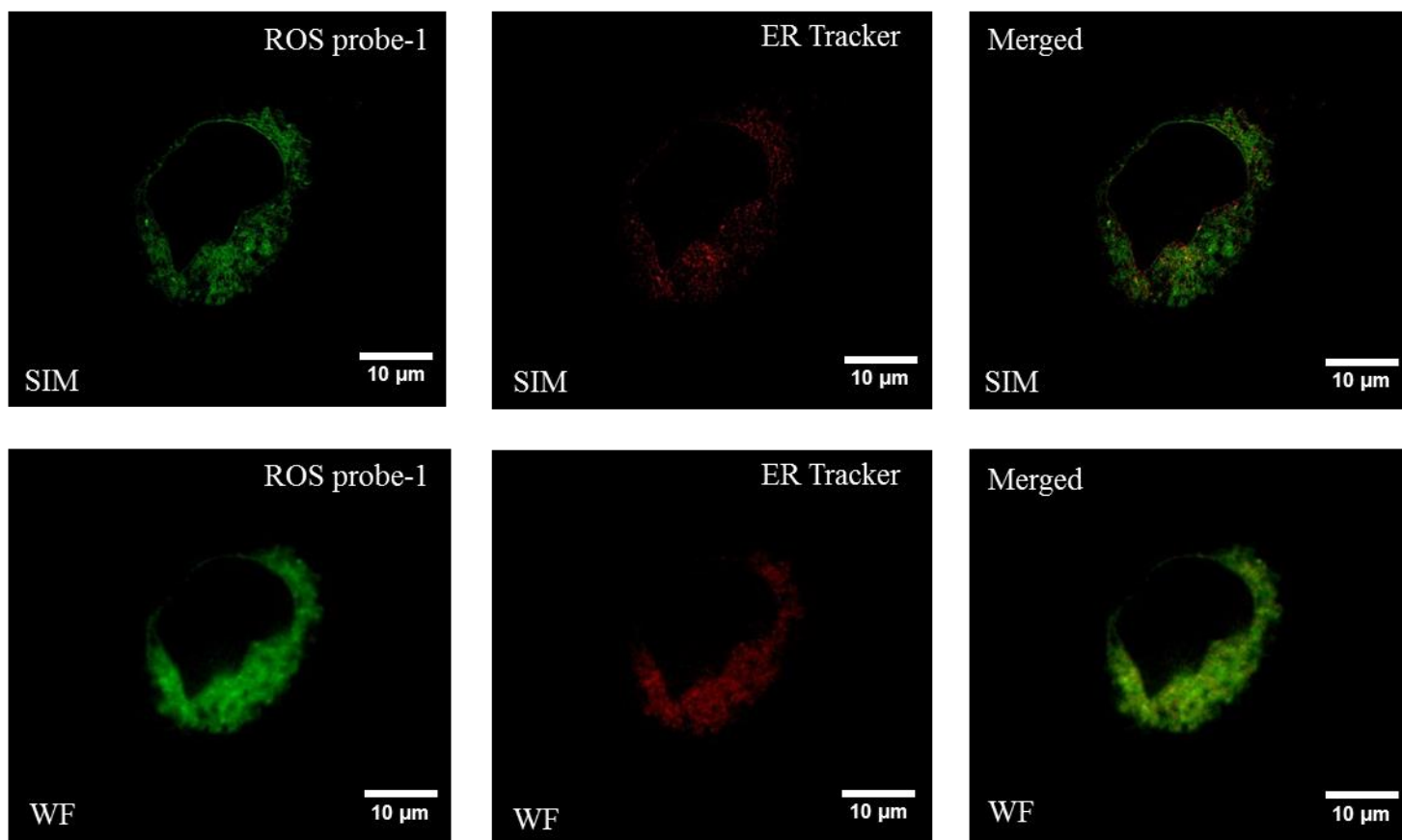
Figure 3.8 Top row (Left to Right): SIM Images of ROS probe-1 in presence of HOCl, ER Tracker green (Individual channel), Colocalized image (Merged) of ROS probe-1 and ER Tracker green. **Bottom row (Left to Right):** Widefield images of the same area showing ROS probe-1 in presence of HOCl, ER Tracker green (Individual channel), Colocalized image (Merged) of ROS probe-1 and ER Tracker green. The experiment was performed on RAW Macrophages

Colocalization data with ER Tracker Green:

Sample Name	Pearson's Coefficient	Mander's Coeffcient (M1)	Mander's Coeffcient (M2)	Treshold ER Channel (500 – 520 nm)	Treshold ROS probe-1 Channel (570–620 nm)	Overlap Coefficient
ROS probe-1 Co-stained with ER Tracker Green	0.0446	0.999	0.999	800	300	0.822

Table 3.1 Colocalization experiments of ROS probe – 1 (In presence of HOCl) with ER Tracker Green

Having established that ROS probe-1 does not detect HOCl generated in the ER. Further colocalization experiments were then carried out with commercially available Cytopainter Golgi Green (CGG). Although there is minimum spectral overlap between the Golgi tracker channel and the ROS probe-1 channel, it was found that CCG was not as photostable as the ROS probe-1, therefore performing SIM over CCG led to no reliable SIM images because of excessive photobleaching of the probe. Consequently, widefield microscopy experiments were performed to determine whether ROS probe-1 detects HOCl generated in the Golgi complex. Pearson's coefficient and related plots were generated by using offline Volocity software. The widefield images (Figure 3.9) revealed a very close spatial correlation between ROS probe-1 and CCG and the calculated Pearson's coefficient of 0.98 (Table 3.2). The result obtained from this colocalization experiments confirm that the ROS probe-1 is indeed detecting HOCl in the Golgi complex.
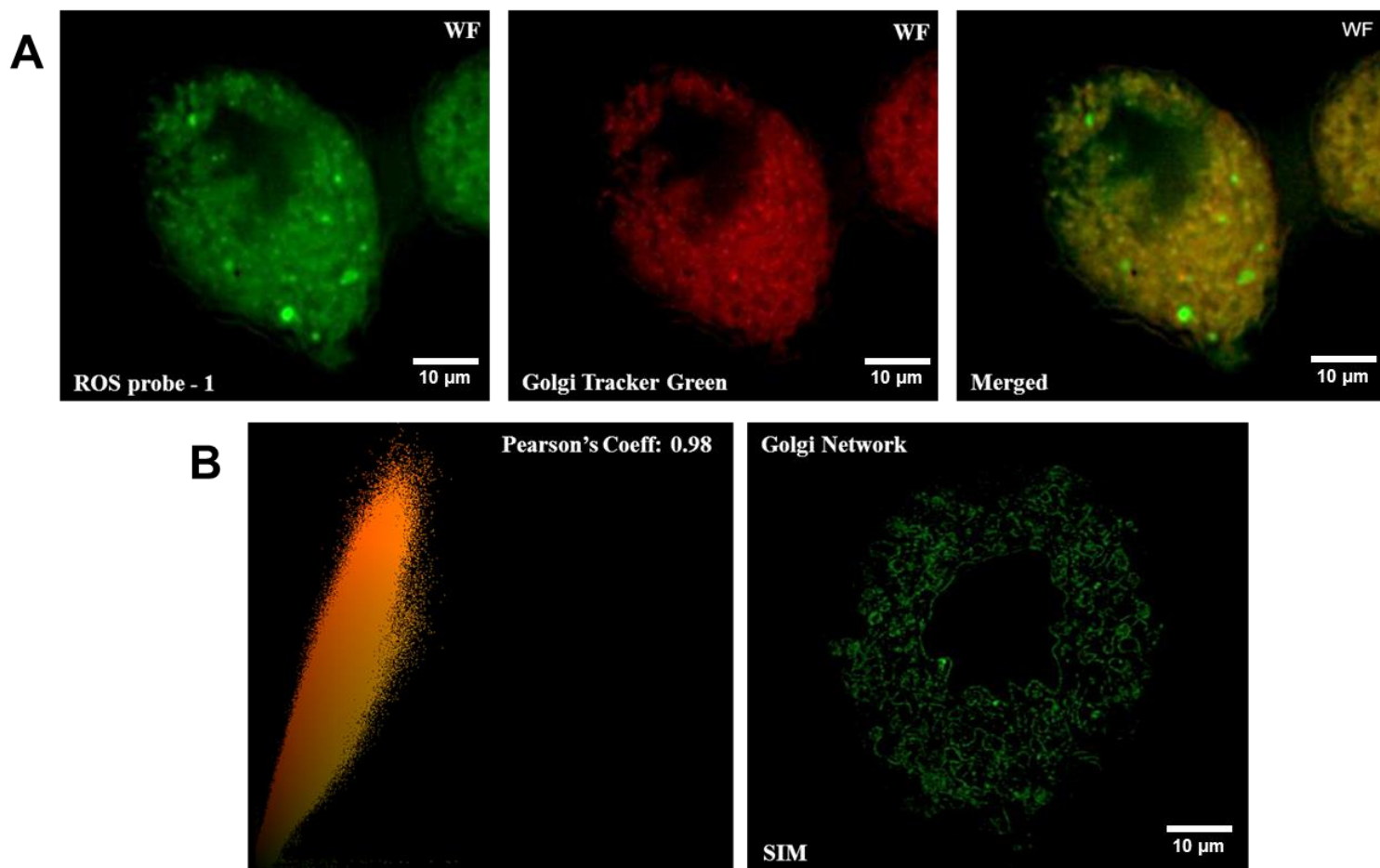
Figure 3.9 (A) From Left to Right: Widefield images of ROS probe-1 in presence of HOCl and Golgi Tracker Green (Individual channel), Colocalized image (Merged) of ROS probe-1 with Golgi Tracker Green **(B)** Pearson's Coefficient for the same, SIM image of Golgi network of RAW Macrophages stained with ROS probe-1

Colocalization data with Cytopainter Golgi Tracker Green:

Sample Name	Pearson's Coefficient	Mander's Coeffcient (M1)	Mander's Coeffcient (M2)	Treshold Golgi Channel (500–520 nm)	Treshold ROS probe-1 Channel (570–620 nm)	Overlap Coefficient
ROS probe-1 Co-stained with cytopainter Golgi Tracker Green	0.98	0.981	0.970	487	241	0.900

Table 3.2 Colocalization experiments of ROS probe – 1 (In presence of HOCl) with Golgi Tracker Green

Although ROS probe-1 is detecting the HOCl formed in the Golgi complex, this might be because the ROS probe-1 is itself localizing on the Golgi complex which would in effect mean generation of HOCl across regions other than the Golgi complex cannot be ruled out. We can therefore infer that as the ROS probe-1 is localizing on the Golgi complex it is detecting HOCl generated in the regions of Golgi complex. This brings us to the identity of the punctated structures which we observed during our initial SIM investigation of HOCl generation using the ROS probe-1. Therefore further colocalization experiments were carried out to determine the identity of the punctated structures.

In many cases oxidative species are generated by lysosomes as shown in the work done by Wang *et al*[164]. Colocalization experiments were hence performed using the standard Lyso Tracker Deep Red dye. Lyso Tracker Deep Red is a very stable probe and withstood SIM acquisition conditions and gave nice SIM images along with the ROS probe-1. When compared to the lysosome specific HOCl detecting probe reported by Wang *et al*[164], ROS

probe-1 was superior in terms of achieving spatial resolution because it is a super resolution probe. Widefield images, 3D-widefield images and 3D-SIM images (Figure 3.10) illustrated that, in addition to detecting HOCl in the Golgi complex, ROS probe-1 also specifically detects HOCl formed in the lysosomes. The results were well supported by the generated Pearson's coefficient (Table 3.3).
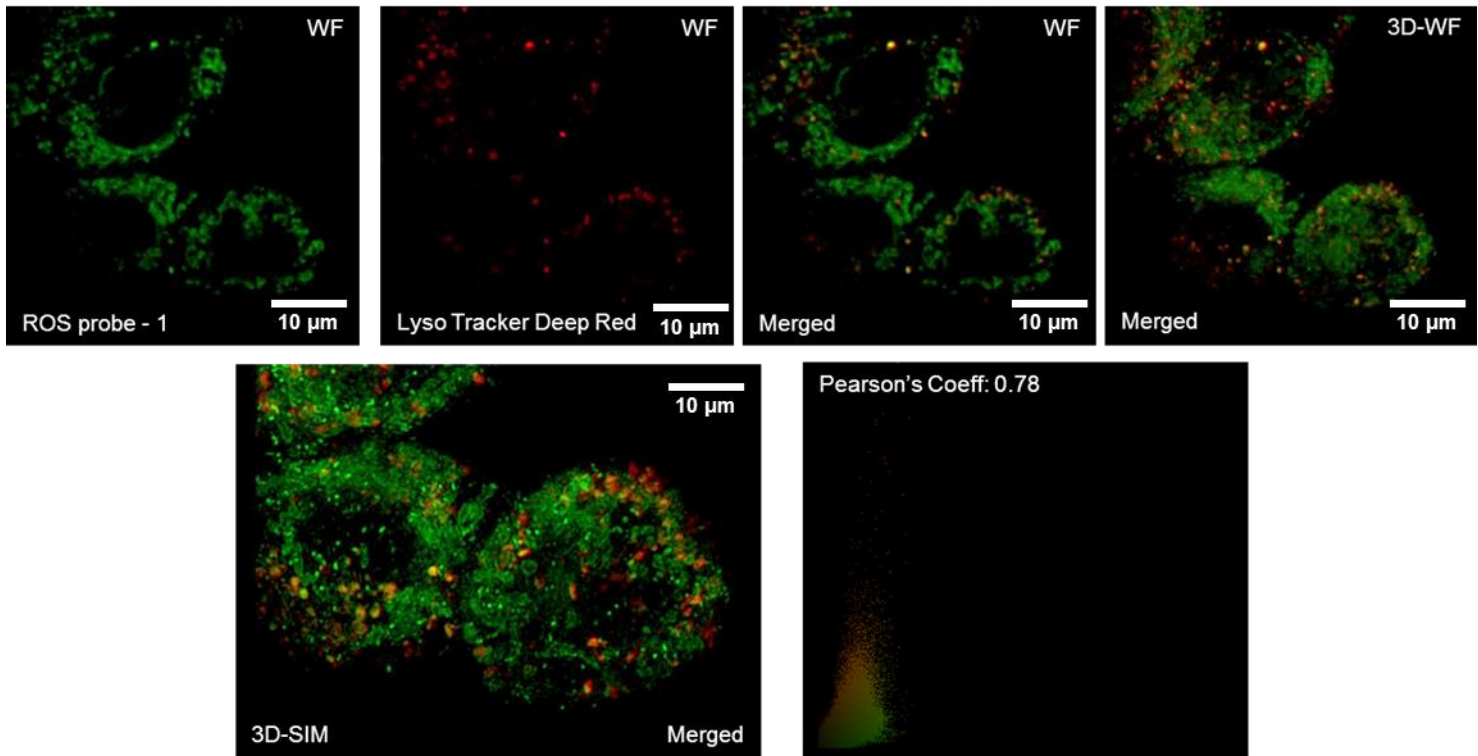
Figure 3.10 Top row (Left to Right): Widefield images of ROS probe-1 in presence of HOCl, Lyso Tracker Deep Red (individual channel), Colocalized image (merged) comprising ROS probe-1 and Lyso Tracker Deep Red, 3D-Widefield image showing colocalization of ROS probe-1 and Lyso Tracker Deep Red. **Bottom row:** 3D-SIM image showing colocalization of ROS probe-1 with Lyso Tracker Deep Red, Pearson's coefficient for the colocalization. The experiment was performed on RAW Macrophages

Colocalization data with Lyso Tracker Deep Red:

Sample Name	Pearson's Coefficient	Mander's Coeffcient (M1)	Mander's Coeffcient (M2)	Treshold Lyso Channel (>670 nm)	Treshold ROS probe-1 Channel (570–620 nm)	Overlap Coefficient
ROS probe-1 co-stained with Lyso Tracker Deep Red	0.781	0.973	0.968	1493	825	0.983

Table 3.3 Colocalization experiments of ROS probe − 1 (In presence of HOCl) with Lyso Tracker Deep Red

Although ROS probe-1 is localized in the Golgi complex and the lysosomes and hence it detects the HOCl formation in these regions, Yuan *et al*[163] has reported an Acedan probe which could simultaneously detect the HOCl formed in the mitochondria and lysosomes, indicating that the detection of HOCl in the intracellular environment relies on the site of localization of the fluorescent probe. Although Yuan *et al*[163] have successfully employed their probe in two-photon imaging of generated HOCl in multiple organelles, in this chapter, we have further improved spatial resolution by imaging the HOCl generated in Golgi complex and lysosomes using super resolution microscopy.

3.5 DUAL COLOUR SIM IMAGING USING ROS PROBE-1

To understand complex biological processes it is often necessary to employ more than one probe so that higher quality imaging or information on simultaneous biological processes can be obtained. Indeed, multi colour image using ROS probes has already been reported by Wrobel *et al*[139] and this shows the importance of multicolour imaging Since ROS probe-1 is a super resolution probe capable of detecting HOCl in multiple organelle, its use in dual colour structured illumination microscopy (Dual-SIM) experiments was investigated. For this technique, a stain for a separate organelle with distinctly different spectral characteristics is required. In this initial study we explored the use of the well-known nuclear stain Hoechst 33442. Using this combination, well-defined dual colour SIM images could be obtained. Indeed the brightness and high photostability of both probes, meant that they could even be used to construct striking 2D- and even 3D-SIM images of individual cells as shown in Figure 3.11 and Fig 3.12.
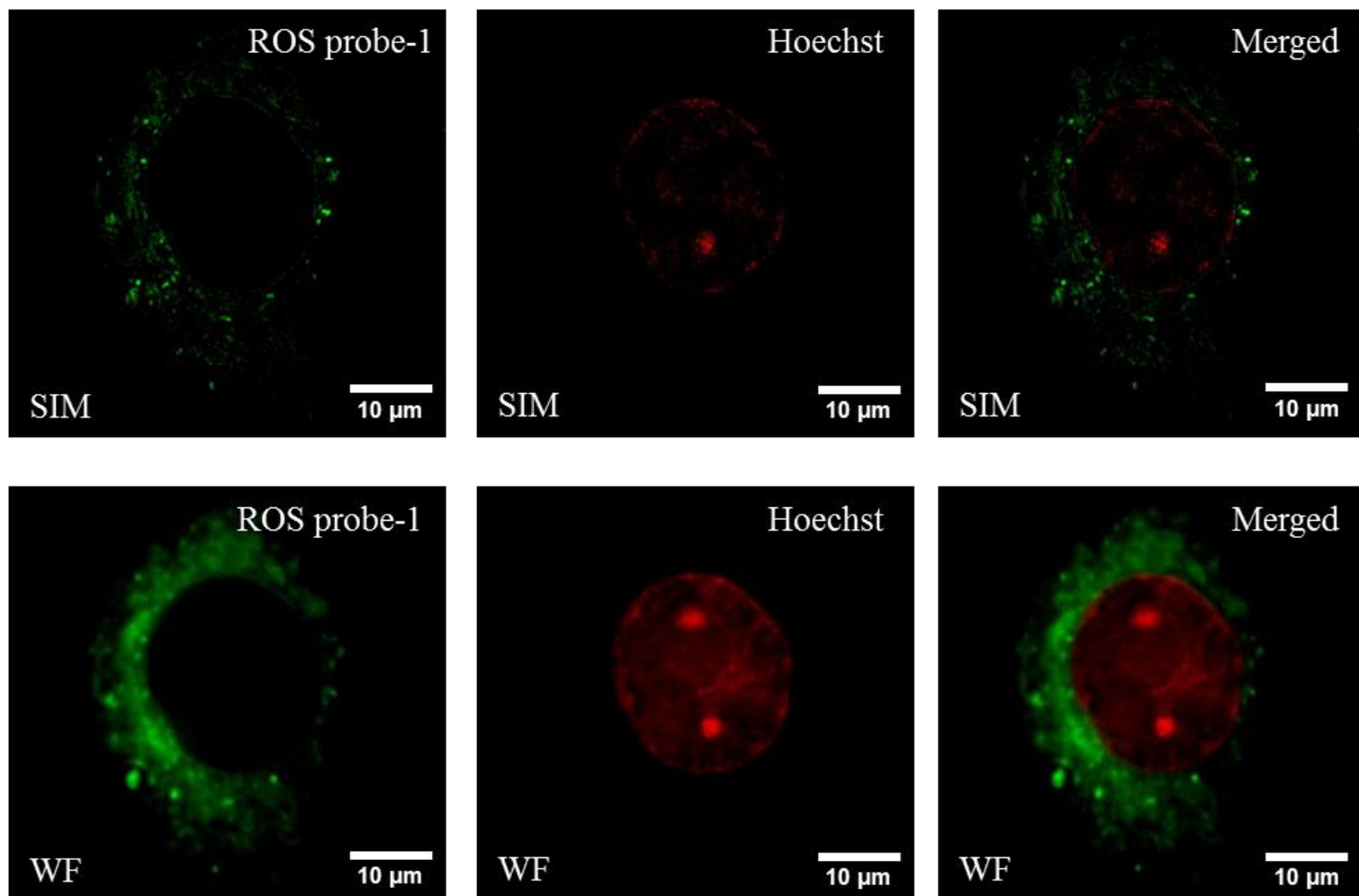
Figure 3.11 Top row (Left to Right): SIM Images acquired in RAW Macrophages showing ROS probe-1 in presence of HOCl, Hoechst (Individual channel), Dual colour merged image comprising ROS probe-1 and Hoechst. **Bottom row (Left to Right):** Widefield images of ROS probe-1 in presence of HOCl, Hoechst (Individual channel), Dual colour merged image of ROS probe-1 and Hoechst combined. The experiment was performed on RAW Macrophages
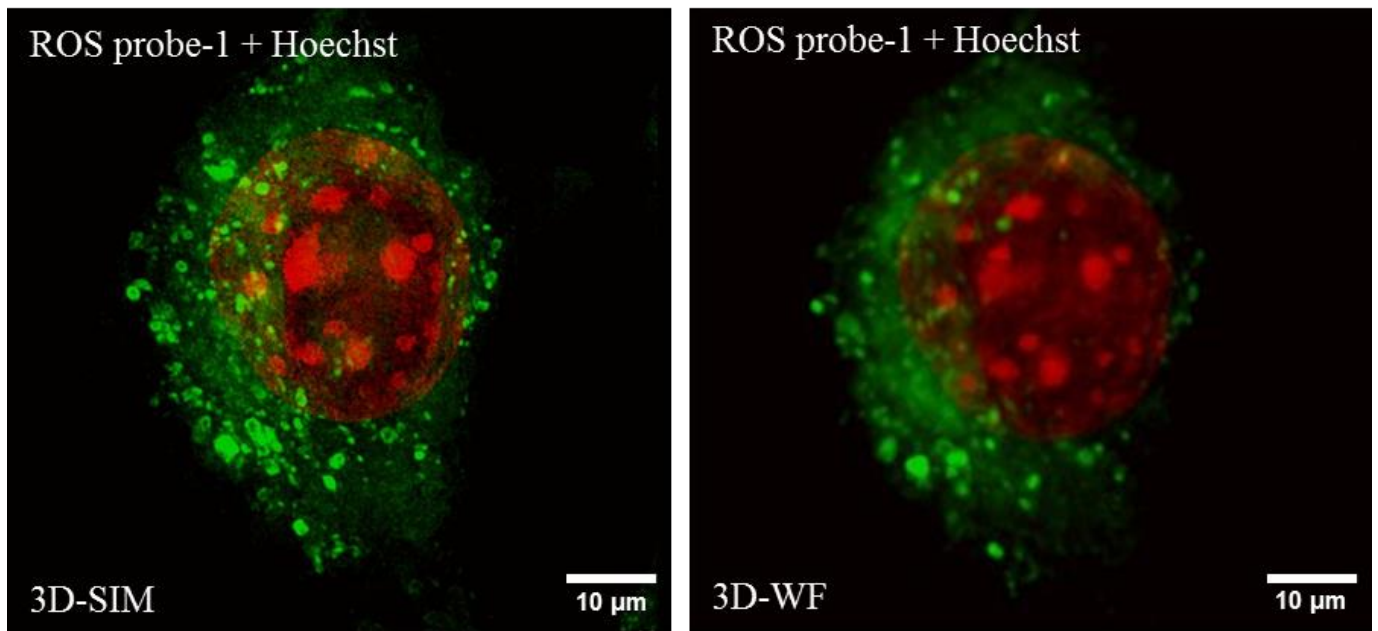
Figure 3.12 Comparative dual colour 3D-SIM and 3D-WF image of ROS probe-1 in presence of HOCl and Hoechst combination of the same area. The experiment was performed on RAW Macrophages

3.6 ROS PROBE FOR DETECTION OF HNO IN CELLS:

3.6.1 Detection of HNO in Macrophages by ROS probe-2

Nitrosyl (HNO) has been identified as an enigmatic reactive nitrogen species and a potential pharmacological agent. It is thought that HNO is generated from $NO^{\bullet}$ synthases through oxidation of N-hydroxy-L-arginine or via reduction of $NO^{\bullet}$ by mitochondrial xanthine oxidase, cytochrome C. Recent advances in the understanding of the chemistry of HNO reveals that this species displays unique cardiovascular properties. Most HNO is generated as part of redox processes in cells, and technologies to detect it are required. Apart from its beneficial effects in cardiovascular disease, HNO is known to inhibit GAPDH, a key glycolytic enzyme for tumor proliferation and cancer cell apoptosis[135,136]. It also interferes with redox-based immunity mechanisms through fast depletion of glutathione, and is more efficient in inhibiting platelet aggregation compared to traditional nitro vasodilators[138].

Reagents that show fluorescence ON response on detection of HNO have an obvious edge for use as an imaging reagent as well as for studying bio-species in living samples. Such reagent also allows high sensitivity, and spatiotemporal resolution. The subcellular distribution of the probe is an important factor to consider as a probe is only able to detect HNO in the regions of the cells where it is localized[138]. Most probes reported in the literature specifically detect HNO in one or more intracellular organelle. Mitochondria seems to the be the main organelle involving the generation of the ROS, but the literature has also suggested that ROS generation happens in organelles other than mitochondria.

Among the various reagents that show a ON response, phosphine-based reagents have received considerable attention. King and co-workers were the first to report the reaction of such reagents with HNO. Since then, molecules that exploit this reaction for specific detection of HNO using flourophores like rhodamine, coumarine, napthalimide and BODIPY have been developed. This reaction has also been exploited in developing FRET based receptors for HNO. In this section ROS probe-2 which specifically detects HNO or the nitroxyl group has been designed. Although several ROS probes which specifically targets HNO have been reported in the literature; for example, Tan *et al*[157], Sunwoo *et al*[148], Wrobel *et al*[139], no super resolution microscopy probes have been reported. Since super-resolution microscopy gives improved resolution across all planes this can be transformed in to 3D-SIM projections, which could ideally help us to give more information about mitroxyl (HNO) generation within cells. In this section the optimisation of ROS probe-2 as a SIM probe to specifically detect HNO

generated *in cellulo* is described. Again, the probe was synthesised by Dr. Firoj Ali at the NCL India. The photostability and brightness exhibited by the ROS probe-2 originates from the BODIPY moiety, the probe also exhibits a sharp Stoke's shift. All these characteristics exhibited suggest the probe would be an excellent SIM probe.

As shown in Figure 3.13, a comparison between widefield and SIM image of the HNO detection of ROS probe-2 shows that ROS probe-2 detects HNO mainly in the cytosol region in cells (RAW Macrophages). The experiment was carried out by externally adding Angeli's salt, 20 µM (a nitroxyl generator), the small molecule is taken up in RAW macrophages and is detected by 1 µM of ROS probe-2 in cells. The comparative images show tremendous resolution improvement in SIM when compared to widefield giving detailed information about the structures involved were the ROS probe-2 localises.
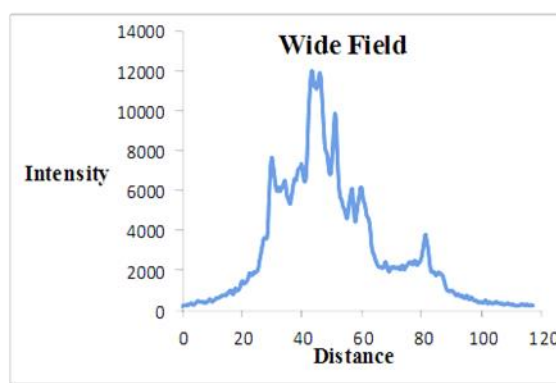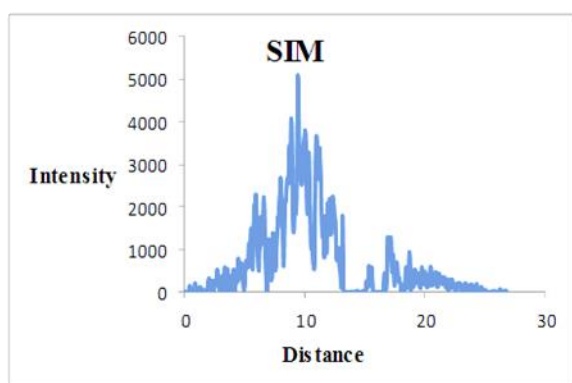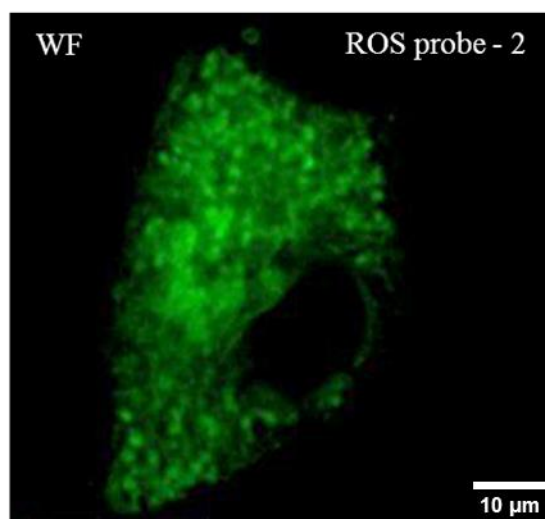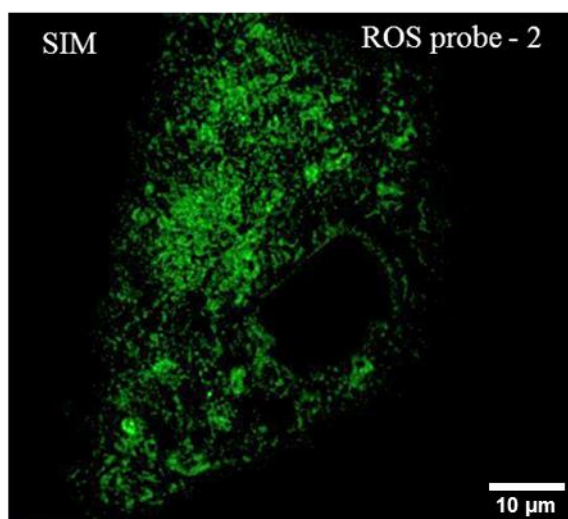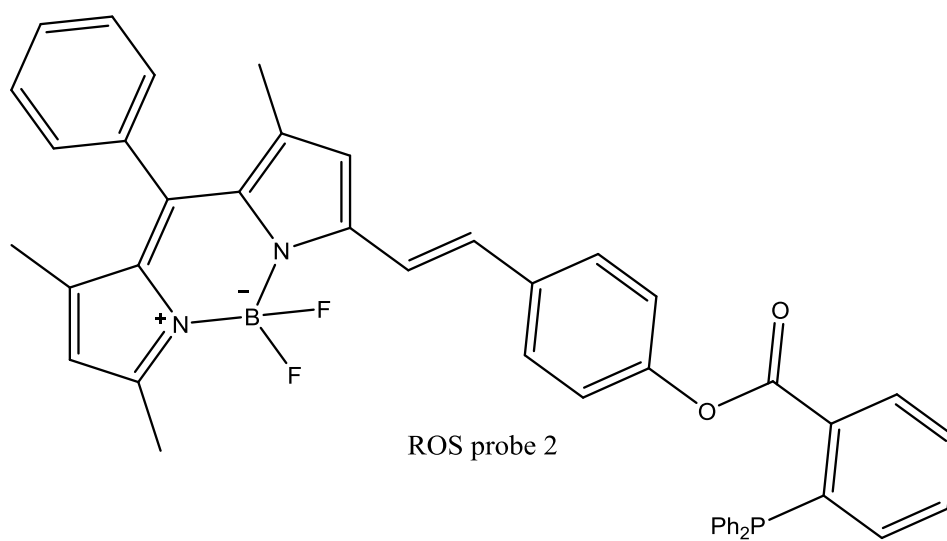
ROS probe 2

Figure 3.13 Top row: Comparative SIM and Widefield images showing HNO detection by ROS probe-2 in RAW Macrophages. **Bottom row:** Corresponding Intensity profiles of SIM and Widefield showing resolution improvement.

3.6.2 Concentration dependent HNO detection (HNO external addition)

The detection of different levels of HNO is an attractive characteristic of a probe. When compared to other HNO detecting probes in the literature as reported by Tan *et al*[157], Sunwoo *et al*[148], Wrobel *et al*[139], the potential novelty of ROS probe-2 lies in detecting HNO probe in cells at resolution higher compared to those reported previously. RAW Macrophages was incubated with ROS probe-2 (1 μM) for 15 min at 37 °C (5% CO_2) displayed no intracellular fluorescence. In contrast, cells incubated with ROS probe-2 (1 μM) and then treated with Angeli's salt at concentration ranging from 0 μM to 50 μM for 30 min – a procedure known to generate HNO - showed strong intracellular fluorescence. These results confirm that ROS probe-2 is sufficiently bright and stable to be used as an imaging reagent for the detection of HNO through SIM imaging.
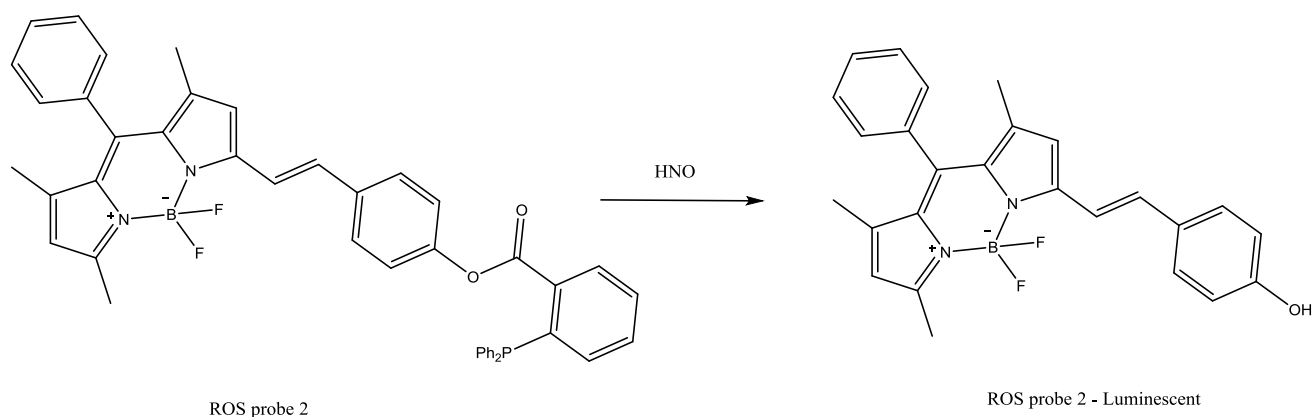
Figure 3.14 Reaction scheme depicting HNO detection of ROS probe-2

132

As shown in Figure 3.15, ROS probe-2 does detect different levels of HNO. This conclusion is well supported by 3D-Surface plots generated from the SIM images using FIJI software.
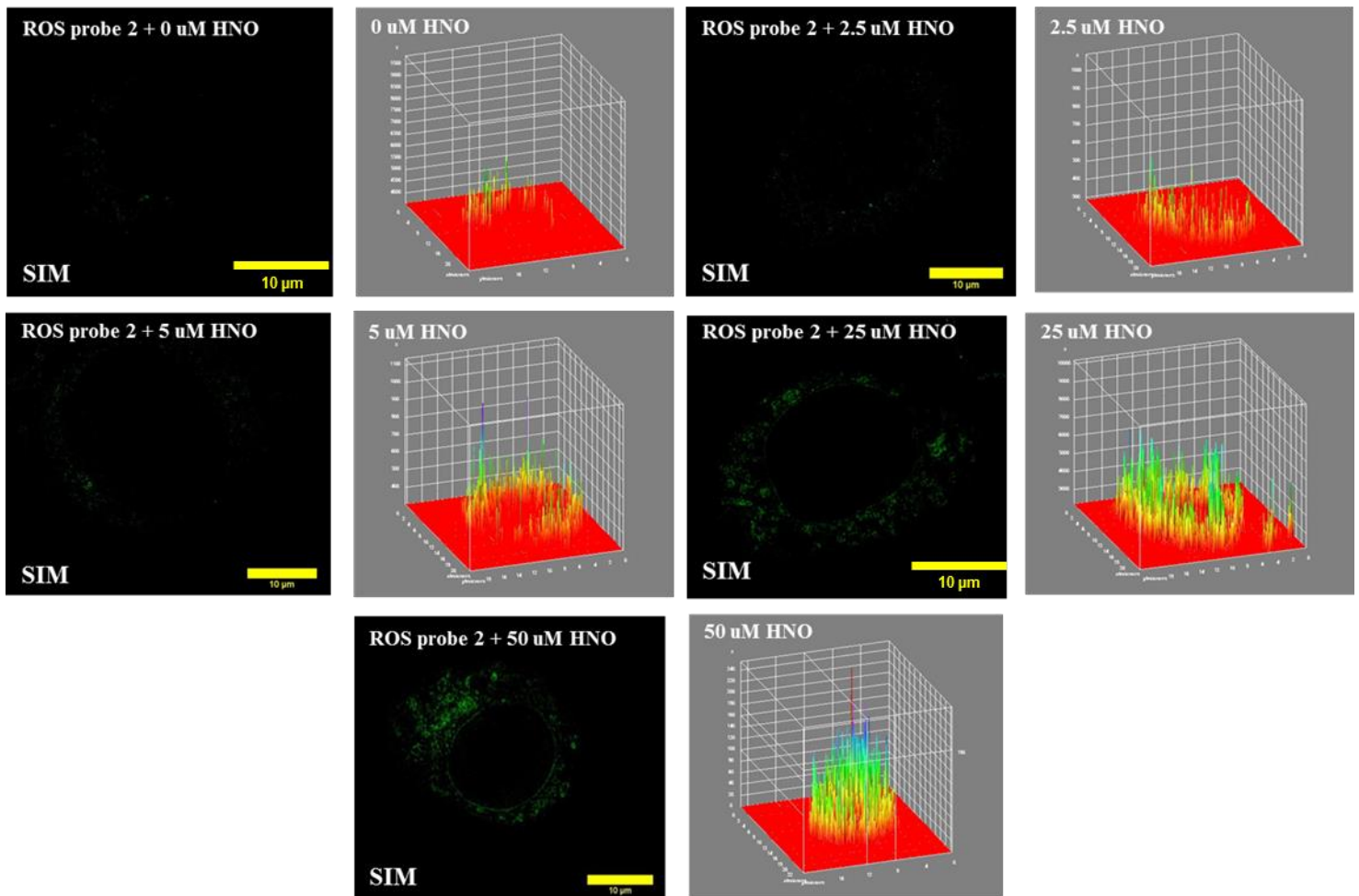
Figure 3.15 SIM Images showing ROS probe-2 and their corresponding 3D-surface plots showing detection of externally added HNO at diverse concentrations in RAW Macrophages. **Scale bar:** 10 μm

3.6.3 Intracellular localization of ROS probe-2 and specific HNO detection

Nitoxyl detection is heavily dependent on the intracellular distribution exhibited by ROS probe-2, as it will only detect HNO generated in regions where it is localised. Therefore colocalization experiments were carried out to investigate where the probe localises. These experiments 2 were initially carried out using ER-Tracker Green. ER Tracker Green is not so photostabl compared to ROS probe-2, which does not photobleach when exposed to SIM conditions. The colocalization experiment was carried out by incubating the ROS probe-2 (1 µM) and Angeli's salt (20 µM) for 30 minutes each after initially incubating the RAW cells with ER-Tracker Green (1 µM) for 25 minutes. The cellular uptake of both the probes were carried out in live cells and then the cells were fixed with 4% PFA and mounted and initially inspected for proper cell morphology by using light microscope and then imaged by using SIM and widefield fluorescence microscopy. These studies revealed that emission from ROS probe-2 treated cells in the presence of HNO showed a very high Pearson's colocalization coefficient with ER-Tracker Green.
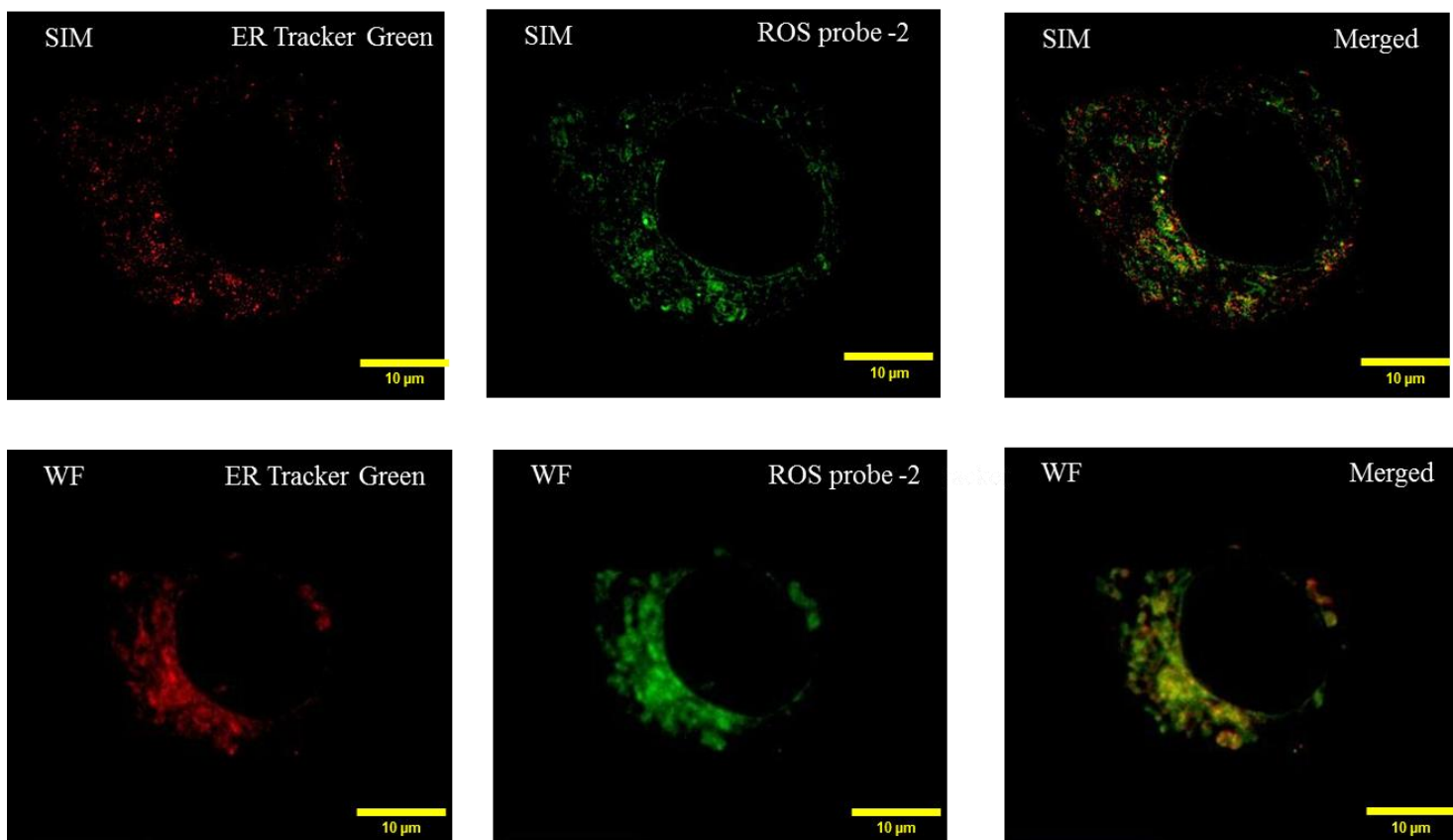
Figure 3.16 Top row (Left to Right): SIM images of ER Tracker Green, ROS probe-2 in presence of HNO (Individual channel), Colocalized image of ER Tracker Green and ROS probe-2. **Bottom row (Left to Right):** Corresponding Widefield images showing ER Tracker Green, ROS probe-2 (Individual channel) in presence of HNO, Colocalized images of ER Tracker Green and ROS probe-2. **Scale bar**: 10 μm

Pearson's Coefficient	Mander's Coeffcient (M1)	Mander's Coeffcient (M2)	Treshold ER Channel (500 – 520 nm)	Treshold ROS probe-2 Channel (570 – 620 nm)	Overlap Coefficient
0.936	0.973	0.986	1000	3200	0.979

Table 3.4 Pearson's coefficient: Colocalization experiments of ROS probe-2 (In presence of HNO) with ER Tracker Green

As explained earlier, ER Tracker Green photobleaches when exposed to SIM conditions, therefore widefield microscopy images were acquired to confirm the localization of ROS probe-2 in the ER. Pearson's method of correlation - which is the most reliable method to establish colocalization based on the pixel by pixel super imposition between the two channels under consideration - gave a very high value of 0.936 showing the colocalization between ROS probe-2 and ER Tracker Green. ROS probe-2 uniquely provides a method of mapping HNO in the endoplasmic reticulum in RAW Macrophages.

3.6.4 Dual colour SIM imaging using ROS probe-2

As mentioned in previous sections, multicolour imaging of ROS probes can provide vital information by helping to track two simultaneous biological processes occuring within cells. The idea of a dual colour or multicolour imaging probe becomes more interesting if all the probes involved could withstand super resolution microscopy conditions. Since it is known that HNO generation in remote cell compartments can affect processes within the nucleus as shown by Arthaut *et al*[158], as an initial proof of concept, we chose to use the common nuclear stain Hoechst 33342 (that groove-binds to, and visualises, chromatin DNA) as a complimentary probe in dual colour Super resolution (SIM) imaging so as to simultaneously visualise HNO in the ER and Hoechst in the nucleus. The microscopy experiments demonstrates that SIM images of both HNO generation in the ER and chromatin morphology can be accomplished through this combination of ROS probe-2 and Hoechst 33342 staining. This provides a route to future studies in which the effects of a specific ROS generation within the ER has on the structure and function of the nucleus can be simultaneously probed.
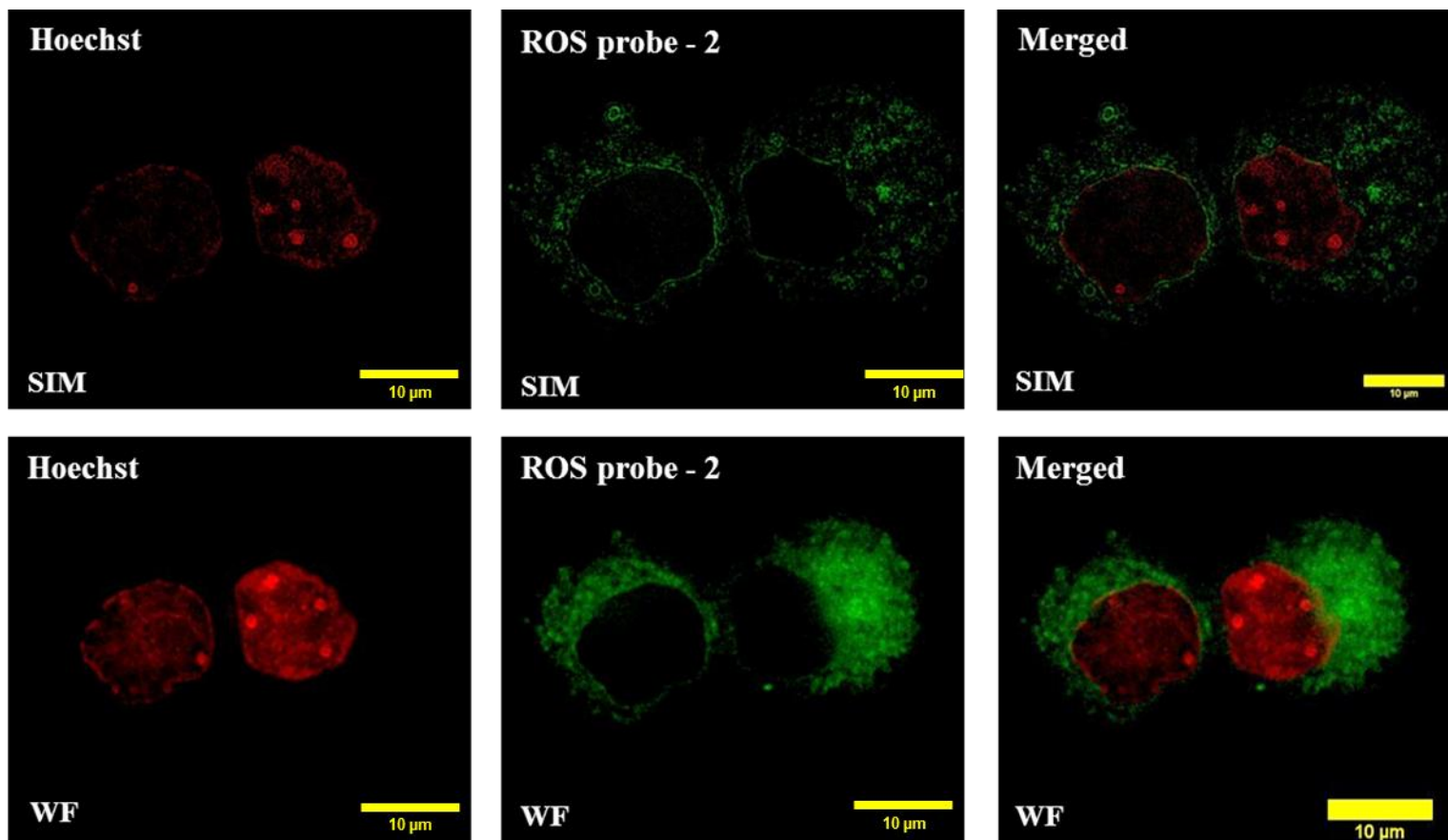
Figure 3.17 Top row (Left to Right): SIM Images of Hoechst and ROS probe-2 in presence of HNO (Individual channel), Dual colour image comprising ROS probe-2 and Hoechst. **Bottom row (Left to Right):** Widefield images of the same for comparision to explain improvement in resolution over it when compared to SIM. **Scale bar**: 10 µm

3.7 MITOCHONDRIA TARGETING ORGANIC PEPTIDE PROBE

In addition to intracellular ROS detecting probes which were examined for suitability as SIM probes, an extremely photostable peptide-based probe, Organic peptide probe-A, was studied to explore its cellular/biological application potential. Since mitochondria are key regulators for much cellular behaviour, imaging to probe the morphology and function of mitochondria is crucial in probing cell function. Furthermore, since mitochondria are key regulators for the intrinsic pathways of cell apoptosis, mitochondria specific reagents for simultaneously targeting, imaging and treatment functions are also of interest as theranostics. Therefore, fluorescent probes are needed to dissect the various details of cell pathways which are directly or indirectly related to mitochondrial function[149,165]. The probe discussed herein is designed to just specifically target mitochondria through a peptide moiety attached to an organic probe moiety.

Traditional fluorescent dyes (like Rhodamine, JC1 dye, Mito Fluor, MitoTracker) have all been used successfully for *in cellulo* imaging of mitochondria, but these all suffer from high photobleaching rates when used in high-intensity cell imaging studies, thus making their use in long-term experiments and many super-resolution techniques unfeasible.

The targeting of probe molecules is greatly improved by conjugation to biomolecules which possess the affinity to bind to specific intracellular organelle. Through conjugating a targeting peptide to a small molecule luminophore such as BODIPY, target oriented probes which localise within specific organelles can be generated. By combining a photostable, high quantum yield luminophore with the target specificity of selected peptides, photostable probes that can be used to study a variety of biological mechanisms within specific organelles over extended time periods or at higher resolutions will be produced.

The potential of this approach, using a prototype photostable dye previously synthesized by Dr. Sumit Kumar Pramanik in NCL, India, was investigated through Structured illumination microscopy. The probe consisted of a BODIPY dye moiety attached to a mitochondrial targeting peptide. As SIM is a widefield microscopy-based technique involving reconstruction of the acquired RAW images, the SIM reconstruction process employs lengthy scanning time, high laser power and loss of cumulative luminescence, the requirements of a stable and bright dye is essential.
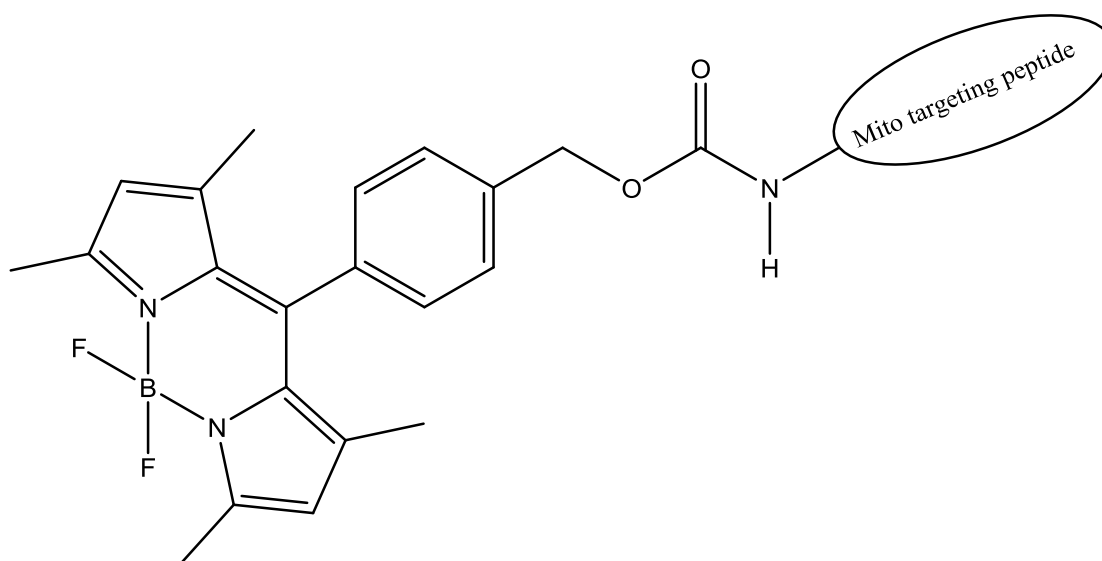
Figure 3.18 Structure of the Mito targeting Organic peptide probe-A, The structural sequence of the Mito targeting peptide = MALLRGVFIVAAKRTPFGAYGC

As shown by Gao *et al*[152], BODIPY based dyes possess sharp fluorescence emission, excellent photostability, high extinction coefficient. When compared to conventional trackers like Mito Tracker Green, BODIPY probes possess better photostability, and their structures/targeting can be modulated in conjugation with target-specific biomolecules like a peptide with specific sequence. The exceptional brightness exhibited by the BODIPY moiety compared to other standard organic probes such as those reported by Jung *et al*[149], enables it to be employed as a super resolution microscopy. Mitochondria targeting peptides when conjugated with BODIPY probes could serve as an ideal vector to deliver to mitochondria, so that SIM and 3D-SIM images obtained using such a SR probe could help in the better understanding of mitochondrial function and dynamics[168].

The compatibility of the mitochondrial targeting organic peptide probe-A to SIM conditions was initially assessed in RAW macrophages. A comparison between widefield and structured illumination microscopy is shown in Figure 3.19. The probe was photostable and it did not bleach out and improvement of resolution by using SIM is shown in Figure 3.19.
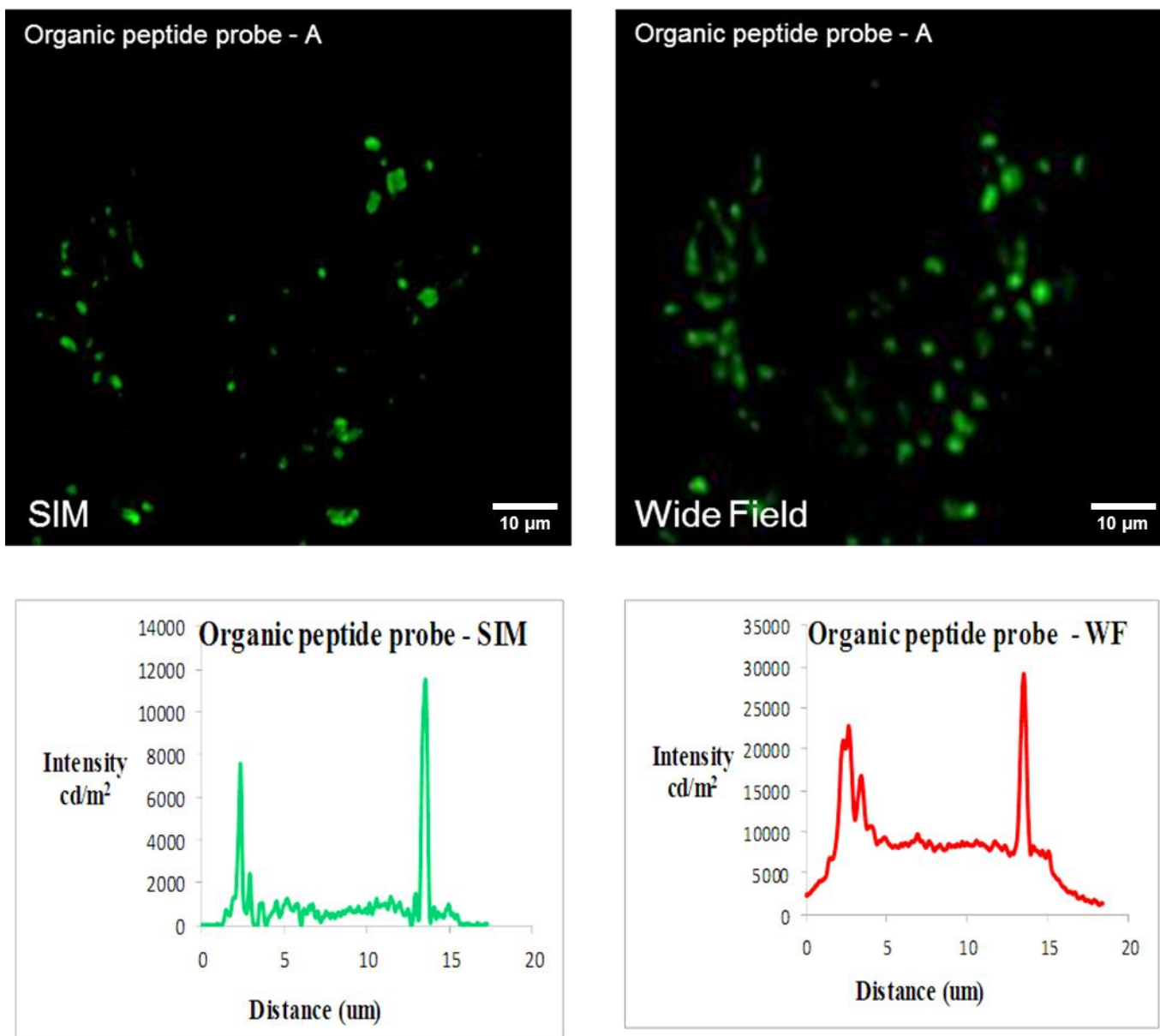
Figure 3.19 Top: Comparative SIM and Widefield images showing resolution improvement of Cellular uptake of Organic peptide probe-A in RAW Macrophages. **Bottom:** Corresponding Intensity profiles for SIM and Widefield

Organic peptide probe-A probe needed to be tested at diverse concentrations to determine the optimal concentration of the probe required to achieve the best super resolution microscopy images. Signal saturation and signal bleaching both contribute to the generation of artefacts during conventional imaging and the presence of artefacts in SIM images will hamper the generation of high quality 3D-SIM images.

Experiments reveal that, whilst considerable *in cellulo* luminescence was observed even for concentrations as low as 10 nM, striking SIM images were obtained for concentration range of 25 nM to 100 nM – Figure 3.20. It seems that 50 nM is the optimal concentration in which high quality images were obtained and hence this concentration would be ideal in obtaining perfect SIM and 3D-SIM images.
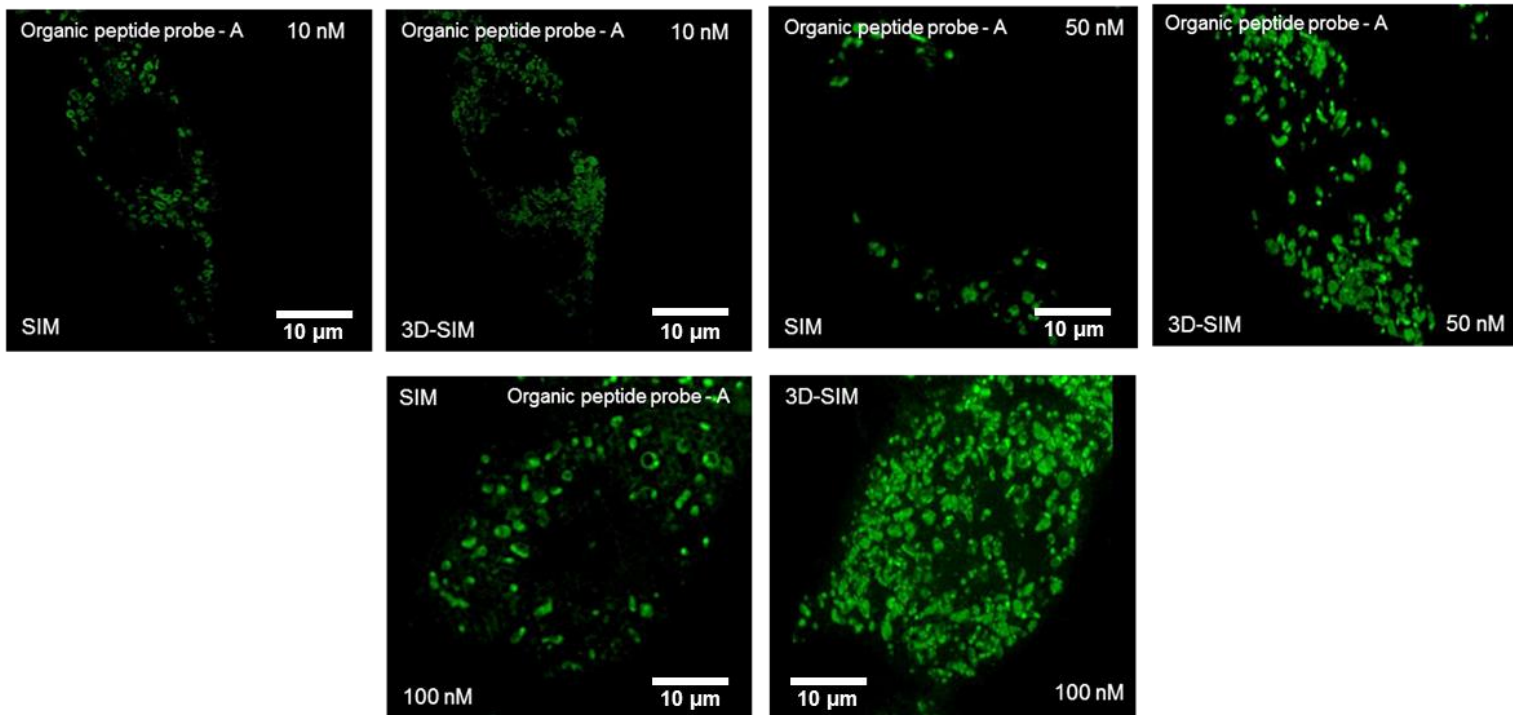
Figure 3.20 SIM and 3D-SIM images showing cellular uptake of organic peptide probe at diverse concentration in RAW Macrophages

3.7.1 Colocalization studies with Mito targeting peptide probe-A

Organic peptide probe-A was designed to target mitochondria specifically as the peptide moiety attached to the probe is known to conjugate with mitochondrial membranes. To confirm this hypothesis colocalisation experiments were carried out.

As Pearson's coefficient relies on the superimposability of pixels obtained from two different channels under consideration and does not exclude blank channels it was essential to employ widefield microscopy for the colocalization experiments. Localization experiments were carried out using Mito Tracker Deep Red and Lyso Tracker Deep Red. As outlined in previous studies, these trackers exhibit good stability and do not bleach out on prolonged exposure to high laser power. Organic peptide probe-A showed emission in the Alexa fluor 568 channel (570 to 620 nm) and Mito and Lyso Tracker Deep Red showed emission in the Deep Red channel (> 670 nm), so there is very little or no crosstalk between channels indicating that the colocalization experiments performed is free from spectral interference or overlap. The experiment with Mito tracker Deep Red gave clear evidence of localization of organic peptide probe-A to the mitochondria as shown in he widefield images of Figure 3.21. Intensity profile diagrams, generated by the offline software FIJI, shows characteristic overlapping among signals indicating colocalization between the two channels. Furthermore, co-localization with Mito Tracker Deep Red was confirmed by a Pearson's coefficient value of 0.96.
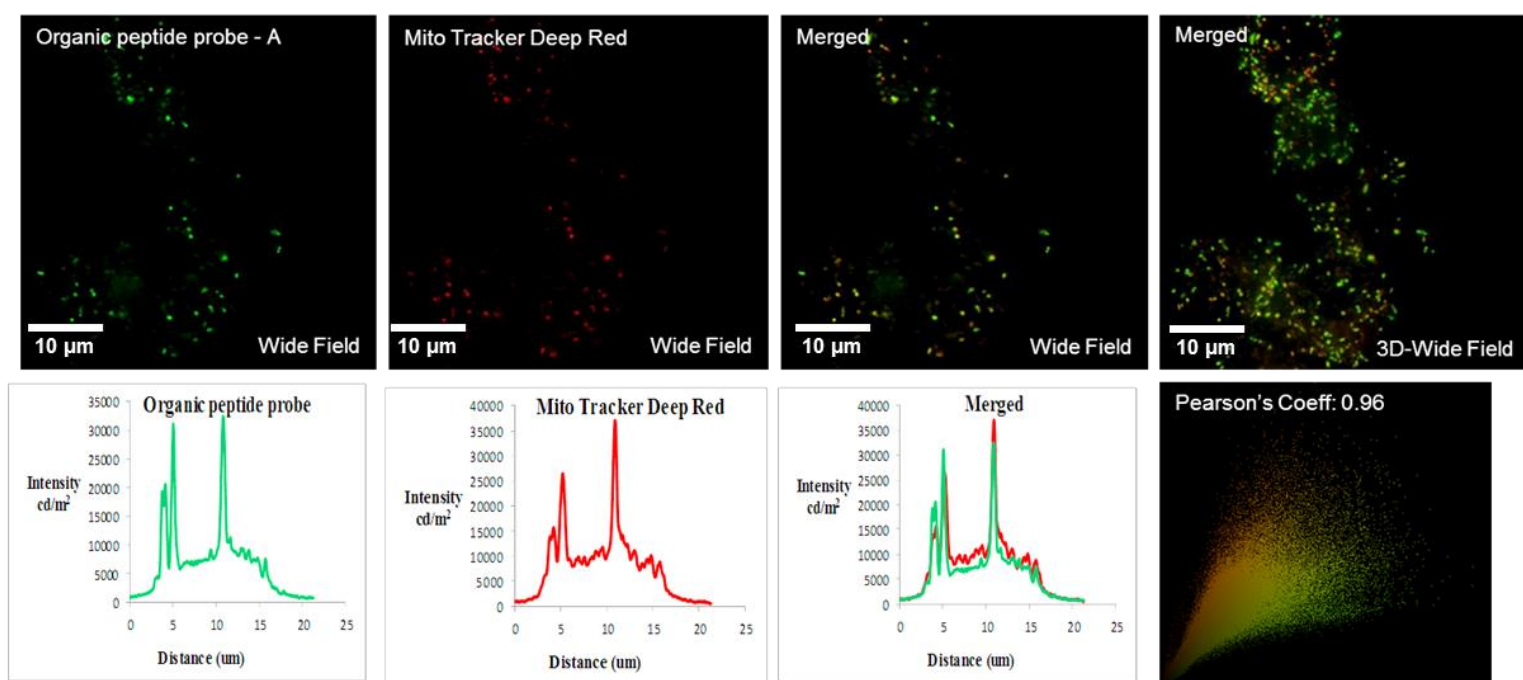
Figure 3.21 Widefield images of organic peptide probe-A and Mito Tracker Deep Red (Individual channel), Colocalized image of organic peptide probe-A and Mito Tracker Deep Red, 3D Widefield projection of the same. **Bottom row:** Intensity profile diagrams for individual and combined channels, Pearson's coefficient for the same. The experiment was carried out on RAW Macrophages

On the other hand, when the colocalization experiments were carried out using Lyso Tracker Deep Red, they yielded widefield images which showed minimum colocalization between the two channels as illustrated by the widefield images, and intensity profile diagrams shown in Figure 3.22. The intensity profile diagram for the merged widefield image showed that the peaks obtained from the lyso tracker deep red do not match with that of the organic peptide probe-A and the Pearson's coefficient gave a very low value indicating the lack of colocalization between two channels. Hence from both colocalization experiments it could be concluded that organic peptide probe-A is localized over mitochondria.
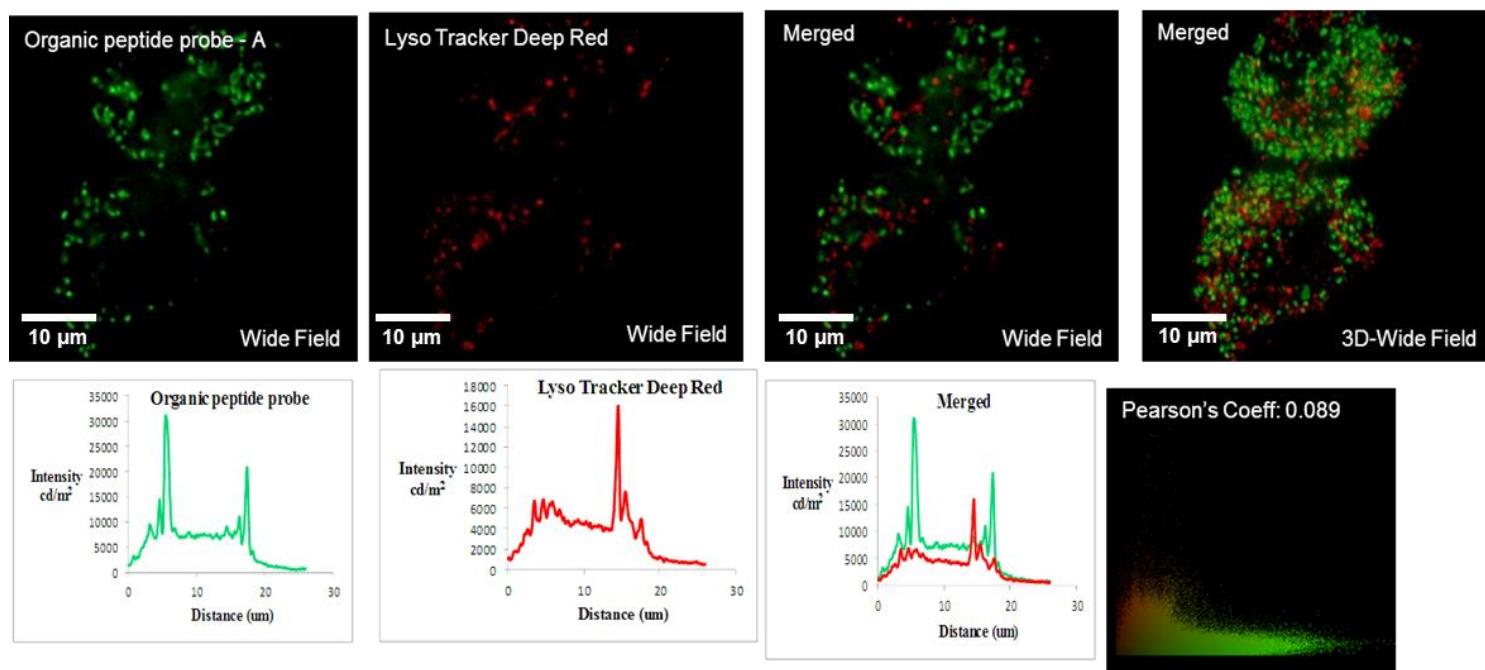
Figure 3.22 Top row: Widefield images of Organic peptide probe-A and Lyso Tracker Deep Red (Individual channel), Colocalized image of organic peptide probe-A and Lyso Tracker Deep Red, 3D widefield projection of the same. **Bottom row:** Intensity profile diagrams for individual and combined channels, Pearson's coefficient for the same. The experiment was carried out on RAW Macrophages

3.7.2 Dual colour imaging for Peptide probe-A

From the previous sections of this chapter it was shown that organic peptide probe-A demonstrated organelle specific SR imaging exclusively localizing on mitochondria. As the probe exhibits a large Stokes shift there is always a possibility of employing a complimentary probe with distinct spectral characteristics to carry out cellular investigation pertaining to another organelle simultaneously. Indeed, Pan *et al*[165] have already demonstrated a mitochondrial targeting cyanine dye, which could be employed as a dual colour probe.

In this work we sought to demonstrate that dual colour SR microscopy could be carried out using our peptide functionalized organic probe. The probe shows emission in the red region (580 to 620 nm) when it is excited at 568 nm and it was used as a dual colour probe along with a Hoechst dye, which has distinct spectral characteristics when compared to organic peptide probe-A. The nuclear imaging probe Hoechst 33342 exclusively images the nucleus while organic peptide probe-A specifically images the mitochondria as shown in Figure 3.23.
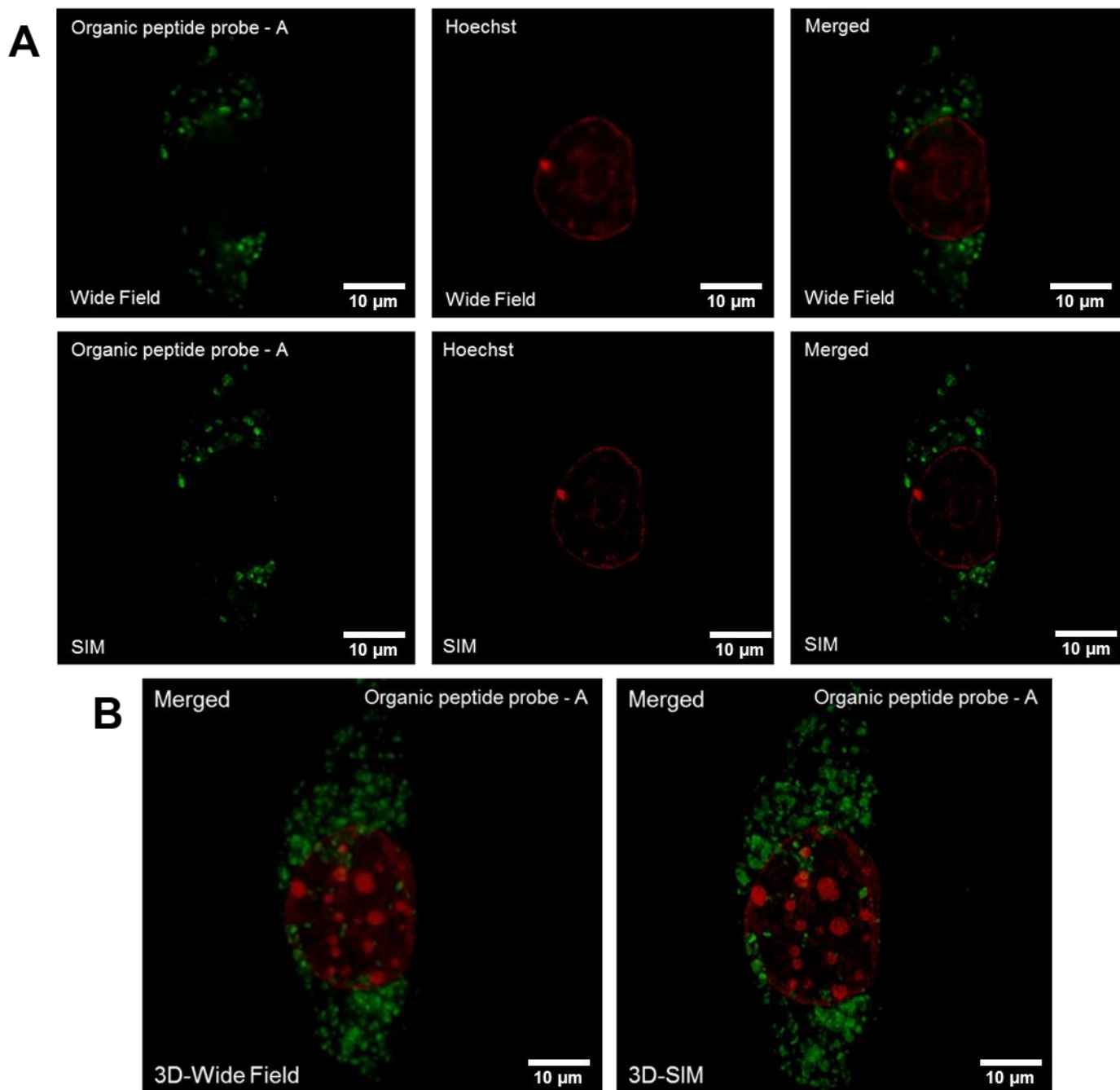
Figure 3.23 (A) Top row (Left to Right): Widefield images of organic peptide probe-A and Hoechst (Individual channel), Dual colour Image of organic peptide probe-A and Hoechst combined. **Bottom row (Left to Right):** SIM images of Organic peptide probe-A and Hoechst (Individual channel), Dual colour Image of Organic peptide probe-A and Hoechst combined. **(B)** Compartive 3D-WF and 3D-SIM of the Dual colour image of the same area. The experiment was carried out on RAW Macrophages

3.8 SUMMARY

ROS/RNS detecting probes and a mitochondria specific probe were optimised as super resolution microscopy probes. The ROS/RNS probes, which were optimised for SIM, gave information about the nature of intracellular localisation, spread of signals across multiple cellular compartments, generation of signals from particular cellular compartments and specific organelles, whilst the mitochondria probe showed clear localization in its target organelle. Further work would involve utilising similar probes targeting different organelles or other reactive species which form the basis of biological disorders with the help of superior microscopy techniques.

4.0 IN CELL OPTICAL MICROSCOPY STUDIES ON NANOMATERIALS

4.1 NANOCAPSULES AS CELLULAR DELIVERY VECTORS

Polymeric nanocapsules have enormous potential within various domains of nanomedicine such as drug delivery, imaging and sensing. Nanocapsules are of interest for biomedical science because they can be used for the controlled release of drugs and specific organelle targeting. Nanocapsules offer unlimited opportunities for the encapsulation of useful compounds, ranging from hydrophobic/hydrophilic drugs, small RNAs, inorganic nanoparticles and imaging/contrast agents. In general, nanocapsule morphology allows a large aqueous core to polymer ratio, facilitating encapsulation of a large payload, which is otherwise not possible for their bulk particle counterparts. To use nanocapsules as drug delivery vehicles, they should be biocompatible, able to protect payload from external environment (*in vivo* degradation), possess site specificity, and enable controlled release of the payload. If they meet these criteria, nanocapsules with tailor-made properties will make a significant contribution to the development of advanced drug delivery systems[171,172,173].

Polymeric nanocapsules can be prepared by using numerous methods such as layer-by-layer assembly, double emulsion technology, nanoprecipitation, coacervation, and (micro-, mini-) emulsion polymerisation techniques[174,175]. Among these different heterophase polymerisation techniques, inverse mini-emulsion has an almost default position, as it allows for effective encapsulation of both hydrophobic as well as hydrophilic compounds – Figure 4.1. Recent advanced technology has been utilized to formulate nanocapsules that preserve the inherent photophysical properties of their components[181].

As the nanocapsules discussed in this section has been generated using the emulsion polymerisation technique an outline of this method is provided in this section. Emulsion polymerization involves mixing homogenous solutions at room temperature. The resulting mini-emulsion is maintained under anhydrous conditions at slightly elevated temperature. Over time this results in the formation of core shells by polymerisation. The particle size, distribution and the polydispersity are all controllable[184]. Multi-potent nanocarriers of excellent homogeneity in size, that can be drug-loaded, have been successfully prepared by mini-emulsion procedures combined with many different reactions, including click chemistry, polycondensation, radical polymerization and oxidative polymerization.

147
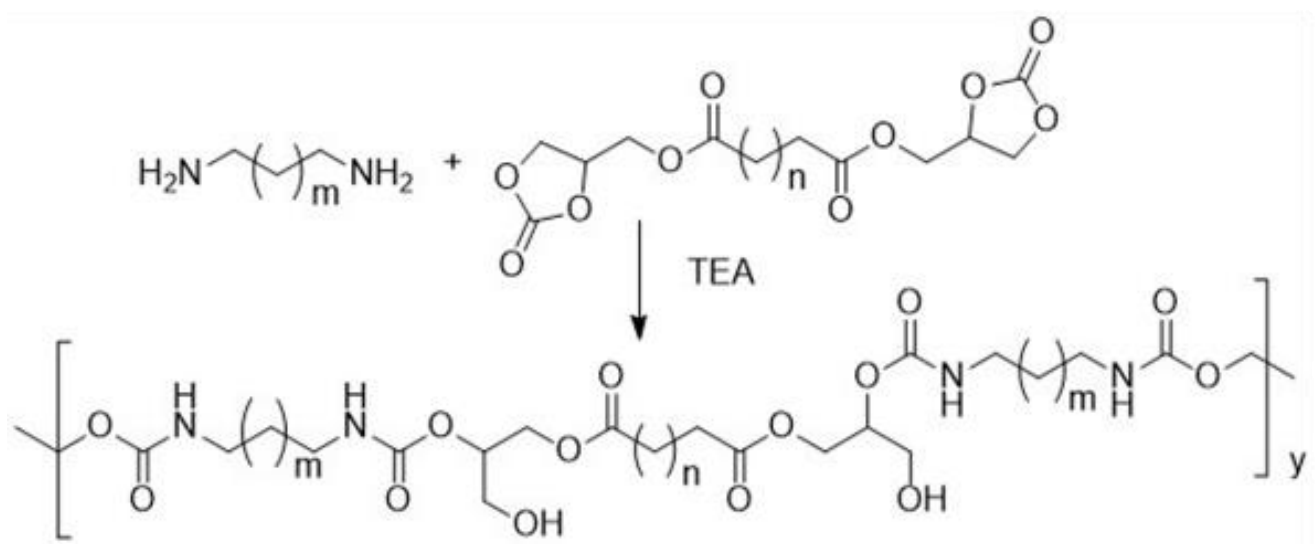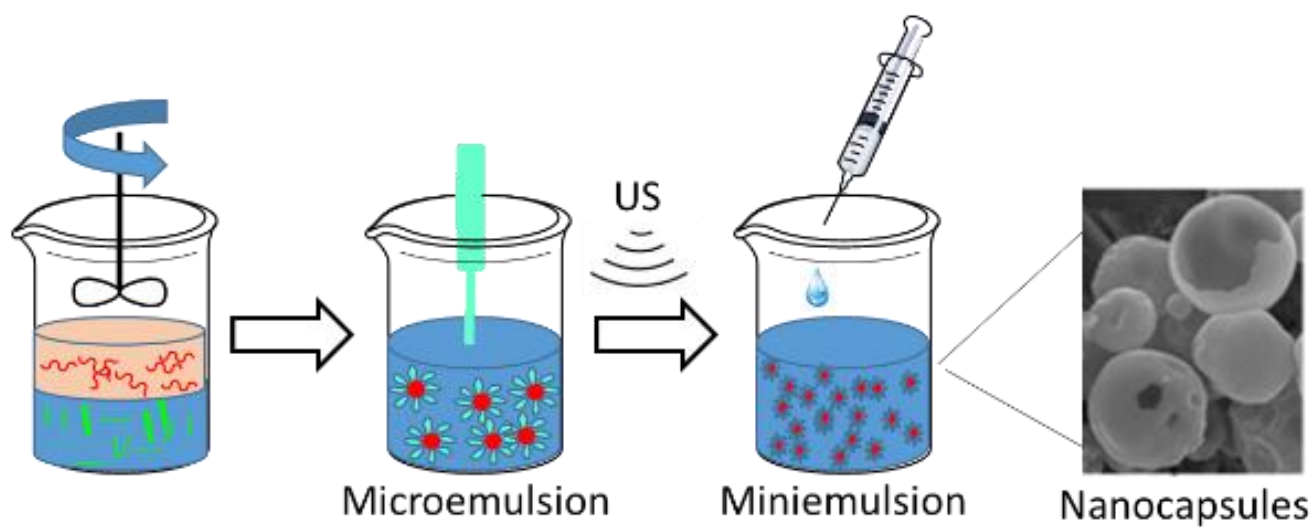
Figure 4.1 Inverse mini-emulsion technique to synthesize nanocapsules

The use of emission-based microscopy, offers huge opportunities for investigating the complex interactions between such nanomaterials and biological entities[131,132]. Furthermore, it allows the behaviour of engineered nanocapsules in complex biological environments to be monitored. Working in the NCL, Pune India, Dr. Sumit Kumar Pramanik employed the inverse mini-emulsion approach to produce nanocapsules containing non-isocyanate polyurethane linkages. Most encapsulation techniques employ either isocyanate in solvent or bulk to construct the core shell. Payloads are then encapsulated into this hydrophilic core shell[183]. Encapsulation delays the release of the payloads[189], which in effect is one of the most important criterion required for cellular drug delivery technologies. The nanocapsules utilized in this project have been constructed by employing environmental friendly techniques. A isocyanate-free, inverse mini emulsion technique was employed to generate nanocapsules with uniform particle size. In this initial study, hydrophilic luminescent dyes (rhodamine green or rhodamine 6G) were used as a model encapsulation guest, so that the cellular uptake of the nanocapsules could be directly monitored by microscopy. The details of loading and size of the nanocapsules, which were determined in India, are summarized in Table 4.1. All of the following optical microscopy studies were carried out in Sheffield.

Red and Yellow nanocapsules:

The inverse mini-emulsion technique was used to produce nanocapsules containing urethane linkages as shown in Figure 4.1, through an interfacial poly-addition reaction between stoichiometric amounts of amine (1,8-diaminooctane) and carbonate (adipate biscarbonate or sebacate biscarbonate) as the respective bi-functional monomers. In this approach, NaCl solution was used to build up the osmotic pressure of the droplets in the continuous hydrophobic phase. Rhodamine green was enacapsulated in the hydrophilic core leading to yellow nanocapsules (YNC) and rhodamine 6G dye was encapsulated in the hydrophilic core leading to red nanocapsules (RNC). Hypermer B246, a polymeric surfactant with outstanding dispersion and emulsion stability properties was used during the encapsulation. The luminescence from the nanocapsules is predominantly generated from the payloads; in other words, the spectral characteristics of the nanocapsules changes only because of these changes in payload. The uniform particle size and surface area of the nanocapsules are important characteristics in efficient encapsulation. The photophysical properties and stability of the loaded nanocapsules guarantees that the in-cell emission expected on controlled release of the payloads can be exploited in bio-imaging.

Capsules	Dispersed phase	Additive phase	Size/PDI (org. phase)	Size/PDI (aq. phase)
YNC	0.57 mmol 1,8-diaminooctane, rhodamine green	0.57 mmol Adipate bis carbonate, TEA	163nm/0.07	241nm/0.19
RNC	0.57 mmol 1,8-diaminooctane, rhodamine 6G	0.57 mmol Sebacate bis Carbonate, TEA	179nm/0.06	248nm/0.21

Table 4.1: Details of the Nanocapsules – Loading and Dimensions

4.2 SIM IMAGING OF NOVEL NANOCAPSULES CARRYING PAY LOADS

4.2.1 CONCENTRATION DEPENDENT CELLULAR UPTAKE OF NANOCAPSULE PAYLOADS

RED NANOCAPSULES (RNC):

Since red nanocapsules encapsulate Rhodamine 6G as the payload, their luminescence is observed in the RFP or Alexa Fluor 568 region in the range of 570 to 600 nm. The brightness of the red nanocapsules meant they are compatible with super resolution SIM microscopy, particularly as they display continuous emission with minimum photobleaching. Optimising the red nanocapsules as SIM probes required a number of parameters to be explored. These included optimal concentration of probe, the identification of suitable cell lines, appropriate laser power, scanning time, size of optical sections to match with the characteristics of the probe.

Concentration dependent experiments are particularly important in SIM as image reconstruction in this technique can produce loss of emission intensity and brightness. Therefore, the choice of the right drug/dye concentration becomes crucial in obtaining high quality images. Using RAW macrophages the concentration dependent uptake of the RNC were investigated. Widefield and SIM images, carried out using OMX-SIM at the University of Sheffield, are shown in Figure 4.2. These images indicate that the RNCs seem to be mainly localised in the cytosol region of RAW Macrophages. The incubation time of 12 hours seemed to suffice for cellular internalisation but a time dependent experiment was also carried out, *vide infra*. Loss of emission intensity happens during SIM reconstruction as this technique rejects non-coherent emission signals, whilst excess brightness can lead to signal saturation generating optical artefacts and blurring leading to loss of super resolution and valuable information. Therefore it is essential to find a probe concentration which compliments the image acquisition parameters. Near perfect SIM and 3D-SIM images were obtained at 15 µg/mL uptake. The sequence of SIM and its corresponding 3D-SIM images, acquired for different concentration, shown in Figure 4.2 (A) confirm this.
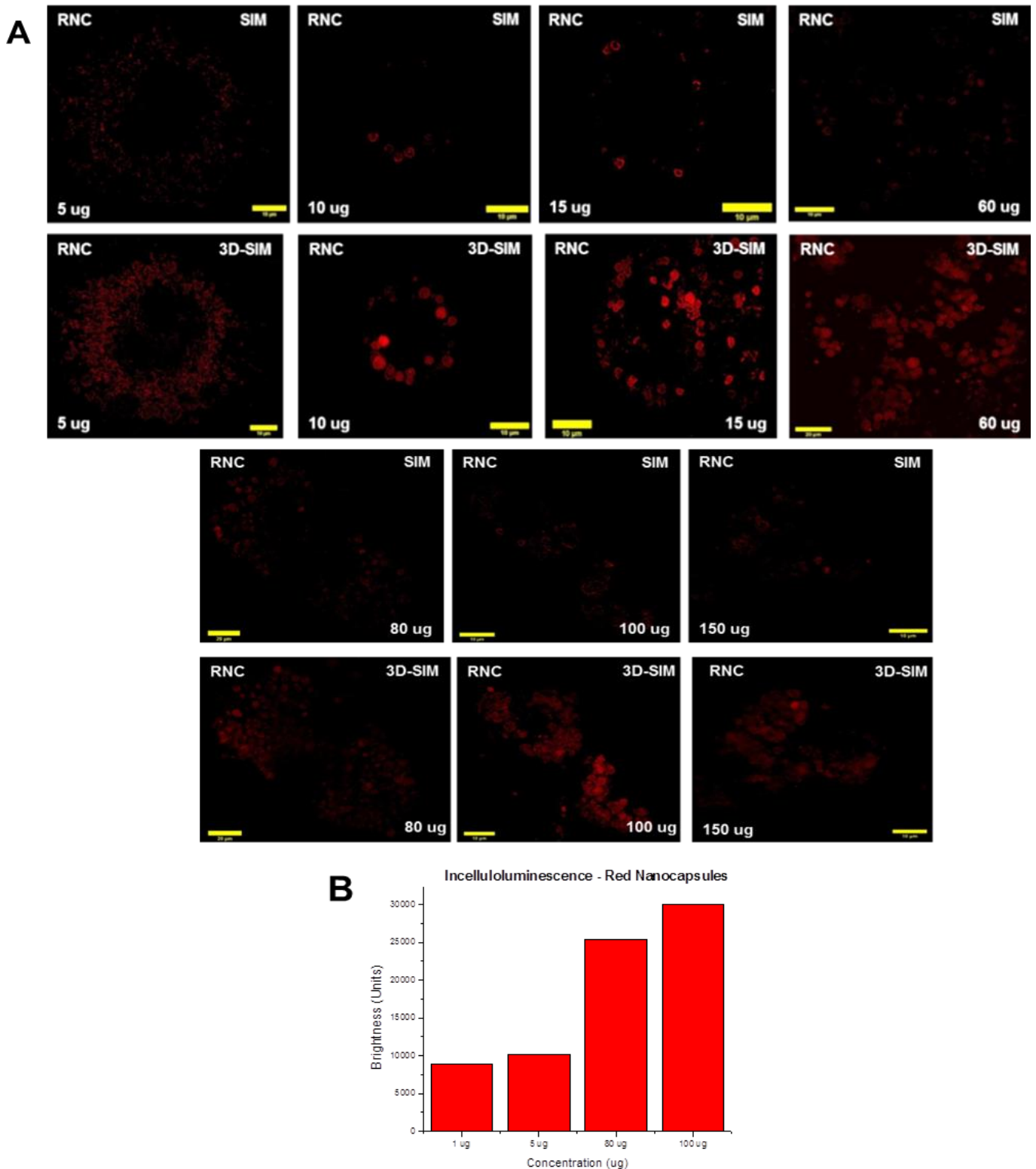
Figure 4.2 (A) Top row (Left to Right): SIM Images of Red nanocapsules (RNC) cellular uptake in RAW Macrophages at diverse concentration, **Bottom row (Left to Right):** 3D-SIM of the same. **(B)** Bar chart showing extent of Incellulo luminescence at diverse RNC concentration. **Scale bar**: 10 μm

4.2.2 YELLOW NANOCAPSULES (YNC):

Yellow nanocapsules with Rhodamine green as payloads were expected to show emission in the GFP or FITC channel. As was mentioned in the previous section, determination of optimum nanocapusles or drug concentration is one of the essential criteria in optimising the nanocapsules for SIM. The concentration dependent uptake of the yellow nanocapsules (YNC) was carried out in a similar way as was in the case of red nanocapsules. Again the extent of cellular uptake in RAW macrophages at different concentration of YNC as shown in Figure 4.3 was determined using widefield and SIM and a nanocapsule treatment of 15 µg/mL for intracellular emission was confirmed to be optimal. SIM and the corresponding 3D-SIM images obtained at different concentration of yellow nanocapsules uptake, as shown in Figure 4.3 (A), indicates that near perfect SIM and 3D-SIM - showing minimum or no artefacts - can be obtained at 15 µg/mL which confirms the applicability of the yellow nanocapsules with SIM.
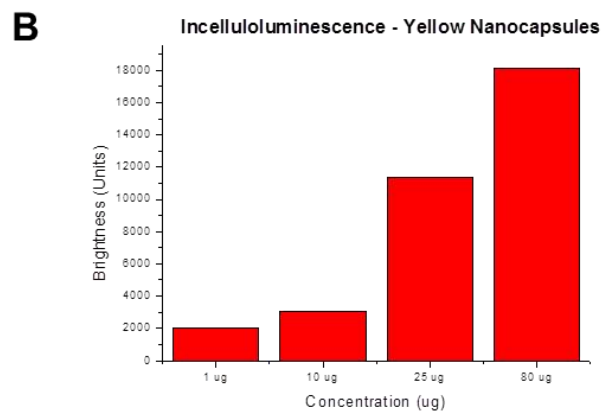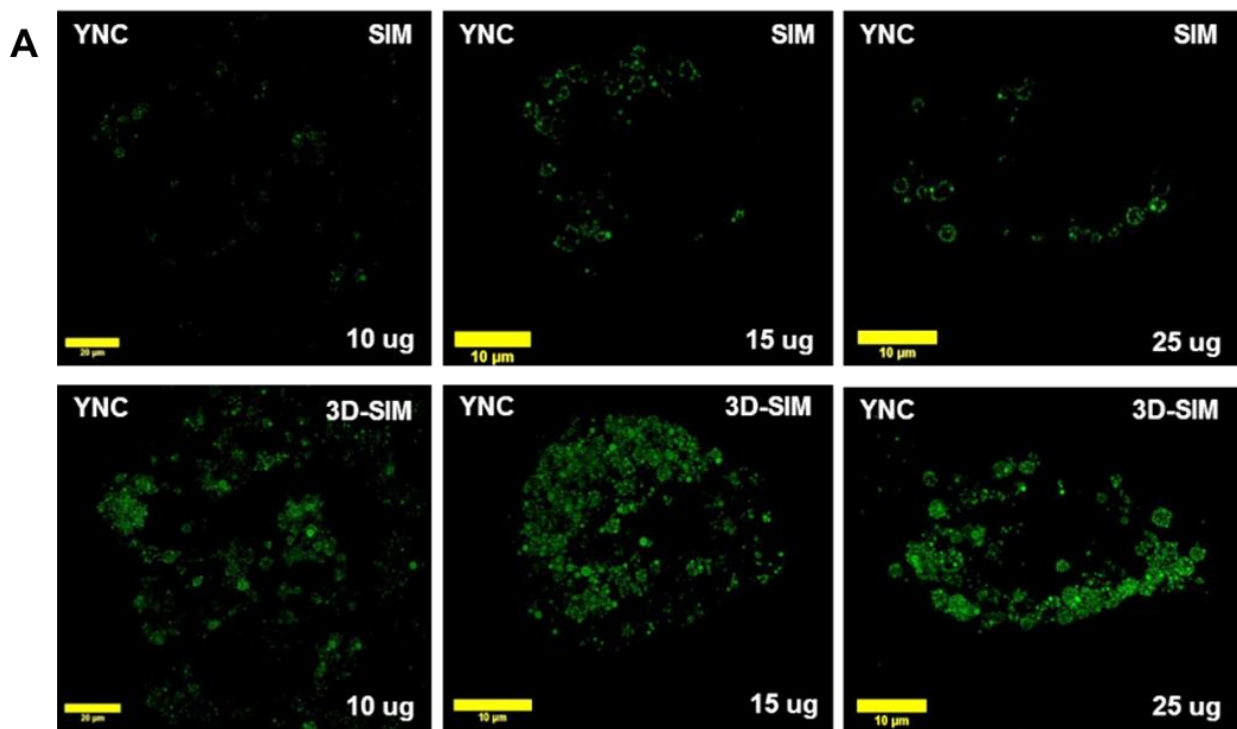
Figure 4.3 (A) Top row (Left to Right): SIM Images of yellow nanocapsules (YNC) cellular uptake in RAW Macrophages at diverse concentration, **Bottom row (Left to Right):** 3D-SIM of the same. **(B)** Bar chart showing extent of Incellulo luminescence at diverse YNC concentration. **Scale bar**: 10 μm

4.2.3 Intracellular colocalisation of nanocapsules

Nanocapsules are mainly applied in bio-imaging application and theranostics because of their dual applicability towards imaging and drug delivery in cells, which in future could be extended to *in vivo* applications. Specific cellular organelle targeting using nanocapsules with the aid of super-resolution microscopy as an imaging platform has been rare because of a variety of limitations exhibited by nanomaterials reported by researchers such as Yu *et al*[183] and Guo *et al*[182]. The limitations of applying nanocapsules as a dependable cellular imaging probe include: the non-cell friendly reagents required to prepare hydrophilic cores (as seen in the work carried out by Yu *et al*[183], lack of specificity towards target cells, poor uptake, and poor stability. Although some reports like Guo *et al*[182] show that the nanocapsules prepared using environmental friendly methods can target cancer cells in particular, these have not been reported to target specific intracellular organelle. Although the lack of super resolution microscopy studies involving nanocapsules was one of the motivations behind this study, its main objective was to investigate whether the new systems target specific organelles within cells.

Intracellular localization of Red nanocapsules:

The i*n cellulo* studies on the loaded nanocapsules discussed in the previous section indicated that the emission signals are originating from the cytosol region in the cells. The exact location was ascertained by colocalization experiments. The initial uptake experiments suggested that the RNC were localising in mitochondria. Like the concentration dependent uptake experiments, these colocalization experiments were carried out using RAW macrophages. Since the loaded RNC are excited at 568 nm and emit at 570 to 620 nm, Mito Tracker Green and Mito Tracker Deep Red were employed as complementary probes as Mito Tracker Green excites at 488 nm and emits in the range of 500 to 550 nm and the Mito Tracker Deep Red excites at 644 nm and emits > 670 nm. Since the spectral profile of Mito Tracker Deep Red is completely different to the Red nanocapsules, colocalization experiments with the commercial probe could be carried out in order to confirm the authenticity of any colocalization results obtained with Mito Tracker Green.   The colocalization experiments showed that the *in cellulo* signals of Mito Tracker Green and RNC matched with a Pearson's coefficient 0.97. The confirmation experiments performed with Mito Tracker Deep Red also showed a very high Pearson's coefficient (0.91) confirming that RNC localize on to the mitochondria.
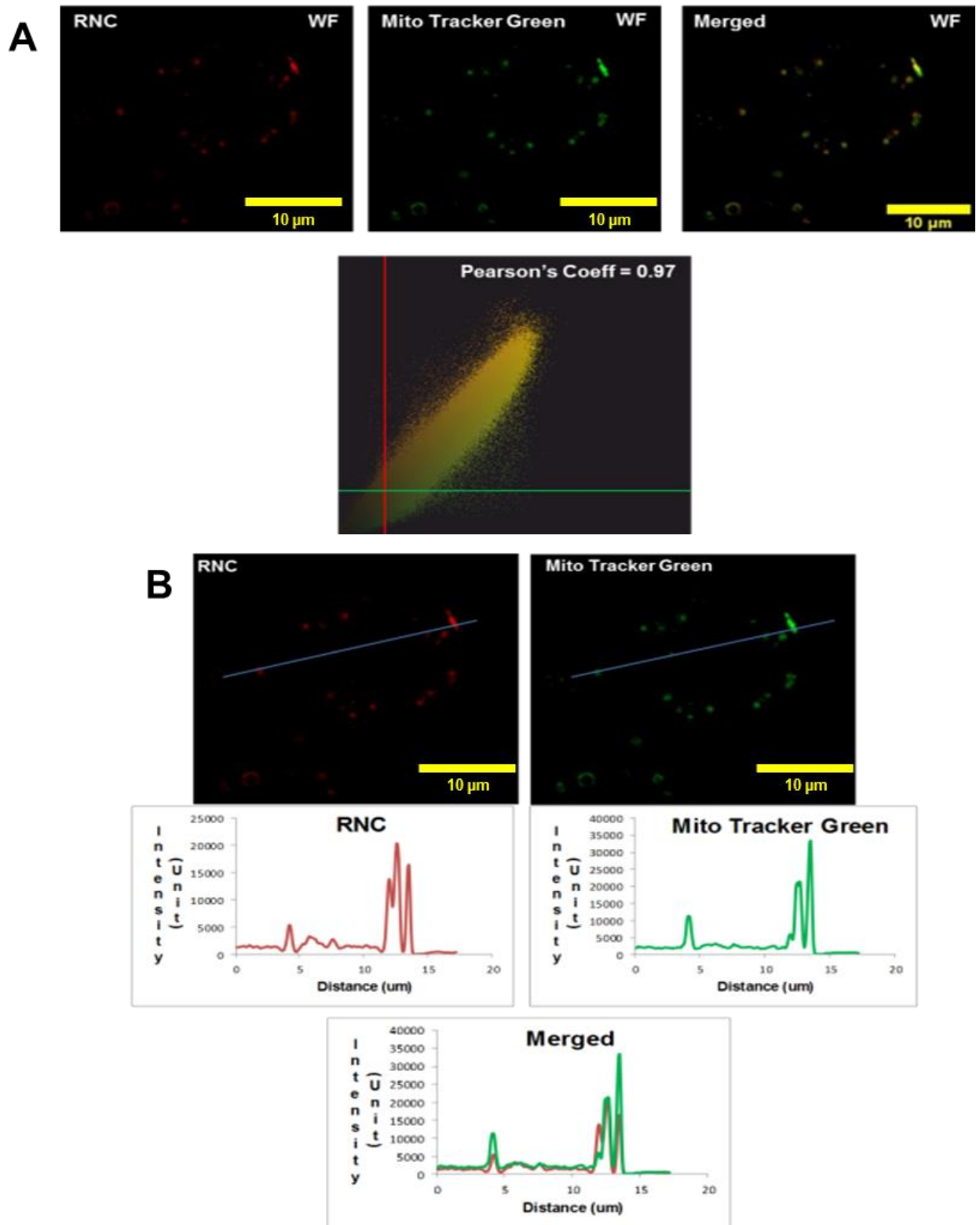
Figure 4.4 (A) Top (Left to Right): Widefield images of Red nanocapsules (RNC) and Mito Tracker Green (MTG) (Individual channel), Colocalized. **Bottom:** Pearson's coefficient of the same **(B)** Comparative widefield images of RNC and MTG and their corresponding Intensity profiles.
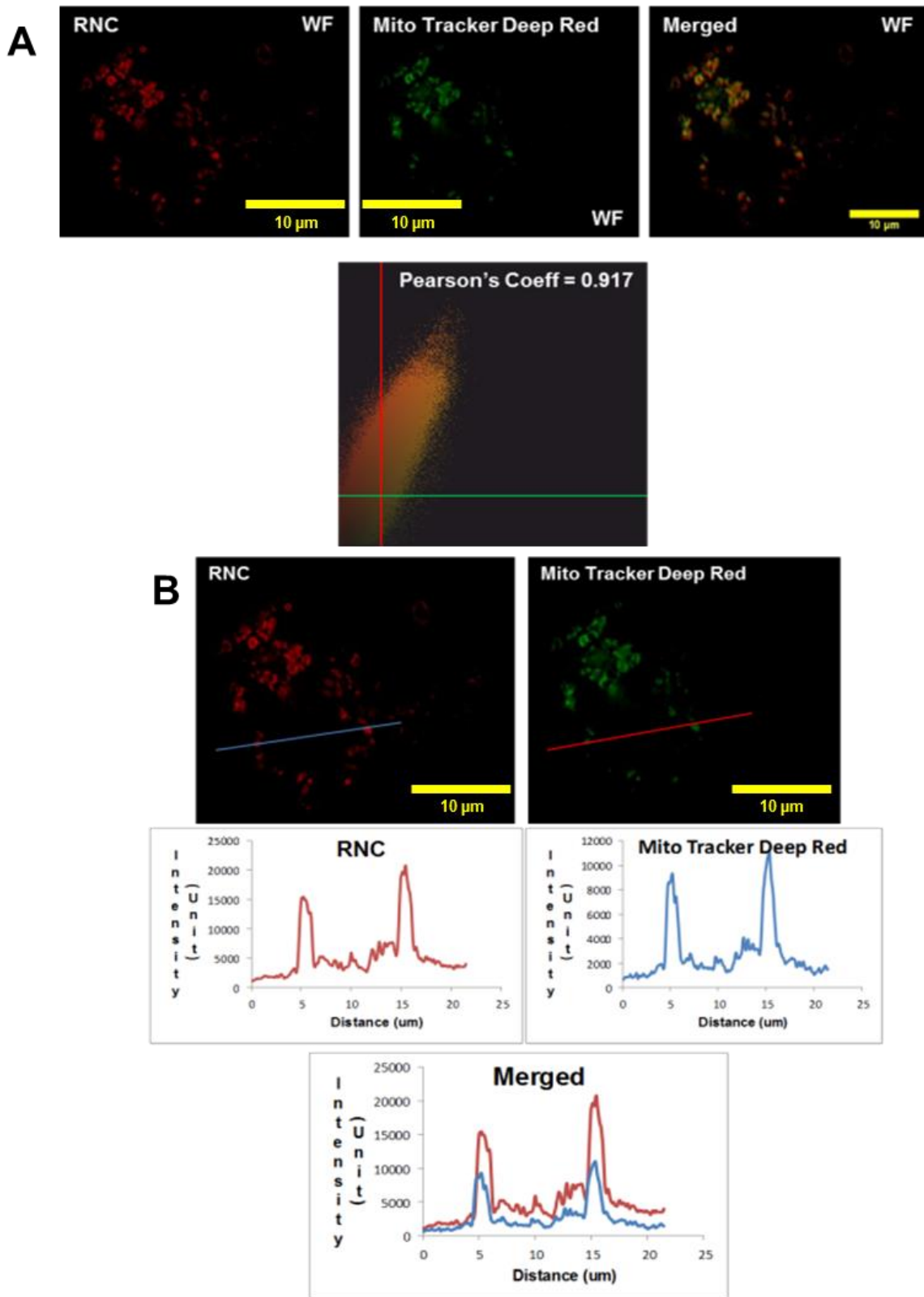
Figure 4.5 (A) Top (Left to Right): Widefield images of Red nanocapsules (RNC) and Mito Tracker Deep Red (MTDR) (Individual channel), Colocalized. **Bottom:** Pearson's coefficient of the same. **(B)** Comparative widefield images of RNC and MTDR and their corresponding Intensity profiles.

4.3 CELLULAR IMAGING USING NOVEL NANOPARTICLES

Introduction:

Nanoparticles (NPs) with targeted localisation offer great potential in therapeutics and imaging technologies. Luminescent NPs shows advantages of low bandwidth, tunable emission with long luminescent lifetime, large Stokes and anti-Stokes shift, high chemical and photo-stability, low auto-florescence and very low toxicity. Through two-photon up-conversion, UC, these systems can be excited with near-infrared light at wavelengths that are within the biological optical window. Anti-Stokes shifts emission exhibited by the UC nanoparticles has gained considerable attention and they are regarded as promising bio-imaging probes because of their versatility in terms of chemical composition, unique optical properties, and facile adaptability towards surface functionalization as demonstrated by Park *et al*[193]. For imaging technologies UC is advantageous as it minimizes scattering and supresses background emission from endogenous fluorophores leading to high signal-to-noise ratios[177,179].

It is known that, hexagonal β-phase $NaYF_4$ is an excellent up-converting host material and many studies have used β-$NaYF_4$ nanoparticles doped with Yb-Er or Yb-Tm or Y-Ho rare-earth ion couples for such studies[177,178]. Although, β-NaYF4: Yb,Er/Tm/Ho luminescent nanoparticles have been used for the detection of avidin, DNA and in imaging cells and tissues, work on biological applications on these systems[179,180], especially in specific subcellular organelle imaging or targeting drug delivery to specific organelles is still rare as seen in the work demonstrated by Yang *et al*[185]. There are also previously reports showing up-conversion polymeric nanocapsules that target cancer cells; for example the work of Bazylinska *et al*[192], but specific organelle targeting was not reported in this case. Also, although it has been shown previously that UC nanoparticles (UCNPs) can promote singlet oxygen and ROS generation when internalised in cells, as demonstrated by Yang *et al*[185], these systems lack specific organelle tracking ability. Herein, UC nanoparticles (UCNPs), whose surface chemistry has been designed to produce low cytotoxicity, high cellular uptake, and specific lysosome targeting are investigated.

In the NCL Pune, NaYF4:Yb, Gd nanoparticles with uniform size that possess intense fluorescence were synthesised by Dr. Sumit Kumar Pramanik using a hydrothermal reaction following a typical Stöber-based surface modification, primary amino groups were introduced on to their surface, allowing chemical coupling between the nanoparticles and other moieties.

In this case the moiety used was the lysosomal targeting peptide (LTP) which was conjugated to the functionalised UCNPs. Specific lysosomal delivery is important for therapeutics which includes cancer, neurodegenerative diseases, and other diseases where reactive oxygen species (ROS) are involved.
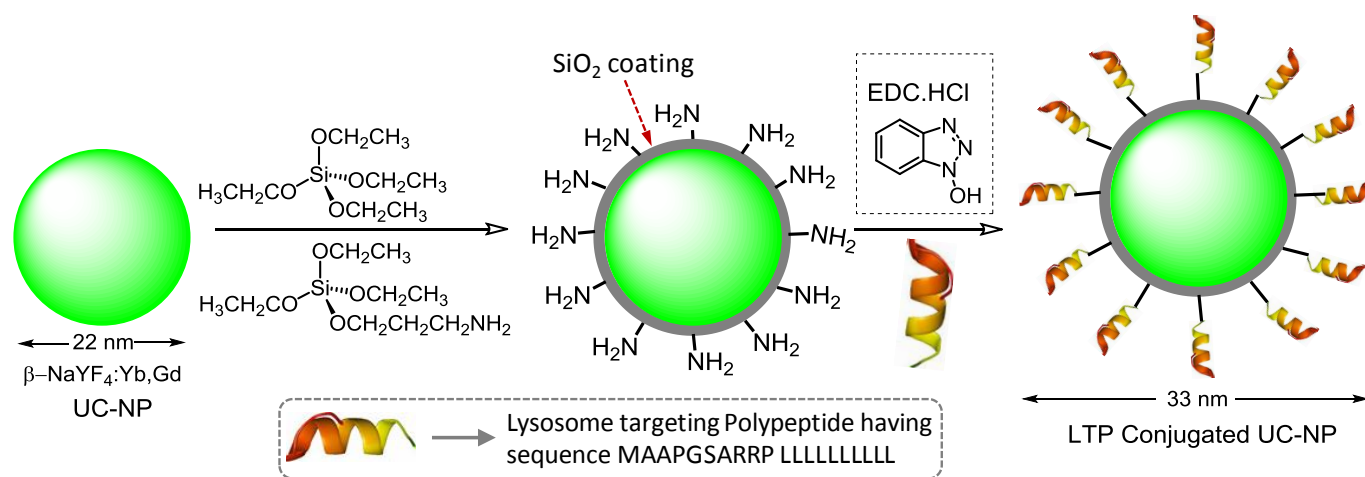
Figure 4.6 Schematic presentation for the development of LTP-Conjugated UC-NP

The surface functionalization of NaYF$_4$:Yb,Gd UCNPs using LTP, a C-terminal 20-residue sequence from the lysosome-associated membrane glycoprotein, is shown as a schematic in Figure 4.6. The sequence of LTP, used for these studies, is MAAPGSARRPLLLLLLLLLL, where the N-terminal is protected with biotin and the C-terminal of leucine is available for facile conjugation to the UCNPs.

The cellular uptake and subcellular localisation property of these LTP appended UCNPs were successfully investigated by two-photon and widefield microscopy using the RAW Macrophages. The main aspects of novelty in these studies on nanoparticles - which separates from those research carried out by Yang *et al*[185], Bazylinska *et al*[192] - include, conjugating the nanoparticles with specific lysosome targeting sequence specific peptide and the high photostability and brightness of the UCNPs, allowing them to be employed as two photon microscopy probes. These experiments reveal that the UCNPs can serve as two-photon bio-labels that show uptake into specific regions of the cytosol in RAW macrophages.

4.3.1 Nanoparticles as concentration dependent Two photon imaging probes

Introduction:

One of the most important consequences of the two-photon up-conversion process in UCNPs is that they can be employed for both widefield imaging as well as total internal reflection imaging. Considerable amount of autofluorescence can be eliminated by using UCNPs as a two-photon probe. As the UCNPs luminescence lies in the visible region, on two-photon excitation at 980 nm, they could be employed as effective bio-imaging probes without causing excessive photo-damage to cells. Concentration dependent uptake studies on UCNPs were carried out to ascertain the areas of localization, extent of uptake and its distribution. As the use of UCNPs leads to low auto fluorescence, high contrast and very low background signals, greater cellular details could be explored and detailed information with regard to the NPs organelle specificity could be ascertained[193].

Concentration dependent uptake experiments to exactly determine the extent of uptake of UCNPs in RAW macrophages were carried out using two-photon microscopy. The intense emission signals obtained on excitation confirmed uptake and indicated that the *in cellulo* luminescence is originating the cytosol region. The images revealed that some regions of the cytosol produce more intense signals than other regions, indicating that the UCNPs might be localizing in one or more specific regions in the intracellular environment. The extent of uptake increases with increase in concentration of the UCNPs and this is shown in the surface plot generated from the microscopy images. The distinctive cytosol accumulation of the UCNPs led us to probe into the details of their localization.
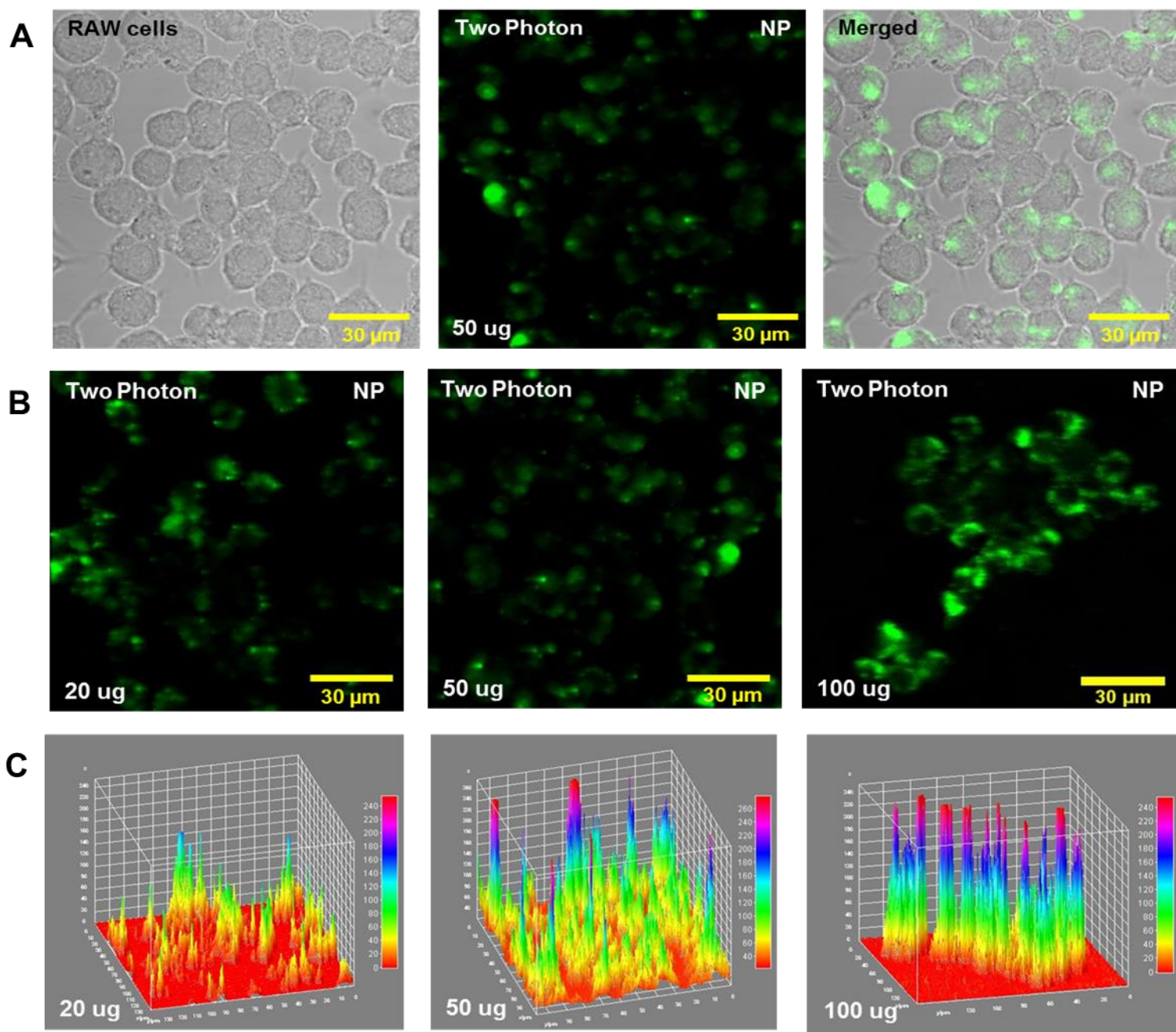
Figure 4.7 (A) Left to Right: Phase contrast image, two-photon image for NP uptake in RAW macrophages, Merged image. **(B)** Two-photon images of NP uptake in RAW macrophages at diverse concentration of NP. **(C)** Corresponding 3D-surface plots for the same.

4.3.2 Intracellular localization of nanoparticles:

Since reports of UCNPs that target specific intracellular organelles are rare, intracellular localisation experiments were carried out on RAW Macrophages with the help of Mito Tracker Deep Red initially using the widefield microscopy option of OMX-SIM. The NPs were excited at 488 nm and their emission is collected in the FITC channel (500 to 550 nm). As Mito Tracker Deep Red channel is far away from the FITC channel, this probe acts as an ideal foil to determine whether the NP are localizing to the mitochondria or not. The spectral distinction between the two channels eliminates the possibility of channel overlap and hence minimizes crosstalk. The results obtained from the colocalization experiments indicated that the nanoparticles do not localise over mitochondria as there is poor overlap in the signals from the two probes. This led to carry out additional experiments with Lyso Tracker Deep Red which has similar spectral characteristics as the Mito Tracker Deep Red, to determine if the nanoparticles localise over the lysosomes. The results obtained in these experiments suggest that the NPs do localise in lysosomes. These results were confirmed by the corresponding intensity profiles and Pearson's profiles derived from these data.
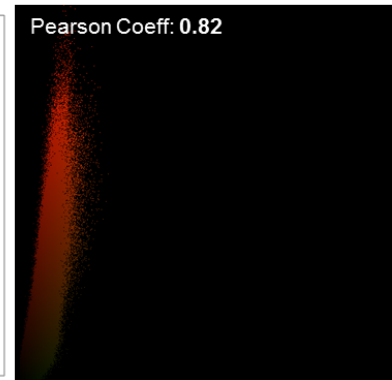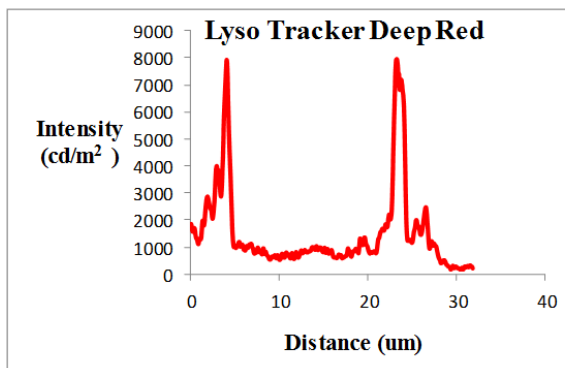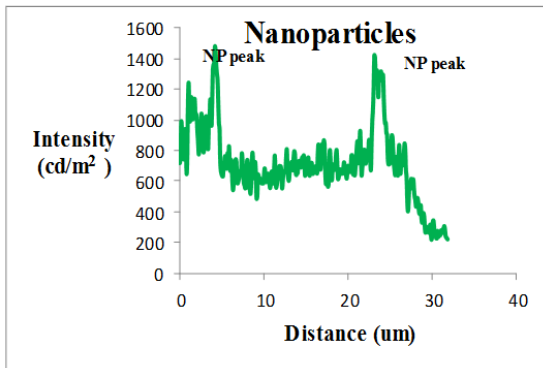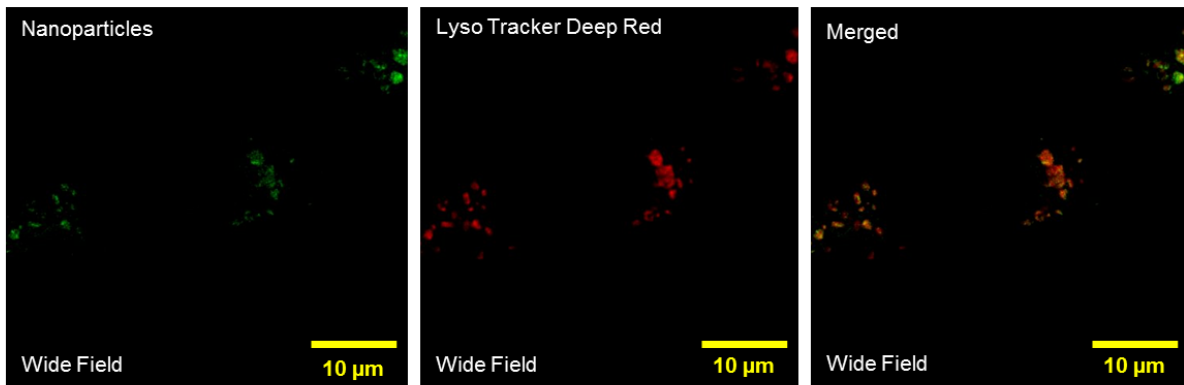
Figure 4.8 Top row (Left to Right): Widefield images of nanoparticles and Lyso Tracker Deep Red (Individual channel), Colocalized image (Merged) of nanoparticles with Lyso Tracker Deep Red. **Bottom row:** Intensity profiles of nanoparticles and Lyso Tracker Deep Red and Pearson's coefficient for the same.

4.4 SUMMARY

Targeted intracellular drug delivery using nanomaterials was achieved and tracked by using Structured illumination microscopy, which helped to delineate the localisation of these nanomaterials in the intracellular environment. The studied nanocapsules and nanoparticles specifically localised in different intracellular organelles namely mitochondria and lysosomes respectively indicating that, in both cases, organelle specific delivery was accomplished. Further work could involve targeting other intracellular organelles for drug delivery using nanocapsules or imaging using the nanoparticles.

5.0 EXPERIMENTS AND ANALYSIS

5.1 RRP PROBE: SYNTHESIS, SAMPLE PREPARATION, MICROSCOPY EXPERIMENTS AND ANALYSIS

5.1.1 RRP Probe ([{Ru(Phen)}$_2$Tpphz]$^{4+}$) – Synthesis:

The synthesis of RRP probe was carried out by the method optimized by Dr. Martin Gill[203].

Step 1:

1,10-phenanthroline   KBrO$_3$ / 60%H$_2$SO$_4$ / RT, 20h   1,10-phenanthroline-5,6-dione (dpq)
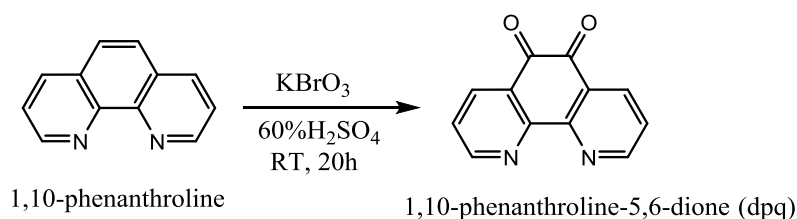
1,10-phenanthroline (5 g, 27.8 mmol) was dissolved into concentrated sulphuric acid (30 mL). Sodium bromide (2.6 g) and nitric acid (15 mL) were then carefully added and the mixture boiled under reflux for 40 minutes. The solution was cooled and poured over ice (400 g) and neutralised to pH 7.0 by addition of aqueous sodium hydroxide. An extraction with chloroform was carried out. The collected organic layers were dried with magnesium sulphate and the solvent removed by rotary evaporation. The yellow product was recrystallised using water/methanol (1:50).

Step 2:

1,10-phenanthroline-5,6-dione (dpq) Tetramethylammonium acetate Tetrapyrido[3,2-a:2',3'-c:3'',2'''-h:2''',3''''-j]phenazine (Tpphz)
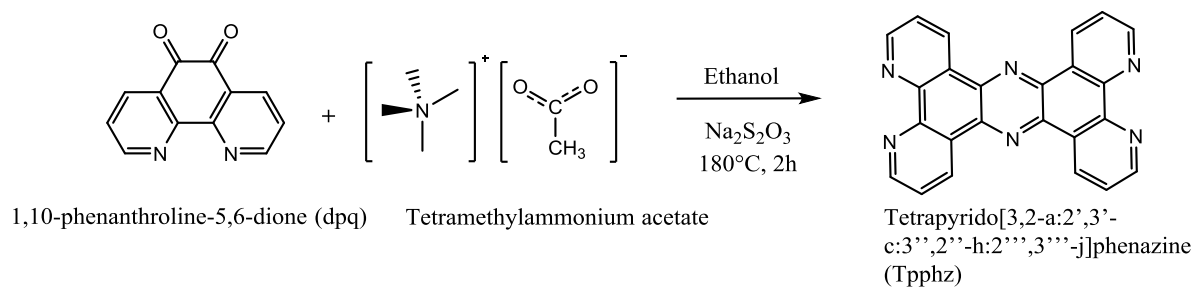
Tetramethylammonium acetate (15 g, 194.6 mmol), dpq (2.90 g, 13.8 mmol) and sodium sulfite (300 mg, 1.72 mmol) were boiled under reflux in ethanol (50 mL) for 2 hours at 180°C under nitrogen. The solution was cooled and water (20 mL) was added resulting the formation of a yellow precipitate which was collected and washed with water, methanol and acetone. The crude product was added to boiling EtOH (100 mL), filtered while hot and dried *in vacuo*.

Step 3:

1,10-phenanthroline + $RuCl_3.3H_2O$ $[Ru(phen)_2(Cl)_2]$
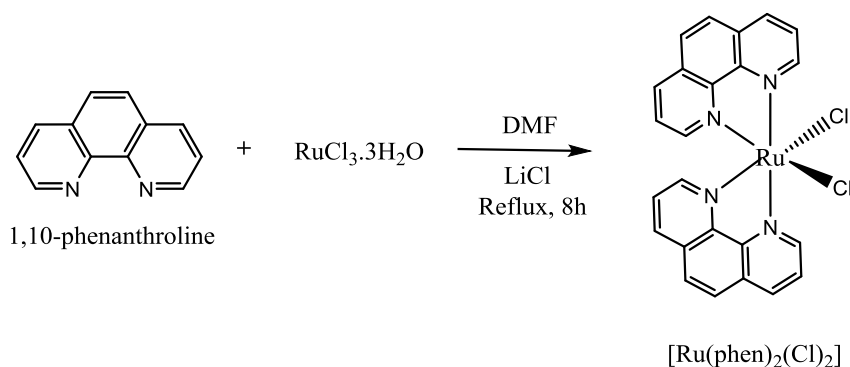
A mixture of $RuCl_3.3H_2O$ (3 g, 11.53 mmol), 1,10-Phenanothroline (22.7 mmol, 4 g),

LiCl (3.1 g, 73.1 mmol) was heated to reflux in N,N-DMF (40 mL) for 8 hours. After cooling to room temperature, 200 mL of Acetone is added. The reaction mixture was maintained at $0-4°C$ for 16 hours. The precipitate was collected by filtration, washed with water and Diethyl ether and dried *in vacuo*.

166

Step 4:

$[Ru(phen)_2(Cl)_2]$ Tetrapyrido[3,2-a:2',3'-c:3'',2''-h:2''',3'''-j]phenazine (Tpphz) $[\{Ru(phen)_2\}_2(tpphz)]^{4+}$ (RRP)
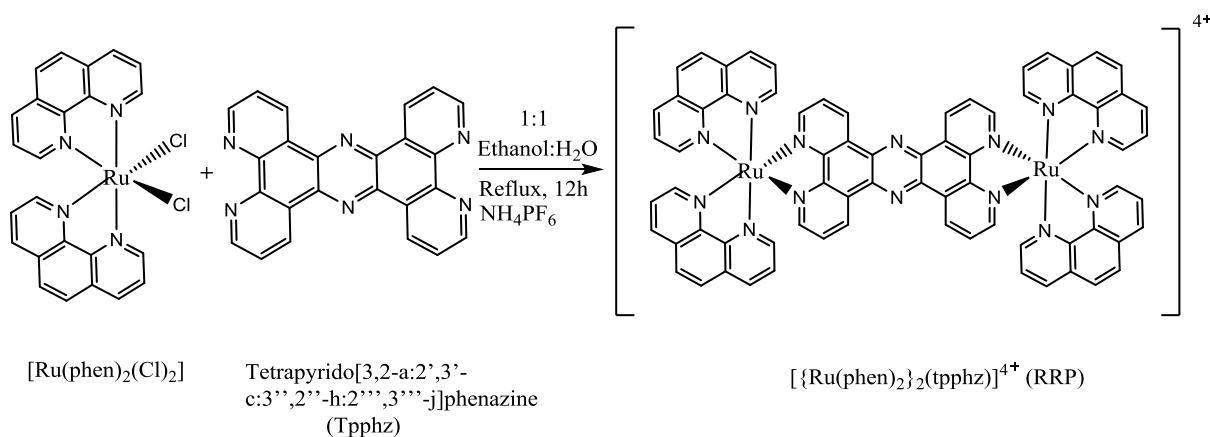
A mixture of $Ru(Phen)_2Cl_2$ (1 g, 2 mmol) and Tpphz (278 mg, 0.72 mmol) in a solution of 1:1 Ethanol-Water (80 mL) was refluxed for 12 hours under nitrogen. The solution was cooled to room temperature and maintained for a further 16 hours at 4°C. The brown solution was filtered and the residual ethanol was removed by rotary evaporation. The addition of NH_4PF_6 resulted in the formation of a dark brown precipitate which was collected by filtration, washed with water and recrystallized in acetonitrile by addition of diethyl ether and dried *in vacuo*. No further purification was required. To carry out the tissue culture experiments, the PF_6 salt of RRP was converted into its chloride salt by anion metathesis in acetone using tetrabutylammonium chloride.

5.1.2 RRP probe: Tissue culture - Sample preparation:

Fixed cells

Single colour experiments:

A2780 cells or MCF7 cells were seeded on cover slips (22 mm X 22 mm, 170 ± 5 μm square cover glasses) placed in six well plates in RPMI culture medium containing (10% FBS and 1% Penicillin Streptomycin) for 24 hours at 37°C, 5% CO_2. After 24 hours, when 70% confluency was achieved, the cells were washed with RPMI culture medium then the cells were treated with the probe for 5 to 10 min. Cells were then washed thrice with culture medium. After that cells were washed again with Phosphate Buffer Saline (2 times). After carrying out the Live cell uptake of RRP, the cells were fixed with 4% paraformaldehyde for 15 minutes and then washed thrice with PBS and two times and then the coverslips were mounted using mounting medium (Vectashield h-1000). The coverslips were then sealed using nail varnish and the samples were then imaged by 3D-STED, STED, SIM, Wide field fluorescence microscopy (Deconvoluted) or Airyscan High resolution microscopy.

Multi colour experiments:

The colocalisation studies were carried out by using Mito Tracker Green, Mito Tracker Red and Mito Tracker Deep Red. MCF7 cells were seeded on cover slips (22 mm X 22 mm, 170 ± 5 μm square Cover glasses) placed in six well plates in RPMI culture medium containing (10% FBS and 1% Penicillin Streptomycin) for 24 hours at 37°C, 5% CO_2. After 24 hours when 70% confluency was achieved the cells were washed with RPMI culture medium and then treated with RRP for 5 to 10 minutes followed by incubation with Mito Tracker Red, Mito Tracker Green or Mito Tracker Deep Red for 30 minutes and washed with 2 times RPMI culture media. Cells were then washed thrice with culture medium. After that, cells were washed again with Phosphate buffer saline (2 times), fixed with 4% paraformaldehyde for 15 minutes and then washed thrice with PBS and then the cover slips were mounted using mounting medium (Vectashield h-1000). The coverslips were then sealed using nail varnish and the samples were then imaged by SIM, Widefield Fluorescence Microscopy (Deconvoluted), Airyscan High resolution microscopy.

Live cells

For live cell microscopy, MCF7 were grown on #1.5H glass bottom slide (Ibidi) and allowed to grow for a minimum of 24 hours. Cells were thoroughly washed with RPMI 1640 and then incubated with RRP (500 μM, 4 hours).for confocal, Hyvolution (dCLSM), 3D-STED and STED microscopy.

5.1.3 Brief description of the types of Microscopy employed

Wide field HR microscopy

Widefield fluorescence microscopy involves collection of greater quantity of light (Including out of focus light) compared the confocal microscopy technique, which involves loss of more than 30% out of focus light discarded during image acquisition in this pointilistic technique. The widefield microscopy technique involves improvement in resolution only after post processing acquired Z-stacks. Processing of this data is done using Fiji software[201,202].

Deconvolution Wide field HR microscopy

The deconvolution procedure herein involves the processing of the raw wide field images obtained from the OMX-SIM (Conventional widefield microscopy mode) and image processing was carried out by using the Soft Worx software. Deconvolution is a computationally intensive image processing technique that helps in improving the contrast and axial resolution post acquisition of the images from 400 nm to 350 nm by removing out of focus blur from a Z-Stack of acquired images[201,202].

SIM

Structured illumination microscopy (SIM) was carried out using the Delta Vision OMX-SIM. SIM is a widefield microscopy technique based on Moire's effect. The resolution improvement is achieved based on the reconstruction of the acquired image using Soft Worx. The Z stacks acquired during the imaging are post-processed using the reconstruction option of Soft Worx. SIM acquisition is dependent mainly on the imaging parameters and acquisition parameters and this varies depending on the sample and in particularly on the nature of the probe[195,201]. The RRP probe was excited at 405 or 488 nm and emission was collected at > 650 nm (Alexa flour 647 channel of the Delta Vision OMX-SIM). The structured illumination (SI) experimental condition employed for single colour experiments were mainly dependent on the thickness of the Z stack (Sections 80 to 100), section spacing (0.125 to 0.250), thickness of the sample (8 to 10). Since the RRP probe is bright with a large Stokes shift, the image volume (Z-stack) was adjusted in such a way that artefacts arising

during the imaging was minimised during the SIM image acquisition. In all single colour experiments, exposure time was between 30 to 60 and %T was in the range of 30 to 50. When colocalisation experiments were performed with Mito Tracker Red, Mito Tracker Green and Mito Tracker Deep Red, the SIM conditions were maintained in accordance to the RRP probe.

STED

In the STED technique the extraordinary photostability and long life times of the RRP probe was exploited. RRP is a super stable probe with long triplet life times. A photostable probe could withstand the harsh image acquisition conditions of STED microscopy and hence superior super-resolutions are possible by using STED. As explained in chapter 1, STED involves two laser sets, one for excitation and another for depletion of already excited luminophore[196,197,198]. The possibility of applying RRP as a STED probe is examined and is explained in this chapter.

5.2 MULTIMODULAR IMAGING USING RRP PROBE

Single colour SIM:

Single colour SIM experiments for RRP were performed for 50 µM RRP on A2780 cells. The uptake was carried out for 5 to10 minutes. The RRP probe was excited at 405 or 488 nm and the emission was collected at > 650 nm. The SIM conditions maintained were: thickness of the Z-stack (sections 50 to 100), section spacing (0.125 to 0.250), thickness of the sample (8 to 11), exposure time was between 10 to 50 and the %T was in the range of 30 to 80. Concentration dependent nuclear-uptake experiments were carried by using widefield deconvolution microscopy at diverse range of RRP concentration ranging from 750 nm to 300 µM. The Widefield conditions maintained were: thickness of the Z stack (sections 40 to 80), section spacing (0.250 to 0.500), thickness of the sample (8 to 11), exposure time was between 10 to 30 and the %T was in the range of 30 to 60. The Airyscan High resolution (HR) microscopy experiments were carried out at RRP concentration of 50 µM.

Dual colour/Colocalization - SIM, STED, Widefield Deconvoluted, Airy scan:

Due to the broad emission spectra of RRP, colocalization experiments were performed with a series of commercial Mito Trackers available: Mito Tracker Red, Mito Tracker Deep Red and Mito Tracker Green. Colocalization experiments were performed by using low concentrations of RRP in to order to monitor RRP colocalization over mitochondria. Dual colour or Multicolour imaging for RRP with Mito Trackers was possible at high RRP concentration.

RRP and Mito Tracker Red:

For the colocalization experiments, MCF7 cells were incubated with RRP (4 μM to 25 μM) for 5 minutes and then the cells were incubated with Mito Tracker Red (1 μM) for 30 minutes. For the Dual colour experiments, MCF7 cells were incubated with RRP (4 μM to 25 μM) for 5 minutes and then incubated with Mito Tracker Red (1 μM) for 30 minutes. The cells were washed regularly three times with culture media and PBS (two to three times), the cells were then fixed with 4% paraformaldehyde and mounted and navigated initially for proper cell morphology by using Light microscope and then imaged by using Structured Illumination Microscopy (SIM), Airyscan HR microscopy, Widefield microscopy (WF). The RRP probe was excited at 405 or 488 nm and the emission was collected in the Alexa fluor 647 channel (> 650 nm) and the Mito Tracker Red was excited at 568 nm and the emission was collected in the Alexa fluor 568 channel (570 nm to 620 nm). The SIM imaging conditions maintained are, For RRP: Thickness of the Z stack (Sections 50 to 100), section spacing (0.125 to 0.250), thickness of the sample (8 to 11), exposure time was between 10 to 50 and the %T was in the range of 30 to 80. For Mito Tracker Red: Thickness of the Z stack (Sections 50 to100), section spacing (0.125 to 0.250), thickness of the sample (8 to 11), exposure time was between 10 to 50 and the %T was in the range of 10 to 50. The Widefield imaging conditions maintained are, For RRP: Thickness of the Z stack (Sections 40 to 80), section spacing (0.250 to 0.500), thickness of the sample (8 to 11), exposure time was between 10 to 30 and the %T was in the range of 30 to 60. The Widefield imaging conditions maintained are, For Mito Tracker Red: Thickness of the Z stack (Sections 40 to 80), section spacing (0.250 to 0.500), thickness of the sample (8 to 11), exposure time was between 10 to 50 and the %T was in the range of 30 to 60.

RRP and Mito Tracker Green:

For the colocalization experiments, MCF7 cells were incubated with RRP (4 μM) for 5 minutes and then the cells were incubated with Mito Tracker Green (1 μM) for 30 minutes. The cells were washed regularly three times with RPMI culture media and PBS (two to three times), the cells were then fixed with 4% paraformaldehyde and mounted and navigated initially for proper cell morphology by using Light microscope and then imaged by using Widefield microscopy (Deconvolved). RRP was excited at 405 nm and the emission was collected in the Alexa fluor 647 channel (> 650 nm) and the Mito Tracker Green was excited at 488 nm and the emission was collected in the FITC channel (500 nm to 550 nm). The Widefield imaging conditions maintained are, For RRP: Thickness of the Z stack (Sections 40 to 80), section spacing (0.250 to 0.500), thickness of the sample (8 to 11), exposure time was between 10 to 30 and the %T was in the range of 30 to 60. The Widefield imaging conditions maintained are, For Mito Tracker Green: Thickness of the Z stack (Sections 40 to 80), Section spacing (0.250 to 0.500), thickness of the sample (8 to 11), exposure time was between 10 to 50 and the %T was in the range of 30 to 60.

RRP and Mito Tracker Deep Red:

For the colocalization experiments, MCF7 cells were incubated with RRP (4 μM) for 5 minutes and then the cells were incubated with Mito Tracker Deep Red (750 nM) for 30 minutes. The cells were washed regularly three times with RPMI culture media and PBS (two to three times), the cells were then fixed with 4% paraformaldehyde and mounted and navigated initially for proper cell morphology by using Light microscope and then imaged by using Wide field microscopy (Deconvoluted). The RRP probe was excited at 405 or 488 nm and the emission was collected in the Alexa fluor 647 channel (> 650 nm) and the Mito Tracker Deep Red was excited at 644 nm and the emission was collected in the Alexa fluor channel (> 650 nm). The Widefield imaging conditions maintained are, For RRP : Thickness of the Z stack (Sections 40 to 80), section spacing (0.250 to 0.500), thickness of the sample (8 to 11), exposure time was between 10 to 30 and the %T was in the range of 30 to 60. The Widefield imaging conditions maintained are, For Mito Tracker Deep Red: Thickness of the Z stack (Sections 40 to 80), section spacing (0.250 to 0.500), thickness of the sample (8 to 11), exposure time was between 10 to 50 and the %T was in the range of 30 to 60.

5.2.1 Time dependent Imaging (Widefield microscopy)

The time-dependent uptake of RRP over mitochondria and the nucleus and concentration-dependent tracking of cellular events was carried out by using Widefield fluorescence microscopy. Images were acquired in a Nikon Dual cam Widefield fluorescence microscope fitted with: a Spectra X LED light source (395 nm, 440 nm, 470 nm, 508 nm, 561 nm, 640 nm); single emission filter sets for DAPI, GFP, RFP, Cy5; a Quad filter for DAPI/GFP/RFP/Cy5 with matching emission filter wheel; a Dual Andor Zyla sCMOS camera 2560 x 2160; 6.5 μm pixels and inbuilt NIS software employed for Widefield deconvolution. For the time-dependent uptake experiments, 10 μM RRP was used and the uptake was monitored for time intervals starting from 2 min to 10 min. For the concentration-dependent tracking of cellular events a range of RRP concentration (1 μM, 5 μM and 50 μM) was used. The RRP was excited at 470 nm and emission collected at > 650 nm (Cy 5 Channel). Mito Tracker Red was excited at 568 nm and emission collected in the RFP channel at 570 to 620 nm. Mito Tracker Green was excited at 488 nm and emission collected in the FITC channel at 500 to 550 nm. Mito Tracker Deep Red was excited at 644 nm and emission collected at > 650 nm (Cy 5 channel).

5.3 RRP PROBE: TECHNIQUES, IMAGING METHODS AND DATA PROCESSING

Technical description and Image acquisition – SIM:

SIM was carried out by using the Delta Vision OMX-SIM. The resolution improvement is achieved based on the reconstruction of the acquired image by using the inbuilt software namely Soft Worx. The Z stacks acquired during the imaging are post-processed by using the reconstruction option of Soft Worx. SIM acquisition is dependent mainly on the Imaging parameters and acquisition parameters and this varies depending on the sample and in particularly on the nature of the probe. The RRP probe was excited at 405 or 488 nm and the emission was collected at > 650 nm (Alexa flour 647 channel of the Delta Vision OMX-SIM). In the case of RRP the Structured Illumination (SI) experimental condition employed for running the SI experiment for Single colour experiments were mainly dependent on the thickness of the Z stack (Sections 80 to 100), section spacing (0.125 to 0.250), thickness of the sample (8 to 10). As RRP probe is a very bright probe with a large Stokes shift therefore the image volume (Z-stack) should be adjusted in such a way that artefacts arising during the

imaging could be minimized during the SIM image acquisition in addition to that %T and exposure time needed to be adjusted during SIM imaging of RRP, a DNA-binding probe. The 3D-SIM image acquisition mode used using RRP probe include, Z piezo step resolution of 5 nm, 800 ms scan speed in a 120 frame per cycle. The image to image interval during a complete Z stack is 8 ms. The power is 300 Hz with 60% quantum efficient CMOS camera with 6.5 um pixel size. Each image in the 3D SIM z-stack is 512X512 pixels, 1 ms exposure per frame, 125 nm step, 8 z-slices, 15 image per slice, 120 images in total for single colour imaging, for colocalization and dual colour the conditions are slightly different but essentially similar. The SIM reconstruction conditions employed include essentially same conditions as Z-stack image acquisition but the exposure time is 5 ms for 3D SIM reconstruction. The pixel size for 60X and 100X objective in SIM were 80 and 48 respectively. In all our Single colour experiments the exposure time was between 30 to 60 and the %T was in the range of 30 to 50. The colocalization experiments were performed with Mito Tracker Red, Mito Tracker Green and Mito Tracker Deep Red. The Dual colour experiments were performed with Mito Tracker Red exploiting the concentration dependent preferential nuclear uptake of RRP at high concentration. In both of these experiments the SIM conditions of these co-staining agents were maintained in accordance to the RRP probe.

Technical description and Image aquisition - STED:

STED images were taken in a commercial LEICA SP8 3X gSTED SMD confocal microscope (Leica Microsystems, Manheim, Germany). The microscope is equipped with 3 depletion lines and it is also equipped with a 3D STED additional vortex to obtain higher spatially resolved images in XY and Z. The excitation laser beam consisted of a pulsed (80MHz) super-continuum white light laser (WLL). For a cleaner emission the excitation lines had a clean-up notch filter (NF) in the optical pathway. The gSTED imaging was taken with a 660 nm depletion laser, and the pulsed STED images with a pulsed 775 nm Laser, again in every case the respective NF were in place. The objective employed was a Leica 100x/1.4 NA oil objective. The pinhole was set at one Airy unit. The gated HyD detectors were set with the gated option on and the temporal gated selected was from 2 to 6.5 ns when depleting at 660 nm. For the 3D STED images the depletion lasers were split in two, the second vortex was set at 50%. Images of live MCF7 cells were taken at 37°C and 5% CO_2. The dye was excited with a WLL at 470 nm, and STED depleted at 775 nm; the emission was collected from 620 to 710 nm and a gating between 2 and 6.5 ns was used.

RRP probe: Image analysis and Data processing – STED:

STED nanoscopy resolved the structure of the mitochondria and DNA with high detail, but as expected the images had low intensity counts, especially when employing the continuous wavelength depletion laser at 660 nm. To maximise signal-to-noise we deconvolved the images using a commercially available software (Huygens package software, SVI, Netherlands). To quantify the background level of noise we used either an automated quantification provided by the software or a manual by means of computing the averaged background intensity from regions outside the cell. Better results were obtained with the manual process. For the deconvolution, 40 iterations, a signal to noise ratio of 15, and the classical maximum likelihood estimation method provided by the software was employed. Colocalization analysis was performed using the Huygens software package and the Pearson colocalization coefficient was quantified. This software allows obtaining the colocalization map of the regions that colocalize. These map regions could be surface rendered and the digital image was employed to obtain quantitative values of the objects that colocalise, such as width, and sphericity. Quantification of the data from the images was obtained by using the Huygens Professional Software Package (Huygens; Scientific Volume Imaging, Hilversum, Netherlands). The general protocol for the analysis of any image related to wide field, Airy Scan, Hyvolution and STED (both single plane XY, YZ and 3D STED, i.e., X, Y and Z) included several steps: object localization, quantification and characterization, plotting, and image representation. As a general rule every single confocal plane of a 3D imaging stack was first deconvolved, the resulting 3D image was surface-rendered, and the 3D iso-surface was used for quantitative analysis; the advance object analysis module of Huygens was used to localize, quantify and characterize the geometry of each individual granule; and the resulting data was exported into graphing and statistics software). The values represented in the population distribution graphs were obtained from the Huygens software. The surface rendered images obtained by Huygens Professional, LAX software (Leica SP8) to generate the surface rendered 3D STED images, and the orthogonal views, the rest of the images has been post procesed with Fiji (ImageJ).

5.4 BICYCLOMETALLATED IRIDIUM METAL COMPLEX PROBES (CC 203-204): EXPERIMENTS AND ANALYSIS

5.4.1 Sample preparation

Cellular Uptake studies for CC 203-204:

A2780 or MCF7 cells were seeded on cover slips (22 mm X 22 mm, 170 ± 5 μm square Cover glasses) placed in six well plates in RPMI culture medium containing (10% FBS and 1% Penicillin Streptomycin) for 24 hours at 37°C, 5% CO_2. After 24 hours when 70% confluency was achieved the cells were washed with RPMI culture medium then the cells were treated with CC 203 or 204 (50 μM or 100 μM) for 24 hours. Cells were then washed thrice with culture medium. After that cells were washed again with Phosphate buffer saline (2 times). After carrying out the live cell uptake of the CC 203 or 204 and then the cells were fixed with 4% paraformaldehyde for 15 minutes and then washed thrice with PBS and then the cover slips were mounted using mounting medium (Vectashield h-1000).The coverslips were then sealed using nail varnish and the sample were then imaged by Wide field fluorescence microscopy using the Dual cam Nikon.

Colocalization studies for CC 203-204:

The Colocalization studies of CC 203 and 204 was carried out by using Mito Tracker Green and Mito Tracker Red. A2780 cells were seeded on cover slips (22 mm X 22 mm, 170 ± 5 μm square cover glasses) placed in six well plates in RPMI culture medium containing (10% FBS and 1% Penicillin Streptomycin) for 24 hours at 37°C, 5% CO_2. After 24 hours when 70% confluency was achieved the cells were washed with RPMI culture medium then the cells were treated with 1 μM (Mito Tracker Green or Mito Tracker Deep Red) for 30 minutes and washed with 2X RPMI culture media and then treated with 50 μM CC 203 or 204 for 24 hours. Cells were then washed thrice with culture medium. After that cells were washed again with Phosphate Buffer Saline (2X PBS). After carrying out the live cell uptake of the CC 203 or 204 and then the cells were fixed with 4% paraformaldehyde for 15 minutes and then washed thrice with PBS and then the cover slips were mounted using mounting medium (Vectashield h-1000). The Coverslips were then sealed using nail varnish and the sample were then imaged by Widefield fluorescence microscopy using the Dual cam Nikon.

5.4.2 Imaging

Single colour imaging:

The complexes CC 203 and 204 were excited at 470 nm and the emission was collected between 570 nm to 620 nm (RFP channel of Dual cam Nikon Wide field fluorescence microscope). The Widefield imaging conditions employed for the cellular uptake studies of the A2780 and MCF7 cells. The Widefield microscopy conditions maintained include, thickness of the Z stack (Sections 40 to 100), section spacing (0.250 to 0.500), thickness of the sample (8 to 15).

Colocalization (Multi colour imaging):

The complexes CC 203 and 204 was excited at 470 nm and the emission was collected between 570 nm to 620 nm (RFP channel), Mito Tracker Green was excited at 470 nm and the emission was collected between 500 nm to 530 nm (GFP channel), Mito Tracker Deep Red was excited at 640 nm and collected between 650 nm to 700 nm (Cy5 channel). The colocalization experiments were carried out using the same microscopy conditions as mentioned for single colour experiments.

5.4.3 Cytotoxicity and ICP-MS studies

ICP-MS:

Cell cultures were grown on 60 mm dishes at a seeding density of 5 x10^5 cells per dish and incubated for 24 hours. Cells were then treated with the complex (solubilised in and maintained at 10% PBS/H_2O: 90% medium throughout all solutions) at the stated concentration and incubated for 24 hours. All complex solution (or control medium) was removed, cells washed and 200 μL serum free medium added. Cells were detached by scraping and transferred to a falcon tube, where 20 μL of each sample was removed for cell counting. Each sample was transferred to a glass sample tube, 1 mL concentrated HNO_3 added, heated to 60°C overnight and then diluted to 5 ml total volume with ultrapure Milli-Q H_2O before analysis of iridium content by inductively coupled plasma mass spectrometry (ICP-MS). Using the obtained iridium concentration, the sample volume, number of cells per sample and the assumption of a cell volume of 2 x10^{-12} L an estimate of intracellular concentration (mol L^{-1}) could be deduced.

Cytotoxicity:

Cells were maintained in RPMI 1640 medium supplemented with 10% FBS, 100 mg mL^{-1} streptomycin, 100 units mL^{-1} penicillin, and 2 mM glutamine at 37°C in a humidified atmosphere containing 5% CO_2. Experimental cultures were grown on 48 well plates at a seeding density of 5 x 10^4 cells per well and incubated for 24 hours. The cells were then treated with complex (solubilised in DMSO and PBS and maintained at a final concentration of 9.99% PBS and 0.01% DMSO throughout all solutions) of a 1 – 200 μM concentration range, in triplicate, and incubated for 48 h. The Culture media was removed and cells incubated with MTT (0.5 mg ml^{-1} dissolved in PBS) for 30 – 40 min. The MTT was removed and formazan product eluted using 120 μL/well acidified isopropanol, 100 μL of which was transferred to a 96 well plate for the absorbance to be quantified by spectrophotometer (540 nm, referenced at 640 nm). An average absorbance for each concentration was calculated and cell viability was determined as a percentage of the untreated negative control wells (0.1% DMSO: 9.99% PBS: 90% medium, average of triplicate). Data were plotted in a graph of concentration against cell viability to produce a curve from which the IC$_{50}$ value could be derived by interpolation.

5.5 ROS PROBE: SAMPLE PREPARATION, MICROSCOPY EXPERIMENTS AND ANALYSIS

5.5.1 ROS PROBE 1

Intracellular HOCl Detection Experiments (SIM and Widefield microscopy)

(A) Detection by External Addition of HOCl:

Intracellular detection of HOCl by ROS probe-1 probe was carried out using SIM. The experiment was carried out by incubating the 70% confluent RAW Macrophages with 10 μM ROS probe-1 in DMEM medium with 10% FBS and 1% Penicillin streptomycin at 37°C, 5% CO_2 for 25 minutes. The cells were further treated with varied concentration of NaOCl as mentioned above for 30 minutes. Both live and fixed cell imaging were carried out by using Widefield fluorescence microscopy. SIM was carried out only on fixed cells.

(B) Endogenous Detection of HOCl:

In order to determine whether the ROS probe-1 could detect HOCl generated inside the cells, we carried out an experiment with Lipopolysaccharide (LPS). The experiment was carried out by incubating the 70% confluent RAW Macrophages with increase in concentration of LPS from 100 ng to 2500 ng in DMEM medium with 10% FBS and 1% Penicillin streptomycin at 37°C, 5% CO_2 for 24 hours. The cells were further treated with 10 μM of ROS probe-1 for 30 minutes. The increase in in cell luminescence with increasing concentration of LPS in the cells was imaged by SIM and also Widefield microscopy.

(C) Intracellular Signal attenuation and spreading experiment:

This experiment was carried out on fixed cells using SIM. The experiment was carried out by incubating the 70% confluent RAW Macrophages with in DMEM medium with 10% FBS and 1% Penicillin streptomycin at 37°C, 5% CO_2 for 24 hours. The cells were first treated with 10 μM of ROS probe-1 for 30 minutes and then treated with LPS (2500 ng) for specific time intervals namely 2 minutes, 15 minutes, 30 minutes, 1 hour, 2 hour, 7 hour and 12 hours. The changes in incellular luminescence according to different time intervals was imaged by Structured illumination microscopy and also Widefield fluorescence microscopy. The signal development and spreading were recorded using SIM and 3D-SIM.

5.5.2 Colocalization SIM and Widefield microscopy Experiments:

(A) Colocalization experiments with ER Tracker Green:

The co-staining experiments with ER Tracker Green was carried out by incubating the ER Tracker Green (1 µM) further for 30 minutes after incubating the RAW Macrophages with ROS probe-1 (10 µM) initially for 25 minutes and NaOCl (20 µM) for a further 30 minutes. The cells were washed regularly three times with DMEM culture media and PBS. The cellular uptake of both the probes are carried out in live cells and then the cells were fixed with 4% paraformaldehyde and mounted and navigated initially for proper cell morphology by using Light microscope and then imaged by using Structured illumination microscopy (SIM) and Wide field microscopy (WF). The ROS probe-1 was excited at 568 nm and the emission was collected in the Alexa fluor channel (570 nm to 620 nm) and the ER-Tracker Green was excited at 488 nm and the emission was collected in the FITC Channel (500 nm to 550 nm). The SIM imaging conditions maintained are, For ROS probe-1: Thickness of the Z stack (Sections 50 to 100), section spacing (0.125 to 0.150), thickness of the sample (8 to 11), exposure time was between 3 to 30 and the %T was in the range of 10 to 50. For ER Tracker Green: Thickness of the Z stack (Sections 50 to 100), section spacing (0.125 to 0.150), thickness of the sample (8 to 11), exposure time was between 10 to 50 and the %T was in the range of 10 to 50. The Widefield imaging conditions maintained are, For ROS probe-1: thickness of the Z stack (Sections 40 to 80), section spacing (0.250 to 0.500), thickness of the sample (8 to 11), exposure time was between 1 to 30 and the %T was in the range of 2 to 30. For ER Traker Green: thickness of the Z stack (Sections 40 to 80), section spacing (0.250 to 0.500), thickness of the sample (8 to 11), exposure time was between 10 to 50 and the %T was in the range of 2 to 30.

(B) Colocalization experiments with Cytopainter Golgi Tracker Green:

The co-staining experiments with Cytopainter Golgi Tracker Green was carried out by incubating the Cytopainter Golgi Tracker Green (1 µM) further for 30 minutes after incubating the RAW Macrophages with ROS probe-1 (10 µM) initially for 25 minutes and NaOCl (20 µM) for a further 30 minutes. The cells were washed regularly three times with DMEM culture media and PBS. The cellular uptake of both the probes are carried out in live cells and then the cells were fixed with 4% paraformaldehyde and mounted and navigated initially for proper cell morphology by using light microscope and then imaged by using structured illumination microscopy (SIM) and Widefield microscopy (WF). The ROS probe-1 was excited at 568 nm and the emission was collected in the Alexa fluor channel (570 nm to 620 nm) and the Cytopainter Golgi Tracker Green was excited at 488 nm and the emission

was collected in the FITC Channel (500 nm to 550 nm). The SIM imaging conditions maintained were: for ROS probe-1: thickness of the Z stack (sections 50 to 100), section spacing (0.125 to 0.150), thickness of the sample (8 to 11), exposure time was between 10 to 50 and the %T was in the range of 2 to 30. The SIM imaging conditions maintained are: for Golgi Tracker Green: thickness of the Z stack (Sections 50 to 100), section spacing (0.125 to 0.150), thickness of the sample (8 to 11), exposure time was between 10 to 50 and the %T was in the range of 2 to 30. The Widefield imaging conditions maintained are: for ROS probe-1: thickness of the Z stack (Sections 30 to 60), section spacing (0.250 to 0.500), thickness of the sample (8 to 11), exposure time was between 2 to 30 and the %T was in the range of 2 to 30. For Golgi Tracker Green: thickness of the Z stack (Sections 80 to 100), section spacing (0.250 to 0.500), thickness of the sample (8 to 11), exposure time was between 2 to 30 and the %T was in the range of 2 to 30.

(C) Colocalization experiments with Mito Tracker Green:

The co-staining experiments with Mito Tracker Green was carried out by incubating the Mito Tracker Green (1 µM) further for 30 minutes after incubating the RAW Macrophages with ROS probe-1 (10 µM) initially for 25 minutes and NaOCl (20 µM) for a further 30 minutes. The cells were washed regularly three times with DMEM culture media and PBS. The cellular uptake of both the probes are carried out in live cells and then the cells were fixed with 4% paraformaldehyde and mounted and navigated initially for proper cell morphology by using Light microscope and then imaged by using Widefield microscopy (WF). The ROS probe-1 was excited at 568 nm and the emission was collected in the Alexa fluor channel (570 nm to 620 nm) and the Mito Tracker Green was excited at 488 nm and the emission was collected in the FITC channel (500 nm to 550 nm). The Widefield imaging conditions maintained are, For ROS probe-1: Thickness of the Z stack (Sections 30 to 60), section spacing (0.250 to 0.500), thickness of the sample (8 to 11), exposure time was between 2 to 30 and the %T was in the range of 2 to 30. For Mito Tracker Green: thickness of the Z stack (Sections 80 to 100), section spacing (0.250 to 0.500), thickness of the sample (8 to 11), exposure time was between 2 to 30 and the %T was in the range of 2 to 30.

(D) Colocalization experiments with Lyso Tracker Deep Red:

The co-staining experiments with Lyso Tracker Deep Red was carried out by incubating the Lyso Tracker Deep Red (500 nM) further for 30 minutes after incubating the RAW Macrophages with ROS probe-1 (10 μM) initially for 25 minutes and NaOCl (20 μM) for a further 30 minutes. The cells were washed regularly three times with DMEM culture media and PBS. The cellular uptake of both the probes are carried out in live cells and then the cells were fixed with 4% paraformaldehyde and mounted and navigated initially for proper cell morphology by using Light microscope and then imaged by using Structured illumination microscopy (SIM) and Widefield microscopy (WF). The ROS probe-1 was excited at 568 nm and the emission was collected in the Alexa fluor channel (570 nm to 620 nm) and the Lyso Tracker Deep Red was excited at 644 nm and the emission was collected in the Cy5 Channel (> 670 nm). The SIM imaging conditions maintained are, For ROS probe-1 : Thickness of the Z stack (Sections 50 to 100), section spacing (0.125 to 0.150), thickness of the sample (8 to 11), exposure time was between 10 to 50 and the %T was in the range of 2 to 30. For Lyso Tracker Deep Red: thickness of the Z stack (Sections 50 to 100), Section spacing (0.125 to 0.150), thickness of the sample (8 to 11), exposure time was between 10 to 50 and the %T was in the range of 2 to30. The Widefield imaging conditions maintained are, For ROS probe-1 : thickness of the Z stack (Sections 30 to 60), Section spacing (0.250 to 0.500), thickness of the sample (8 to 11), exposure time was between 2 to 30 and the %T was in the range of 2 to 30. For Lyso Tracker Deep Red: Thickness of the Z stack (Sections 80 to 100), section spacing (0.250 to 0.500), thickness of the sample (8 to 11), exposure time was between 2 to 30 and the %T was in the range of 2 to 30.

(E) Dual colour SIM and Widefield microscopy Experiments:

The Dual colour experiments with Hoechst as the nuclear stain was carried out by incubating the Hoechst (500 nM) further for 30 minutes after incubating the RAW Macrophages with ROS probe-1 (10 μM) and NaOCl (20 μM) for a further 30 minutes. The cells were washed regularly three times with DMEM culture media and PBS. The cellular uptake of both the probes are carried out in live cells and then the cells were fixed with 4% paraformaldehyde and mounted and navigated initially for proper cell morphology by using light microscope and then imaged by using Structured illumination microscopy (SIM) and Widefield microscopy. The ROS probe-1 was excited at 568 nm and the emission was collected in the Alexa fluor channel (570 nm to 620 nm) and the Hoechst was excited at 405 nm and the emission was collected in the DAPI Channel (420 nm to 500 nm). The SIM imaging conditions maintained are, For ROS probe-1: Thickness of the Z stack (Sections 40 to 80),

section spacing (0.125 to 0.150), thickness of the sample (5 to 8), exposure time was between 10 to 50 and the %T was in the range of 10 to 50. The SIM imaging conditions maintained are, For Hoechst: Thickness of the Z stack (Sections 40 to 80), section spacing (0.125 to 0.150), thickness of the sample (5 to 8), exposure time was between 50 to 100 and the %T was in the range of 10 to 50. The WF imaging conditions maintained are, For ROS probe-1: Thickness of the Z stack (Sections 20 to 50), section spacing (0.250 to 0.500), thickness of the sample (5 to 9), exposure time was between 10 to 50 and the %T was in the range of 2 to 30. The Widefield imaging conditions maintained are, For Hoechst: Thickness of the Z stack (Sections 20 to 50), section spacing (0.250 to 0.500), thickness of the sample (5 to 9), exposure time was between 10 to 50 and the %T was in the range of 2 to 30.

5.5.3 ROS PROBE 2

Imaging experiments with ROS Probe 2:
Concentration dependent uptake experiments:
ROS probe-2 probe according to the mechanism has the potential of showing fluorescence when it traps the HNO in cell free conditions. The intracellular detection of HNO by ROS probe-2 probe was proven by using Structured illumination microscopy, were an increase in luminescence is observed on increase in addition of Angeli's salt which generated HNO. Angeli's salt concentration was varied from 0 µM to 20 µM during a live cell uptake experiment. The experiment was carried out by incubating the 70% confluent RAW Macrophages with 1 µM ROS probe-2 in DMEM medium with 10% FBS and 1% Penicillin streptomycin at 37°C, 5% CO_2 for 25 minutes. The cells were further treated with varied concentration of Angeli's salt (0 µM to 20 µM) for 30 minutes. The increase in incellular luminescence with increase of generated HNO concentration in the cells was imaged by Structured illumination microscopy (SIM) and also Widefield fluorescence microscopy. Both live and fixed cell imaging were carried out by using Widefield fluorescence microscopy. SIM was carried out only on fixed cells.

Colocalization SIM and Wide field microscopy experiments:

The Co-staining experiments with ER-Tracker Green was carried out by incubating the ER Tracker Green (1 µM) further for 30 minutes after incubating the RAW Macrophages with ROS probe-2 (1 µM) and Angeli's salt (20 µM) initially for 25 minutes each. The cells were then washed three times with DMEM culture media and PBS. The cellular uptake of both the probes are carried out in live cells and then the cells were fixed with 4% paraformaldehyde and mounted and initially checked for proper cell morphology by using light microscope and then imaged by using SIM and Widefield. ROS probe-2 was excited at 568 nm and the emission was collected in the Alexa fluor channel (570 nm to 620 nm) and ER-Tracker Green was excited at 488 nm and the emission was collected in the FITC channel (500 nm to 550 nm). The SIM imaging conditions maintained are: for ER-HNO probe: thickness of the Z stack (Sections 40 to 80), section spacing (0.125 to 0.150), thickness of the sample (7 to 10), exposure time was between 10 to 50 and the %T was in the range of 2 to 30. The SIM imaging conditions maintained are, For ER-Tracker Green: thickness of the Z stack (sections 40 to 80), section spacing (0.125 to 0.150), thickness of the sample (7 to 10), exposure time was between 50 to 100 and the %T was in the range of 10 to 50. The Widefield imaging conditions maintained are: for ROS probe-2: Thickness of the Z stack (Sections 30 to 60), section spacing (0.250 to 0.500), thickness of the sample (7 to 10), exposure time was between 10 to 50 and the %T was in the range of 2 to 30. The Widefield imaging conditions maintained are: for ER-Tracker Green: thickness of the Z stack (Sections 30 to 60), section spacing (0.250 to 0.500), thickness of the sample (7 to 10), exposure time was between 50 to 100 and the %T was in the range of 10 to 50.

5.5.4 ORGANIC PEPTIDE PROBE-A

Concentration dependent uptake of peptide probe-A in RAW Macrophages:

Concentration dependent experiments using peptide probe-A was carried out using minimum concentration in the scale of nanomoles. The probe was very bright even at low concentration and also displayed low toxicity, therefore handling was facile. However, from the microscopy point of view especially SIM, in which loss of emission intensity and brightness is observed during generation of images (during image reconstruction), choosing precise concentrations of drug uptake for generating good SIM images becomes vital for in cell studies. The range of concentration employed varied between 10 nM to 100 nM.

Colocalization experiments for peptide probe-A:

The intracellular organelle localisation of peptide probe-A was tracked using Lyso Tracker Deep Red and Mito Tracker Deep Red. For the colocalisation experiments, RAW Macrophages were incubated with the peptide probe (50 nM) for 12 hours and then the cells were incubated with Lyso Tracker Deep Red (750 nM)/Mito Tracker Deep Red (750 nM) for 30 minutes. The cells were washed regularly three times with DMEM culture media and PBS (two to three times), the cells were then fixed with 4% paraformaldehyde and mounted and navigated initially for proper cell morphology by using light microscope and then imaged by using Widefield microscopy (deconvoluted) using OMX-SIM. Peptide probe-A was excited at 568 nm and its emission was collected in the RFP channel (570 to 620 nm). Lyso Tracker Deep Red/Mito Tracker Deep Red was excited at 644 nm and their emission was collected in the Alexa Fluor 647 channel (> 650 nm). The Widefield imaging conditions were: for peptide probe-A: thickness of the Z stack (Sections 40 to 80), section spacing (0.250 to 0.500), thickness of the sample (8 to 11), exposure time was between 10 to 30 and the %T was in the range of 30 to 60. For Lyso Tracker Deep Red/Mito Tracker Deep Red: thickness of the Z stack (Sections 40 to 80), section spacing (0.250 to 0.500), thickness of the sample (8 to 11), exposure time was between 10 to 50 and the %T was in the range of 30 to 60. SIM imaging conditions maintained are; for peptide probe: thickness of the Z stack (Sections 40 to 80), section spacing (0.125 to 0.150), thickness of the sample (7 to 10), exposure time was between 10 to 50 and the %T was in the range of 2 to 30. For Lyso Tracker Deep Red/Mito Tracker Deep Red: thickness of the Z stack (sections 40 to 80), section spacing (0.125 to 0.150), thickness of the sample (7 to 10), exposure time was between 50 to 100 and the %T was in the range of 10 to 50.

5.6 NANOCAPSULES: SAMPLE PREPARATION, MICROSCOPY

5.6.1 Red and Yellow nanocapsules

Sample preparation:

Cellular uptake experiments of the nanocapsules (Single colour SIM/ Widefield deconvoluted microscopy)

RAW Macrophages were seeded on cover slips (22 mm X 22 mm, 170 ± 5 μm square cover glasses) placed in six well plates in DMEM culture medium containing (10% FBS and 1% Penicillin Streptomycin) for 24 hours at 37°C, 5% CO_2. After 24 hours when 70% confluency was achieved the cells were washed with DMEM culture medium. Cells were then washed thrice with culture medium. After that cells were washed again with Phosphate buffer saline (2 times). After carrying out the live cell uptake of the nanocapsules for 12 hours, the cells were washed with DMEM media, then the cells were fixed with 4% paraformaldehyde for 15 minutes and then washed thrice with PBS and two times and then the coverslips were mounted using mounting medium (Vectashield h-1000). The coverslips were then sealed using nail varnish and the sample were then imaged by SIM, two photon and Widefield fluorescence microscopy (deconvoluted).

5.6.2 Imaging

Cellular uptake of nanocapsules (Single colour imaging)

Single colour SIM experiments for both the nanocapsules were performed for concentration dependent and time dependent uptake experiment on RAW Macrophages. The live cell uptake was carried out in 12 hours. The concentration dependent uptake experiments were carried out in order to determine the extent of uptake happening in RAW Macrophages (Mouse blood murine cell line). The concentration uptake SIM and Widefield images indicated that both the nanocapsules localized mainly in the cytosol region in RAW Macrophages and the optimum concentration is around 15 μg. The Yellow nanocapsules were excited at 488 nm and the emission was collected between 500 to 550 nm, whilst nanocapsules (Red nanocapsules) were excited at 568 nm and emission collected between 570 to 620 nm. For imaging: thickness of the Z stack (Sections 50 to 100), section spacing (0.125 to 0.250), thickness of the sample (8 to 11), exposure time was between 10 to 50 and the %T was in the range of 30 to 80. Concentration dependent uptake experiments were

carried by using SIM and Widefield deconvolution microscopy at diverse range of RNC and YNC concentration ranging from 1 µg to 100 µg. The Widefield conditions maintained were thickness of the Z stack (Sections 40 to 80), section spacing (0.250 to 0.500), thickness of the sample (8 to 11), exposure time was between 10 to 30 and the %T was in the range of 30 to 60.

SIM and Wide field microscopy - Colocalization and Dual colour experiments

SIM was carried out by using the Delta Vision OMX-SIM. For single colour experiments, Yellow nanocapsules were excited at 488 nm and the emission was collected at FITC channel (500 to 550 nm) and Red nanocapsules were excited at 568 nm and the emission was collected at Alexa fluor 568 Channel (570 to 620 nm) of the Delta Vision OMX-SIM. For both the nanocapsules the Structured Illumination experimental condition employed for single colour experiments were mainly dependent on the thickness of the Z stack (Sections 80 to 100), section spacing (0.125 to 0.250), thickness of the sample (8 to 10). The WF conditions maintained were thickness of the Z stack (Sections 40 to 80), section spacing (0.250 to 0.500), thickness of the sample (8 to 11), exposure time was between 10 to 30 and the %T was in the range of 30 to 60. The colocalization experiments were performed with Mito Tracker Green and Mito Tracker Deep Red. The Dual colour experiments were performed with Hoechst.

5.7 NANOPARTICLES: SAMPLE PREPARATION, MICROSCOPY

Cellular uptake of Nanoparticles (NP) (Single colour Imaging)

Single colour Widefield experiments with the nanoparticles were performed for diverse concentrations of NPs from 20 µg to 200 µg/mL. The uptake was carried out for 12 hours. The NPs was excited at 488 nm and the emission was collected at 500 to 550 nm. The Widefield microscopy conditions maintained were thickness of the Z stack (Sections 40 to 80), Section spacing (0.250 to 0.500), thickness of the sample (8 to 11), exposure time was between 10 to 30 and the %T was in the range of 30 to 60.

Two photon microscopy

Two photon microscopy experiments for UCNP were carried out using Zeiss LSM 510Meta upright or inverted confocal microscope. The live cell uptake of the UCNPs (20 μg to 100 μg/mL) was carried out over 12 hours. The UCNP was excited at 975 nm and emission collected between 500 to 550 nm. The LSM 510 Meta microscope has high numerical aperture (NA) lenses (Plan-Neofluar 10x/0.3, Plan-Neofluar 40x/1.3 Oil DIC, C-achroplan NIR 40x/0.8 W and Plan-Apochromat 63x/1.4 Oil DIC), a confocal scan-head (Zeiss LSM510) to select one optical plane at a certain depth in the specimen and make images void of background. As excitation light sources, a set of three lasers: one Argon (458, 477, 488, 514 nm) and two HeNe lasers (543, 633 nm) which fully cover the whole spectrum of excitation needed for the most commonly used fluorophores. The system is equipped with sensitive photomultiplier tubes (PMT) and a META detector system. Two photon images (Single colour) were acquired for NPs (20 μg, 50 μg, 100 μg) cellular uptake on to RAW cells. The data processing was carried out by using FIJI and LSM (Free software).

Colocalization Experiments (Multi colour imaging)

UCNPs and Lyso Tracker Deep Red:

The colocalization experiments were performed using Lyso Tracker Deep Red due to the distinct spectral characteristic of the UCNP. For the colocalization experiments, RAW Macrophages were incubated with UCNPs (50 μg/mL) for 12 hours and then the cells were incubated with Lyso Tracker Deep Red (750 nM) for 30 minutes. The cells were washed three times with DMEM culture media and PBS (two to three times), the cells were then fixed with 4% paraformaldehyde and mounted and initially screened for proper cell morphology by using light microscope and then imaged by using deconvolved Widefield microscopy using OMX-SIM. The UCNPs were excited at 488 nm and the emission was collected in the FITC channel (500 to 550 nm). Lyso Tracker Deep Red was excited at 644 nm and the emission was collected in the Alexa fluor 647 Channel (> 650 nm). The Widefield imaging conditions maintained are, for NP: thickness of the Z stack (Sections 40 to 80), section spacing (0.250 to 0.500), thickness of the sample (8 to 11). Exposure time was between 10 to 30 and the %T was in the range of 30 to 60. For Lyso Tracker Deep Red: thickness of the Z stack (Sections 40 to 80), section spacing (0.250 to 0.500), thickness of the sample (8 to 11), exposure time was between 10 to 50 and the %T was in the range of 30 to 60.

CONCLUSION AND FUTURE WORK

In this research work; metal complexes, organic probes, nanomaterials were optimized as super resolution microscopy probes. Metal complexes with DNA binding capabilities were studied thoroughly and applied as bioimaging probes. The Metal complexes, were optimized as a multimodel super resolution optical microscopy probe. In particular, SIM and STED imaging was carried out using RRP as a cellular imaging probe. The improvement in resolution provided by these two techniques helped us to study structural details of RRP's chromatin and mitochondrial localization. The extraordinary photostability of RRP helped to dissect the three dimensional cross section of stained nuclei with extraordinary super-resolution beyond 50 nm across all dimensions (lateral and axial). Striking dual colour STED and SIM were also obtained. Microscopy studies were extended to optimize the use of organic ROS probes to detect and monitor the generation of ROS inside cells. In particular, ROS generation and spread through the cell was studied using the super resolution SIM technique. Nanocapsules as drug delivery systems and UCNPs as imaging agents were also studied using SIM and other optical microscopy techniques.

Future work will involve extending these studies on super resolution probes to investigate binding towards other organelles and structures. For example, more detailed investigations need to be carried out with regard to the specific DNA binding characteristics exhibited by RRP - and its future derivatives - towards a variety of G-quadruplexes using super-resolution microscopy techniques such as STED and SIM.

REFERENCES

1) Blackburn, G. M.; Gait, J. M. *Nucleic acids in Chemistry and Biology, Oxford University Press,* **1996**

2) Franklin, S. E.; Gosling, R.G. *Nature*, **1953**, *171*, 740–741

3) Jamieson, E. R.; Lippard, S.J. *Chem. Rev.,* **1999**, *99*, 2467

4) Pil, P. M.; Lippard, S. J. *Science*, **1992**, *256* (5054), 234–237

5) Takahara, P. M.; Rosenzweig, A. C.; Frederick, C. A. Lippard, S. J. *Nature*, **1995**, *377*, 649

6) Watson, J. D.; Crick, F. H. C. *Nature*, **1953**, *171*, 737

7) Felsenfeld, G.; Davis, D. R.; Rich, A. *J. Am. Chem. Soc.,* **1957**, *79*, 2023–2024

8) Lippard, S. J.; Berg, J. M. *Principles of Bioinorg. Chem., University Science Books*, Mill Valley, California, **1994**

9) Ren, J.; Chaires, J. B. *Biochem.*, **1999**, *38*, 16067–16075

10) Haq, I.; Lincoln, P.; Suh, D. C.; Norden, B.; Chowdhry, B. Z.; Chaires, J. B. *J. Am. Chem. Soc.,* **1995**, *117*, 4788–4796

11) Patel, D. J. *Proc. Natl. Acad. Sci. U.S.A.,* **1982**, *79*, 6424–6428

12) Goddard, W.; Plaxco, K. *Biochem.,* **1994**, *33*, 3050

13) Jenette, K. W.; Lippard, S. J.; Vassilides, G.A.; Bauer, W.R. *Proc. Natl. Acad. Sci. U.S.A*, **1974**, *71*, 3839

14) Barton, J. K.; Dannenberg, J. J.; Raphael, A.L. *J. Am. Chem. Soc.,* **1982**, *104*, 4967– 4969

15) Barton, J. K.; Danishefsky, A. T.; Goldberg, J.M. *J. Am. Chem. Soc.,* **1984**, *106*, 2172– 2176

16) Rehmann, J. P.; Barton, J.K. *Biochem.,* **1990**, *29*, 1701–1709

17) Jenkins, Y.; Friedman, A. E.; Turro, N. J.; Barton, J. K. *Biochem.*, **1992**, *31*, 10809-10816

18) Barton, J. K.; Goldberg, J. M.; Kumar, C.V.; Turro, N. J. *J. Am. Chem. Soc.,* **1986**, *108*, 2081–2088

19) Puckett, C.A; Barton, J. K. *J. Am. Chem. Soc.,* **2009**, *25*, 8738

20) Kumar, C.V.; Barton, J. K.; Turro, N. J. *J. Am. Chem. Soc.,* **1985**, *107*, 5518–5523

21) Pyle, A. M.; Rehmann, J. P.; Meshoyrer, R.; Kumar, C.V.; Turro, N.J.; Barton, J.K. *J. Am. Chem. Soc.,* **1989**, *111*, 3051–3058

22) Hirot, C.; Lincoln, P.; Norden, B.; *J. Am. Chem. Soc.,* **1993**, *115*, 3448–3454

23) Amouyal, E.; Homsi, A.; Chambron, J. C. *Dalton Trans.,* **1990**, *6*, 1841–1845

24) Mckinley, A.W.; Lincoln, P.; Tuite, E. M. *Coord. Chem. Rev.,* **2011**, *255*, 21, 2676– 2692

25) Friedman, A.E.; Chambron, J.C.; Sauvage, J. P.; *J. Am. Chem. Soc.,* **1990**, *112*, 12, 4960 –4962

26) Fees, J.; kaim, W.; Moscherosch, M.; Matheis, W.; Klima, J.; Krejcik, M.; Zalis, S. *Inorg. Chem.* **1993**, *32*, 166–174

27) Zhang, R.; Ye, Z. Q.; Wang, G.L.; Zhang, W. Z.; Yuan, J. L. *Chem. Eur. J.*, **2010**, *16*, 6884

28) Erkkila, K. E.; Odom, D. T.; Barton, J. K. *Chem. Rev.*, **1999**, *99*, 2777–2795

29) Gunther, K.; Mertig, M.; Seidel, R. *Nucleic acids Res.,* **2010**, *38*, 6526–6532

30) Wang, M. J. *J. Mol. Biol.,* **1965**, *13*, 269–282

31) Wanner, G.; Formanek, H. *J. Struct. Biol.,* **2000**, *132*, 147-161

32) Linde, S.; Kasper, R.; Heilemann, M.; Sauer, M. *Appl. Physics B*, **2008**, *93*, 725–731

33) Dempsey, G. T. *J. Am. Chem. Soc.,* **2009**, *131*, 18192–18193

34) Folling, J. *Nat. Meth.,* **2008**, *5*, 943–945

35) Neault, J. F.; Tajmir-Riahi, H.A. *Biophys. J.,* **1999**, *76*, 2177 - 2182

36) Fernandez-Moreira, V.; Thorp-Greenwood, F. L.; Coogan, M. P. *Chem. Commun.,* **2010**, *46*, 186

37) Amoroso, A. J.; Arthur, R. J.; Coogan, M.P.; Court, J. B.; Fernandez-Moreira, V.; Hayes, A.J.; Lloyd, D.; Millet, C.; Pope, S. J. A. *New. J. Chem.,* **2008**, *32*, 1097

38) Han, Y.; Li, M.; Qiu, F.; Zhang, M.; Zhang, Y.H. *Nat. Commun.,* **2017**, *8*, 1307

39) Rego, E. H.; Shao, L.; Macklin, J. J.; Winoto, L.; Johansson, A. G.; Hughes, N. K.; Davidson, M. W.; Gustaffson, M. G. L. *PNAS,* **2012**, 109, 135–143

40) Suarez, M. F.; Ting, A. Y. *Nat. Reviews*, **2008**, 9, 929–943

41) Butkevich, A. N.; Mitronova, G. Y.; Sidenstein, S. C.; Kolocke, J. L.; Kamin, D.; Meineke, D. N. H; D'Este, E.; Kraemer, P. T.; Danzl, J. G.; Belove, V. N.; Hell, S. W. *Angew. Chem. Int. Ed.,* **2016**, 55, 3290–3294.

42) Butkevich, A. N.; Belov, V. N.; Kolmakov, K.; Sokolov, V. V.; Shojaei, H.; Sidenstein, S. C.; Kamin, D.; Matthias, J.; Vlijm, R.; Engelhardt, J.; Hell, S. W. *Chem. Eur. J.,* **2017**, 23, 12114–12119

43) Cox. S. *Dev. Biol.,* **2015**, 401, 175–181

44) Bates, M.; Hunag, B.; Dempsey, G. T.; Zhunag, X. *Science*, **2007**, 317, 1749–1753

45) Leung, B. O.; Chou, K. C. *Appl. Spectroscopy,* **2011**, 65, 967–980

46) Schermelleh, L.; Heintzmann, R.; Leonhardt, H. *J. Cell. Biol.,* **2010**, 190, 165–175

47) Wegel, E.; Gohler, A.; Langerholm, B. C.; Wainman, A.; Uphoff, S.; Kaufmann, R.; Dobbie, I. M. Sci. Rep., **2016**, *6*, 27290

48) Bates, M.; Hunag, B.; Zhuang, X. *Curr. Opin. Chem. Biol.,* **2008**, 12, 505–514

49) Van de Linde, S.; Loschberger, A.; Klien, T.; Hiedbreder, M.; Wolter, S.; Hielemann, M.; Sauer, M. *Nat. Prot.,* **2011**, 6, 991–1009

50) Persson, F.; Bingen, P.; Staudt, T.; Engelhardt, J.; Tegenfeldt, J. O.; Hell, S. W. *Angew. Chem. Int. Ed.,* **2011**, 50, 5581–5583

51) Godin, A. G.; Lounis, B.; Cognet, L. *Biophys. J.,* **2014**, 107, 1777–1784

52) Musatkina, E.; Amouri, H.; Lamourex, M.; Chepurnykh, T.; Cordier, C. *J. Inorg. Biochem.,* **2007**, *101*, 1086

53) Baggaley, E.; Gill, M.R.; Green, N.H.; Turton, D.; Smythe, C.; Haycock, J.W.; Weinstein, J. A.; Thomas, J. A. *Angew. Chem. Int. Ed.*, **2014**, *53*, 3367-3371

54) Gill*,* M. R.*;* Garcia-Lara, J.; Foster, S. J.; Smythe, C.; Battaglia, G.; Thomas, J. A. *Nat. Chem.* **2009**, *1*, 662–667

55) Lidke, D. S.; Lidke, K. A.; Rieger, B.; Jovin, T. M.; Arndt-Jovin, D. J. *J. Cell. Biol.*, **2005**, *170*, 619–626

56) Huang, B.; Babcock, H.; Zhuang, X., *Cell*, **2010**, *143*, 1047-1058

57) Bates, M.; Dempsey, G. T.; Chen, K.H.; Zhuang, X. *Chem. Phys. Chem.,* **2012**, *13*, 99–107

58) Benke, A.; Manley, S. *Chem. Bio. Chem.,* **2012**, *13*, 298–301

59) Dani, A.; Huang, B.; Bergan, J.; Dulac, C.; Zhuang, X., *Neuron*, **2010**, *68*, 843-856

60) Wu, M.; Huang, B.; Graham, M.; Raimondi, A.; Heuser, J.E.; Zhuang, X.; De Camilli, P., *Nat. Cell Biol.,* **2010** *12*, 902-908

61) Huang, B.; Wang, W.; Bates, M.; Zhuang, X. *Science*, **2008**, *319*, 810-813

62) Rust, M. J.; Bates, M.; Zhuang, X., *Nat. Meth.,* **2006**, *3*, 793-795

63) Betzig, E.; Patterson, G. H.; Sougrat, R.; Lindwasse, O. W.; Olenych, S.; Juan S. Bonifacino, Michael W. Davidson, Jennifer Lippincott-Schwartz, Harald F. Hess, *Science,* **2006,** *313*, 1642-1645

64) Betzig, E. *Science*, **2006**, *313*, 1642-1645

65) Betzig, E.; Trautman, J. K. *Science*, **1992**, *257*, 189-195

66) Gustafsson, M. G.; Shao, L.; Carlton, P. M.; Wang, C. J.; Golubovskaya, I. N.; Cande, W. Z.; Agard, D. A.; Sedat, J. W.; *Biophys. J.*, **2008**, *94*, 4957-4970

67) Gustafsson, M. G. L.; Rego, E. H.; Kner, P.; Shao, L. *Nat. Meth.,* **2011**, 8, 1044-1046

68) Schermelleh, L.; Carlton, P. M.; Haase, S.; Shao, L.; Winoto, L.; Kner, P.; Burke, B.; Cardoso, M. C.; Agard, D. A.; Gustafsson, M. G.; Leonhardt, H.; Sedat, J. W. *Science*, **2008**, *320*, 1332-1336

69) Klar T. A.; Jakobs, S.; Dyba, M.; Egner, A.; Hell, S. W. *Proc. Nat. Acad. Sci.*, **2000**, *97*, 8206-8210

70) Lakadamyali, M.; Babcock, H.; Bates, M; Zhuang, X.; Lichtman, *J. PLoS One*, **2012**, *7*, 30826

71) Shroff, H.; Galbraith, C. G.; Galbraith, J. A.; White, H. ; Gillette, J.; Olenych, S. ; Davidson, M. W. ; Betzig, E. *Proc. Nat. Acad. Sci.*, **2007**, *104*, 20308-20313

72) Van Zanten, T. S; Cambi, A.; Koopman, M.; Joosten, B.; Figdor, C. G.; Garcia-Parajo, M. F.; *Proc Nat. Acad. Sci.* **2009**, *44*, 18557- 18562

73) Ichinose, N.; Tanaka, T.; Kawanishi, S.; Majima, T. *Chem. Phys. Lett.,* **2000**, *326*, 293–298

74) Hein, B.; Willing, K.I.; Hell, S.W. *Proc. Natl. Acad. Sci. U.S.A*, **2008**, *105*, 14271-14276

75) Dyba, M.; Keller, J.; Hell, S. W. *New J. Phys.*, **2005**, *7*, 134

76) Belov, V. N.; Wurm, C. A.; Boyarskiy, V. P.; Jakobs, S.; Hell, S. W. *Angew. Chem. Int. Ed.,* **2010**, *49*, 3520–3523

77) Willig, K. I.; Rizzoli, S. O.; Westphal, V.; Jahn, R.; Hell, S. W. *Nature*, **2006**, *440*, 935-939

78) Donnert, G.; Keller, J.; Wurm, C. A.; Rizzoli, S. O.; Westphal, V.; Schönle, A.; Jahn, R.; Jakobs, S.; Eggeling, C.; Hell, S.W. *Biophys. J.*, **2007**, *92*, 67-69

79) Westphal, V.; Rizzoli, S. O.; Lauterbach, M. A.; Kamin, D.; Jahn, R.; Hell, S. W. *Science*, **2008**, *320*, 246-249

80) Wildanger, D.; Rittweger, E.; Kastrup, L.; Hell, S. W. *Opt. Exp.*, **2008**, *16*, 9614-9621

81) Bates, M.; Huang, B.; Dempsey, G. T. ; Zhuang, X. *Science*, **2007**, *317*, 1749-1753

82) Shroff, H.; Galbraith, C. G.; Galbraith, J. A.; White, H. ; Gillette, J.; Olenych, S. ; Davidson, M. W. ; Betzig, E. *Proc. Nat. Acad. Sci.*, **2007**, *104*, 20308-20313

83) Punge, A.; Rizzoli, S. O.; Jahn, R.; Wildanger, J. D.; Meyer, L.; Schönle, A.; Kastrup, L.; Hell, S. W. *Microsc. Res. Tech.*, **2008**, *71*, 644-650

84) Shtengel, G.; Galbraith, J. A.; Galbraith, C. G.; Lippincott-Schwartz, J.; Gillette, J. M.; Manley, S.; Sougrat, R.; Waterman, C. M.; Kanchanawong, P.; Davidson, M. W.; Fetter, R. D.; Hess, H. *Proc. Nat. Acad. Sci.*, **2009**, *106*, 3125-3130

85) Rusk, N. *Nat. Cell. Biol.,* **2009**, *11***,** S8–S9

86) Baker, M. *Nature,* **2011**, *478***,** 137–142

87) Sokol, D. L., Zhang, X. L.; Lu, P. Z.; Gewitz, A. M. *Proc. Natl. Acad. Sci., U.S.A.* **1998**, *95***,** 11538–11543

88) Denk, W., Strickler, J. H.; Webb, W. W. *Science,* **1990**, *248***,** 73–76

89) Helmchen, F.; Denk, W. *Nat. Meth.,* **2005**, *2***,** 932–940

90) Durr, N. J. Larson, T.; Smith, D. K.; Korgel, B. A.; Sokolov, K.; Ben, Y. A. *Nano Lett.,* **2007**, *7***,** 941–945

91) Pawlicki, M.; Collins, H. A.; Denning, R. G.; Anderson, H. L. *Angew. Chem. Int. Ed.,* **2009**, *48***,** 3244–3266

92) Heilemann, M.; Van de Linde, S.; Schüttpelz, M.; Kasper, R.; Seefeldt, B.; Mukherjee, A.; Tinnefeld, P.; Sauer, M. *Angew. Chem. Int. Ed.,* **2008**, *47***,** 6172–6176

93) Eggeling, C.; Willig, K. I.; Sahl, S. J.; Hell, S. W. *Quart. Rev. Biophys.,* 2015, *48***,** 178–243

94) Gill, M. R.; Thomas, J. A. *Chem. Soc. Rev.,* **2012**, *41***,** 3179–3192

95) Coogan, M. P.; Fernández-Moreira, V. *Chem. Commun.,* **2013**, *50***,** 384

96) Gill, M. R.; Ceccin, D.; Walker, M. G.; Mulla, R. S.; Battaglia, G.; Smythe, C.; Thomas, J. A .*Chem. Sci.,* **2013**, *4***,** 4512–4519

97) Byrne, A., Burke, C. S.; Keyes, T. E. *Chem. Sci.,* **2016**, *7***,** 6551–6562

98) Pellett, P. A.; Sun, X.; Gould, T. J.; Rothman, J. E.; Xu, M. Q.; Corrêa, I. R.; Bewersdorf, J. *Biomed. Opt. Exp.,* **2011**, *2*, 2364–2371

99) Walker. *A Thesis submitted for the Degree of Doctor of Philosophy*, University of Sheffield: Sheffield, **2013**, p. 291

100) Saeed, H. K.; Saeed, I. Q.; Buurma, N. J.; Thomas, J. A. *Chem Eur J*, **2017**, *23*, 5467–5477

101) Tian, X.; Gill, M. R.; Cant, I.; Thomas, J. A.; Battaglia, G. *Chem. Bio. Chem.*, **2011,** *12***,** 548-551.

102) Metcalfe, C.; Adams, H.; Haq, I.; Thomas, J. *Chem. Commun.,* **2003**, *44*, 1152–1153

103) González, V. G. *A Thesis submitted for the Degree of Doctor of Philosophy*, University of Sheffield: Sheffield, **2006**, p. 224

104) Spector, D.L.; Goldman, R. D. Basic *Methods in microscopy – Protocols and Concepts from Cells: A Laboratory Manual*, **2006**, p. 382

105) Punge, A.; Rizzoli, O. S.; Jahn, R.; Wildanger, J. D.; Meyer, L.; Schonle, A.; Kastrup, L.; Hell, S. W. *Microscopy Research and Technique*, **2008**, *71*, 644-650

106) Hesse, M.; Raulf, A.; Pilz, G. A.; Haberlandt, C.; Klien, A. M.; Jabs, R.; Zaehres, H.; Fugermann, C. J.; Zimmermann, K.; Trebicka, J.; Welz, A.; Pfeifer, A.; Roll, W.; Kotlikoff, M. I.; Steinhauser, C.; Gotz, M.; Scholer, H. R.; Fliechmann, B. K. *Nat. Comm.,* **2012**, *3*, 1076

107) Agasti, S. S.; Wang, Y.; Schueder, F.; Sukumar, A.; Jungmann, R.; Yin, P. *Chem. Sci.,* **2017**, 8, 3080–3091

108) Szczurek, A.; Klewes, L.; Xing, J,; Gourram, A.; Birk, U.; Knecht, H.; Dobrucki, J. W.; Mai, S.; Cremer, C. *Nucleic acids Research*, **2017**, *45*, 56

109) Thompson, A. D.; Omar, M. H.; Molina, F. R.; Xi, Z., Koleske, A. J.; Toomre, D. K.; Schepartz, A. *Angew. Chem. Int. Ed.,* **2017**, *56*, 10408–10412

110) Lukinavicius, G.; Blaukopf, C.; Pershagen, E.; Schena, A.; Reymond, L.; Derivery, E.; Gaitan, M. G.; D'Este, E.; Hell, S. W.; Gerlich, D. W.; Johnsson, K. *Nat. Comm.,* **2015**, *6*, 8497

111) Nagerl, U. V.; Willing, K. I.; Hein, B.; Hell, S. W.; Bonhoeffer, T. *PNAS,* **2008**, *105*, 18982–18987

112) Fernandez, A.; Bautista, M.; Stanciauskus, R.; Chung, T.; Pinaud, F. *ACS. Appl. Mat. Interfaces,* **2017***, 9,* 27575–27586

113) Niehorster, T.; Loschberger, A.; Gregor, I.; Kramer, B.; Rahn, H. J.; Patting, M.; Koberling, F.; Enderlien, J.; Sauer, M. *Nat. Meth.,* **2015**, *3*, 257–262

114) Gao, J.; Yang, X.; Djekidel, M. N.; Wang, Y.; Xi, P.; Zhang, M. Q. *Quantitative Biology,* **2016**, *4*, 129–147

115) Hein, B.; Willig, K. I.; Hell, S. W. *PNAS*, **2008**, *105*, 14271–14276

116) Uphoff, S.; Kapanidis, A. N. *DNA Repair*, **2014**, *20*, 32–40

117) Lacoste, T. D.; Michalet, X.; Pinaud, F.; Chemla, D. S.; Alivisatos, A. P.; Weiss, S. *PNAS*, **2000**, *97*, 9461–9466

118) Jin, C.; Liu, J.; Chen, Y.; Guan, R.; Ouyang, C.; Zhu, Y.; Ji, L.; Chao, H. *Sci. Rep.,* **2016**, *6*, 22039

119) Mandal, S.; Poria, D. K.; Ghosh, R.; Ray, P. S.; Gupta, P. *Dalton Trans.,* **2014**, *43*, 17463-17474

120) Mukhopadhyay, S.; Singh, R. S.; Paitandi, R. P.; Sharma, G.; Koch, B.; Pandey, D. S. *Dalton Trans.,* **2017**, *46*, 8572–8585

121) Shao, F.; Elias, B.; Lu, W.; Barton, J. K. *Inorg. Chem.,* **2007**, *46*, 10187–10199

122) Lu, L.; Liu, L. J.; Chao, W. C.; Zhong, H. J.; Wang, M.; Chen, X. P.; Lu, J. J.; Li, R. N.; Ma, D. L.; Leung, C. H. *Sci. Rep.,* **2015**, *5*, 14544

123) Wang, F. X.; Chen, M. H.; Hu, X. Y.; Ye, R. R.; Tan, C. P.; Ji, L. N.; Mao, Z. W. *Sci. Rep.,* **2016**, *6*, 38954

124) Yuan, L.; Wang, L.; Agrawalla, B. K.; Park, S.-J.; Zhu, H.; Sivaraman, B.; Peng, J.; Xu, Q. H.; Chang, Y.-T. *J. Am. Chem. Soc.* **2015**, *137*, 5930–5938

125) Panizzi, P.; Nahrendorf, M.; Wildgruber, M.; Waterman, P.; Figueiredo, J. L.; Aikawa, E.; McCarthy, J.; Weissleder, R.; Hilderbrand, S. A. J. Am. Chem. Soc. **2009**, *131*, 15739–15744

126) Jung, H. S.; Han, J.; Lee, A.-H.; Lee, J. H.; Choi, J.-M.; Kweon, H.-S.; Han, J. H.; Kim, J.-H.; Byun, K. M.; Jung, J. H.; Kang, C.; Kim, J. S.; *J. Am. Chem. Soc*. **2015**, *137*, 3017−3023

127) Chen, X.; Lee, K. A.; Ren, X.; Ryu, J.-C.; Kim, G.; Ryu, J.-H.; Lee, W. J.; Yoon, J. *Nat. Prot.,* **2016**, *11*, 1219-1228

128) Zhou, J.; Li, L.; Shi, W.; Gao, X.; Li, X.; Ma, H. *Chem. Sci*. **2015**, *6*, 4884-4888

129) Ali, F.; Anil, H. A., Taye, N.; Gonnade, R. G.; Chattopadhyay, S.; Das, A. *Chem. Commun*. **2015***, 51*, 16932-16935

130) Kim, J.; Kim, Y. *Analyst* **2014**, 139, 2986–2989

131) Hand book of Biological Confocal Microscopy, third edition, edited by James B. Pawley, *Springer science and Business Media*, *New York* **2006**, 453–469

132) Shao, L.; Kner, P.; Rego, E. H.; Gustafsson, M. G. L. *Nat. Meth.,* **2011**, *8*, 1044

133) Sydor, A. M.; Czymmek, K. J.; Puchner, E. M.; Mennella, V. *Trends in Cell biol.*, **2015**, *25*, 730-748

134) Hobbs, A. J.; Fukuto, J. M.; Ignarro, L. *J. Proc. Natl. Acad. Sci.,* **1994**, *91*, 10992–10996

135) Bartberger, M. D.; Fukuto, J. M.; Houk, K. N. *Proc. Natl. Acad. Sci.*,**2001**, *98*, 2194–2198

136) Shafirovich, V.; Lymar, S. V. *Proc. Natl. Acad. Sci.,* **2002**, *99*, 7340–7345

137) Rosenthal, J.; Lippard, S. J. *J. Am. Chem. Soc*., **2010**, *132*, 5536-5537

138) Rivera-Fuentes, P.; Lippard, S. J.; *Acc. Chem. Res*., **2015**, *48*, 2927-2934

139) Wrobel, A. T.; Johnstone, T. C.; Liang, A. D.; Lippard, S. J.; Fuentes, P. R. *J. Am. Chem. Soc*., **2014**, *136*, 4697-4705

140) Zhou, Y.; Liu, K.; Li, J.-Y.; Fang, Y.; Zhao, T.-C.; Yao, C.; *Org. Lett*., **2011**, *13*, 1290-1393

141) Suárez, S. A.; Bikiel, D. E.; Wetzler, D. E.; Martí, M. A.; Doctorovich, F. *Anal. Chem*., **2013**, *85*, 10262-10269

142) Reisz, J. A.; Zink, C. N.; King, S. B. *J. Am. Chem. Soc*., **2011**, *133*, 11675-11685

143) Reisz, J. A.; Klorig, E. B.; Wright, M.W.; King, S. B. *Org. Lett*., **2009**, *11*, 2719-2721

144) Kawai, K.; Ieda, N.; Aizawa, K.; Suzuki, T.; Miyata, N.; Nakagawa, H. *J. Am. Chem. Soc*., **2013**, *135*, 12690-1269

145) Zhang, H.; Liu, R.; Tan, Y.; Xie, W. H.; Lei, H.; Cheung, H.-Y.; Sun, H. *ACS Appl. Mater. Inter.,* **2015**, *7*, 5438-5443

146) Sena, L.A.; Chandel, N. S. *Mol. Cell*., **2012**, *48*, 158-167

147) Reddy, G. U.; Ali, F.; Taye, N.; Chattopadhyay, S.; Das, A. *Chem. Commun.***, 2015**, *51*, 3649-3652

148) Sunwoo, K.; Bobba, K. N.; Lim, J.-Y.; Park, T.; Podder, A.; Heo, J. S.; Lee, S. G.; Bhuniya, S.; Kim, J. S.; *Chem. Commun*., **2017**, *53*, 1723-1726

149) Jung, H. S.; Lee, J. H.; Kim, K.; Koo, S.; Verwilst, P.; Sessler, J. L.; Kang, C.; Kim, J. S. *J. Am. Chem. Soc.,* **2017**, *139*, 9972–9978

150) Shepherd, J.; Hilderbrand, S. A.; Waterman, P.; Heinecke, J. W.; Weissleder, R.; Libby, P. *Chem. Biol.,* **2007**, *14*, 1221–1231

151) Van Duijnhoven, S. M. J.; Robillard, M. S.; Langereis, S.; Grull, H. *Contrast Media Mol. Imaging.,* **2015**, *10*, 282–308

152) Gao, T.; He, H.; Huang, R.; Zheng, M.; Wang, F. F.; Hu, Y. J.; Jiang, F. L.; Liu, Y. *Dyes and Pigments*, **2017**, *141*, 530–535

153) Lei, E. K.; Kelley, S. O. *J. Am. Chem. Soc.,* **2017***, 139*, 9455–9458

154) Zhu, H.; Fan, J.; Du, J.; Peng, X. *Acc. Chem. Res.,* **2016**, *49*, 2115–2126

155) Zhang, H.; Liu, R.; Tan, Y.; Xie, W. H.; Lei, H.; Cheung, H. Y. ; Sun, H. *ACS. Appl., Mater. Interfaces,* **2015**, *7*, 5438–5443

156) Jiao, X.; Li, Y.; Niu, J.; Xie, X.; Wang, X.; Tang, B. *Anal. Chem.,* **2018**, *90*, 533–555

157) Tan, Y.; Liu, R.; Zhang, H.; Peltier, R.; Lam, Y. W.; Zhu, Q.; Hu, Y.; Sun, H. *Sci. Rep.,* **2015**, *5*, 16979

158) Arthaut, L. D.; Jourdan, N.; Mteyrek, A.; Procopio, M.; Esawi, M. E.; Harlingue, A. D.; Bouchet, P. E.; Witczak, J.; Ritz, T.; Klarsfeld, A.; Birman, S.; Usselman, R. J.; Hoechker, U.; Martino, C. F.; Ahmad, M. *PLOS one,* **2017**, *12*, e0171836

159) Pino, N. W.; Davis, J.; Yu, Z.; Chan, J. *J. Am. Chem. Soc.,* **139**, *51*, 18476–18479

160) Zhou, J.; Li, L.; Shi, W.; Gao, X.; Li, X.; Ma, H. *Chem. Sci.,* **2015**, 6, 4884–4888

161) Zhang, Z.; Zou, Y.; Deng, C.; Meng, L. *Luminescence,* **2016**, 31, 997–1004

162) Lv, J.; Wang, F.; Wei, T.; Chen, X. *Ind. Eng. Chem. Res.,* **2017**, 3757–3764

163) Yuan, L.; Wang, L.; Agarwalla, B. K.; Park, S. J.; Zhu, H.; Sivaraman, B.; Peng, J.; Xu, Q. H.; Chang, Y. T. *J. Am. Chem. Soc.,* **2015**, *137*, 5930–5938

164) Wang, Y.; Wu, L.; Liu, C.; Guo, B.; Zhu, B.; Wang, Z.; Duan, Q.; Ma, Z.; Zhang, X. *J. Mater. Chem. B,* **2017**, *5*, 3377–3382

165) Pan, G. Y.; Jia, H. R.; Zhu, Y. X.; Wang, R. H.; Wu, F. G.; Chen, Z. *ACS Biomater. Sci. Eng.,* **2017**, *3*, 3596–3606

166) Zielonka, J.; Joseph, J.; Sikora, A.; Hardy, M.; Ouari, O.; Vivar, J. V.; Cheng, G.; Lopez, M.; Kalyanaraman, B. *Chem. Rev.,* **2017**, *117*, 10043–10120

167) Han, Y.; Li, M.; Qiu, F.; Zhang, M.; Zhang, Y. H. *Nat. Commun.,* **2017**, *8*, 1307

168) Jean, S. R.; Ahmed, M.; Lei, E. K.; Wisnovsky, S. P.; Kelly, S. O. *Acc. Chem. Res.,* **2016**, *49*, 1892–1902

169) Xu, J.; Zhang, Y.; Yu, H.; Gao, X.; Shao, S. *Anal. Chem.,* **2016**, *88*, 1455–1461

170) Miao, Z.; King, S. B. *Nitric Oxide,* **2016**, *57*, 1–14

171) Wang, X.; Hu, J.; Liu, G.; Tian, J.; Wang, H.; Gong, M.; Liu, S. *J. Am. Chem. Soc.,* **2015**, *137*, 15262-15275

172) Kang, B.; Opatz, T.; Landfester, K.; Wurm, F. R. *Chem. Soc. Rev.,* **2015**, *44*, 8301-8325

173) Jiang, S.; Landfester, K.; D. Crespy. *RSC Adv.,* **2016**, *6*, 104330-104337

174) Tian, H.; Du, J.; Wen, J.; Liu, Y.; Montgomery, S. R.; Scott, T. P.; Aghdasi, B.; Xiong, C.; Suzuki, A.; Hayashi, T.; Ruangchainikom, M.; Phan, K.; Weintraub, G.; Raed, A.; Murray, S. S.; Daubs, M. D.; Yang, X.; Yuan, X. b.; Wang, J. C.; Lu, Y. *ACS Nano*, **2016**, *10*, 7362-7369

175) Hofmeister, I.; Landfester, K.; Taden, A. *Macromolecules*, **2014**, *47*, 5768-5773

176) Tong, R.; Gabrielson, N. P.; Fan, T. M.; Cheng, J. *Curr. Opin. Solid state & mat. Sci.,* **2012**, *16*, 323-332

177) Ihata, O.; Kayaki, Y.; Ikariya, T. *Angew. Chem. Int. Ed.,* **2004**, *43*, 717-719

178) Kathalewar, M. S.; Joshi, P. B.; Sabnis, A. S.; Malshe, V. C. *RSC Adv.,* **2013**, *3*, 4110-4129

179) Nienhaus, K.; Nienhaus, G. U. *Chem. Soc. Rev.,* **2014**, *43*, 1088-1106

180) Caruso, F.; Caruso, R. A.; Möhwald, H. *Science*, **1998**, *282*, 1111

181) Chen, Y.; Chen, H.; Zeng, D.; Tian, Y.; Chen, F.; Feng, J.; Shi, J. *ACS Nano,* **2010**, *4,* 6001–6013

182) Guo, R.; Li, R.; Li, X.; Zhang, L.; Jiang, X.; Liu, B. *Small,* **2009**, *5,* 709–717

183) Yu, J.; Javier, D.; Yaseen, M. A.; Nitin, N.; Kortum, R. R., Anvari, B.; Wong, M. S. *J. Am. Chem. Soc.,* **2010**, *132,* 1929–1938

184) Van Den Dungen, E. T. A.; Klumperman, B. *Journal of Polymer Science: Part A: Polymer chemistry,* **2010**, *48,* 5215–5230

185) Yang, X.; Xiao, Q.; Niu, C.; Jin, N.; Ouyang, J.; Xia, X.; He, D. *J. Mater. Chem. B,* **2013**, *1,* 2757–2763

186) Cheng, L.; Wang, C.; Ma, X.; Wang, Q.; Cheng, Y.; Wang, H.; Li, Y.; Liu, Z. *Adv. Funct. Mater.,* **2013**, 23, 272–280

187) Kothamasu, P.; Kanumur, H.; Ravur, N.; Maddu, C.; Parasuramrajam, R.; Thangavel, S. *BioImpacts,* **2012**, *2,* 71 – 81

188) Adler, J.; Parmryd, I. *Cytometry Part A,* **2010**, *77A,* 733–742

189) Chelora, J.; Zhang, J.; Chen, R.; Chandran, H. T.; Lee, C. S. *Nanotechnology,* **2017**, *28,* 285102

190) Liang, L.; Care, A.; Zhang, R.; Lu, Y.; Packer, N. H.; Sunna, A.; Qian, Y.; Zvyagin, A. V. *ACS Appl. Mater. Interfaces,* **2016**, *8,* 11945–11953

191) Wang, X. D.; Achatz, D. E.; Hupf, C.; Sperber, M.; Wegener, J.; Bange, S.; Lupton, J. M.; Wofbeis, O. S. *Sensors and Actuators B,* **2013**, *188,* 257–262

192) Bazylinska, U.; Wawrzynczyk, D.; Kulbacka, J.; Frackowiak, R.; Cichy, B.; Bednarkiewicz, A.; Samoc, M.; Wilk, K. A. *Sci. Rep.,* **2016**, *6,* 29746

193) Park, Y.; Lee, K. T.; Suh, Y. D.; Hyeon, T. *Chem. Soc. Rev.,* **2015**, *44,* 1302–1317

194) Bejar, M. G.; Soriano, L. F.; Prieto, J. P. *Front. Bioeng. Biotech.,* **2016**, *4,* 3389

195) Schermelleh, L.; Heintzmann, R.; Leonhardt, H. *J. Cell. Biol.,* **2010**, *190,* 165–175

196) Lukinavičius, G.; Umezawa, K.; Olivier, N.; Honigmann, A.; Yang, G.; Plass, T.; Mueller, V.; Reymond, L.; Corrêa, I. R.; Luo, Z. G.; Schultz, C.; Lemke, E. A.; Heppenstall, P.; Eggeling, C.; Manley, S.; Johnsson, K. *Nat. Chem.,* **2013**, *5,* 132–139

197) Meyer, L.; Wildanger, D.; Medda, R.; Punge, A.; Rizzoli, S. O.; Donnert, G.; Hell, S. W. *Small,* **2008**, *4,* 1095–1100

198) Eggeling, C.; Ringemann, C.; Medda, R.; Schwarzmann, G.; Sandhoff, K.; Polyakova, S.; Belov, V. N.; Hein, B.; Von Middendorff, C.; Schönle, A.; Hell, S. W. *Nature,* **2009**, *457,* 1159–1162

199) Bottanelli, F.; Kromann, E. B.; Allgeyer, E. S.; Erdmann, R. S.; Wood Baguley, S.; Sirinakis, G.; Schepartz, A.; Baddeley, D.; Toomre, D. K.; Rothman, J. E.; Bewersdorf, J. *Nat Commun.,* **2016**, *7,* 10778

200) Lukinavičius, G.; Reymond, L.; Umezawa, K.; Sallin, O.; D'Este, E.; Göttfert, F.; Ta, H.; Hell, S. W.; Urano, Y.; Johnsson, K. *J. Am. Chem. Soc.,* **2016**, *138,* 9365–9368

201) Gustafsson, M. *J. Micros.,* **2000**, *198,* 82–87

202) Gustafsson, M. *Proc. Natl. Acad. Sci. U.S.A.,* **2005**, *102,* 13081–13086

203) Gill, M. R. *A Thesis submitted for the Degree of Doctor of Philosophy,* University of Sheffield: Sheffield, **2010**, p. 232

APPENDIX

Chapter 2

❖ **Sreejesh Sreedharan**, Martin R Gill, Esther Garcia, Hiwa K Saeed, Darren Robinson, Aisling Byrne, Ashley J Cadby, Tia E Keyes, Carl G Smythe, Patrina Pellett*, Jorge Bernardino de la Serna*, **Jim A Thomas*** Multi model Super-resolution microscopy using a Transition metal complex probe provides unprecedented capabilities for imaging both nuclear chromatin and mitochondria. *Journal of the American Chemical Society*, **2017,** *139***,** 15907-15913

❖ **Sreejesh Sreedharan**[#], Alessandro Sinopoli[#], Paul. J. Jarman, Darren Robinson, Christopher Clemmet, Paul A. Scattergood, Craig R. Rice, Carl. G. W. Smythe, **James A Thomas***, Paul I.P. Elliott* Mitochondria-localizing DNA binding biscyclometalated phenyltriazole iridium(III) dipyridophenazene complexes: syntheses and cellular imaging properties. *Dalton Transactions*, **2018**, *47,* 4931-4940
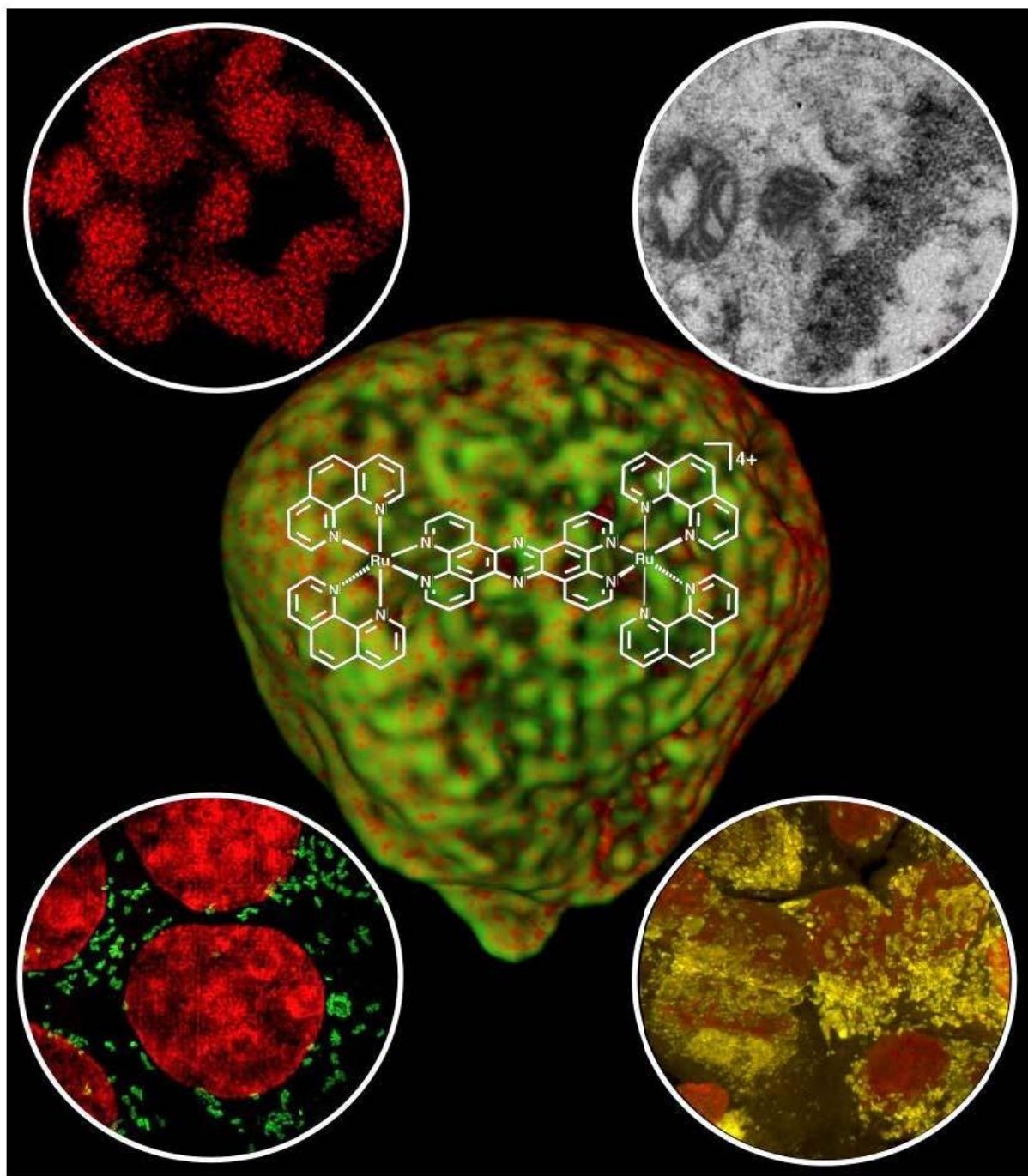
Chapter 3

❖ Firoj Ali, **Sreejesh Sreedharan**, Anila H A, Hiwa K Saeed, Carl G Smythe, **Jim A Thomas***, Amitava Das* A Super-resolution probe to monitor HNO levels in the Endoplasmic Reticulum of RAW cells**.** *Analytical Chemistry,* **2017**, *89*, 12087-12093

❖ Firoj Ali[#], Sunil Aute[#], **Sreejesh Sreedharan**[#], Anila H A, Hiwa K Saeed, Carl G Smythe*, **Jim A Thomas***, Amitava Das* A Luminescent probe for Super-resolution imaging of Endogenous HOCl in multiple Cellular Compartments in Macrophages. *Chemical Communications,* **2018,** *54***,** 1849-1852

Chapter 4

❖ Sumit Kumar Pramanik[#], **Sreejesh Sreedharan**[#], Harwinder Singh, Nicola H Green, Carl G Smythe, **Jim A Thomas***, Amitava Das* Imaging cellular trafficking processes in real time using lysosome targeted up-conversion nanoparticles. *Chemical Communications,* **2017**, *53*, 12672-12675

* Corresponding author
# These authors contributed equally